

UCL

Engineering a Tissue Mimic for Predictive Nanoparticle Assessment

Noah S Tan

For the degree of Doctor of Philosophy

2015

Declaration

I, Noah Tan, confirm that the work presented in this thesis is my own. Where information has been derived from other sources, I confirm that this has been indicated in the thesis.

A handwritten signature in black ink, consisting of stylized, overlapping loops and a long horizontal line extending to the right.

Acknowledgements

With land now appearing on the horizon, my time on this vessel of discovery is coming to an end. It has been both an intellectual and emotional odyssey which has helped me to develop professionally as well as personally. Professor Robert Brown has been immensely supportive with his intellectual guidance, and his inimitable passion for his work is an inspiration. I am very grateful for the huge amount of patience he has shown me. It has been a privilege working with him and I only hope this work will do him proud. I would like to thank Professor Vivek Mudera for the invaluable help and advice he has given me. I owe it to Rebecca Porter, Katerina Stamati, Dr Tijna Alekseeva, Dr Hedeer Jawad, Prasad Sawadkar, Josephine Wong, Tarig Magdeldin and Claire Walsh for making this journey more manageable. Without their assistance and friendship, it would have been a lot more painstaking. I would also like to thank Lyn Vuong who has continuously encouraged me and supported me through this arduous voyage. Last, but not least, I am indebted to my parents who have afforded me the opportunity to travel halfway across the world to live and study here in London. They have always shown faith in my every endeavor. This is for them.

Abstract

Bio-scientific research has relied heavily on models of cell monolayers cultured on plastic. For most cell types, this does not represent their *in vivo* tissue organisation well. As a result they behave differently *in vitro* from *in vivo*, leading to poorly predictive data. Plastic compression (PC) of collagen is used to engineer constructs with more tissue-like conditions. The aim of this study was to test the feasibility of using these constructs as a three-dimensional tissue model for assessing the fate of hyaluronan nanoparticles (HA-NP).

Collagen hydrogels were seeded with cells and HA-NP and subjected to PC. Due to their small size, HA-NP retention following PC was investigated. HA-NP uptake by cells was then compared to conventional monolayer cell cultures. $19.1 \pm 1.2\%$ of the initial HA-NP load was retained following PC, which could be increased to $31.1 \pm 3.1\%$ by multi-layering. This entrapment was found to be largely physical as HA-NPs were released from the construct following cellular remodeling, but not without it. Cells in monolayer reached their maximum HA-NP uptake in 3 days whilst cells in collagen peaked at 7 days. This maximum uptake was 60.1 a.u., twice as large as that of 3D-cultured cells (32.8 a.u). A novel method was developed to analyse local collagen densities which revealed particular collagen distributions in micro-patterned constructs depending on the shape of template used; round grooves had a $21.4 \pm 4\%$ increase in collagen density at their bases, whilst rectangular grooves displayed two peaks corresponding to their internal corners, which were $15.2 \pm 4\%$ and $16.9 \pm 3\%$ denser than the unpatterned regions.

This work has enabled greater understanding of the PC and micro-moulding which will aid in creating more complex tissue constructs in a predictable and controlled way. The importance of 3D tissue organisation in *in vitro* models, particularly for nanoparticle testing, has also been demonstrated in this work.

Table of Contents

<u>Table of Contents</u>	6
<u>List of Figures</u>	9
<u>List of Tables</u>	14
<u>Chapter 1: Introduction</u>	15
<u>1.1. Cell-ECM interactions</u>	18
<u>1.2. What is 3D to cells?</u>	27
<u>1.3. Nanoparticles as drug delivery systems</u>	30
<u>1.4. Evaluation of therapeutics</u>	33
<u>1.5. Toxicological testing</u>	37
<u>1.6. Non-2D systems</u>	40
<u>1.6.1. Sponges</u>	41
<u>1.6.2. Cell aggregates</u>	42
<u>1.6.3. Cellular Multilayers</u>	44
<u>1.6.4. Fibrillar biomaterials</u>	45
<u>1.6.5. Decellularised tissues</u>	47
<u>1.6.6. Hydrogels</u>	48
<u>1.7. Collagen</u>	51
<u>1.8. Embossing of soft substrates</u>	55
<u>1.9. Plastic compression</u>	59
<u>1.10. Thesis overview</u>	64
<u>Chapter 2: Materials & Methods</u>	68
<u>2.1. Cells</u>	68
<u>2.2. Preparation of hyaluronan nanoparticle suspension</u>	68
<u>2.3. Preparation of acellular collagen gels</u>	69
<u>2.4. Preparation of cellular collagen gels</u>	70
<u>2.5. Preparation of nanoparticle-loaded collagen gels</u>	70
<u>2.6. Preparation of nanoparticle-loaded cellular collagen gels</u>	71
<u>2.7. Plastic compression of collagen gels</u>	71
<u>2.8. Creating constructs with a horizontal density gradient</u>	72
<u>2.9. Micro-moulding – Introducing surface patterns</u>	73
<u>2.10. Histology</u>	74
<u>2.11. Staining</u>	75
<u>2.11.1. Haematoxylin and Eosin</u>	75
<u>2.11.2. Sirius red</u>	75
<u>2.11.3. Hoechst 33342 and Phalloidin</u>	76
<u>2.12. Microscopy</u>	76
<u>2.12.1. Light microscopy (Olympus BH-2, Olympus Camedia 2020Z)</u>	76
<u>2.12.2. Fluorescence microscopy (Olympus BX61)</u>	77
<u>2.12.3. Scanning electron microscopy (Jeol, JSM 5500 LV, Japan)</u>	77
<u>2.13. Image analysis</u>	77
<u>2.13.1. Horizontal gradient constructs</u>	77
<u>2.13.2. Micro-moulding analysis</u>	78
<u>2.13.3. Fluid leaving surface analysis</u>	78

Table of Contents

2.14.	<u>Fluorometry</u>	79
2.15.	<u>Statistical analyses</u>	81
Chapter 3: Methods Development & the Fluid Leaving Surface		82
3.1.	<u>Scaling up the multi-well compression system</u>	82
3.2.	<u>Collagen density analysis</u>	88
3.2.1.	<u>Image processing</u>	90
3.2.2.	<u>Validation</u>	93
3.2.3.	<u>Image analyses</u>	97
3.3.	<u>Lein optical confocal device measurements</u>	99
3.3.1.	<u>Interpretation of scans (in collaboration with Dr D Daly, Lein Applied Diagnostics, UK)</u>	104
3.3.2.	<u>Detection of variables within compressed constructs</u>	110
3.4.	<u>Primary and secondary FLS generation</u>	113
3.5.	<u>Discussion</u>	128
Chapter 4: Characterisation of Compressed Collagen Constructs/Measurement of Compressed Collagen Scaffold Thickness		130
4.1.	<u>Introduction</u>	130
4.2.	<u>Scaling down (in construct size)</u>	132
4.3.	<u>Thickness measurements</u>	134
4.4.	<u>Materials & Methods</u>	135
4.4.1.	<u>Preparation of plastically compressed collagen</u>	135
4.4.2.	<u>Determination of the rate of fluid removal during plastic compression</u> 135	
4.4.3.	<u>Measurement of total fluid lost due to plastic compression</u>	135
4.4.4.	<u>Lein CTS-2 measurements</u>	136
4.4.5.	<u>Comparison of cell proliferation</u>	136
4.5.	<u>Results</u>	138
4.5.1.	<u>Determination of rate of fluid loss using paper plungers and weights</u> 138	
4.5.2.	<u>Determination of rate of fluid loss using fibre plungers</u>	139
4.5.3.	<u>Collagen construct thickness changes after compression</u>	153
4.5.4.	<u>Calculations of the hydraulic resistance of the FLS (R_{FLS})</u>	156
4.5.5.	<u>Thickness measurements</u>	163
4.5.6.	<u>Investigation of the re-swelling of compressed constructs</u>	164
4.5.7.	<u>Cell proliferation comparison</u>	168
4.6.	<u>Discussion</u>	171
4.7.	<u>Conclusion</u>	175
Chapter 5: Micro-Density Analysis of Compressed Collagen Constructs: Rapid Method Development		177
5.1.	<u>Introduction</u>	177
5.2.	<u>Materials & Methods</u>	181
5.3.	<u>Results</u>	184
5.3.1.	<u>Groove depth infidelity</u>	184
5.3.2.	<u>Density analysis development</u>	186
5.3.3.	<u>Micro-moulding - image analysis</u>	187

Table of Contents

5.3.4.	<u>Full thickness transverse density analysis</u>	192	
5.4.	<u>Discussion</u>	196	
5.5.	<u>Conclusions</u>	202	
<u>Chapter 6: Understanding Local Tissue Fate of Nanoparticles: The Insufficiency of <i>Non-2D</i> Cell Culture</u>			203
6.1.	<u>Introduction</u>	203	
6.2.	<u>Materials & Methods</u>	208	
6.2.1.	<u>Multilayering</u>	208	
6.2.2.	<u>Preparation of chitosan-Nile Red nanoparticles</u>	208	
6.2.3.	<u>Riboflavin crosslinking</u>	210	
6.2.4.	<u>Determination of free FITC</u>	210	
6.2.5.	<u>Measurement of cellular uptake of HA-NP</u>	210	
6.2.6.	<u>2D cell culture and measurement of cellular uptake of HA-NP</u>	211	
6.2.7.	<u>Histology and fluorescence microscopy</u>	211	
6.3.	<u>Results</u>	213	
6.3.1.	<u>Plastic compression, and the mobility of HA-NP</u>	213	
6.3.2.	<u>Hyaluronan nanoparticle release from compressed constructs</u>	215	
6.3.3.	<u>Hyaluronan nanoparticle entrapment within compressed collagen constructs</u>	219	
6.3.4.	<u>Chitosan nanoparticle entrapment within compressed collagen constructs</u>	223	
6.3.5.	<u>Hyaluronan nanoparticle entrapment within compressed collagen constructs in the presence of cells</u>	226	
6.3.6.	<u>Riboflavin crosslinking</u>	230	
6.3.7.	<u>Determination of release/escape of free FITC from HA-nanoparticles</u> 233		
6.3.8.	<u>Cell uptake of hyaluronan nanoparticles</u>	235	
6.3.9.	<u>2D versus 3D cell culture of HA-NP uptake</u>	236	
6.4.	<u>Discussion</u>	241	
6.5.	<u>Conclusions</u>	251	
<u>Chapter 7: General Discussion</u>			253
7.1.	<u>Summary</u>	253	
7.2.	<u>Conclusions</u>	257	
7.3.	<u>Further work</u>	257	
<u>References</u>			261
<u>List of Conference Abstracts</u>			296
<u>List of Publications</u>			298

List of Figures

Chapter 1

Figure 1.1 Cell-matrix interactions initiate intracellular signaling pathways either as responses to external forces (outside-in signaling) or as feedback through cell contractility (inside-out signalling). 20

Figure 1.2 Schematic depicting the 3D cell-matrix interactions with extracellular matrix components. 25

Figure 1.3 Diagram of a cell and its interactions with its substrate when cultured in 2D and 3D. Cells only interact with their substrate via their ventral surface when cultured on a flat surface, whereas cells in 3D have cell-substrate interactions all around. 29

Chapter 2

Figure 2.1 Determination of HA-NP size by TEM and DLS. 79

Figure 2.2 Calibration curve of HA-NP fluorescence in in the range of 0 – 0.05 µg/ml. 81

Chapter 3

Figure 3.1 Photographs of the custom-built machine used to produce paper plungers, a paper plunger used for 24-well plates and of fibre plungers. 86

Figure 3.2 Absorption of water by paper and fibre plungers. 87

Figure 3.3 Image processing for the collagen density analysis. 91

Figure 3.4 Digital image of a Sirius red-stained compressed collagen construct after conversion from colour to greyscale (A) and then inverted (B). 92

Figure 3.5 Schematics representing the shapes of gels formed with 2, 3 and 4 ml collagen cast at an angle of 25° and plastic compression (upward flow method) of a collagen gel cast with an angle. 95

Figure 3.6 An example graph of the density analysis results from one graded construct. 95

Figure 3.7 Graph of measured gradients of constructs. 96

Figure 3.8 Screenshot image of the analysis of local collagen density distributions in a compressed collagen construct (marked out by the red dotted

List of Figures

lines) using cross-section measurement domains (yellow rectangles) and the corresponding graph of measured mean pixel intensity values.	98
Figure 3.9 Diagrams and photographs of the CTS-2.	101
Figure 3.10 Schematic depicting the light paths in the CTS-2.	102
Figure 3.11 Schematic demonstrating how the CTS-2 works and an example CTS-2 measurement of a compressed collagen construct using Lein's pControl software.	103
Figure 3.12 Diagram depicting the laser path during a scan of a construct.	105
Figure 3.13 Screenshots of the software graphical user interface (GUI).	106
Figure 3.14 Thickness measurements of collagen constructs using the Lein CTS-2 and histology.	109
Figure 3.15 A screenshot of a scan of a 1.5 ml (initial volume) compressed collagen construct and a scan of a triple-layered compressed collagen construct.	112
Figure 3.16 Histology image of an acellular compressed collagen construct stained with eosin only.	113
Figure 3.17 Schematic on FLS and secondary FLS formation and collagen accumulation during the compression of thinner gels and thicker gels.	117-118
Figure 3.18 Fluorescence micrographs of cross-sections of compressed collagen constructs.	121
Figure 3.19 Light micrographs of cross-sections of 0.5, 1.0, 1.5 and 2.0 ml (initial volume) compressed collagen constructs stained with Sirius red, showing the distribution of collagen within the constructs.	122
Figure 3.20 Analysis of fluorescent HA-NP distribution within compressed collagen constructs.	125
Figure 3.21 Analysis of Sirius red (collagen) distribution within compressed collagen constructs.	127
Chapter 4	
Figure 4.1 Time-lapse photographs of a collagen gel under-going plastic compression.	131
Figure 4.2 Photograph of the components used for plastic compression.	133

List of Figures

- Figure 4.3 Plots showing the cumulative weight gained by paper or fibre plungers during compression to compare and contrast the rates of fluid absorption between plunger types. 141
- Figure 4.4 Graphs showing the time taken to reach completion of compression of 0.5, 1.0, 1.5 and 2.0 ml gels using either paper or fibre plungers. 142
- Figure 4.5 Graphs showing the rates of compression as determined by fluid loss. 146
- Figure 4.6 Graphs of the rates of fluid loss during the first 5 minutes of compression using either paper plungers (A) or fibre plungers (B) for different initial gel volumes. 147
- Figure 4.7 Graphs of the rates of fluid loss during the first 5 minutes of compression using either paper plungers with a weight or fibre plungers. 148
- Figure 4.8 Graph showing the percentage of total fluid lost from gels of different starting volumes and compressed using the two different plunger types, as determined by plunger weight measurements. 149
- Figure 4.9 Final construct weight immediately after compression using paper plungers and a fixed load or fibre plungers. 152
- Figure 4.10 Total fluid loss from gels of different initial volumes and compressed using the two different plunger types determined by final construct weight. 153
- Figure 4.11 Calculated hydraulic resistances generated in 0.5, 1.0, 1.5 and 2.0 ml constructs during the first 5 min of compression using paper or fibre plungers. 161
- Figure 4.12 Calculated hydraulic resistances generated in 0.5, 1.0, 1.5 and 2.0 ml constructs during compression using paper or fibre plungers. 162
- Figure 4.13 Thickness measurements of 0.5, 1.0, 1.5 and 2.0 ml constructs compressed with paper plungers or fibre plungers immediately after compression and after 24 hours and the difference between thicknesses at $t = 0$ and $t = 24$ h. 166
- Figure 4.14 Compressed construct thickness measurements immediately after compression and 24 H later following fixation with formalin. 167
- Figure 4.15 Cell proliferation rates, as determined by alamar blue reduction, of cells cultured in 2D on tissue culture plastic, compliant uncompressed collagen hydrogels and stiffer compressed collagen constructs, and in 3D within

List of Figures

uncompressed collagen hydrogels and within compressed collagen constructs . 170

Chapter 5

Figure 5.1 Schematic of the plastic compression set-up. Collagen gels were set in multi-well plates (12-well plates in this case). 182

Figure 5.2 Measured dimensions of round grooves produced using 100 or 200 μm stainless steel wires. 183

Figure 5.3 Histological image of a construct micro-moulded with 100 μm stainless steel wires stained with eosin and a SEM micrograph of a collagen construct micro-moulded with stainless steel wires of 200 μm diameter. 187

Figure 5.4 Collagen displacement analysis of an unpatterned (flat, non-micro-moulded) construct, a construct patterned with glass fibres and a construct patterned with a Kapton template. 190

Figure 5.5 Graphs of the mean percentage increase in intensity of grooved regions. 191

Figure 5.6 Image analysis of an unpatterned PC scaffold, one that is patterned with round grooves, and one with rectangular grooves. 194

Figure 5.7 Graph showing the ratios of the pixel intensities at the top surface/bottom surface of unpatterned, rectangular-grooved and round-grooved constructs. 195

Figure 5.8 Collagen constructs stained with sirius red. 198

Figure 5.9 Schematic of secondary FLS formation and fluid expulsion from under the template. 200

Figure 5.10 A schematic diagram of a region of a PC construct embossed with a rectangular groove. 201

Chapter 6

Figure 6.1 Schematic depicting the arrangements of cells in/on different substrates. 207

Figure 6.2 Determination of GCPQ-NR nanoparticle size by SEM and DLS. 209

Figure 6.3 Fluorescence micrographs of cross-sections of compressed nanoparticle-loaded constructs of different initial volumes. 214

List of Figures

Figure 6.4	Retention of HA-nanoparticles in collagen scaffolds cultured over a period of 3 weeks.	217
Figure 6.5	Fluorescence micrographs of sections of HA-NP-loaded compressed constructs, with or without cells, cultured over a period of 3 weeks.	218
Figure 6.6	Photographs of HA-NP-loaded and unloaded collagen constructs.	221
Figure 6.7	Results of the entrapment of HA-NP in constructs following compression with micrographs of cross-sections of different construct variants.	222
Figure 6.8	Photographs of GCPQ-NR-loaded and unloaded collagen constructs.	224
Figure 6.9	Results of the entrapment of GCPQ-NR in constructs following compression with micrographs of cross-sections of different construct variants.	225
Figure 6.10	Diagram depicting the different collagen construct variants used to test the hypothesis that the inclusion of cells in collagen layers would increase nanoparticle entrapment.	227
Figure 6.11	Fluorescence micrographs of double layered compressed constructs, with a 0.5 ml nanoparticle-loaded bottom layer and a 'blank' or a cellular 2.0 ml upper layer.	228
Figure 6.12	Entrapment efficiency of HA-NP in different construct variants with/without cells.	229
Figure 6.13	Box-and-whisker plot showing the percentage of HA-NP retained in compressed constructs following cross-linking with riboflavin.	232
Figure 6.14	Schematic of the formation (A) of FITC-loaded hyaluronan nanoparticles, with most of the FITC encapsulated within nanoparticles, but a small proportion remains loosely associated or free.	234
Figure 6.15	Entrapment of HA nanoparticles following plastic compression and determination of 'free' FITC in HA-NP suspension.	235
Figure 6.16	Fluorescence micrographs of cells culture as a monolayer or cells initially cultured in 3D then re-plated onto 2D for imaging.	238
Figure 6.17	Graph comparing nanoparticle uptake by cells cultured in 2D or in 3D as determined by cell fluorescence.	240

List of Tables

Figure 6.18 Schematic illustrating the trapping and escaping of nanoparticles/free FITC during compression.	244
Figure 6.19 Schematic of the process of compressing a collagen hydrogel.	245
Figure 6.20 Schematic illustrating the trapping of nanoparticles during compression in single layer, or double layers.	246
Figure 6.21 Schematic depicting cellular exposure to nanoparticles.	252

List of Tables

Chapter 4

Table 4.1 Total fluid loss and overall rates of fluid loss following compression using paper plungers.	139
Table 4.2 Total fluid loss and overall rates of fluid loss following compression using fibre plungers.	140
Table 4.3 Changes in thickness of collagen gels in the 24-well format following plastic compression.	155
Table 4.4 R_{FLS} of constructs of different initial volumes during the first 5 minutes of compression using paper plungers with a fixed load.	158
Table 4.5 : R_{FLS} of constructs of different initial volumes during the first 5 minutes of compression using fibre plungers.	160

Chapter 5

Table 5.1 Area of pattern template in contact with collagen construct.	198
--	-----

Chapter 6

Table 6.1 Amount of fluid remaining in compressed constructs.	236
---	-----

Chapter 1: Introduction

For many years, cell monolayers have been the standard technique for cell culture because of the convenience and ease of growing cells on flat surfaces such as Petri dishes, tissue culture flasks and multi-well plates. Despite the monolayer actually having a thickness, such culture systems are generally said to be 2-dimensional (2D). These 2D systems are routinely used for many different assays by many laboratories including those in drug discovery. However, it has been known for some time that there are more similarities in the phenotypes and behaviour of cells in whole tissues to cells grown in 3D *in vitro* than in 2D culture [1-5].

Monolayer cell culture has enabled the discoveries of what we know today about cell behavior and processes, and has undoubtedly led to the acquisition of a large amount of knowledge. However, the growth of the field of tissue engineering has led to the exposure of the limitations of this 2D culture. Fibroblasts have been shown to behave differently in terms of cell signaling, migration, proliferation and maturation when cultured in a 3D environment than when grown on stiff tissue culture plastic (TCP) [2,6-10].

As a result, the successful translation of knowledge from conventional 2D cell culture assays to animal models or clinical trials is widely considered to be poor. Many therapeutic candidates have initially shown potential overcoming the first hurdle (2D assays) but this success does not replicate when brought up a level to

animal models. Compounds which are apparently safe in monolayer culture, prove to have serious and unpredicted toxicity problems. Drugs developed to have one function end up with additional functionalities *in vivo*. This has resulted in huge losses of money, animals and time. Therefore, the translation of success from *in vitro* assays to *in vivo* studies has to be vastly improved in order to reduce such inefficiencies. It would thus be advantageous to have an intermediate step between monolayer cell culture and *in vivo* systems.

A logical step would be to recreate 3D models of the *in vivo* environment in a dish. This may be done using *ex vivo* tissues in culture, or developing 3D *in vitro* models that represent native tissue structure and organisation. *Ex vivo* cultures contain almost all the components and complexities that are present in the body. However, the supply for *ex vivo* cultures is limited, samples are undefined, inter- and intra-sample variations are likely and are only viable for a short amount of time (a few days at most). Therefore, creating an artificial environment that mimics native tissue using a tissue engineering approach is a good alternative for studying cell behavior in a tissue environment.

However, fabricating a native 3D 'model tissue' from scratch does require a clear understanding of which environmental cues are key to the 3D life of resident cells. Growth factors are important in determining and regulating cell fate and function, with the effects of autocrine and paracrine signalling clearly seen during embryonic development [11]. The development of the ventral spinal cord in mouse is dependent on a gradient of sonic hedgehog (SHH) emanating from the ventral floor

plate. Particular gene expression profiles and cell fates could be induced by controlling the concentration of SHH [12]. The distribution of soluble growth factors is controlled by the extracellular matrix. Movement through a tissue is hindered by the network of matrix proteins and molecules. Additionally, some growth factors bind to the ECM, preventing further diffusion. Furthermore, the cell-ECM interactions have been shown to influence cell morphology and behaviour through altering cytoskeletal organisation and mechanical signalling [13,14].

Almost all cells in tissues are embedded within a fibrous meshwork of extracellular matrix (ECM) components with complex 3D organisation particular to any given tissue type [15]. This is opposed to cells living on the surface of their support materials or in large cavernous holes (many times their own diameter). The ECM is an intricate network of a variety of fibrillar proteins, mainly collagen with others such as laminin, and polysaccharides which provides structural support to resist tension and compression [9,16]. Cells are able to sense these mechanical forces of the surrounding matrix because of the intimate connection they have with the ECM through their cytoskeleton and membrane receptors. Thus, cells not only communicate with each other, but also with the ECM. It is known that this cell-ECM connection is not inert, and is important in the regulation of cell migration, differentiation and proliferation as the ECM presents cells with not only mechanical, but also biochemical cues [17-21]. There have been several studies showing that cells behave differently when grown in 2D or in 3D [6,22-26]. For example, human embryonic stem cells (hESCs) cultured in collagen gels differentiated into hepatocyte-like cells, displaying characteristic ultrastructural

features, morphologies and gene expression patterns indicative of hepatocytes in the body. Murine ESCs (mESCs) cultured in fibrin gels showed a greater capacity for migration, proliferation and differentiation compared to mESCs cultured on top of fibrin gels (in 2D) [27]. Healthy mammary epithelial cells, when cultured in a 3D environment, behaved more naturally and differentiated into acini that resembled the original tissue, whereas they behaved more like tumour cells when cultured in conventional monolayer cultures [28]. Embryonic stem cells displayed greater chondrogenic potential when cultured in 3D than in a 2D monolayer [29]. Bott et al. showed that primary human fibroblasts exhibited different proliferation profiles when cultured in collagen gels or on tissue culture plastic [30]. In addition, primary human hepatocytes cultured in 2D were subject to time-dependent dedifferentiation probably due to excessive stress experienced by the cells in an unnatural environment. This was overcome when the cells were grown within collagen gels [31].

1.1. Cell-ECM interactions

The differences observed when cells are cultured in 2D or in 3D are due to the differences in how the cell interacts with its microenvironment. The added dimensionality, the composition, the flexibility and the stiffness of the substrate may all affect how the cell 'feels' its surroundings and determine how it responds (Figure 1.1). The cytoskeleton of cells is affected by the mechanical properties of their substrate. Cells attach to and pull on their substrates to gauge the stiffness of

their surroundings, and respond through cellular processes such as changes in contractile forces, cytoskeletal changes and migration. Fibroblasts cultured in polyacrylamide gels of stiffnesses between 1 and 5 kPa had a diffuse distribution of cortical actin rather than organised into bundles of actin (stress fibres) seen in cells cultured within polyacrylamide gels of 10 kPa stiffness or on glass (stiffness of ~1 GPa) [32].

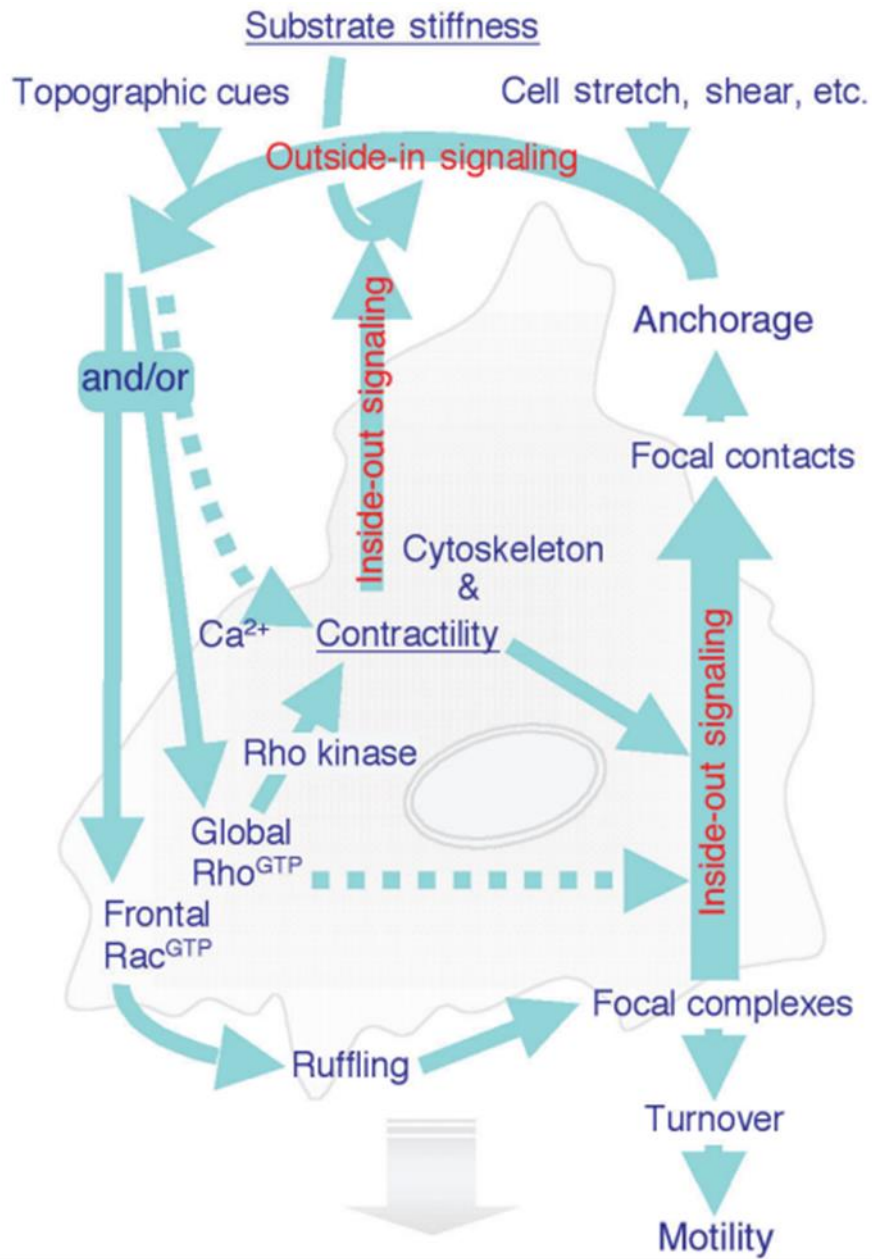


Figure 1.1: Cell-matrix interactions initiate intracellular signaling pathways either as responses to external forces (outside-in signaling) or as feedback through cell contractility (inside-out signalling). Figure adapted from [1].

There have been several proposed mechanisms through which cells sense mechanical forces. Conformational changes brought about by mechanical disturbance can cause protein unfolding resulting in the exposure of ligand binding sites or the release of ligands [33]. Tension in the cell membrane has been proposed to regulate mechanosensitive ion channels [34].

The large latent complex (LLC) comprising TGF- β 1, latency associated protein (LAP; interacts with integrins as well) and TGF- β binding protein 1 (LTBP-1), has been thought to be used by cells to sense the mechanical properties of their surrounding environments and has been shown to be involved in the fibroblast-myofibroblast transition and differentiation of embryonic stem cells into smooth muscle cells [35-37]. The LLC is bound to the cytoskeleton as well as to extracellular matrix proteins [38]. Changes in the arrangement of the protein complex lead to signaling to the cell; the attachment of the LLC sensor to both the cytoskeleton and the extracellular matrix creates a tension in the complex. Cellular contraction upsets the tensional equilibrium, causing conformational changes in the LLC resulting in the release of TGF- β 1, which binds to the cell and initiate signaling cascade events.

The Hippo signalling network has emerged relatively recently as a mechano-sensing pathway which includes the kinases MST and LATS, and two transcriptional co-activators, Yes-associated protein (YAP) and transcriptional coactivator with PDZ-binding motif (TAZ) [39,40]. The intracellular distribution of YAP/TAZ has been shown to be influenced by substrate mechanical properties such as topography and

stiffness [41,42]. Mammary epithelial cells grown on fibronectin-coated polyacrylamide hydrogels with a stiffness of 0.7 kPa displayed cytosolic localisation of YAP/TAZ, whereas, these transcriptional co-activators localised to the nucleus to activate proliferative genes when the cells were cultured on stiffer (40 kPa) gels [41]. Cell morphology also has an effect on subcellular localisation of YAP/TAZ. When cells were induced to adopt a more rounded geometry by plating them on 300 μm^2 islands, YAP/TAZ were found to be in the cytoplasm [43]. Cells adopted a flattened morphology when given a larger space (10000 μm^2) to grow. YAP/TAZ in these flat cells were found to be active and in the nuclei of cells.

The machinery through which cells sense external forces is the focal adhesion. Cells cultured on stiff tissue culture plastic have large focal adhesions on their basal surface, comprising more than 100 different proteins. However, when cells were cultured either on or in soft, compliant matrices (fibrin gels, basement membrane extract, matrigel, cell-derived matrix and collagen), focal adhesions were found to be small and had different protein compositions [6,10,44-50].

Cells react to biochemical and mechanical cues from the ECM through signal transduction between integrins and the cytoskeleton. Integrins are cell adhesion receptors which not only mediate cell attachment to the ECM (and occasionally cell-cell attachment), but they are also involved in transmitting signals to regulate cell proliferation and differentiation. There are more than 20 versions of heterodimeric integrins derived from 18 α subunits and 8 β subunits, with different dimers having specificities and affinities for different ECM molecules [51]. Many integrin subunits

bind to the cell adhesion sequence arginine-glycine-aspartate (RGD) found in fibronectin, entactin, osteopontin, vitronectin, laminin and collagen [52,53]. Cell contact with the ECM triggers a sequence of cellular events such as attachment, membrane extension, formation and contraction of stress fibres which lead to cell spreading and further attachment. Thus, distinct integrin expression profiles by a cell determine what the cell can bind to, which directs the composition of integrin adhesomes, downstream signaling cascades, and thus cell behavior and fate. Integrins are able to impart these mechanical and biochemical signals to the cell through direct contact with the actin cytoskeleton. Additionally, these cell-ECM interactions affect the morphology of the cytoskeleton of the cell which in turn affects the nuclear organisation which can lead to changes in the cellular phenotype [54].

Human mesenchymal stem cells cultured in 3D poly(ethylene terephthalate) (PET) matrices proliferated slower and fewer times than when grown in 2D on conventional tissue culture plastic [24,30]. The difference in cell proliferation rates is not just due to the additional dimensionality, but also on the stiffness of the substrate. For example, in compliant free-floating collagen hydrogels, adult human dermal fibroblasts did not proliferate after 1 week of culture [55]. Whereas, when the same collagen hydrogels were tethered, allowing tension to develop through cellular forces, the cells doubled after 6 days. Proliferation rates were increased with increasing stiffness through the plastic compression of these hydrogels.

Chapter 1: Introduction

Cells cultured in 2D are attached to the substrate only at their basal surface, with only the apical segment of membrane being able to interact with the overlying culture media. The culture media itself represents another shortcoming of 2D cell culture. Cells in 2D culture are exposed to a homogenous solution of nutrients, growth factors and cytokines in the media. Inversely, cells in 3D are exposed to these soluble factors in gradients of concentration and in directions which help to instruct cell behaviour due to the spatial organisation in the x-, y- and z-planes and barriers to transport of large molecules [56]. Furthermore, cells in 2D are restricted to planar morphologies, inhibiting more complex configurations observed *in vivo* resulting in differences in epigenetic information, proliferation, apoptosis and gene expression [57-59]. Therefore, to recreate the *in vivo* cellular microenvironment, several factors need to be taken into account, such as the presence of bulk ECM, which has more physiological mechanical properties, helps to organise cells in 3D, degrades with cell activity at a rate roughly matched with deposition of new material, as well as being a transport barrier to recapitulate diffusion gradients.

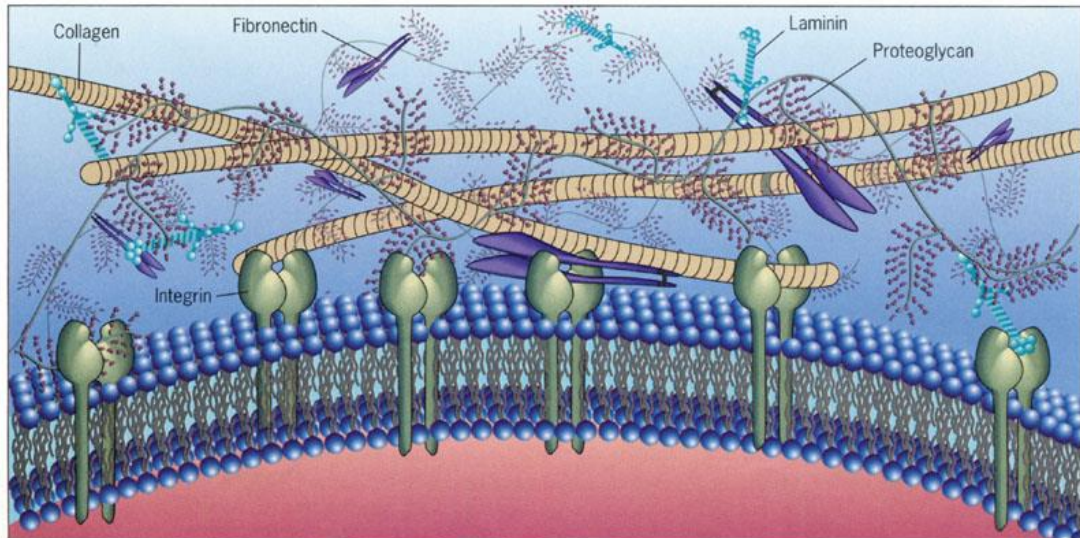


Figure 1.2: Schematic depicting the 3D cell-matrix interactions with the extracellular matrix proteins and glycosaminoglycans. Cells attach to the ECM via integrins and focal adhesions. Figure adapted from [60].

It is not only simply the composition of the ECM that makes a difference, but also the stiffness of the substrate on/in which the cells are grown. Cells in native tissue are normally attached to less stiff and directionally compliant (i.e. anisotropic) materials than the tissue culture plastic that is most commonly used for *in vitro* studies. Cells are usually attached to substrates with elastic moduli of between 10 Pa 310 Pa, which can be deformed by cellular forces through attachment sites [61]. Tissue culture plastic which is very rigid (elastic modulus of 1-2 GPa) cannot be deformed by cells. Studies have shown that mechanical cues can have as big an effect as chemical signals with regard to cellular structure and function [57,62-65]. Smooth muscle cells had a rounded morphology when grown on soft gels, but displayed a flattened dendritic morphology on stiffer substrates. Endothelial cells

have been shown to form a greater number of networks of capillary-like structures on more compliant substrates than on stiffer ones [66-68]. Thus cell morphology and behaviour is affected by the mechanical properties of the substrate the cells are cultured on or in. This flat system leads to the loss of key phenotypic characteristics. It is important, therefore, to make the switch from 2D cell culture towards tissue-like cell culture to be able to predictively correlate *in vitro* findings to *in vivo* studies.

There are a number of reports using 3D cell culture to understand how the added complexity allows more natural cell behaviour, but only a few reporting the use of 3D cell culture to assess the effects of therapeutics *in vitro*. The need for predictive *in vitro* assays has become progressively important to understand the mechanisms of disease and the treatment of disease [69]. This is especially critical for the pharmaceutical industry where there is a rising cost-to-delivery ratio. The costs of drug testing rise exponentially as it nears market release [70]. Thus, it is beneficial to identify drug candidates with high probabilities of success and limited toxicity as early in the development process as possible [71].

1.2. What is 3D to cells?

The ability to maintain cells outside the body has been invaluable and the benefits gained from it is immeasurable. However, the method of culturing cells *in vitro* has not changed significantly since the inception of the technique. The knowledge acquired so far has been based on experiments conducted on cells cultured as monolayers on an unnatural and stiff substrate, imposing physical constraints on the cells. Advances in the field of tissue engineering have led to the exposure of shortcomings of conventional cell culture. Cells embedded in the ECM are arranged in three dimensions in terms of tissue organisation as well as morphology. Cells sense and respond to both biochemical and mechanical signals in complex ways. If only 2D culture is used, certain cell behaviors are likely to be missed. The culturing of cells as a sheet on rigid plastic surfaces is an old technique and is in need of an update in order for us to better understand how the body works.

Importantly, culturing cells in tissue culture flasks allows only the attachment of the bottom surfaces, and on their sides (to other cells) when they become confluent. On the other hand, cells in the body normally have all surfaces surrounded by matrix proteins and/or cells, except for certain cell types like epithelial and endothelial cells. Fibroblasts for example, do not have this stark polarity *in vivo*, but an apical-basal polarisation is forced in them when cultured as a monolayer [72,73]. Hepatocytes lose a specific set of proteins normally expressed on their apical,

basolateral and sinusoidal membrane when cultured in monolayer [74]. Thus, in most cases, the *in vitro* culturing of cells results in their unnatural polarisation in an environment that is largely liquid. Flat monolayer culture systems lead to the loss of key phenotypic characteristics. It is important, therefore, to make the switch from 2D cell culture towards tissue-like cell culture to be able to predictably correlate *in vitro* findings to the *in vivo* realities.

Signalling in the body is governed by biochemical signals such as morphogen gradients and auto-/paracrine signaling and mechanical stimuli [11]. Morphogen gradients have been shown to be critically important during development, where a fine balance between opposing or synergising gradients can have dramatic effects [75,76]. Metabolic zonation in the liver is another area where morphogen gradients are critical in regulating homeostasis through moderation of metabolic enzymes such as glutamine synthetase [77-80]. However, in monolayer culture systems, no such morphogen gradient exists since anything the cells produce is immediately lost in the sea of media, except at close proximities [81,82].

Cells attach to and sense mechanical changes in the ECM through the interactions of the actin cytoskeleton, integrins and ECM proteins. Fibroblasts cultured in either 2D or 3D have one key difference – the degree of ECM-anchorage. In 2D, fibroblasts only interact with their substrate through their dorsal membranes, whilst in true 3D, integrins all around the cell can be engaged simultaneously (Figure 1.2). Cell processes extend into and interact with the matrix fibril network. Integrins are known to regulate several key processes such as gene expression, migration,

apoptosis, growth, differentiation and proliferation via multiple signaling pathways (PI3K, Akt, ERK, cyclin D1) [83,84]. Furthermore, integrin-mediated attachment modulates signaling via soluble factors like epidermal growth factor and platelet-derived growth factor.

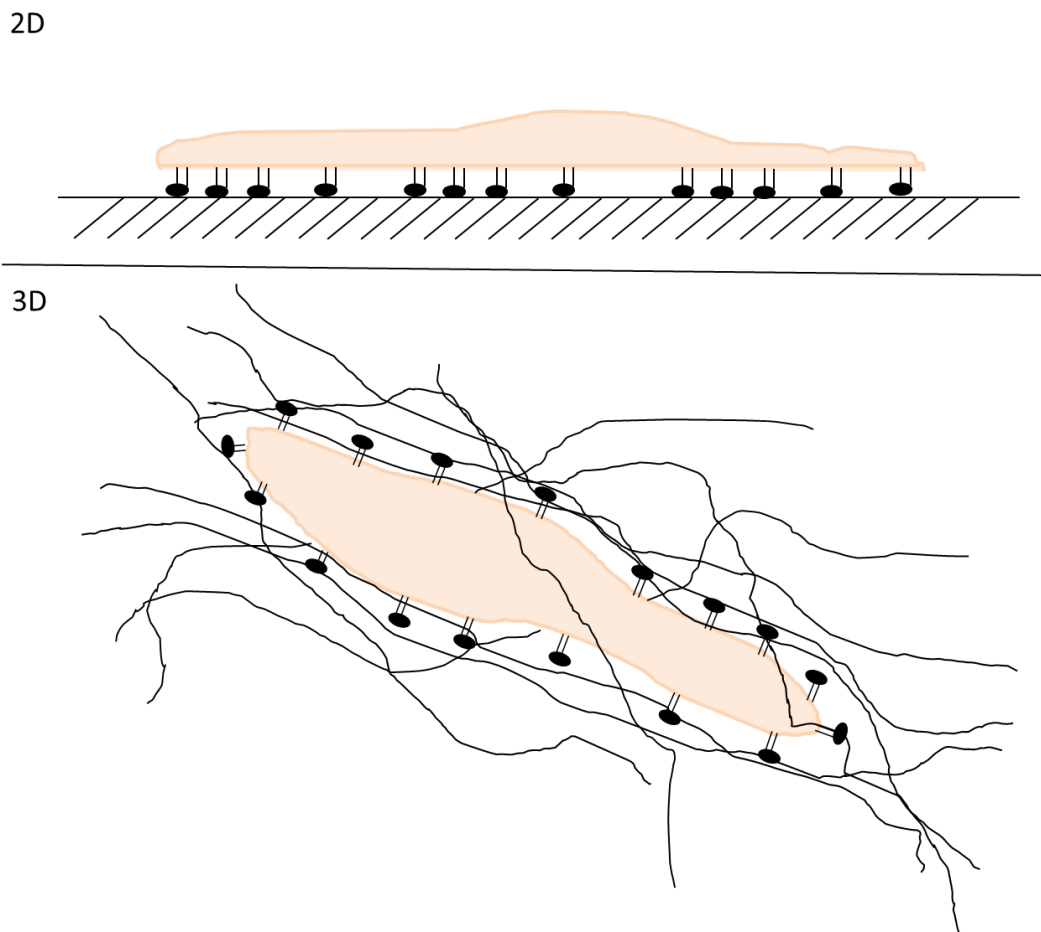


Figure 1.3: Diagram of a cell and its interactions with its substrate when cultured in 2D and 3D. Cells only interact with their substrate via their ventral surface when cultured on a flat surface, whereas cells in 3D have cell-substrate interactions all around.

1.3. Nanoparticles as drug delivery systems

The efficacies of conventional drugs can usually be increased through the use of drug delivery systems (DDS). DDS intended for systemic administration include micro- and nanoparticles (capsules, shells, spheres, drug-polymer conjugates), liposomes, micelles and dendrimers. Such carrier systems are advantageous as they modify the biodistribution and pharmacokinetics of their cargo by granting protection from degradation, prolonging circulation time, sustaining drug effects in target tissue, enhancing solubility and reducing harmful side effects [85-89].

The small sizes of these DDS along with the increased circulation time allow passive targeting occur which help these DDS to reach their target sites via the enhanced permeability retention (EPR) effect [90-92]. The EPR effect occurs because of leaky vasculature present at tumour sites or inflamed tissues which leads to the gradual accumulation at these locations. Such drug delivery systems may also employ active targeting whereby a chemical moiety, which specifically interacts with target cells, is conjugated to the carrier. All these lead to greater drug efficacy at the desired sites of action, which negates the need for high doses of free-drug and thus reducing the consequential harmful side effects.

Nanoparticles have great potential for *in vivo* therapeutic applications (e.g. drug delivery) as well as diagnostic applications (e.g. cell tracking) [93]. The rates of drug release from their carrier enhance the effectiveness of the drug delivery system. Drugs within carriers are inactive and need to be released to have any therapeutic

effect. If the drug is released too quickly in the body, the pharmacokinetics and distribution of the DDS might be similar to administration of the drug in its 'free' form. And if the drug is released too slowly, the delivery system may have lower therapeutic effects than unencapsulated drug [94,95]. For active or passive targetted DDS, it is important that the particles have long enough half-lives *in vivo* to accumulate at their target tissue. Therapeutic levels of free drug must also be maintained and sustained for a period of time once at the target site. Different drugs have different mechanisms of action and will require tailored release profiles. DDS need to be initially assessed *in vitro* to determine their release rates, half-lives, how cells interact with them and their toxicity before they are deemed safe for *in vivo* studies.

Some drugs need to be delivered into the cell rather than released from their carrier extracellularly [96]. This would require passage through biological barriers such as epithelia and mucosa, to reach target tissues. The encapsulated drug would then have to enter the cell through the plasma membrane and to the target organelle. Cells take up nanoparticles via several different processes. Most cell types can take up nanoparticles through endocytosis; clathrin-mediated, caveolae-mediated, macropinocytosis and others (clathrin-caveolae-independent endocytosis).

Clathrin-mediated endocytosis (CME) may be receptor-dependent or receptor-independent. Receptor-dependent CME provides a way of targetted entry into cells through the attachment of specific ligands to the surfaces of nanoparticles such as

low density lipoprotein (LDL), epidermal growth factor (EGF) or folic acid (FA) [97]. Folic acid binds with a low affinity to the folate receptor present in most cells, but with a high affinity to the glycosylphosphatidylinositol-linked folate receptor often overexpressed in cancer cells [98,99]. This makes FA a popular ligand for surface modification of anticancer nanoparticles. CME intake of material end up in lysosomes containing acid hydrolases and low pH. This can be utilised as a release mechanism through carrier biodegradation within lysosomes, though the drug molecule must be tailored to resist the harsh lysosomal environment. Caveolae-mediated endocytosis (CvME) leads to the formation of cytosolic caveolar vesicles, which provides a 'safe' route into the cell, avoiding the lysosomes. Macropinocytosis is a non-selective, clathrin-independent endocytic mechanism which involves micrometer-sized endocytic vesicles. These large vesicles acidify and may fuse with lysosomes. Phagocytosis is another mechanism of uptake but is limited to certain cell types (macrophages, monocytes, dendritic cells, neutrophils, fibroblasts, epithelial and endothelial cells).

Nanoparticle size can affect entry into cells. Polystyrene nanoparticles within the size range of 20 – 1000 nm were not endocytosed by human umbilical vein endothelial cells, whereas 20 – 100 nm particles were endocytosed by HepG2 hepatocytes [100]. Caco-2 cells take up 100 nm PLGA particles more readily than 500 – 10000 nm PLGA particles [101]. Drug-carrying nanoparticles can be made more effective by surface charge manipulation. Due to the negative charge on cell membranes, positively-charged carriers show greater cell interactions and uptake. PLA-PEG nanoparticles with positively-charge stearylamine were taken up by HeLa

cells at a faster rate and to a greater degree than the uncoated, negatively-charged PLA-PEG nanoparticles [102]. Uptake by phagocytic cells can be altered by adjusting the hydrophilicity/hydrophobicity of the nanoparticle surface to influence interactions with opsonins, and in turn, phagocytosis.

Thus, nanoparticles can be modified in many ways to increase the efficiency of drug delivery, but this has to be balanced with any potential toxic effects. Testing nanoparticles in models of biological barriers and tissues would allow the assessment of nanoparticles in an *in vivo*-like environment for the development of nanoparticles with predictable and reproducible behaviour and low toxicity.

1.4. Evaluation of therapeutics

Before drug candidates are tested in man, they are first assessed in cell-based assays, and those with high potential are then evaluated in animals. Cell-based assays have been a valuable tool in weeding out toxic and non-functional compounds due to the efficiency of drug testing on cell cultures [103]. However, even though these cell-based assays have become entrenched in the developmental process for reasons discussed above, their predictive capabilities for *in vivo* responses are somewhat uncertain. This is likely because the cells are cultured in an unnatural way for these assays, giving rise to abnormal phenotypes, behaviours and responses [58,104-108]. For example, trovafloxacin was shown to be safe for human use when tested on primary human hepatocytes cultured on

tissue culture plastic. However, the drug causes acute liver failure in humans, amongst other serious side effects [109,110]. Single-walled carbon nanotubes (SWCNT) were found to affect Schwann cells differently when the cells were cultured in 2D or in 3D [111]. When cells were cultured conventionally as monolayers on tissue culture plastic, proliferation and morphology were affected by the addition of SWCNT; proliferation decreased and the cells became flatter and more fibroblast-like compared to their usual bipolar morphology. Schwann cells cultured in 3D within collagen-Matrigel composite hydrogels were unaffected by the presence of SWCNT in terms of morphology and proliferation. It was also pointed out that cells cultured on the hydrogel, in a 2D environment, adopted a different morphology to cells within the matrix. Like the cells cultured on tissue culture plastic, these cells on the hydrogel altered their morphologies when SWCNT were added. In addition, *in vivo* studies in animal models have only limited predictive capacities [112-114].

It has been estimated that a modest increase of 10% in the predictive accuracy of pre-clinical tests could save at least \$100 million in drug development costs [115]. Only about 1 out of 10 new molecular entity (NME) entering phase I clinical development reaches the marketing stage [116]. The efficiency of drug selection and development has been in steady decline, with more and more money being spent per successful drug candidate [117]. Efforts have been made to overcome this problem by ramping up risk assessments during the discovery stage before large sums of money and time are spent. Common causes that have led to failure, such as pharmacokinetic characteristics, drug metabolism, absorption, excretion and

toxicity, are now being tested for in the discovery phase to minimise the risk later on [118].

During the drug discovery stage, biological targets that are deemed to be important in alleviating disease are selected. The targets are then evaluated as possible sites of action for amending pathophysiological pathways. Then experimental models recapitulating the disease are developed. At this point, chemists join the biologists to determine chemical structures specific to the target. A range of assays are used to narrow down the options and identify those with desirable properties for further testing. Many candidates are tested using a range of technologies, and the time and money invested at each step increases. It is therefore important that the right targets are identified from the beginning. However, as discussed above, cell growth in a monolayer or within a matrix in 3D can lead to very different gene expression and drastically altered behaviours. Cells cultured as a monolayer may produce the target protein, but do not when cultured in 3D, or *in vivo*. Therefore, depending on which type of system is used, a selected biological target may or may not be valid. The high failure rate of new molecular/biological entities may be because the target protein selected initially was present in the cells *in vitro* but the same cells did not express the target protein *in vivo*. Therefore, better cell culture systems need to be developed specifically to mimic the target native tissue, so that suitable target sites can be selected which would improve the productivity of therapeutics development, speed up drug identification and reduce costs through improving predictability of *in vivo* outcomes [119].

Nanoparticles have a more varied range of toxic activity than drug molecules due to their size, shape, composition, charge and solubility, amongst others. Their small sizes facilitate uptake into cells and transcytosis across cell layers [120]. Shape has also been shown to aid tissue or cell penetration – rod-shaped nanoparticles have a higher probability of infiltrating tissues and cell membranes [121]. Furthermore, nanoparticles may also generate free radicals which would harm cells. Therefore, the assessment of nanoparticles in 3D *in vitro* models is critical in order to fully understand their effects.

A key aspect of native tissue that should be included in *in vitro* culture systems is the presence of barriers which limit diffusion, especially for the evaluation of therapeutics. In 2D cell culture, the therapeutic compound/nanoparticle is homogeneously suspended in culture media, allowing free movement of the sample which would not be the case *in vivo*. Such a system would expose cells not only to larger amounts of therapeutic candidates, but also at a higher rate than would be experienced *in vivo*. This likely contributes to the poor predictive power of 2D assays. The added dimension imposes a significant barrier to macromolecular mobility as the diffusion of therapeutic agents within cavities and the interstitial tissue limits the treatment of some cancers and other pathologies [122].

1.5. Toxicological testing

The benefits from the advancement of nanotechnology not only encompass the development of better therapeutic products, but also a variety of other products such as cosmetics, computer chips, computer hard drives and sports equipment to name a few. These industries stand to make billions of pounds with the application of advanced nanotechnology. With such a large growth potential comes great risk.

Nanotechnology first has to be deemed safe for use with regards to the consumer, as well as to the environment, to avoid a recurrence of past mistakes such as the heavy use of asbestos without the knowledge of its deadly toxicity to humans (multi-billion dollar remediation headache). Therefore nanotoxicological tests need to be carried out on new engineered nanoparticles, as well as on unintentionally produced nanoparticles, before such materials are used.

In vitro models have several advantages: the ability to investigate direct effects and mechanisms of action of test agents on the target cell type(s) without the complications that arise following interaction with the body, the ability for high-throughput studies which are cost-effective and quick, the general ease of improving such systems or adding on complexity and the reproducibility of experiments and results [123,124].

Monolayer cultures of cells have primarily been used for nanotoxicological testing on a variety of cell types [125] - Human Hep3B cells [126], Balb/3T3 mouse fibroblasts [127], mesothelial cells (MSTO-211H) [128], MRC-9 fibroblasts [129], to

name a few. However, cells in these 2D cultures are in an unnatural environment, so these systems do not provide a realistic situation in which to assess the effects the nanoparticles have on cells. A vital property of tissue physiology that is missing from 2D culture is the presence of a barrier to particle diffusion and kinetics. Without this, nanoparticles move around unhindered through the culture media, which likely causes an 'artificially' high number of cell-nanoparticle interactions that would not occur in tissues [130]. Sayes et al. compared the *in vitro* and *in vivo* results from toxicity testing of five different particles (carbonyl iron, crystalline silica (Min-U-Sil 5, α -quartz), precipitated amorphous silica, nano-sized zinc oxide and fine-sized zinc oxide) ranging from 90 – 500 nm in a dry state [131]. For their *in vitro* studies, they used monolayer cultures of rat epithelial lung cells, rat BAL macrophages or co-cultures of both, and compared these to intratracheal instillation of particles to Sprague Dawley rats by looking at cytotoxicity end points (lactate dehydrogenase release; MTT assay), and found little to no correlation between *in vitro* and *in vivo* studies.

There have been several attempts at improving nanotoxicological testing by co-culturing multiple cell types. Bhabra et al. used a two-cell type system of BeWo (placental) cells and human fibroblast cells to test the effects of cobalt-chromium nanoparticles [132]. Rothen-Rutishauser et al. developed a triple co-culture system of the human respiratory tract by sandwiching epithelial cells with macrophages and dendritic cells on the apical and basal surfaces of the epithelial sheet respectively [133]. This study highlighted the importance of organising *in vitro* systems to mimic native tissue architecture. Simply co-culturing multiple cell types

in the same well with no regard to cellular arrangement would not mirror cellular behavior in the body – although, it has been shown that co-culturing cells does generate differences to monolayer cultures [124,134].

Liver models have become increasingly important for toxicity testing in recent years. Unforeseen liver toxicity has been a major stumbling block for drug candidates during clinical trials [116], even after comprehensive testing with *in vitro* and *in vivo* models. The main *in vitro* models used are cell lines, microsomes, liver slices and primary hepatocytes [78,135-137]. However, these *in vitro* models face difficulties in maintaining tissue organisation, long term viability, high-throughput capabilities, cell morphology, normal tissue levels of functions [138]. A further challenge for *in vitro* hepatocyte culture models is long-term culture. Serious hepatic issues have been known to be caused by chronic exposure to drugs. Nuclear receptors and target genes which are involved in many physiological functions may be affected by prolonged drug exposure. The specificities of nuclear elements for their ligands are low and may interact non-specifically with drug molecules or drug-induced proteins leading to aberrant cell behavior [139,140]. However, hepatocyte function is lost during standard cell culture conditions [141,142]. It has been shown that hepatocytes cultured in a 3D environment retain their tissue morphology and polarity and maintain their function [143,144].

Furthermore, many cell types such as the Kupffer cells, liver sinusoidal endothelial cells and hepatic stellate cells, make up the liver. These all work together and in concert with any extracellular matrix to ensure the proper functioning of the liver.

Therefore, single cell-type culture models are insufficient for predictive toxicology studies. Many groups have since worked on developing more sophisticated systems to include co-cultures of cell types and incorporating 3D architecture.

Biondi et al. developed an *in vitro* 3D model using low density collagen hydrogels (0.24%) to study the cytotoxic effects of Doxorubicin-loaded PLGA-PEG nanoparticles within a matrix. Doxorubicin (an anthracycline), on its own, does not have tumour specificity and can cause harmful side effects such as cardiotoxicity and nephrotoxicity. Thus, many research groups have been working on improving doxorubicin delivery methods to increase specificity and reduce toxicity. Biondi et al. encapsulated the drug in poly(D,L-lactic-co-glycolic acid) (PLGA)-*block*-poly(ethylene glycol) (PEG) copolymer to enable tumour targeting through the EPR effect. They showed that the cytotoxicity of the nanoparticles depended on particle size and the amount of matrix separating the cells and nanoparticles, thus highlighting the importance of the matrix barrier which is lacking in many *in vitro* culture systems [145].

1.6. Non-2D systems

Many 3D culture systems are based on hydrogels (eg. alginate, collagen, PEG), sponges (eg. cellulose, collagen, fibroin, hydroxyapatite, silk, PLGA) and cellular aggregates/spheroids (eg. rotating wall bioreactors, hanging drop, micro-carrier

systems) [69,146-162]. However, not all of these methods are strictly three-dimensional, and some that are, do not recapitulate the native tissue environment.

1.6.1. Sponges

Sponges made from several different materials (chitosan, collagen, alginate, poly(L-lactic acid)-poly(lactic-co-glycolic) acid (PLLA-PLGA), basement membrane) have been developed and used with reasonable success [163-169]. Sponges usually contain pores with dimensions in the hundreds of micrometers - 10-fold greater than average cell dimensions. This presents cells with flat/curved surfaces within pores on which to grow, leading to unnatural flat cell morphologies and highly asymmetric cellular organisation, much like 2D cell culture (i.e. pseudo-3D) [23,170-172]. Collagen sponges have been prepared by the lyophilisation of low collagen density (<1%) solutions [173-176]. These have been used to engineer skin-like tissue constructs [177], bone [176,178], adipose tissue [179], cartilage [180], lung and tendon [181]. Pore size can be controlled to an extent by varying the rate of freezing and lyophilisation. However, the dimensions of the pores largely remain in the tens of micrometers. Faraj et al. showed that by freezing collagen solutions at -196°C, pore sizes of 20 – 30 µm could be attained [181], whilst Lloyd et al. demonstrated that similar pore sizes could be achieved by freezing with liquid nitrogen at rates of at least -40 °C/min [177]. With these smaller pore sizes, cells are more likely to attach to the matrix via all three axes, but they would not be enmeshed in collagen fibrils as they are in native tissue. Furthermore, repopulating

the matrix is an issue faced when using sponges. Cells cannot be seeded in the matrix and have to be seeded on it, relying on cell migration for matrix penetration.

On the other hand, nanofibrous sponges have also been developed using techniques such as electrospinning, which generates scaffold with nanometer-sized pores. Cells can only be seeded after the manufacture of the scaffold, and because the pore sizes are so small, the cells cannot penetrate into the scaffold and so must grow on the surface rather than within the bulk material. Although these sponges bring some aspects of 3-dimensionality to cell culture, they do not accurately mimic native tissue structure and organisation.

1.6.2. Cell aggregates

Cell aggregates have been given several different names: spheroids, spheres, mammospheres, aggregates, tumouroids, micromasses and organoids [182-192]. These cell agglomerates are based on cells having greater affinities for each other than to the substrate they are on. Several techniques have been developed to produce cell aggregates such as spinner flasks, hanging drops, static liquid-overlaying and rotating wall vessels [149,160,182,193-198]. The spinner flask and rotating wall vessel systems use continuous movement to prevent cells from attaching to the flasks, which leads to the moving cells attaching to one another and aggregating. These allow the generation of 3D clumps of cells, but require specialised equipment, and the size and shape of cell aggregates are difficult to

control. While these systems enable the culture of cells in a 3D environment, they are not physiological tissue mimics.

Hanging drop systems utilise gravity to induce cell agglomeration inside a suspended droplet, away from any surface that may allow cell attachment [160,196,199]. The liquid overlay technique works in a similar manner by preventing cells in suspension from adhering to the substrate surface [193]. With nothing else to attach to, the cells thus stick to each other to form a cellular mass.

Lee et al. developed an inverted colloidal crystal topology substrate with low cell affinity to induce spheroid formation using human hepatocarcinoma (HepG2) cells [149]. Using these spheroids as a 3D *in vitro* model of liver, they showed that the toxicity of cadmium telluride and gold nanoparticles in spheroid cultures was lower than in 2D cultures. Similarly, Luo et al. developed a high-throughput spheroid system to test the effects of bismuth nanoparticles and found that the toxic effects of these nanoparticles were lower when cells were in a 3D environment than in monolayer culture [200].

Although the multicellular spheroid closely mimics the heterogeneity and hypoxia conditions exhibited by *in vivo* tumours, it does not fully capture the interactions that take place *in vivo* such as host immune reactions and angiogenesis. Also, the size of the spheroid is difficult to control and the direct contact of media with cells does not account for the blood vessel barrier *in vivo* [201,202].

1.6.3. Cellular Multilayers

The layering of cells allows the fabrication of tissue-like structures which are rich in cells, but have minimal matrix components. This involves using cell types that are adept at making sheets, such as epithelial or endothelial cells [203,204]. These thin cellular monolayers are then stacked in the z-plane to produce cell-dense tissue-like constructs. Watanabe et al. produced corneal epithelial sheets for ocular surface reconstruction [204], while Ide et al. used similar technologies to generate corneal endothelial sheets [205].

Cell sheet engineering has been used to produce ocular, tracheal and cardiac tissues [205-208]. However, the technique is limited in its ability to fabricate matrix-rich tissues, like skin and tendon, and to incorporate 3D micro-scale architecture. Attempts have been made to overcome this limitation by incorporating layers of ECM proteins to increase the matrix density in such layer engineering. The laboratories of Kano and Akashi both used a cellularised ECM model by alternately layering cellular monolayers with 6 nm-thick fibronectin-gelatin layers, resulting in a multi-layered structure comprising 5 cellular layers to create an artificial 3D model of fibrotic tissue 30-50 μm in thickness [209,210].

Using this cell-ECM multilayered model, Hosoya et al. studied the diffusion of FITC-conjugated dextran of various sizes through the tissue-like construct. They demonstrated that the thicker the cell multilayer or the larger the size of dextran, the lower the permeability. Modelling molecular migration through 3D tissues is

not really possible using conventional monolayer culture, though it is common to measure the permeation of molecules through cell monolayers [211-214].

1.6.4. Fibrillar biomaterials

Tissue engineers aim to fabricate native tissue-like constructs. This requires the use of appropriate biomaterials with suitable mechanical properties relative to the tissue of choice, together with the appropriate cells, and matrix architecture. Natural tissue is organised into an interwoven network of fibrils that surrounds the cells (like olives within a spaghetti ball). As such, many researchers have put their efforts into developing scaffolds made from meshwork of fibres. However, the benefits of such matrix architecture diminish if scale is not appropriately considered.

Constructs with fibre diameters in the tens of microns (several fold larger than cell dimensions) will appear an ideal scaffold at the gross level. However, cells are actually in contact with a substrate which to them is 2D and slightly curved. Other techniques such as electrospinning can produce fibres as small as tens of nanometers. In electrospinning, liquid jets of viscous polymer solutions are induced through the use of high voltages. Fibres form as the solvent evaporates during the process. Electrospun scaffold morphologies can be controlled by varying fibre dimensions through alterations in the experimental set-up such as changing the power of the electric field used, distance between the collector and ejection needle

or the rate of ejection. Fibre dimensions are reliant on the properties, concentrations of the polymer and solvent used, and range from the tens of nanometers to hundreds of nanometers. Some examples of electrospun scaffolds used for tissue engineering include neural tissue [215], bone constructs [216], cardiac tissue [217] and vascular tissue [218] using synthetic materials such as poly (L-lactic) acid (PLA), poly (ϵ -caprolactone) (PCL), poly(D,L-lactide-co-glycolide) (PLGA), poly vinyl alcohol (PVA) or natural polymers used include hyaluronic acid [219], chitosan [220], gelatin [221], and collagen [222,223]. Synthetic materials lack the cell promoting qualities natural polymers possess, whilst natural polymers tend to lack mechanical strength. It is increasingly common for blends using both synthetic and natural polymers for electrospinning scaffolds for tissue engineering.

However, like lyophilised sponges, these methods require scaffold preparation before cell seeding, which makes it difficult to get cells inside the matrix with pore sizes several times smaller than the cells.

Thus, the ideal nanofibrillar network is formed around the cells, entrapping them within the matrix. The self-assembly of hydrogels does exactly this. Cells can be included in the gel solution before allowing it to set, in which case fibril networks form around the cells.

1.6.5. Decellularised tissues

Tissues contain a complex mixture of cells, matrix proteins, soluble proteins and GAGs. Replication of such a composition and organisation is very difficult. Therefore, decellularisation was seen as the ideal method to obtain functional ECM scaffolds for implantations [224]. Any cellular material has to be completely removed from the tissue to prevent inflammatory reactions and immune rejection of the scaffolds following implantation. The treatment processes used to remove cells are harsh and will compromise the mechanical integrity and biological activity of the ECM. These include physical methods such as sonication and freeze-thawing, chemical treatments like acids and detergents (sodium dodecyl sulfate, Triton X-100) and enzymatic methods like trypsin and endo-/exonucleases. These work by damaging the cell membrane to empty cell contents and to disconnect cell-ECM and cell-cell bonds, to expedite the removal of cell traces from the ECM [225]. There are several key factors that need to be carefully controlled: the ECM needs to be sufficiently disturbed to allow diffusion of the chemical and enzymatic agents throughout the ECM, and also to allow cellular material to be extruded from the ECM. But, to maintain native tissue mechanics and architecture, this disruption needs to be minimal.

Due to the diversity of tissue organisation, a decellularisation protocol has to be optimised for each tissue type. Protocols using trypsin in the decellularisation process has been previously reported to be successful for complete cell removal from both human and ovine aortic valves [226,227]. However, trypsin was found to be less effective on porcine heart valves [228,229]. Grauss et al. compared two

decellularisation protocols on porcine aortic valves. Decellularisation of porcine aortic valves using Triton X-100 resulted in the complete removal of cellular components from the valve leaflet, though some cellular fragments were found in the aortic wall and myocardium. Triton X-100 reduced the collagen density and removed most of the glycosaminoglycans, chondroitin sulphate, laminin and fibronectin. Trypsin treatment left picnotic nuclei which could not be removed, and resulted in a similar loss of laminin and fibronectin, greater loss of chondroitin sulphate but a smaller reduction in the loss of other glycosaminoglycans.

These decellularised ECMs then need to be thoroughly inspected for cell and chemical traces as these may elicit detrimental immune reactions. The treatment methods used undoubtedly affects the composition, structure and mechanics of the tissue ECM which limit its biological activity, strength and stiffness. In addition, it is difficult to repopulate the decellularised tissue with cells due to the architecture of the ECM, and especially so since GAGs and adhesive proteins had been removed during the decellularisation process. Protocols have to be fine-tuned to achieve maximal decellularisation whilst minimising negative effects on the ECM.

1.6.6. Hydrogels

Hydrogels are formed from a network of polymeric fibres which are able to absorb many times their dry weight in water. These can be either natural materials (collagen I, laminin, hyaluronic acid, fibrin, alginate, agarose, gelatin) or synthetic

(PLA, PGA, PEG). They are used because of their ability to simulate the nature of most soft tissues, can be easily formed with cell-friendly methods, and most importantly, cells can be embedded within the hydrogels [230]. The diversity of the structure, architecture and content of the ECM suggests that different cell types will behave and function in a more natural way if embedded within their native matrix [231]. However, hydrogels have been used to culture cells 'in 3D' by placing cells *on* top of a polymerised gel rather than *in*, which presents cells with a 2D environment that is softer than tissue culture plastic [232].

Synthetic hydrogels are well-defined scaffolds with tuneable properties, but suffer from their inferior cytocompatibility. Synthetic polymers [poly(L-lactic acid) (PLLA), poly(vinyl alcohol), polyglycolic acid (PGA), poly(lactic-co-glycolic)acid (PLGA), polyethylene glycol (PEG)] need to be modified biochemically to include cell attachment sites, their surface properties (hydrophilicity, hydrophobicity) as well as their structure (fibril diameter, porosity) need to be adjusted to improve biocompatibility. Despite their great potential for modification and refinement, they lack endogenous factors that enable natural cell behaviour, making it a challenge to match *in vivo*-like conditions. For example, PLLA and PEG hydrogels have been modified to include the Arg-Gly-Asp (RGD) cell attachment site, as well as matrix metalloproteinase (MMP) substrates, to improve cytocompatibility and biodegradability [233,234]. The functionalised PEG hydrogel has been shown to provide a more acceptable substrate for human epithelial ovarian cancer cells than the standard 2D culture environment as the cells self-organised to form structures similar to that seen in patients [234]. However, two major factors limiting the use of

synthetic polymers are the release of degradation products (which may possibly be harmful) and the presence of fabrication remnants.

Hydrogels prepared from natural polymers have the advantage of cell attachment and promoting cell function due to the presence of endogenous factors [235]. Their inherent biocompatibility and biodegradability allows for cells to reside within and in some cases, to remodel the matrix. Collagen hydrogels have been shown to be able to house triple co-cultures of myoepithelial cells, luminal epithelial cells and fibroblasts, resulting in an organisation that resembled native breast tissue [236]. Colon cancer cells (LS174T) grown together with fibroblasts in a collagen hydrogel organized into glandular structures with the fibroblasts forming a network around them. The fibroblasts were also shown to express genes that are characteristic of activated tumour fibroblasts [237].

Hydrogels represent a simple model of tissue which has been used to assess nanoparticles in terms of their stabilities within a tissue-like environment, ECM-nanoparticle interactions and diffusion rates through cross-linked networks. It has been demonstrated that particles as small as 130 nm in diameter may be greatly hindered in movement by the fibrillar network of the ECM and that by altering particle surface properties, binding affinities and hence diffusion rates may be controlled [122,238].

1.7. Collagen

Collagen is the most abundant protein in mammals, being the major component of many tissues such as tendons, ligaments, bone and dentin, skin, cartilage and cornea. Collagens come in many forms (at least 28 different types), though those which contribute to fibril formation are very similar in structure [239]. Most bulk material collagen tissues are predominantly type I (e.g. skin, tendon, bone, lung and cornea), though the cartilages are largely type II. Others are increasingly specialised with cell interaction or fibril modification functions. However, in biomaterials terms, type I collagen is most attractive. Collagen I gels are simple to produce, usually by neutralising and warming chilled, acid-dissolved monomeric collagen I, resulting in a natural 3-dimensional biomimetic material. Collagen molecules assemble to form larger collagen fibrils which have diameters of 50-500 nm, depending on tissue type. The molecules are arranged with a characteristic stagger of 64-67 nm – known as the *D* periodicity, which is seen as a banding pattern under an electron microscope.

The fibrous collagen protein has a hierarchical structure with collagen molecules being the most basic building block. Collagen molecules are triple-helical chains with a diameter of 1.5 nm and lengths of ~300 nm. These triple-helices can be homotrimeric or heterotrimeric. Collagen I molecules are made up of two identical $\alpha 1(I)$ chains and a single $\alpha 2(I)$ chain, whereas collagen II molecules are made up of three identical $\alpha 1(II)$ chains. A common feature amongst collagen α chains is the presence of a repetitive amino acid sequence which gives rise to a central triple-helical region within each α chain. This sequence is Gly-X-Y, where X and Y can be

any amino acid but often are proline and hydroxyproline, and is repeated 337-343 times depending on collagen type.

The triple helical collagen molecules (1.5 nm diameter) group together in parallel to make up larger collagen fibrils (50 – 500 nm), which form even larger bundles of fibres and fascicles (10 µm). This hierarchical structure of collagen was demonstrated using patterned compressed collagen whereby multiple alignments were present, depending on the length scale used [240]. At the macroscopic level, an orthogonal pattern reflecting the nylon mesh used was seen on the surface of the collagen. Down the length scale, parallel fibres were perceived, which were comprised of randomly arranged collagen fibrils at the nano-scale. Cells can be enmeshed within randomly orientated collagen nanofibrils, whilst being organised into micro-structures to mimic native tissue architecture. This hierarchy allows engineering of collagen at each level, giving greater degree of control over complexities for direct tissue engineering.

Although collagen molecules are typically of fixed dimensions (1.5 nm in diameter, 300 nm in length), the fibrils they make up vary in both diameter and length, depending on tissue type and function. Larger diameter fibrils are necessary for withstanding high tensile forces in tissues such as tendon, whilst smaller fibrils are more useful for resisting creep. The organisation of the collagen fibrils is also critical for the proper functioning of the tissue. As tendon is only required to resist strain along its axis, fibrils are uniaxially aligned to provide the necessarily high tensile strength (100-140 MPa) required to transmit muscle forces, while remaining flexible

enough to accommodate shape deformations with joint movement [241]. Collagen fibrils in the cornea have uniform diameters (31 – 34 nm depending on age) and are organised into parallel structures called lamellae which are about 2 µm thick and up to 0.2 mm broad. Fibrils within each lamella run parallel to each other but each lamella is at an angle to the adjacent lamellae [242]. This arrangement gives the cornea radial strength and more importantly, confers transparency to the tissue.

Fibrillar collagen is soluble at low pH and fibrils can be spontaneously reconstituted by raising the pH and temperature to physiological levels. This *in vitro* fibrillogenesis is influenced by the presence of other collagen types, the condition of the telopeptides, composition and temperature. These factors affect the rate, size and quality of fibril formation. For example, the presence of phosphate is required for the formation of compact fibrils with a clear banding pattern. Thicker fibrils form at lower temperatures (20°C) than at a higher temperature (34°C) [243].

Collagen is highly conserved between species and is inherently biocompatible and biodegradable by many cells. It is therefore a good material for tissue engineering purposes. However, collagen hydrogels, as mentioned above, are mechanically very weak, usually having densities of just 0.2-0.5% collagen (w/w), with the remaining 99.5% being fluid. These gels do not have sufficiently high densities to mimic native tissue physiology (commonly between 20-30% (w/w)). Plastic compression of collagen hydrogels solves this problem by removing a large amount of this fluid and condensing the collagen fibrils to produce scaffolds with densities approaching tissue levels. Our aim was to use this tissue-like system to investigate the behaviour

of nanoparticles *in vitro*, to have a greater understanding of the fate of the nanoparticles *in vivo*.

The process of plastic compression involves the expulsion of a large amount of fluid within the collagen gel through the use of an absorbent plunger. Due to the small size of nanoparticles, they will follow the flow of fluid through the compressing collagen gel until the size of the fibril network mesh reduces to that which can limit that particular diameter of particle or its larger aggregates. At a point in the process, the collagen fluid leaving surface becomes compact enough to block the nanoparticle flow, whilst still allowing water molecules to escape. This results in the generation of thin but dense sheets of collagen with entrapped nanoparticles within the collagen fibrils. Compressed constructs have densities approaching native tissue levels and thus mimic the natural *in vivo* environment better than most 3D systems.

One of the advantages of using collagen is that cells can be enmeshed in the collagen fibres, like they would be in tissue, allowing cell-matrix attachments to form all around the cell. Cellularised collagen can be plastically compressed with minimal or no detectable damage to the cells. When both cells and nanoparticles are loaded into compressed collagen constructs, a system is created *in vitro* which echoes body tissues following administration of nanoparticles. This is an excellent tool for investigating the fate of the nanoparticles, how cells interact with them and affect them, and how they affect cells, all within a 3-dimensional space.

Good 3D *in vitro* models will greatly benefit research, especially for the pharmaceutical industry. As talked about above, a huge amount of money has been pumped into therapeutics research, with the discovery of many possible drugs but very few successful ones. The monolayer cell culture technology most often used for testing has undoubtedly been beneficial but it suffers from having poor predictive power. Cells cultured on stiff plastic as monolayers are in an environment that is alien to them [1,65,84]. Therefore, it can be expected that unusual cellular behaviors will be observed. With better 3D cell culture systems, cells would behave in a more natural way and respond to stimuli in a more natural manner, thus giving more predictable results when testing goes to the next level – *in vivo* studies.

1.8. Embossing of soft substrates

Tissues in the body have micro-architecture which help to maintain tissue homeostasis. Some examples include blood vessels (internal structure), rete ridges in skin and limbal epithelial crypts in the cornea (both surface structures). Therefore, to properly mimic native tissue, such architectural characteristics should not be overlooked and be incorporated into the engineered construct.

Surface anisotropy has been shown to be important in controlling cell alignment and proliferation and differentiation [244-246]. Cells align themselves parallel to grooves present on the surface of substrates [247,248]. The dimensions of the micro-texture were shown to affect cell responses. Both the repeat distance

between grooves and the depths of the grooves have been found to affect cell alignment, with the latter having the greater influence [249]. Baby hamster kidney (BHK) cells showed greater degrees of alignment with increasing groove depths over the range of 100 – 400 μm . Similarly, fibroblasts aligned more in the direction of the grooves the deeper the grooves were [250].

The nucleus of a cell has been found to be segregated into regions of differing degrees of gene activities by nucleoskeletal intermediate filaments A, B1, B2 and C (which make up the nuclear lamina) [251-254]. The nuclear lamina provides both support to the nucleus and a physical connection to the cytoskeleton. Therefore, changes in cell shape can affect nuclear organisation and thus gene expression. Using micro-grooves, hTERT BJ-1 fibroblasts were found to reposition chromosomes resulting in significant changes in gene expression levels [255]. This suggests that external mechanical forces affect subcellular organisation which in turn affects downstream gene expression pathways.

Topography also has implications in stem cell niches. The epidermis of skin is made up of five layers, one of which – the basal layer, contains stem cells. Within this population of stem cells there are two sub-divisions of stem cells located either at the top or bottom of rete ridges [256-258]. The rete ridges in ageing skin were found to be flattened and stem cell markers have been shown to be downregulated [259]. This implicates the peaks and troughs of the rete ridges in providing specialised microenvironments for the maintenance of skin stem cells. Limbal stem cells of the eye reside in micro-scale crypts where it is conducive for the

maintenance of their plasticity [260]. Stem cells migrate from these limbal epithelial crypts (LECs) towards the centre of the cornea during wound healing or corneal regeneration. Therefore, micro-topographical patterning is necessary in engineered tissue to capture the natural behaviour and responses of cells in their local microenvironment.

Micro-topographical patterning has been performed using wet etching, micro-contact printing, photolithography, hot embossing, microfluidic patterning, polishing grinding, abrasion, plasma spraying, acid etching and grit-blasting [261]. However, these techniques are viable only for synthetic, usually hard materials such as glass and metals. Soft lithography is an approach that has been used for fabricating micro-structures on organic materials. Replica moulding, solvent-assisted micro-moulding, microcontact printing, micro-moulding in capillaries (MIMIC), phase-shifting edge lithography, decal transfer lithography and nanoskiving are examples of soft lithography techniques [262]. Soft lithography has been used to pattern silk films [263], collagen films [264-266], gelatin and collagen-glycosaminoglycan films [267], collagen gels [268-270], calcium alginate hydrogels [271], methacrylated hyaluronic acid (MeHA) and poly(ethylene glycol) diacrylate (PEGDA) [272]. These generally involve the use of photolithography to generate a pattern template usually using polydimethylsiloxane (PDMS). The template is then either pushed into pre-polymerised solution or the pre-polymer is cast over the template. Separation of the two yields a gel with topography moulded into a surface.

Micro-patterned collagen films were prepared by pouring collagen solution over a patterned PDMS template and air-dried overnight [266]. These films required chemical cross-linking for stabilisation. Similarly, micro-patterned 'basal lamina analogs' were fabricated by coating a PDMS template with either gelatin or collagen-GAG solutions. These were air-dried overnight, peeled off the template and cross-linked by thermal dehydration under vacuum [272]. Tang et al. used microtransfer moulding as well as MIMIC to pattern collagen gels into hexagonal or rectangular shapes while Yeh et al. showed that micro-scale square prisms, discs or strings could be produced from MeHA or PEGDA using soft lithography and photo-crosslinking.

However, soft lithography for micro-patterning membranes creates useful materials only for investigations on the effects of 2D topography on cell behaviour and not 3D. The use of hydrogels instead of films with soft lithography does have the added functionality of the third dimension, but in most cases, micro-patterning has been performed to create discrete micro-gels (of different shapes and sizes), rather than gels with micro-topography. Furthermore, the hydrogels used were highly hydrated, with densities much lower than that of native tissues.

Micro-patterning of hydrogels has also been done by casting a hydrogel around a removable pattern template [273]. Chrobak et al. cast collagen gels around a 120 μm -diameter needle [268]. Pulling out of the needle left a ~ 120 μm -diameter channel within the gel. Golden and Tien encapsulated a pre-formed pattern made from gelatin within collagen, fibrinogen or Matrigel [274]. Raising the temperature

of the set-up to 37°C resulted in the melting of the gelatin pattern, which was then washed out to leave a hollow pattern in the shape of the original gelatin mould. Dissolution of conical phosphate-based glass fibres cast within compressed collagen constructs have been shown to form micro-channels in a directional and temporal manner [275,276]. 3D-printing has been used to fabricate carbohydrate glass lattices which were then placed within pre-polymer solutions of PEGDA/acrylate-PEG-RGDS, fibrin, Matrigel, agarose or alginate [277]. Exposure of the lattice-gel composite to complete medium for 10 min led to the dissolution of the carbohydrate-glass, leaving behind an interconnected tubular network within the hydrogels.

1.9. Plastic compression

Collagen gels have several advantages such as their biocompatibility, biodegradability and low antigenicity. However, collagen gels contain a large proportion of water (~99.5%) with just 0.5% collagen content (similar density in a cup of tea with sugar), with densities usually in the range of 1-5 mg/ml, which is many times lower than the densities of native tissues (~20-30%). Roeder et al. showed that collagen gels of concentrations varying between 0.3 – 3.0 mg/ml (0.03 - 0.3% w/w) had linear moduli between 1.5 and 24.3 kPa [278], whilst 0.4% collagen gels were shown by Hadjipanayi et al. to have a Young's modulus of 42.2 ± 22 kPa [55]. These values were many times smaller than that of plastically compressed collagen constructs (20% w/w; 1805.3 ± 214 kPa). Thus the gels are mechanically

very weak with non-tissue levels of density [279]. Despite this, such compliant gels have enabled research on cellular mechanics to be done. Collagen gels have been known to be easily contracted by cells, as originally described by Bell et al. [280]. This allows the measurement of forces generated by cells within collagen gels [281] or to apply forces on cells [282,283]. Others have utilised this to increase the mechanical properties of their collagen constructs [284-286].

There have been other attempts to improve the mechanical properties of collagen gels using chemical cross-linking. However, these methods proved to be cytotoxic [287-289]. Other methods include reverse dialysis of collagen against PEG, but this technique is only feasible with small volumes of collagen and achieving high collagen concentrations requires time [290]; evaporation of collagen solutions to obtain up to 40 mg/ml [291], slow injection of low concentration collagen into microchambers can produce matrices approaching tissue-levels of density but they always have a steep gradient of concentration 5-1000 mg/ml [292], a combination of injection and dialysis to improve mechanical properties (25% w/v density) [293]. Helary et al. used ultrasonic waves or centrifugation followed by solvent evaporation to concentrate collagen to 40 mg/mg (4% w/v) [294,295]. Puetzer and Bonassar extracted collagen from rat tendon, centrifuged the acid-solubilised collagen and lyophilised the pellet before reconstituting the collagen in acetic acid at 20 and 30 mg/ml, which were used to prepare 1% and 2% collagen hydrogels [296]. These methods all have their advantages, but a critical disadvantage they have is that cells cannot be incorporated within the collagen, which diminishes the benefits of using collagen in the first place. Another method for improving the

mechanical properties of collagen gels is through mechanical conditioning. Loading collagen gels with tensile or compressive forces promotes fibril alignment which improves the mechanical strength of the gel in the direction of fibre orientation [297,298]. However, load-induced fibre orientation so far takes several hours to days to occur.

Brown et al. developed a technique termed 'plastic compression' (PC) that vastly increases the collagen densities and mechanical properties of collagen gels [299]. A collagen gel consists of a loose mesh of collagen fibrils 'containing' a relatively large volume of water. Brown et al. discovered that this bulk fluid could be removed without it returning, and at the same time compacting the collagen fibril mesh, to produce thin sheets of collagen with much lower water content than before. The expulsion of water can be controlled, allowing collagen density to be controllable and predictable. Only the water, small particles and solutes are lost, whilst cells and micro-scale particles are held in the gel [279,299]. Other advantages of this technique include speed and ease of the process, reproducibility, cytocompatibility and importantly it is a cell-independent process. Not relying on cells to produce desired materials and structures gives the experimenter control over the direct fabrication of tissues [300,301]. Furthermore, plastic compression increases the mechanical properties of collagen gels to a greater extent in a much shorter time than cell-contracted gels [302]. Plastically compressed collagen has been used to engineer a number of tissue types such as nerve [303], cornea [304,305], cancer [306], vasculature [307], bladder [308], skin [309,310], heart [311] and tendon [312] for *in vitro* investigations as well as for tissue replacement.

The top-down (indirect) approach to tissue engineering relies on cells to fabricate natural tissue structures. Cells can be cultivated on a synthetic scaffold which degrades slowly over time, whilst the cells produce their own matrix to replace the disappearing scaffold [301,313]. Cells take time to produce extracellular matrix, making indirect tissue engineering a time-consuming process. Furthermore, cells cannot be controlled; only the cell culture conditions can be manipulated to achieve some form of optimal condition (akin to agricultural farming) [314]. The direct approach is more controllable and much more rapid, usually taking hours at most (compared to weeks for cell-reliant culture) [299]. Bottom-up approaches to engineering collagen constructs allow for the entrapment of cells within networks of collagen fibrils formed from collagen monomers during fibrillogenesis, much like their native tissue environment. Top-down tissue engineering methods usually involve seeding cells onto a material and waiting for cellular invasion into the scaffold.

During plastic compression, the fluid leaving surface (FLS) of the collagen gel behaves as a dynamic filter, with decreasing pore sizes as the process progresses. At the early phases of compression, water, solutes and small particles are able to pass through the FLS easily but not cells, collagen fibrils and larger particles. Due to the combined effect of fluid discharge translocating collagen protein to the FLS and a compressive force acting on the gel, collagen fibril accumulations at the FLS become increasingly dense further along in the process [279,299]. The density and congestion at the FLS becomes so high that even fluid flow through it is limited

[315]. Fluid filtration by the FLS creates an anisotropic distribution of lamellae - layers of compacted fibrils, parallel to the FLS with the densest forming at the FLS. This anisotropy is important for instructing cell behaviour through mechanical signalling and for the mechanical properties of the construct [316,317]. Plastic compression of collagen gels, then, is a good system for engineering dense biomimetic collagen sheets with good mechanical properties, tissue-like organisation of cells and matrix and can also be imbued with tissue-like architecture.

1.10. Thesis overview

The aim here was to develop an *in vitro* system which would mimic the native tissue environment for the assessment of hyaluronan nanoparticle fate. This was carried out by adopting a direct tissue engineering approach using type I collagen, a protein naturally found in many tissues, and the technique of plastic compression, to present cells and nanoparticles with a dense 3D matrix environment, micro-scale architecture and molecular transport barriers.

Plastic compression has previously been performed using 5 ml rectangular moulds and then scaled up and re-engineered to a 12-well format [319,320]. Here we took it a step further to a 24-well format to improve efficiency. The system was first characterised – determining the optimal amount of paper in a plunger for a 16 mm diameter well (instead of 22 mm), calculating the fixed load needed to be placed on top of the plungers et cetera (Chapter 3). Compression in this system as well as the final constructs were characterised through measuring rates of fluid removal from the gels, calculations of the hydraulic resistances of the fluid leaving surfaces and measuring the thicknesses of the constructs (Chapter 4). We obtained an optical confocal device (CTS-2; Lein A.D., UK) that would allow real-time thickness measurements to be taken, *in situ*. Firstly, understanding the machine and interpreting the results were necessary in order to assess the meter's capability and functionality. It was then used to determine the thicknesses of compressed constructs and compared with histology, an end-point technique that is normally used.

Compression of collagen gels results in an anisotropic distribution of collagen in the constructs, with the top (where the FLS is) accumulating more collagen than the bottom – although, there are exceptions which will be discussed in later chapters. At the time, there was no technique for analysing the collagen distribution in compressed constructs. In Chapter 3, we devised a method that allowed us to look at local density distributions in collagen constructs. We hypothesised that staining sections of constructs with a collagen-specific dye (Sirius red) would result in staining intensities corresponding to collagen densities, which could then be analysed using ImageJ (Chapters 3 & 5). To validate the method, density gradient gels were cast to generate increasing concentration of collagen fibrils along the constructs following compression [246]. These were then stained and analysed. Once the method was validated, micro-patterned constructs were analysed to study the distribution of collagen to gain insight into fluid flow during the compression process.

Formation of collagen-dense fluid leaving surfaces was also investigated using the collagen density analysis method (Chapter 3). It was observed that in larger constructs, there appeared to be a second region of high density collagen on the opposite surface to the primary FLS. This was looked into further so as to better understand the dynamic mechanics of compression.

Cell- and nanoparticle-loaded compressed collagen constructs were investigated in Chapter 6 as models of tissue following nanoparticle administration. Hyaluronan

Chapter 1: Introduction

nanoparticles were incorporated into the collagen constructs rather than simply adding them on top together with the culture medium. Due to the small size of the particles, it was hypothesised that much of the initial nanoparticle load would be lost with the bulk fluid by the end of compression, and whatever remained would be trapped at the dense FLS. Collagenase digestion was used to release retained HA-NPs and fluorometry was carried out to quantify the HA-NP amounts.

These cell- and nanoparticle-loaded constructs were then cultured for up to three weeks. Firstly, the diffusion of the particles from the matrix was studied. We hypothesised that in an acellular construct, there would be limited nanoparticle movement since they would be trapped within the dense fibrillar network of collagen. With cells however, there would be particle release from the matrix due to cellular remodeling over time. Constructs were solubilised at set time points and the amount of HA-NP remaining in the constructs determined by fluorometry. Secondly, cellular uptake of the particles was investigated. Due to the dense matrix being a barrier not only to nanoparticle diffusion but also to cell movement, we hypothesised that cellular uptake in this 3D system would be lower than if the cells were cultured as a monolayer. This would give insight into possibilities as to why *in vivo* data often does not reflect the *in vitro* results. Uptake of HA-NP was determined by measuring the fluorescence of cell suspensions following culture.

The materials and methods used for this work are described in Chapter 2. Chapter 3 focusses on FLS formation analyses and the development of methods used in this thesis - the setting up of the 24-well PC system, collagen density detection method

Chapter 1: Introduction

using histology and image analysis, optical confocal meter evaluation. Characterisation of the 24-well compression process and the resultant constructs are described in Chapter 4. The focus of Chapter 5 is the application of the novel method developed to look at the local density distributions in micro-moulded constructs to understand the effects of fluid and collagen movement during micro-moulding on groove depth fidelity. Chapter 6 covers the investigation on HA-NP incorporation into compressed constructs, including determining the entrapment efficiency after PC, HA-NP diffusion from constructs over time in culture, and a comparison of HA-NP uptake by cells in conventional monolayer culture and cells within compressed constructs. Finally, the main outcomes are summarised in Chapter 7.

Chapter 2: Materials & Methods

This chapter is a compilation of the materials and methods that were routinely used throughout this project. Variations of these and specialised techniques will be described in the “Materials & Methods” sections of relevant chapters.

2.1. Cells

Neonatal human dermal (foreskin) fibroblasts purchased from American Type Culture Collection (ATCC), were cultured in Dulbecco’s modified Eagle’s medium (DMEM) (Sigma, UK) supplemented with 10% foetal calf serum (FCS; First Link, UK), 2 mmol/l glutamine (Gibco Life Technologies, UK) and penicillin – streptomycin (500 unit mL⁻¹ and 500 µg mL⁻¹) (ICN Biochemicals, UK).

2.2. Preparation of hyaluronan nanoparticle suspension

Lyophilised HA-NP (485.3 nm diameter) was prepared and provided by D. Ossipov from Uppsala University [325-327]. Briefly, a hyaluronan (HA) derivative containing the reactive chemoselective groups, thiol (-SH) and hydrazide (-hy), was prepared (HA-hy-SH). Hydrozone cross-linking of the HA derivative with an aldehyde-derivatised HA resulted in the formation of a hydrogel. Hydrophobic cargo (in this case, fluorescein isothiocyanate (FITC), was then covalently linked via a thiol exchange reaction to the hydrazone network of the modified HA gel. Hyaluronidase digestion of the HA hydrogel forms FITC-cojugated-HA nano-gels (nanoparticles).

The HA-nanoparticles (HA-NP) were sized using dynamic light scattering (DLS) and then lyophilized (Figure 2.1). De-ionised water was added to make a 100 µg/ml suspension and placed on a rolling machine for 30 min at 37°C to disperse the particles. HA-NP suspensions were stored in the dark at 4°C, and were mixed well using a vortex shaker before use.

2.3. Preparation of acellular collagen gels

Collagen gels were prepared as previously described [299]. Briefly, collagen solution was prepared in a wide-base 100 ml container as a mixture of 8 parts acid-solubilized rat tail collagen type I (2.06 mg/ml; First Link, UK), 1 part 10X minimal Eagle's medium (MEM) (Gibco, UK) and 1 part Dulbecco's Modified Eagle's Medium (DMEM) (Sigma, UK) supplemented with 10% (v/v) foetal calf serum (FCS) (First Link, UK) and penicillin/streptomycin (500 unit mL⁻¹ and 500 µg mL⁻¹) (ICN Biochemicals, UK). All components were kept chilled in an ice box (+4°C). 5M NaOH was then added drop-wise to neutralise the solution. Once the solution was neutralised, it was left to stand in the ice box for 30 min to allow bubbles within the solution to dissipate. Following which, the collagen solution was then aliquoted with required volumes into wells of a multi-well plate (12- or 24-wells; Orange Scientific, Belgium), and allowed to gel at 37°C for 30 min.

2.4. Preparation of cellular collagen gels

Collagen solution was prepared using a ratio of 8:1:1 of collagen I, 10X MEM and DMEM. The monomeric collagen solution was first mixed with the 10X MEM and then neutralised drop-wise using 5M NaOH. This was to prevent cell exposure to an acidic environment. This solution was left to stand to de-gas once neutralised. After 30 min, cells resuspended in DMEM were then added to the de-gassed, neutralised collagen solution. Human dermal fibroblasts were used at a seeding density of 10^5 cells/ml. The cell-collagen mixture was then gently swirled to distribute the cells evenly throughout the collagen and minimize bubble generation. This was then pipetted into wells and placed for 30 min in an incubator (37°C) to set.

2.5. Preparation of nanoparticle-loaded collagen gels

Nanoparticle-loaded collagen gels were prepared by mixing a solution of type I rat tail collagen, 10X MEM and nanoparticles suspended in DMEM, in a ratio of 8:1:1. The collagen preparation without the DMEM component was first neutralized drop-wise with 5M NaOH before the nanoparticles in DMEM were added. This was to prevent nanoparticle exposure to an acidic environment which may alter nanoparticle chemistry. Changes to the chemistry of the nanoparticles may lead to changes to their characteristics such as size and charge. Nanoparticles may also unravel or open up, resulting in the release of their cargo. HA-NPs were used at a concentration of 10 µg/ml. The mixture was then left to stand on ice for 30 min to de-gas. Following which, the nanoparticle-loaded collagen was pipetted into wells and placed at 37°C for 30 min to set.

2.6. Preparation of nanoparticle-loaded cellular collagen gels

Collagen was prepared using type I rat tail collagen (80%), 10X MEM (10%) and DMEM (10%). Collagen in dilute acetic acid was first mixed with 10X MEM and then neutralised drop-wise using 5M NaOH. Once neutralized, this was left to stand for 30 min to de-gas. Cells and nanoparticles were re-suspended together in DMEM at the desired concentrations. This cell-nanoparticle suspension was then added to the de-gassed neutralised collagen solution and gently swirled to distribute the cells and nanoparticles evenly. The cell-nanoparticle-collagen mix was then pipetted into wells and incubated at 37°C for 30 min to allow the gels to set.

2.7. Plastic compression of collagen gels

Once set, collagen hydrogels were then compressed as described previously [299], using a modified method of PC [319]. This modified method differs in the direction of fluid removal. Multi-well compression expels fluid upwards through the top surface of a gel, whereas fluid flows downwards and out through the bottom surface of the gel using the original method. Briefly, absorbent plungers (made from Whatman I filter paper or fibre) were placed on the set gels. The plungers absorbed removed fluid and pushed down on the gels simultaneously to compress the collagen.

Paper plungers: Whatman I filter paper (40 mm x 100 m, Whatman, UK) was wound around a spindle using a machine provided by TAP Biosystems. For the 12-well and 24-well formats, 175 and 95 cm of paper was used, respectively, to produce the plungers of appropriate diameter for each well size. Additionally, paper discs were cut out from Whatman I paper to match the dimensions of the wells. Two of these discs were used for each gel to prevent the compressed scaffolds from sticking to the plungers. A pressure of 1243.9 Pa was applied to each gel using stainless steel weights (provided by TAP Biosystems, UK), taking the mass of the plunger into account.

Fibre plungers: An alternative plunger type made from fibres (provided by TAP Biosystems, UK) was to compress collagen gels. No weights or paper discs were used together with this type of plunger.

12-well format: 1.2 m of chromatography paper 1 (4.0 cm X 100 m, Whatman, UK) was reeled into cylinders of ~22 mm diameter for use as absorbent plungers. Whatman I paper discs (Whatman, UK) were cut to size (~22 mm diameter). On top of each of the collagen gels, two of these paper discs and one paper roll, along with fixed loads (43.8 g) were placed on top of the gels.

2.8. Creating constructs with a horizontal density gradient

To create a horizontal density gradient within a collagen construct, a slightly-modified upward flow method of PC was used. Collagen gels with a density gradient were prepared by casting 3 ml or 4 ml of collagen mixture into wells of a 12-well

plate (Orange Scientific, Belgium). The plate was placed at an angle of 25° and incubated at 37°C for 30 minutes. This gave gels cast with an angle and so a surface incline of 25° (Figure 3.5). The plate was then returned to the horizontal. As above, a guide plate, two paper discs and a paper roll were placed on top of each gel, but no weight was added. The hydrated collagen gel is mechanically very weak, so it deforms and breaks apart easily. Addition of the weight would flatten out the wedge-shaped gel, reducing or even completely removing the pre-set angle. The gels were still compressed as absorption of water plus the weight of the paper plunger is sufficient for PC at a reduced rate. The 3 and 4 ml gels were allowed to compress for 20 and 30 min respectively. These timings were different to those used normally not only because of the exclusion of weights, but also because of the increase in thickness at one end of wedge-shaped gels which required a longer time to reach equilibrium compression (i.e. where fluid loss reduced to near zero).

2.9. Micro-moulding – Introducing surface patterns

To introduce topography to the surface of collagen constructs, two different template patterns were used for micro-moulding. These template patterns were placed on top of the collagen gel (where the FLS will be formed) before the initiation of PC.

The first template that was used was made from Kapton (a polyimide) which had a ladder-like pattern, with the rungs of the ladder being pushed into the collagen gels to create parallel rectangular-shaped grooves. These ‘rungs’ were 75 µm thick and 50 µm wide. The upward flow method of PC was used, whereby the Kapton

template (provided by TAP Biosystems, UK) was placed on the top surface of a collagen gel, before the addition of the paper discs, plunger and weight.

The second template was formed using stainless steel wires (wires.co.uk) of either 100 μm or 200 μm diameter, used with upward flow PC. 1.5 cm segments of wire were cut. 6 pieces of wire were placed on top of each scaffold. These 6 wires were lined up parallel to each other and manually spread evenly across the whole scaffold surface.

2.10. Histology

Constructs were prepared for histology using a routine protocol. Briefly, samples were fixed in 10% formalin solution and processed for routine paraffin embedding and sectioning in the transverse plane at 8 μm thickness. The sections were then dried at 58°C overnight. The sections were then de-waxed in 3 washes of xylene of 4 min each. These were then re-hydrated through 2 changes of absolute alcohol, then 90% alcohol, and 70% alcohol, for 4 min each. They were washed in running tap water for 30 s before staining. Sections were dehydrated through an alcohol series to absolute alcohol, cleared in xylene, and mounted in DPX (BDH, UK),

2.11. Staining

2.11.1. Haematoxylin and Eosin

Haematoxylin (Sigma, UK) and eosin (Sigma, UK) is a widely used stain in histopathology. Haematoxylin is basic and binds to the nucleic acids of cells, colouring the nuclei deep purple. Eosin is acidic and binds to basic structures such as the surrounding extracellular matrix and the cytoplasm of cells.

2.11.2. Sirius red

To study the morphology of plastically compressed constructs more closely, Sirius red (DirectRed 80, CI number 3578; Sigma, UK) was used. This dye has been shown to bind more specifically and selectively to collagen fibres, and even stains the finer fibrils intensely. This allowed us to visualise the distribution of collagen within compressed constructs more clearly [320,328]. Sirius red solution was prepared using 0.5 mg Direct Red 80 powder dissolved in 45 ml distilled water and 50 ml absolute alcohol. 1 ml 1% NaOH was then added to the solution along with 20% NaCl whilst stirring the mixture until a fine precipitate was observed. The mixture was left overnight and filtered before use. Sirius red was added to sections for 1 hour following rehydration. After which, samples were washed, dehydrated and mounted, as above.

2.11.3. Hoechst 33342 and Phalloidin

Hoechst 33342 (Gibco, UK) was dissolved in PBS at a concentration of 0.1 µg/ml. To view the cells using fluorescence microscopy, Hoechst 33342 was used to stain cell nuclei. This dye is cell-permeable and binds to the minor groove of DNA, thus labeling the nuclei. On histology samples, Hoechst was added to sections during the staining step (above) following rehydration, for 30 min before rinsing off excess dye.

Alexa Fluor® 594 Phalloidin (Gibco, UK) was added to PBS containing 1% BSA and 0.2% Triton-X100 to give a final concentration of 3.0×10^{-2} µM, to which, Hoechst 33342 was added for whole construct imaging. Samples were first washed with PBS 3 times and then fixed using 10% formalin for 30 min. After which, the samples were again washed 3 times with PBS. The phalloidin-containing solution was then added to the samples and left on a shaker for 45 min. Following which, PBS was used to wash the samples 3 times, before mounting the samples for imaging.

2.12. Microscopy

2.12.1. Light microscopy (Olympus BH-2, Olympus Camedia 2020Z)

Haematoxylin/Eosin- and Sirius red-stained sections were visualised using an Olympus BH-2 microscope, with images taken using an Olympus Camedia 2020Z.

2.12.2. Fluorescence microscopy (Olympus BX61)

Fluorescently-labelled samples and samples containing FITC- / Nile red-loaded nanoparticles were viewed and imaged using an Olympus BX61.

2.12.3. Scanning electron microscopy (Jeol, JSM 5500 LV, Japan)

Samples were fixed in 2% glutaraldehyde in 0.1 M sodium cacodylate buffer for 30 min. They were then put through an ascending alcohol series for dehydration. Hexamethyldisilazane was then added and left on to dry overnight. This protocol ensured that samples were thoroughly dehydrated prior to SEM imaging. Processed samples were then sputter-coated with gold-palladium and imaged using a Jeol JSM 5500 LV SEM at a voltage of 20 kV.

2.13. Image analysis

2.13.1. Horizontal gradient constructs

Constructs prepared for histology were photographed along their entire length to capture the whole construct (Olympus BH-2 photomicroscope). Images were converted to greyscale and inverted for analysis using ImageJ (version 1.45). Using the “Line selection”, construct sections within each image was highlighted and “Plot Profiles” for each image were generated. As much of the construct as possible was selected without including the background. These were then compiled sequentially to obtain an overall plot profile of a construct. In this case, the plot profiles

measure the average pixel intensities in the z-plane of the construct against the length of the construct (x-y plane). Lines of best fit were then calculated to obtain the gradient (change in pixel intensity against distance along the construct) of the construct.

2.13.2. Micro-moulding analysis

Micro-moulded constructs were analysed using “line selections” with the line width set at 20. Line lengths were set to correspond to the thickness of the construct beneath the engineered grooves. Multiple line selections were then positioned vertically along the construct in a chronological order. Mean pixel intensities of each line selection was then measured and plotted against its position along the construct to generate a graph of mean pixel intensities against position along the construct.

2.13.3. Fluid leaving surface analysis

Single line selections were used to highlight sections of a construct in the z-plane. Plot profiles were generated to obtain the mean pixel intensities across the construct going from the top to the bottom (or vice versa).

2.14. Fluorometry

Compressed collagen constructs were placed individually in 30 ml universal tubes with 1 ml of 0.2% bacterial collagenase I (Gibco, UK) in phosphate buffered saline (PBS) and digested on a rotating shaker for 20 min (600 rpm) at 37°C. Following digestion of the collagen matrix, 8 µl of each digestion mixture was diluted in 4 ml phosphate buffered saline (PBS) for fluorometric measurement (Perkin-Elmer LS 50B) at excitation/emission wavelengths of 495/520 nm and 552/636 nm for HA-NP and GCPQ-NR respectively.

Hyaluronan nanoparticles (HA-NP) were resuspended in PBS at concentrations of 0.001, 0.005, 0.00325, 0.01, 0.0125, 0.025 and 0.05 µg/ml for calibration using the fluorimeter. Measurements in this range resulted in a plot (Figure 2.1) which had a correlation coefficient, r , of 0.9996226 and coefficient of determination, r^2 , of 0.9992454. This indicates a strong correlation over this range between HA-NP and fluorescence intensity and that reliable predictions of HA-NP concentrations can be made from fluorescence intensity measurements.

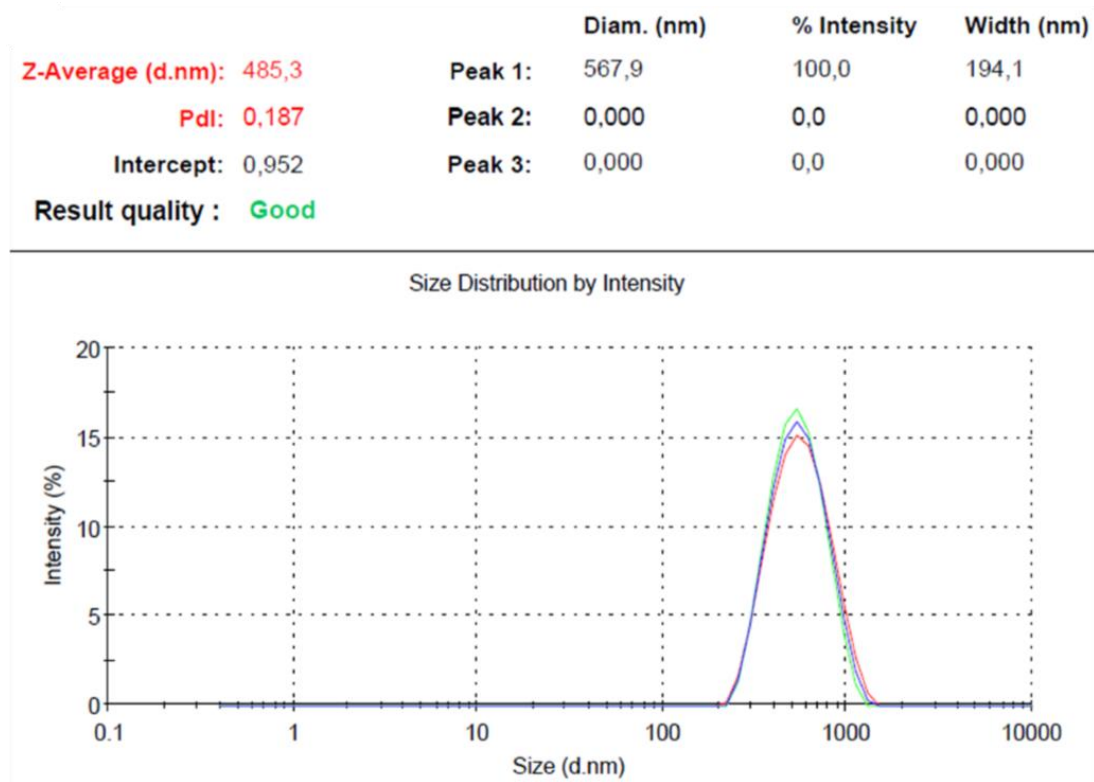


Figure 2.1: DLS measurement results showing that the hyaluronan nanoparticles were on average, 485.3 nm in diameter. The polydispersity value (Pdl) was low at 0.187, indicating uniformity in the sample.

2.15. Statistical analyses

All experimental conditions were conducted with a sample size of 3 or more and data were represented as mean \pm standard deviation. Where two groups were compared, t-test was used. Multiple group comparisons was done using one-way ANOVA (analysis of variance). Statistical differences were considered to be significant when $p < 0.05$.

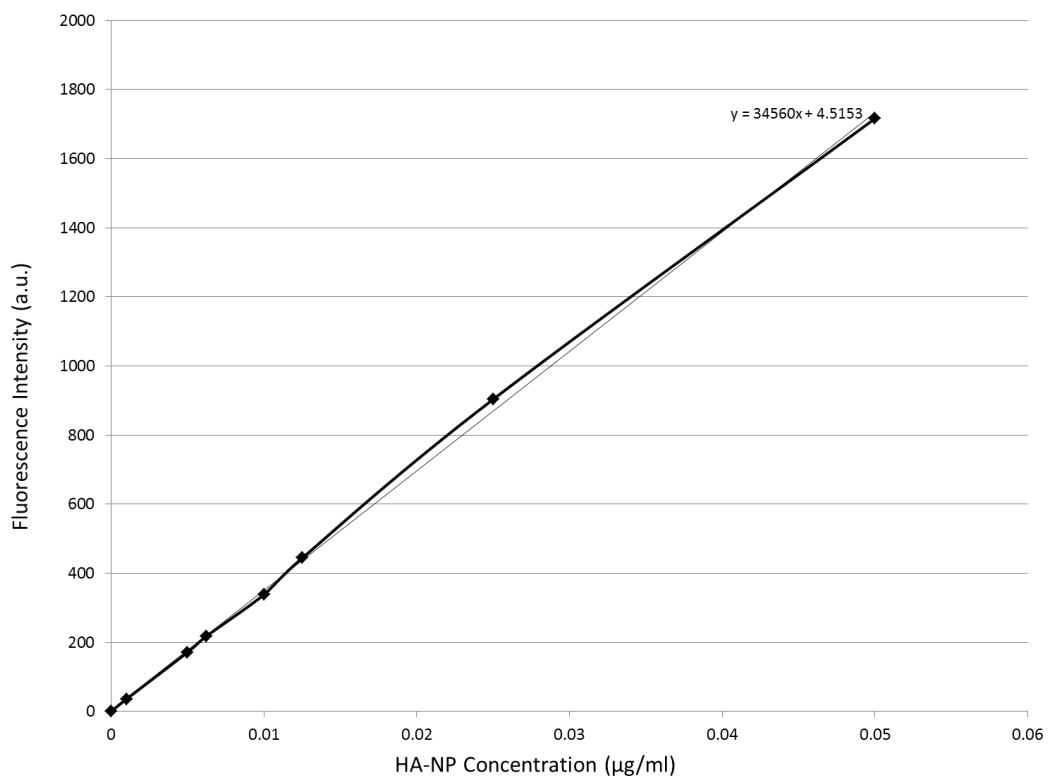


Figure 2.2: Calibration curve of HA-NP fluorescence in in the range of 0 – 0.05 µg/ml. The linear relationship between this concentration range and fluorescence intensity indicates good correlation between the two variables.

Chapter 3: Methods Development & the Fluid Leaving Surface

In this chapter, we describe and discuss the development of several experimental methods and techniques, and also the formation of the fluid leaving surface(s) (FLS).

3.1. Scaling up the multi-well compression system

Much research carried out using plastically compressed collagen has been by using custom-made rectangular moulds [55,244,246,299,329-331]. In this technique, the gels were sandwiched between two nylon meshes. A glass slide and a fixed load were placed on top of the gel and filter paper for compression and fluid removal. Whilst this set-up has undoubtedly led to new knowledge and possible therapeutic applications, it has a low output, with the production of only 1 - 2 compressed constructs at a time. It involves much gel manipulation and produces an FLS on the basal, filter paper-side surface. This was then scaled up (in terms of output) to a multi-well system where 12 constructs can be made simultaneously in conventional closed bottom wells [304,319]. Furthermore, the experimental set-up was simplified to using a 12-well plate, paper plungers on top and a fixed load. Sample handling was reduced, minimising infection and damage to the constructs. Here we take it a step further to fabricating 24 constructs at a time (in a 24-well plate). The system is fundamentally the same as the 12-well system, but adjustments had to be made and characterisation of these smaller constructs were carried out.

Wells in a 24-well plate measure 16 mm in diameter (compared to 22 mm for the 12-well plate). Therefore the size of the paper plungers was reduced accordingly. Whatman I filter paper (40 mm x 100 m, Whatman, UK) was wound around a spindle using a machine provided by TAP Biosystems (Figure 3.1A). 95 cm of paper was used to produce the plungers. Paper discs were cut out from Whatman I paper to fit the wells. Two of these discs were used for each gel to prevent the compressed scaffolds from sticking to the plungers. Using a fixed load of 43.8 g in the 12-well system, the applied pressure was calculated to be 1243.9 Pa, taking the mass of the plunger into account. The required mass for exerting the same amount of pressure for the 24-well format could then be calculated:

12 – well system, Pressure exerted by plunger and fixed load:

$$\text{Diameter of well (12 – well format)} = 22 \text{ mm}$$

$$\text{Area} = \pi r^2$$

$$\text{Area} = \pi (0.011 \text{ m})^2$$

$$\text{Area} = 3.801 \times 10^{-4} \text{ m}^2$$

$$M_L = 43.8 \text{ g}$$

$$M_{PP} = 4.4 \text{ g}$$

$$M_T = 48.2 \text{ g}$$

$$\text{Pressure} = \frac{\text{Force}}{\text{Area}}$$

$$\text{Pressure} = \frac{(0.0482)(9.81)}{3.801 \times 10^{-4}} \text{ Pa}$$

$$\text{Pressure} = \mathbf{1243.9 \text{ Pa}}$$

The mass required to exert 1243.9 Pa in the 24 well-system is as calculated:

24 – well system, Mass needed on top of plunger:

Diameter of well (24 – well format) = 16 mm

$$Area = \pi r^2$$

$$Area = \pi (0.008 \text{ m})^2$$

$$Area = 2.0106 \times 10^{-4} \text{ m}^2$$

$$Force = Pressure \times Area$$

$$Force = 1243.9 \text{ Pa} \times 2.0106 \times 10^{-4} \text{ m}^2$$

$$Force = 0.2501 \text{ N}$$

$$M_T = \frac{0.2501}{9.81}$$

$$M_T = 25.5 \text{ g}$$

$$M_L = M_T - M_{PP}$$

$$M_L = 25.5 \text{ g} - 3.48 \text{ g}$$

$$M_L = \mathbf{22.02 \text{ g (per well)}}$$

where M_{PP} , M_L and M_T are the paper plunger mass, mass of the fixed load and the total mass.

Fibre plunger system: An alternative plunger type made from fibres (provided by TAP Biosystems, UK) was used to compress collagen gels (Figure 3.1B). No weights or paper discs were used together with this type of plunger, resulting in decreased pressure applied to the collagen gels. The pressure exerted by a fibre plunger was

calculated to be just 149.8 Pa, 10-fold smaller than the pressure exerted by the paper plunger system.

Pressure exerted by fibre plunger:

$$M_{FP} = 3.07 \text{ g}$$

$$Pressure = \frac{Force}{Area}$$

$$Pressure = \frac{(0.00307)(9.81)}{2.0106 \times 10^{-4} \text{ m}^2}$$

$$Pressure = \mathbf{149.8 \text{ Pa}}$$

where M_{FP} is the mass of a fibre plunger. This reduced pressure explains the greater compression times required when fibre plungers are used. The pressure exerted by the fibre plunger system is a lot smaller than with the paper plunger method, but the lack of pressure is accompanied by greater absorbency. However, the greater absorptive power does not fully compensate for the lack of pressure on the gels, resulting in longer compression times. Compression times were similar for 0.5 and 1.0 ml gels (3 min for both; 5 and 6 min for paper and fibre plungers respectively), but greater for 1.5 and 2.0 ml gels (7 and 11 min; 12 and 15 min) (see Chapter 4).

Absorbency was compared by first measuring the dry weights of the plungers, then placing them into a shallow bath containing water for 1, 10, 20 and 30 seconds. Figure 3.2 shows that at 1 second, there was not much difference between the amount of water absorbed by paper (1.17 ± 0.2 ml) and fibre (1.12 ± 0.17) plungers. By 10 seconds, fibre plungers (2.63 ± 0.17 ml) absorbed a statistically significantly greater amount of water compared to the paper plungers (2.19 ± 0.09 ml). This

shows that the fibre plungers have greater absorbency compared to paper plungers. After this point, the amount of water absorbed by fibre plungers only increased very slightly (2.99 ± 0.14 ml after 30s) as this was close to their maximum capacity. Paper plunger absorption continued up until 90 seconds where it reached its full capacity of 7.73 ml (data not shown).

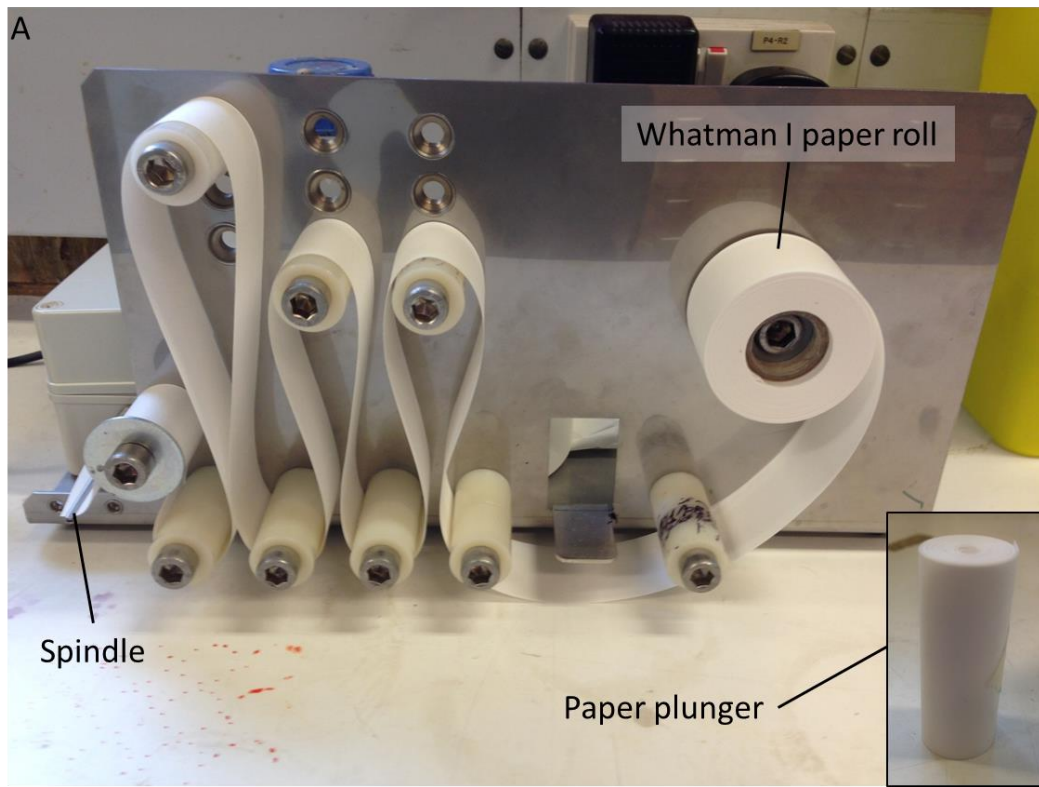


Figure 3.1: The two types of plungers used for compression. (A) Photograph of the custom-built machine used to produce paper plungers (fabricated by Mr M. Purser, TAP Biosystems). Inset: Photograph of a paper plunger used for 24-well plates. (B) Photograph of fibre plungers.

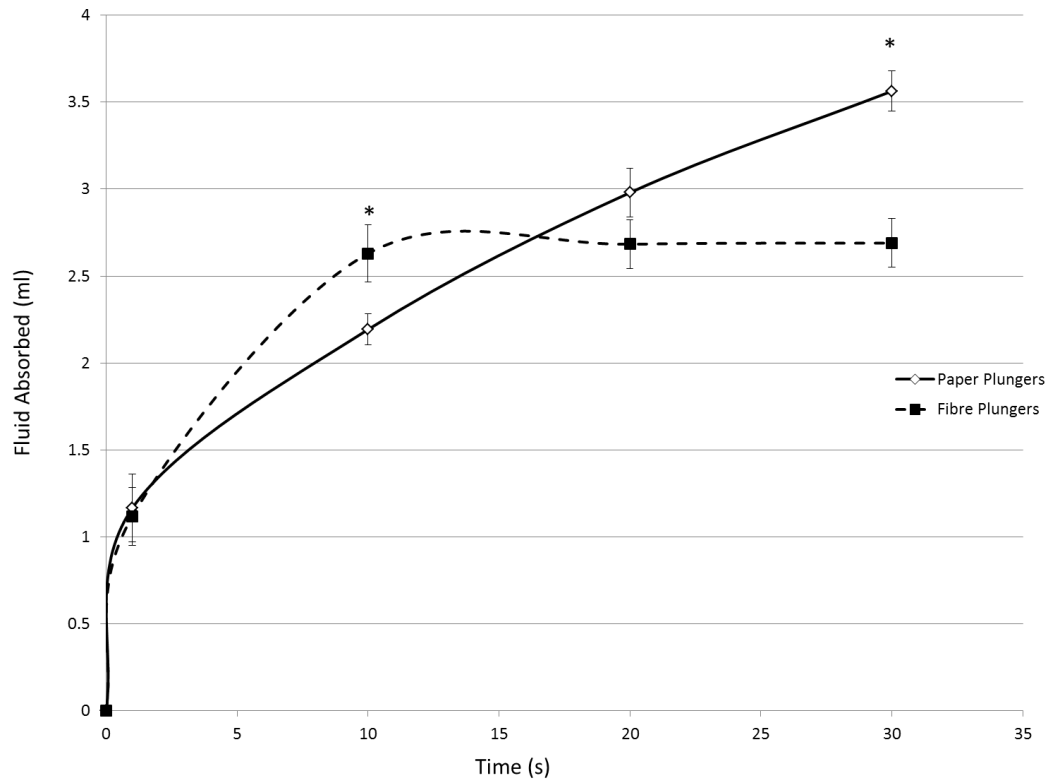


Figure 3.2: Greater rate of absorption of water by fibre than paper plungers. Fibre plungers showed greater absorbance than paper plungers in the first 10 seconds, when it then reached its maximum capacity. Error bars depict the standard deviations of the mean ($p < 0.05$; $n = 3$).

3.2. Collagen density analysis

Plastic compression of collagen gels results in an anisotropic compaction of collagen fibrils, with the FLS side being the densest and the opposite side (usually) being the least dense [330]. The larger the initial volume of gel used, the more likely a secondary FLS will form during the compression. Formation of a secondary FLS changed the distribution of collagen within a construct as collagen fibril accumulation followed fluid movement. Other factors may also affect collagen distribution during compression such as micro-patterning (or micro-moulding) and multi-layering. It is important to know what the patterns and densities of collagen distribution are as these will affect cell behaviour (more about this in Chapter 4). However, there is no simple technique for quantifying the local collagen density in collagen constructs. Therefore, we aimed to develop a method for doing so.

Histology of cross-sections of collagen constructs gives a good view of the collagen fibrils and lamellae that form because of the compression. From samples stained with eosin, it could be seen that there were differences in staining intensities in different regions of a construct. Therefore, we decided to take a histological approach to quantifying local collagen densities. Added benefits for doing so include its simplicity and that we routinely perform histology.

Various dyes are used to stain for collagen fibres in histological samples, such as van Gieson stain, and the various forms of trichrome staining. However, these stains lack the selectivity and specificity for collagen molecules, especially the very thin fibres [334]. As such, a more collagen-specific dye was needed. Previous studies

have shown that sirius red stained even the finer collagen fibres more intensely than the traditional dyes [332,335]. Anionic sirius red binds to collagen fibres through interactions of its own sulphonic acid groups with the basic groups of (hydroxy)lysine and arginine's guanidine groups [333].

Junqueira et al. showed that blocking interactions with collagen basic groups resulted in a drastic decrease in Sirius red staining. For example, deamination of collagen samples reduced Sirius red staining by 43%, while acetylation of guanidine and amino groups and chlorination of amino groups reduced staining by 83% and 85% respectively. Tullberg-Reinert and Jundt assessed the specificity of the Sirius red stain on several different ECM components including laminin, heparin sulphate proteoglycans, fibronectin, collagen I, collagen III and collagen IV. They showed that only collagen I gave an intense red staining with sirius red, which was concentration-dependent and twice as effective as on collagen III [336]. In hepatology, the collagen proportional area (CPA) is used to determine the extent of liver fibrosis. Masson's trichrome has routinely been used for this purpose whilst others have used sirius red [379]. Huang et al. compared the two staining methods and showed that with sirius red, more accurate and reproducible results were obtained than with Masson's trichrome [380]. Since sirius red has been reported to be advantageous over other collagen stains, we decided to use this dye for our analysis method.

3.2.1. Image processing

Coloured photographs were first converted to greyscale with values ranging from 0 (black) and 255 (white) so that the construct appeared dark on a light background), and then reversed so that the construct appeared white on a dark background to avoid confusion over pixel values (Figure 3.3); in this way, a higher value will correspond to a higher fibril intensity (Figure 3.4).

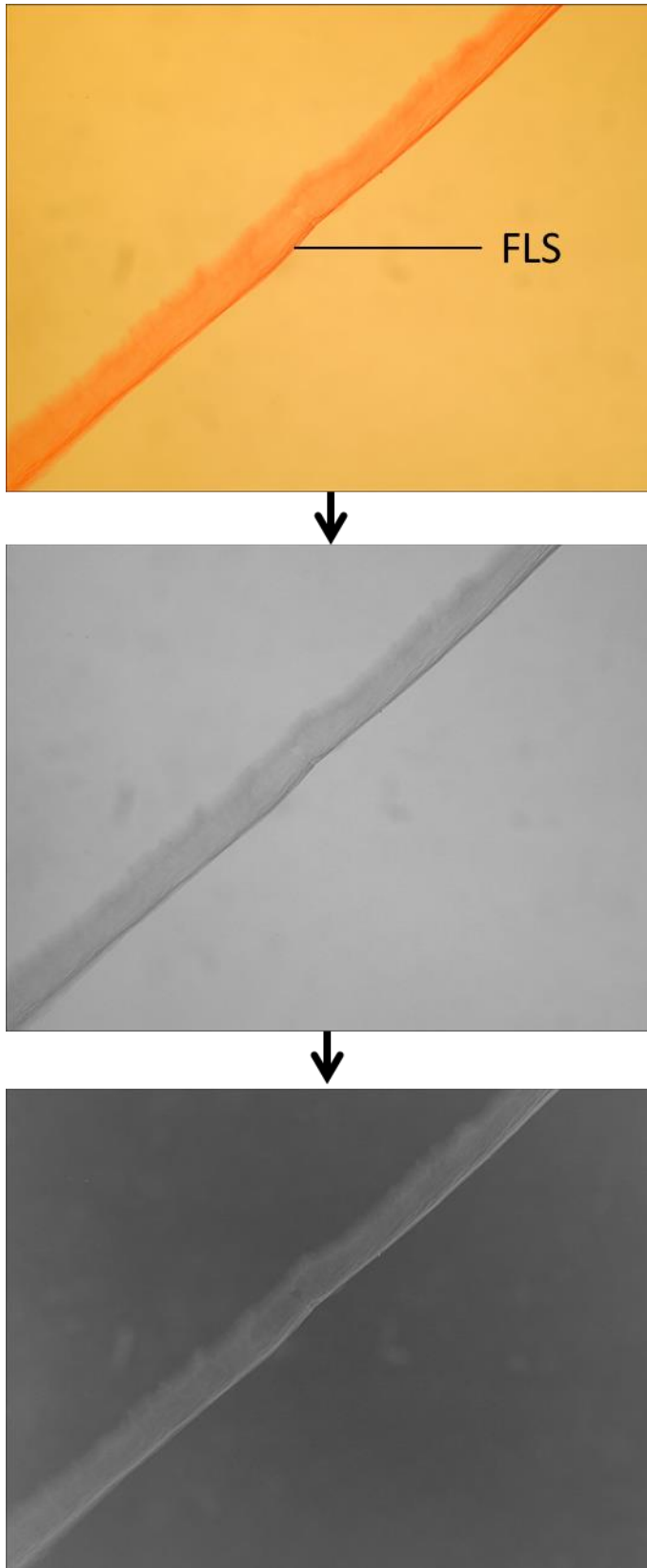


Figure 3.3: Image processing for the collagen density analysis. A coloured photograph of the cross-section of a compressed collagen construct stained with sirius red is first converted into black-and-white. The construct appears dark on a light background after this first step. The image is then inverted so that the construct appears bright on a dark background.

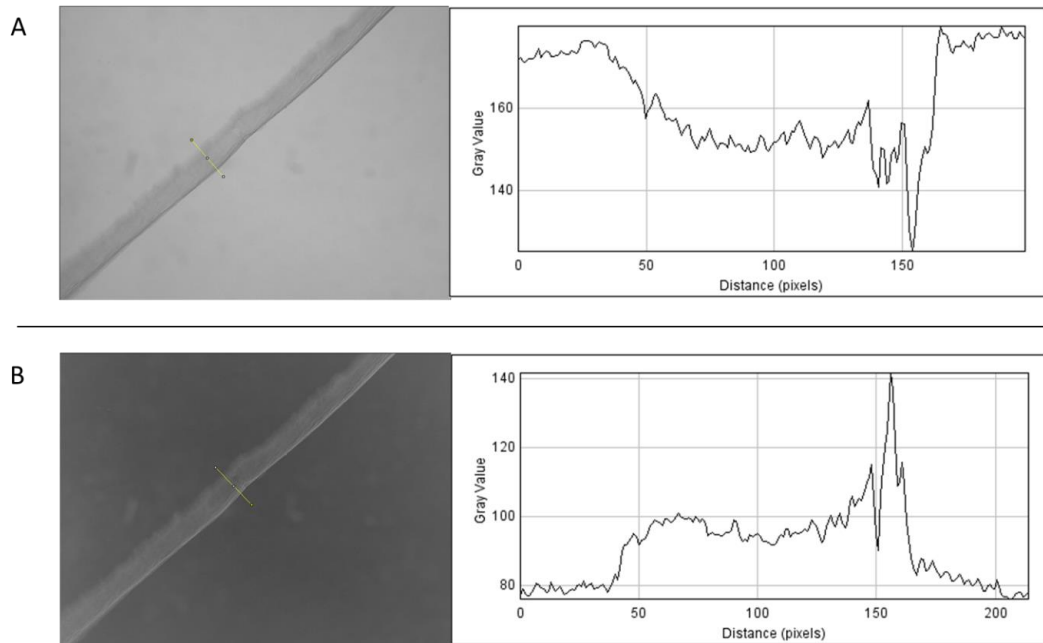


Figure 3.4: Digital image of a Sirius red-stained compressed collagen construct after conversion from colour to greyscale (A) and then inverted (B). The graphs on the right of the images are the plot profiles across the constructs in the z-plane (line shown in (B)). As can be seen in A, the lower pixel values correspond to the construct, which may cause some confusion. Therefore the image was inverted so that high pixel intensity corresponded to the intensity of the dye (B).

3.2.2. Validation

To verify that image analysis would detect differences in staining intensities within constructs, a known model for fabricating constructs with density gradients was used [246]. Collagen solution was pipetted into multi-well plates as per usual. The plates were then tilted at a defined angle during the setting stage to generate wedge-shaped gels. Compression of these gels would produce constructs with a gradient of collagen density along the original slope of the wedge (Figure 3.5). The aim was to test if this density gradient would be reflected by Sirius red staining, serving as a way of validating the analysis technique.

Three angles (19°, 25° and 31°) were tested to generate three different gradients on three initial gel volumes (2, 3 and 4 ml) in 12-well plates (Figure 3.5). 2 ml gels were extremely thin after compression, making it impossible to handle without causing them damage. 31° was the maximum possible for 4ml gels before the collagen solution began to spill out of the well. But with such a steep angle, and the compliancy of collagen gels, the weight of the plungers caused deformations in the slope during compression. This problem did not occur with the smaller 25° angle as more of the gel was in contact with the plunger to support its weight at the start of compression. Hence the 25° angle was used routinely.

Graded constructs were prepared and photographed along their entire lengths for the analysis resulting in about 20 images taken per construct as described in section 2.13.1. Line selections were used to highlight the construct within each image. "Plot profiles" were then created using the ImageJ function resulting in around 20

individual plot profiles per construct. These were then compiled in the right order, to generate a graph of mean pixel intensities across a whole construct. Results showed that where gradients were present, gradients of staining intensity were also present, and importantly, in the predicted direction (Figure 3.6). Figure 3.7 shows the compiled results from 3 and 4 ml (initial volume) constructs either set at an angle of 25° or flat (control). The results show that the analysis method did not pick up a significant intensity gradient in constructs created without a density gradient (3 ml: $(2.2 \pm 1.73) \times 10^{-4} \mu\text{m}^{-1}$; 4 ml: $(2.6 \pm 1.64) \times 10^{-4} \mu\text{m}^{-1}$). Constructs cast at an angle did display changes in staining intensities, with the 3 and 4 ml constructs having gradients of $(1.1 \pm 0.67) \times 10^{-3} \mu\text{m}^{-1}$ and $(6.6 \pm 3.2) \times 10^{-4} \mu\text{m}^{-1}$ respectively. These gradients were statistically significantly different to the constructs made without gradients. Another point to note here is that the measured gradients of the 3 and 4 ml constructs were not significantly different. As these were cast at the same angle, the same rate of change of density would be expected.

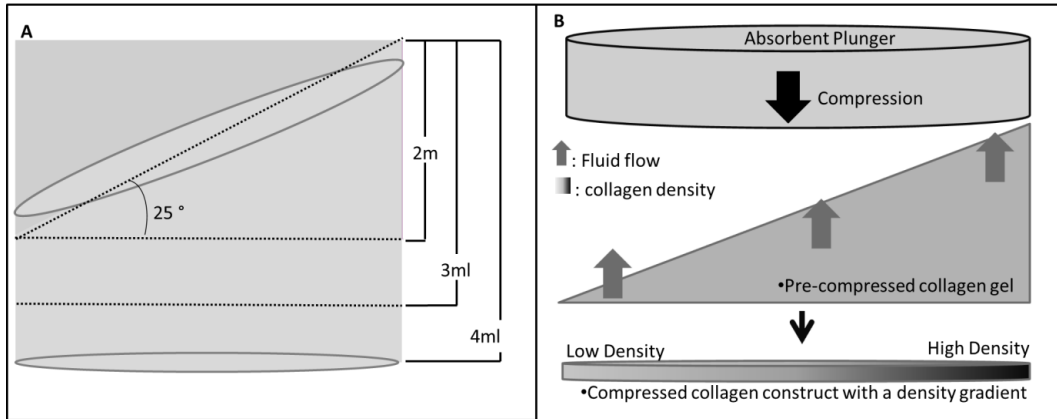


Figure 3.5: (A) Schematic representing the shapes of gels formed with 2, 3 and 4 ml collagen cast at an angle of 25°. (B): A schematic showing the plastic compression (upward flow method) of a collagen gel cast with an angle. Wedge-shaped gels would be compressed to give a construct with uniform thickness across, but with a density gradient of collagen.

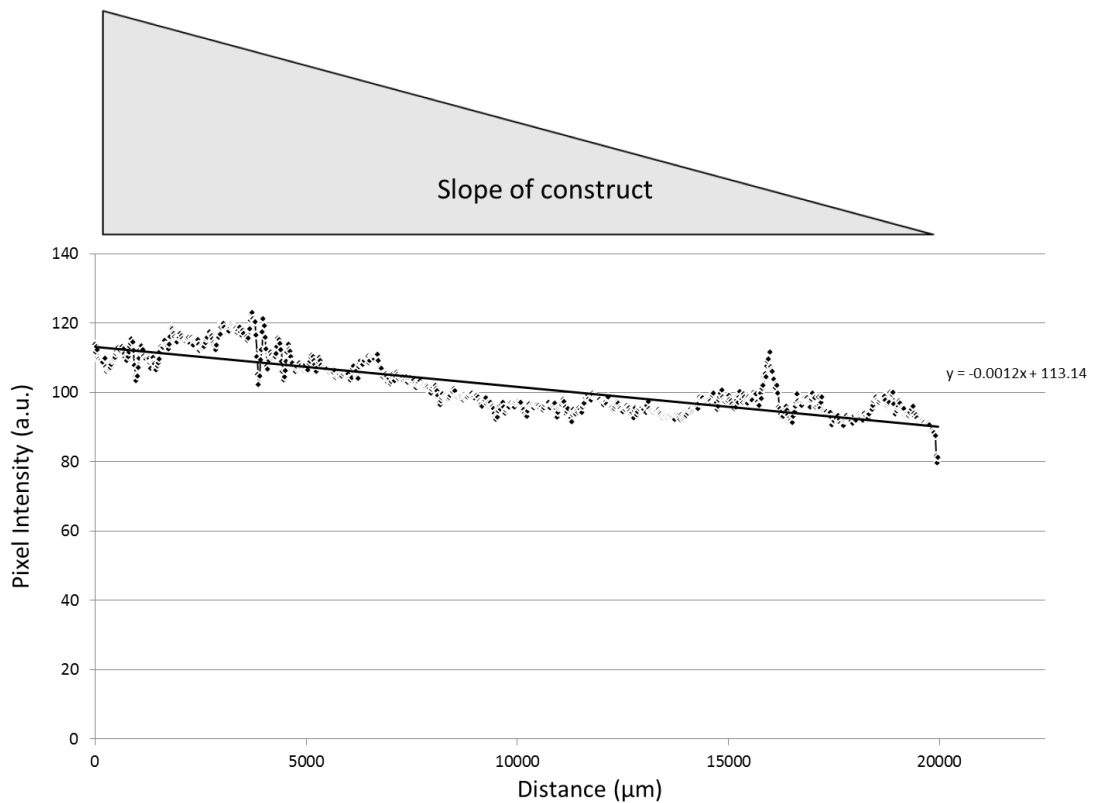


Figure 3.6: An example graph of the density analysis results from one graded construct. Plot profiles from individual images were compiled to create an overall plot profile for the construct. The important point here is that the detected gradient matches the direction of the slope of the construct.

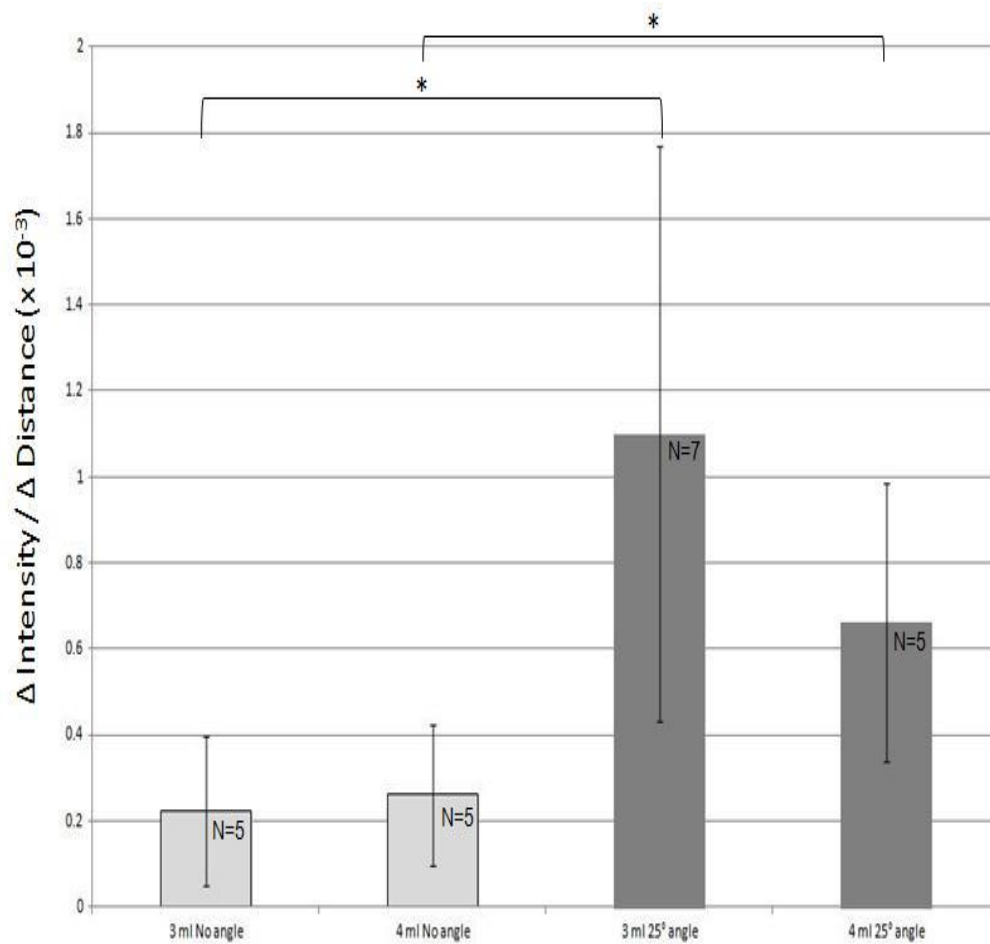


Figure 3.7: Graph of measured gradients of constructs showing that density changes were detected in the predicted directions. Notice there was no significant difference between gradients as the gradients should have been the same, just across different density scales. Error bars depict the standard deviations of the mean ($p < 0.05$).

3.2.3. Image analyses

Two semi-quantitative methods of analyses were used. The first way we analysed constructs was to look at collagen distribution along the cross-section (x-y plane) as described in section 2.13.2. This was done using line selections set at a fixed width as it allowed the repeated use of the same line, thus ensuring that the area of the region measured was identical each time. Lines were arranged side by side, perpendicular to the FLS, along a section of the construct being analysed (Figure 3.8). The mean pixel intensities within each rectangular segment was measured. This method was used for analysing micro-moulded constructs where solid blocks were pushed into the FLS to create grooves. Micro-moulding would change the fluid flow mechanics and possibly collagen distribution. Therefore, we wanted to see if there were any changes and to identify what they were.

The second was to scan across a construct using a line selection, perpendicular to the FLS, to study the distribution of collagen in the z-plane (Figure 3.4) as described in section 2.13.3. Several functions from ImageJ helped with the visualisations of the scans performed. "Plot profile" plots the pixel intensity measurements as a graph, whilst the "3D plot" function digitises the region scanned and renders a 3D image of that region. This method allowed us a greater understanding of the compression process and how fluid flow and collagen accumulation occur.

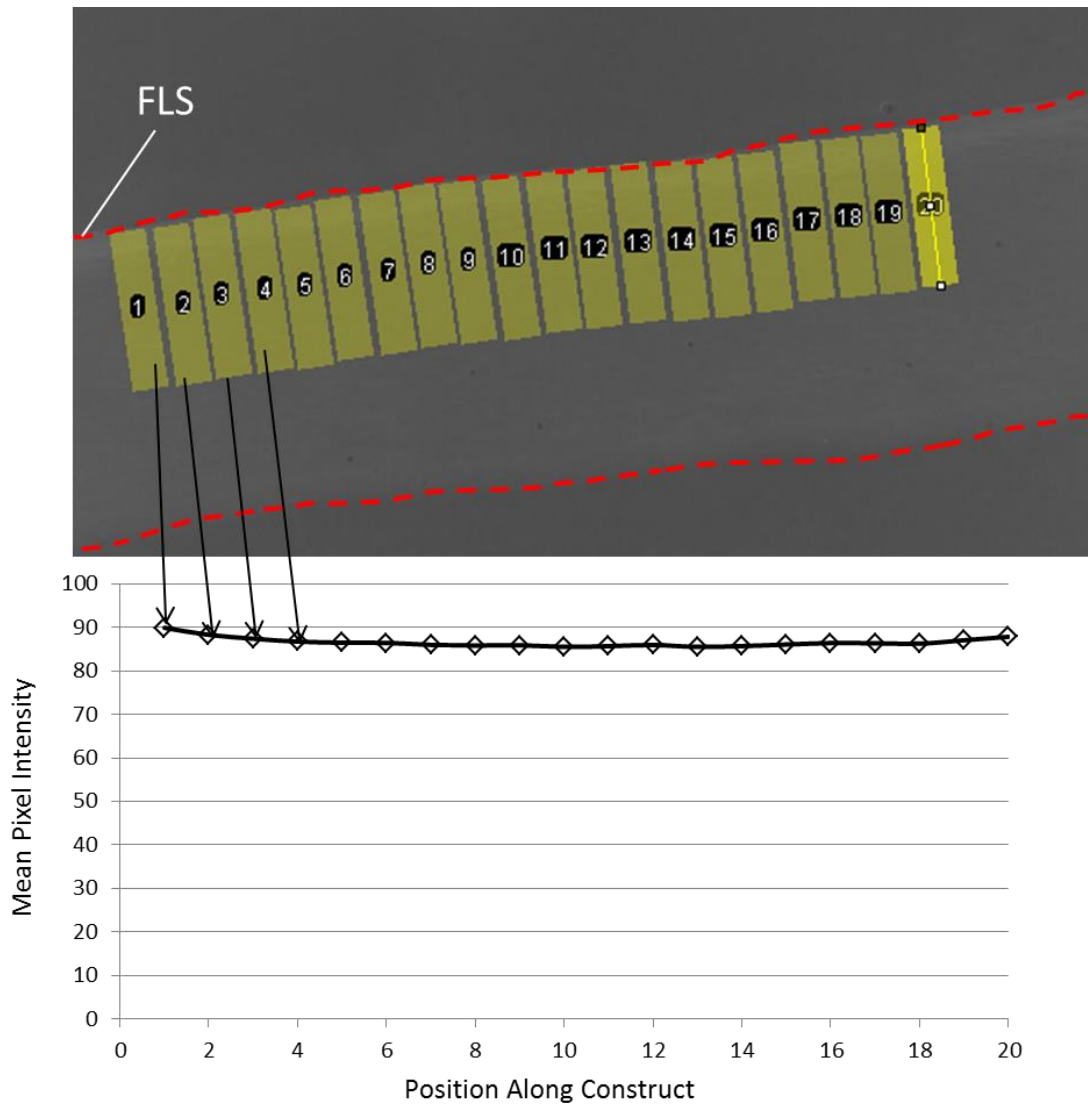


Figure 3.8: Screenshot image of the analysis of local collagen density distributions in a compressed collagen construct (marked out by the red dotted lines) using cross-section measurement domains (yellow rectangles) and the corresponding graph of measured mean pixel intensity values. Average pixel intensities were measured for each yellow boxed region which were then plotted against its corresponding position along the construct to obtain the graph.

3.3. Lein optical confocal device measurements

Plastic compression of collagen hydrogels allows the controlled fabrication of constructs. Two controllable properties are collagen density and layer thickness which are interconnected characteristics in this system. Densities of constructs can be increased by increasing matrix compaction and thus decreasing construct thickness, to suit a variety of purposes such as bone, nerve or skin tissue engineering. It is necessary to be able to accurately determine these properties of constructs for reproducibility and functionality.

Histology has been the primary method for determining the thicknesses of these scaffolds. However, this is only able to give end-point results. Furthermore, the heavy processing steps involved in histology (alcohol and dehydration) to obtain a stained section ready for imaging likely alters the thicknesses of these constructs, thus giving inaccurate information. Scanning electron microscopy (SEM) can also be used to find out the thickness of a sample, but it involves radical dehydration of the sample resulting in smaller/thinner samples when imaged. An optical method for determining tissue thickness in real time without the need for processing is necessary in order to make accurate measurements and to be able to study the process of plastic compression [338-340].

There are several methods for determining tissue thickness such as magnetic resonance imaging (MRI), computerized tomography (CT), ultrasound, microspectrophotometry, confocal microscopy and optical coherence tomography (OCT) [341-346]. Ultrasonography, MRI and CT scans have good penetration but

poor resolution (hundreds of microns), whilst confocal microscopy and OCT have sub-cellular resolutions. Thus, the latter two suit our purpose of determining the thicknesses of compressed collagen constructs typically tens of microns up to hundreds of microns. However, both of these techniques require big, expensive machinery for producing images. Additionally, confocal microscopy usually requires samples to be removed from sterile conditions for scanning. Thus there is a lack of a low-cost method for determining engineered tissue thickness non-invasively.

The CTS-2 (Lein Applied Diagnostics, UK; Figure 3.9) is an optical device developed to allow non-contact measurements to be made *in situ* in less than 1 second [347]. It works by emitting a low-powered (Class I, λ :1310 nm) laser beam which passes through a sample and captures reflected light back off media-gel interfaces which the laser propagates through where they have different refractive indices (e.g. a glass-air interface). The focal point moves through the sample during the scan, and any reflected light returns to the CTS-2 detector via the same path as the emitted light (Figure 3.10) to give a map of reflection points (or media interfaces) within the entire scan range (<1 mm), with reflection points registering as peaks (Figure 3.11).

As compressed collagen scaffolds are very thin, physical handling may damage the scaffold architecture or may be improperly placed on the instrument, giving inaccuracies in measurements. This system negates the need for sample transfer and scaffolds can be measured directly in their wells. The ability to make measurements *in situ* is a great asset as subsequent readings may be taken over long periods of time – unlike histology which is an end-point process.

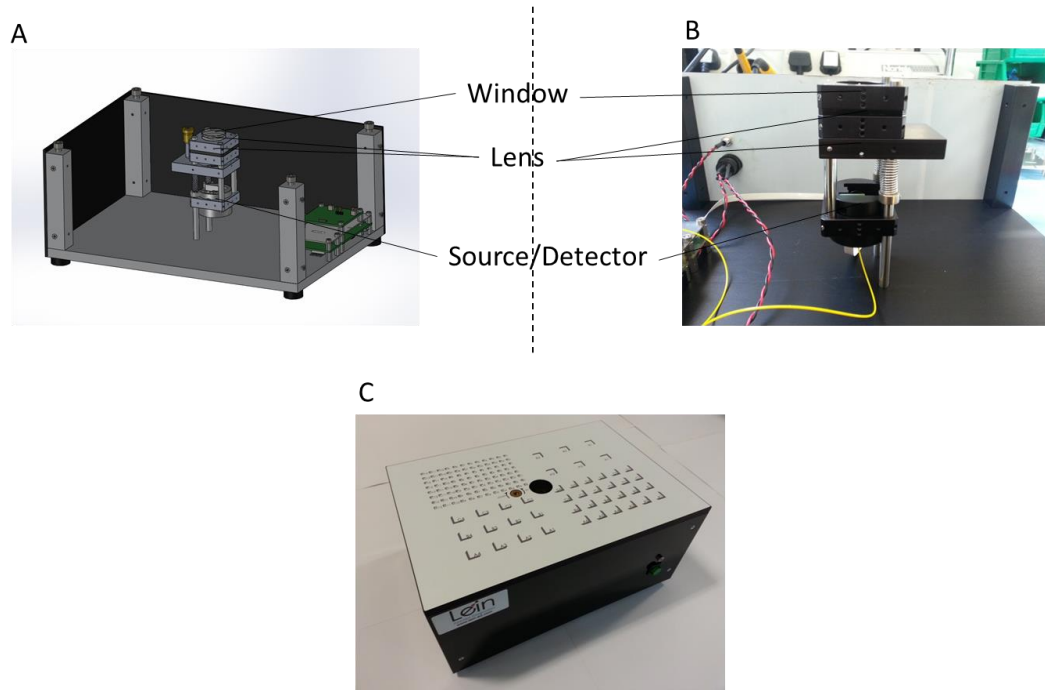


Figure 3.9: A diagram and photographs of the CTS-2. (A): Diagram showing the internal components of the CTS-2. (B): Photograph of the optical components of the CTS-2. (C): Photograph of the assembled CTS-2 as was used for experiments, where samples *in situ* were simply placed over the measurement window.

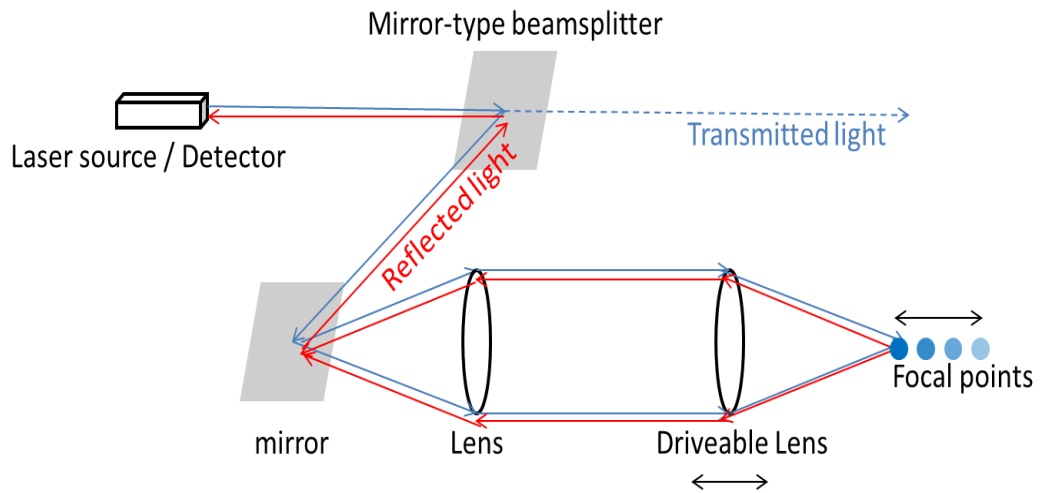


Figure 3.10: Schematic depicting the light paths in the CTS-2. Light from the laser source first comes into contact with a mirror-type beamsplitter, reflected onto a dichroic mirror, through lenses and into the sample. The light from here then passes through two lenses which focus the light. The second lens moves during the scanning, which shifts the focal point. Any reflection off the sample follows the same route to back to the source/detector as the source light but in opposite directions. Blue line: source light; Red line: Reflected light (Note: the red line should actually be overlaid on the blue line, but was drawn otherwise for clarity).

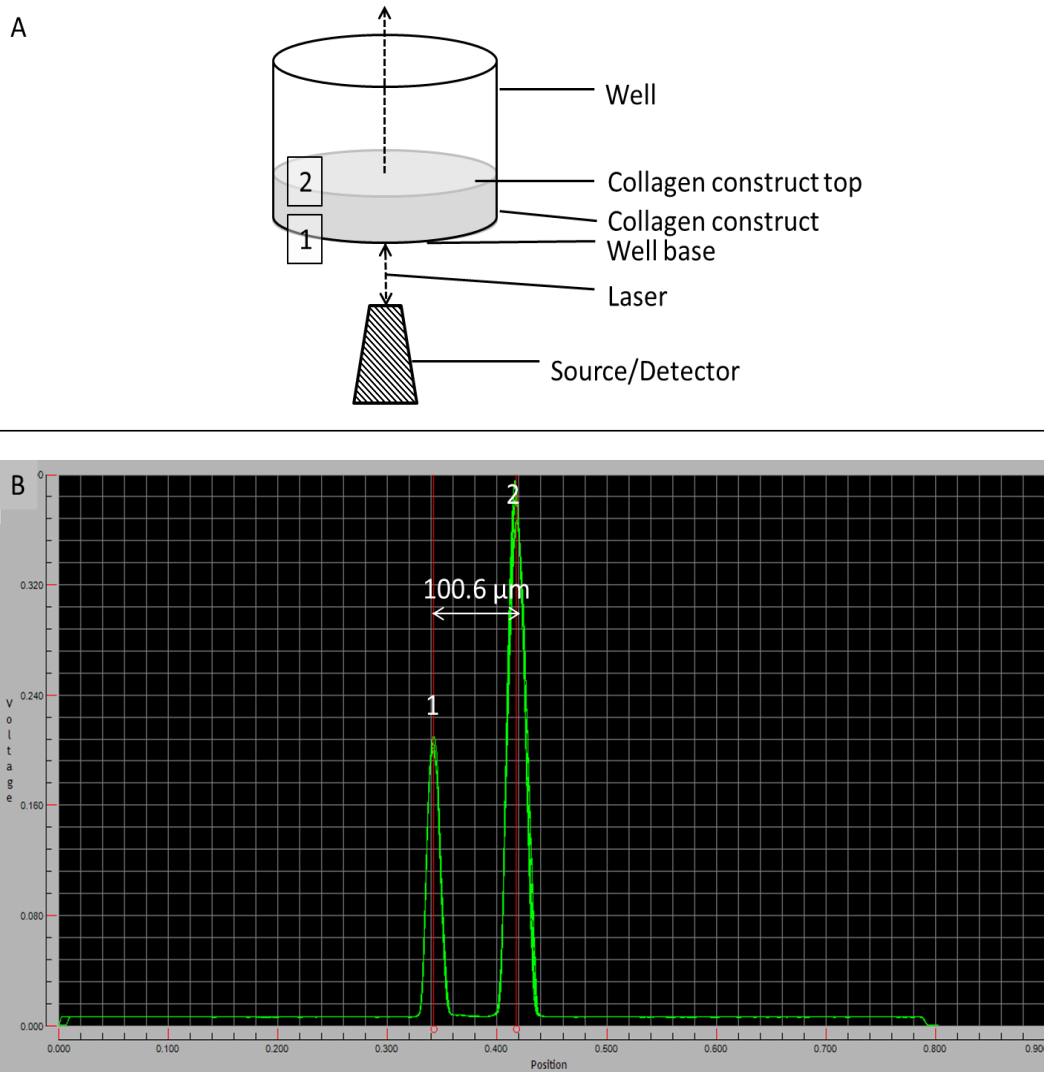


Figure 3.11: (A): Schematic demonstrating how the CTS-2 works. Laser from the source is emitted upward through the well and sample, with any downward refracted light being captured by the detector. **1** is the first point of reflection (change in refractive index) that the system detects, which corresponds to the plastic-collagen interface of the top of the well base and the bottom of the collagen construct. **2** is the second reflection point, corresponding to the interface of the top of the construct and air. (B): Example CTS-2 measurement of a compressed collagen construct using Lein’s pControl software. The two peaks correspond to regions **1** and **2** from (A). Thus **1** and **2** mark out the highest and lowest points of a construct to give a measurement of thickness, in this case, 100.6 μm .

3.3.1. Interpretation of scans (in collaboration with Dr D Daly, Lein Applied Diagnostics, UK)

During a scan of a sample, laser is projected through the base of the plastic multi-well plate, which has a certain thickness (954.9 μm in this case), through the plate, into the sample and then out of the sample (Figures 3.12 and 3.13A). The laser typically passes through three interfaces during a scan of a sample – (1) the air-plastic interface at the base of the plate, (2) the plastic-sample interface at the base of the well and (3) the sample-air interface at the top of the sample Figure 3.12. The materials through which the laser passes have different refractive indices. The plastic of the multi-well plate, collagen construct and air have refractive indices of 1.5649, 1.335 and 1.0003 respectively. At these interfaces, there are changes in refractive indices which create points of internal reflection. As the laser progresses through a scan, light is reflected off these interfaces, downwards and into the detector in the CTS-2 and picked up as peaks in a graph. Since the maximum limit of the machine is about 1 mm, not all these interface peaks can be displayed on one graph.

Once the bases of the plate and well have been found, the emitter/detector is adjusted to shift the graph to the left for the detection of any additional interface. In Figure 3.13B, the well was empty, so only the plastic-air interface was detected. As can be seen, this large peak actually has three much smaller peaks to the left of it. This shape of 3 small + 1 large peaks is characteristic of scans from the CTS-2. The shapes have been slightly distorted in Figure 3.13A due to the machine being close to its measuring capability.

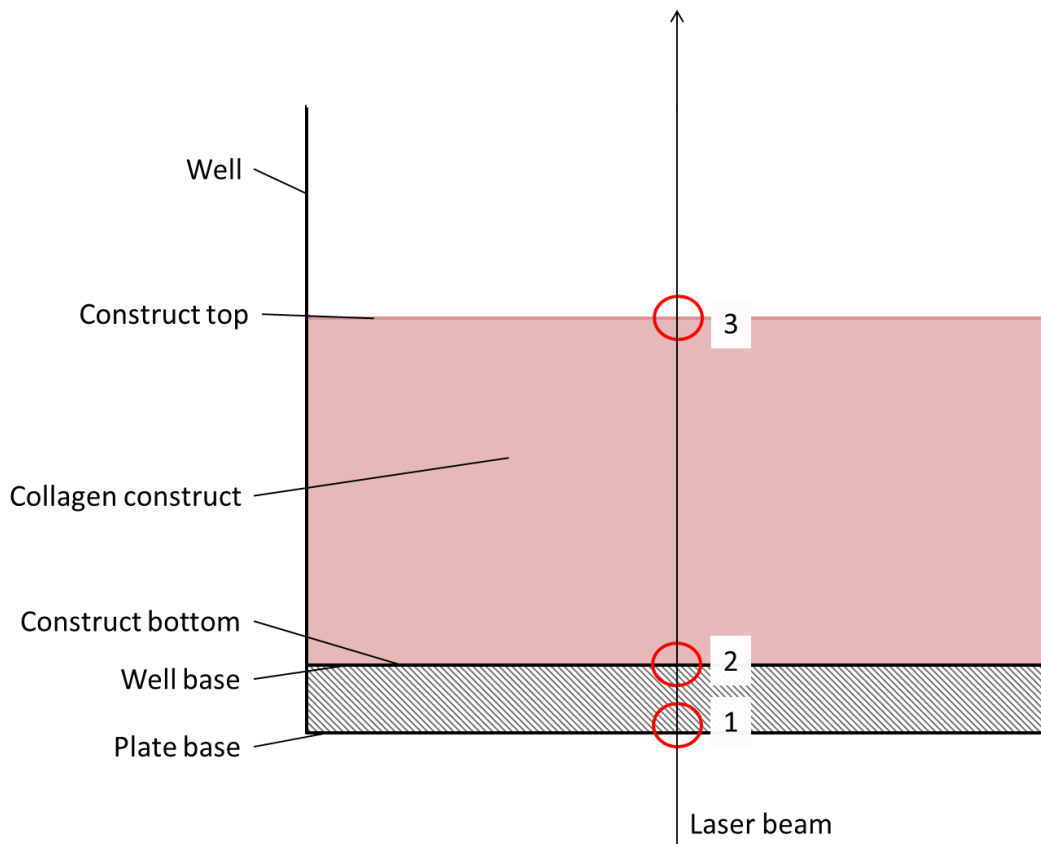


Figure 3.12: Diagram depicting the laser path during a scan of a construct. Laser from the source is emitted through the plastic of the multi-well plate, into and then out of the collagen construct. In doing so, the laser beam passes through three interfaces (red circles; 1 – 3). The first interface the laser encounters is the air/plastic interface (1) at the bottom of the plate. Light then travels through the plastic and crosses the plastic-collagen interface (2) as the laser travels out of the plastic and into the collagen. The third interface is the collagen-air interface (3) as the laser exits the collagen gel. The laser beam has been simplified as a single vertical arrow.

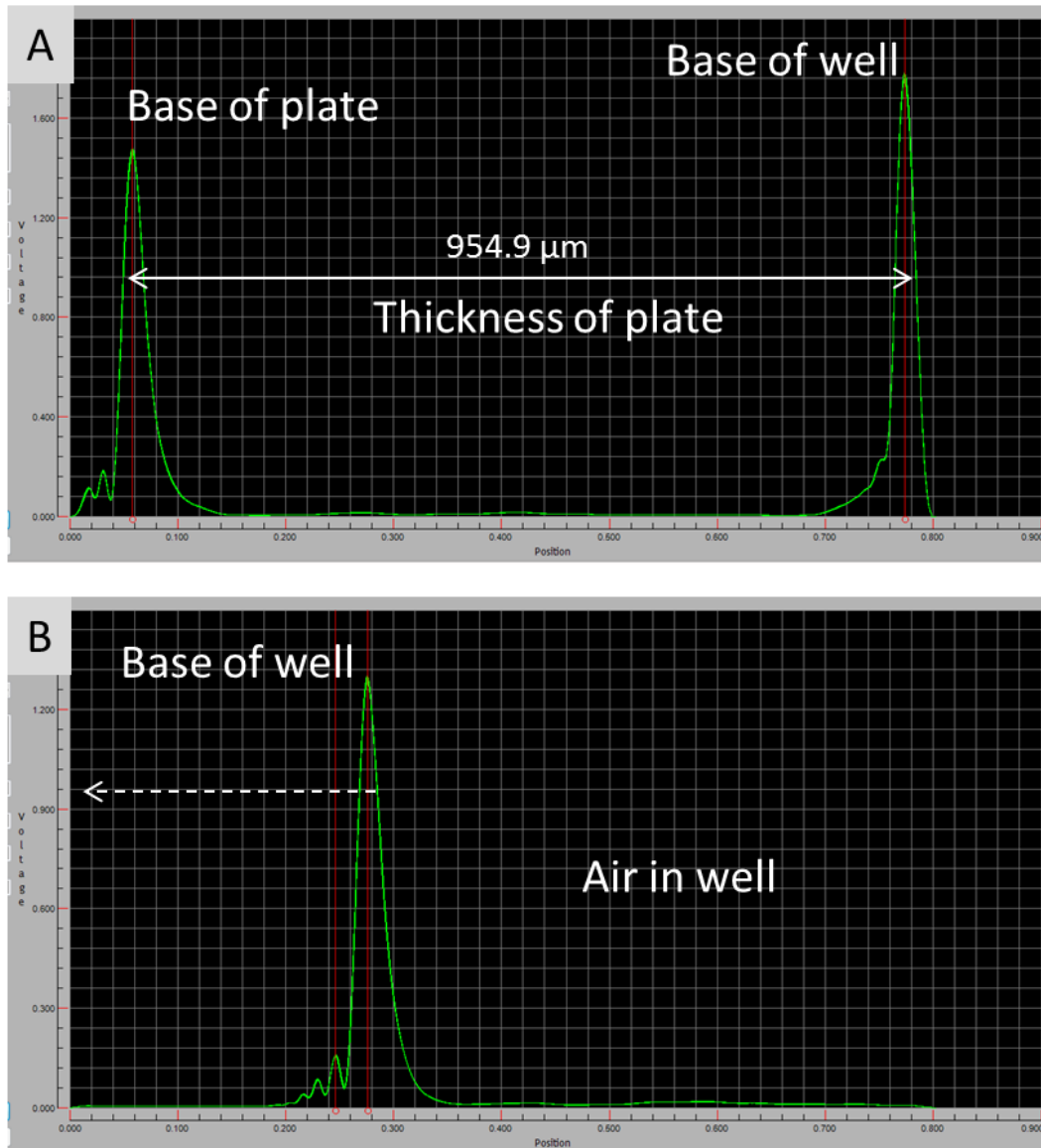


Figure 3.13: Screenshots of the software graphical user interface (GUI). (A) Initial adjustments to the position of the emitter/detector had to be made prior to sample scanning. The base of the well had to be found which corresponds to the bottom of a construct. This peak had to be distinguished from the base of the plate. (B) Once the two peaks had been identified, the emitter/detector was raised so that any interface above the base of the well could be detected. In this case, the well was empty, so there were no further changes in refractive index in the laser beam path.

A scan of a sample produced two large peaks which corresponded to the well-base-construct-bottom interface and the construct-top-air interface, with the distance between the two peaks equating to the thickness of the construct. Measurements were found to be more consistent when constructs were not submerged in liquid. The device has a high sensitivity and detects tiny movements of fluid which affects the measurements. So before readings were taken, fluid was removed from the wells to obtain more consistent measurements.

0.5, 1.0, 1.5 and 2.0 ml collagen gels were cast in 24-well plates and compressed. Immediately after compression, PBS was added to all the constructs to prevent them from drying out. Just prior to measuring the thicknesses of constructs, the PBS was removed. One benefit of the CTS-2 is that measurements can be made *in situ*, so the constructs would not need to be interfered with, minimising the risk of sample damage or incorrect placement of samples. The multi-well plates were simply placed on top of the device with the construct to be examined positioned over the device window. As the beam width is small (4 μm), at least three different points around a construct were taken, with 30 scans per point, for a better representation of construct thickness.

For comparison, 0.5, 1.0, 1.5 and 2.0 ml constructs were compressed and prepared for histology. Cross-sections of these constructs were stained using Sirius red and photographed to determine their thicknesses using ImageJ. A graticule was used as a scale to size the constructs.

The results from both techniques were then compiled and plotted as a histogram (Figure 3.14A). What is apparent is that the real-time measurements (using the CTS-2) were consistently larger than those made using histology and image analysis. 0.5, 1.0, 1.5 and 2.0 ml constructs measured using the CTS-2 measured 43.0 ± 2.27 , 87.7 ± 7.35 , 124.5 ± 15.2 and 160.3 ± 28.6 μm respectively. The histologically processed constructs measured 27.7 ± 8.9 , 52.7 ± 13.2 , 99.6 ± 19.4 and 139.3 ± 14.0 μm respectively using digital image analysis. The average difference between histological and optical confocal measurements was 24.1 ± 8.28 μm (Figure 3.14B), showing a fairly constant underestimation of construct thickness by histology across all the collagen constructs and represents a greater percentage error for thinner constructs. This difference shows a clear under-representation of construct thickness when the collagen constructs undergo histological processing.

In some scans however, multiple peaks were detected in between the two main peaks (Figure 3.14A). Reflections off accumulations of collagen in the construct were likely to have caused these smaller peaks. Plastic compression generates collagen lamellae to form within the constructs, with a decreasing gradient of density from the top to the bottom. The three small peaks in Figure 3.14A are close to the FLS at the top of the construct, and decrease in height from top to bottom. This may possibly reflect the collagen lamellae layout within the construct, though this cannot be verified as it could just be the artefact triplets ahead of the main peak as mentioned above.

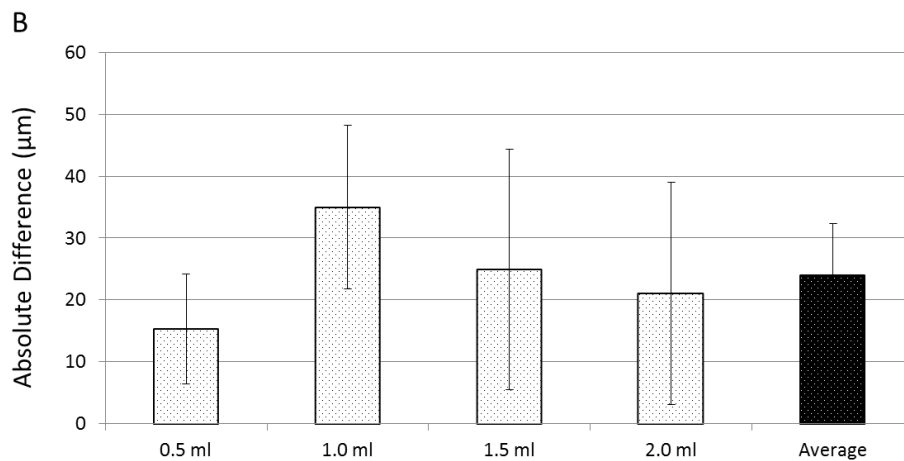
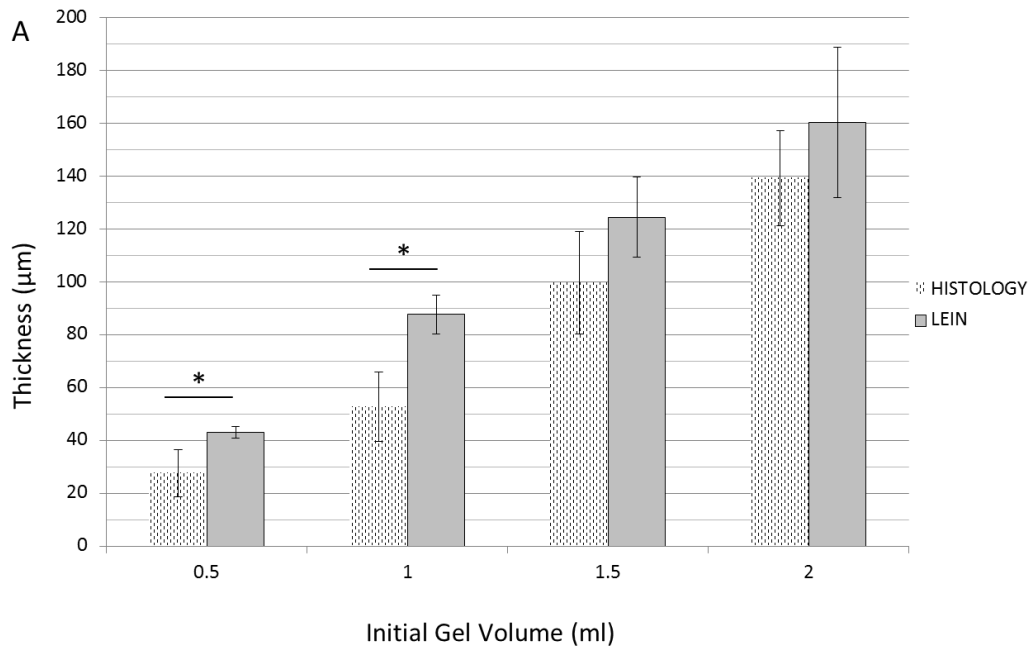


Figure 3.14: Thickness measurement comparison showing that the histology method constantly underestimates the thicknesses of constructs. (A) Thickness measurements of collagen constructs using the Lein CTS-2 and histology. (B) The absolute differences between the two measurement techniques. These show that measurements made using image analysis of histology images were constantly smaller than real-time measurements using optical confocal scanning by $24.1 \pm 8.3 \mu\text{m}$ on average. Error bars depict the standard deviations of the mean ($p < 0.05$; $n = 9$).

3.3.2. Detection of variables within compressed constructs

Multi-layering collagen constructs allows the complexities of the tissue mimics to be increased, and tailored for specific purposes. For example, different cell types may be seeded into different layers of collagen to mimic native tissue organisation. There are three possible modes to create multi-layered constructs: (1) The quickest way to create layered constructs is to separately compress several gels and then to stack them up once compression is completed. This method is the fastest way as there is no extra waiting time for the gelation of additional gels. However, there is also no integration between the separate layers [320,330,337]. (2) The second method is to sequentially compress layers of collagen, whereby each new layer is compressed on top of the previously compressed layer. This method provides some useful integration between the layers. (3) The method which gives the best inter-layer integration is when multiple collagen gels are stacked prior to compression and then simultaneously compressed together at one go. Due to the fluid movement during the process, collagen fibrils are dragged across inter-layer interfaces, providing a physical link between the layers, i.e. they become mechanically integrated [320].

Simultaneously-compressed double-layered constructs were scanned using the Lein CTS-2 meter to test if the inter-layer interface could be detected by optical means. However, none of these interfaces were detectable, only the peaks corresponding to the bottoms and tops of the constructs were detectable. This was most likely due to the refractive indices being too similar (Figure 3.15A). To determine if structures within compressed constructs could be detected by the CTS-2, a triple-layered

construct was devised. This multi-layered construct consisted of a 0.5 ml layer loaded with hydroxyapatite particles, sandwiched by two 1.0 ml 'empty' layers. The hypothesis was that this would create a thin layer of hydroxyapatite within the construct which would reflect light back to the detector. A scan of this triple-layer construct is shown in Figure 3.15B. Marked out by the yellow circle is a small peak roughly in the middle of the two main peaks. This middle peak could have been caused by reflection off the hydroxyapatite layer. However, not all of the scans showed a peak in the middle. The hydroxyapatite particles may not have been uniformly distributed through the layer or the concentration of particles was too small such that there were areas where no particles were present to give backscatter. Nonetheless, there is some promise from this preliminary study on the ability to detect internal structures/content within compressed constructs.

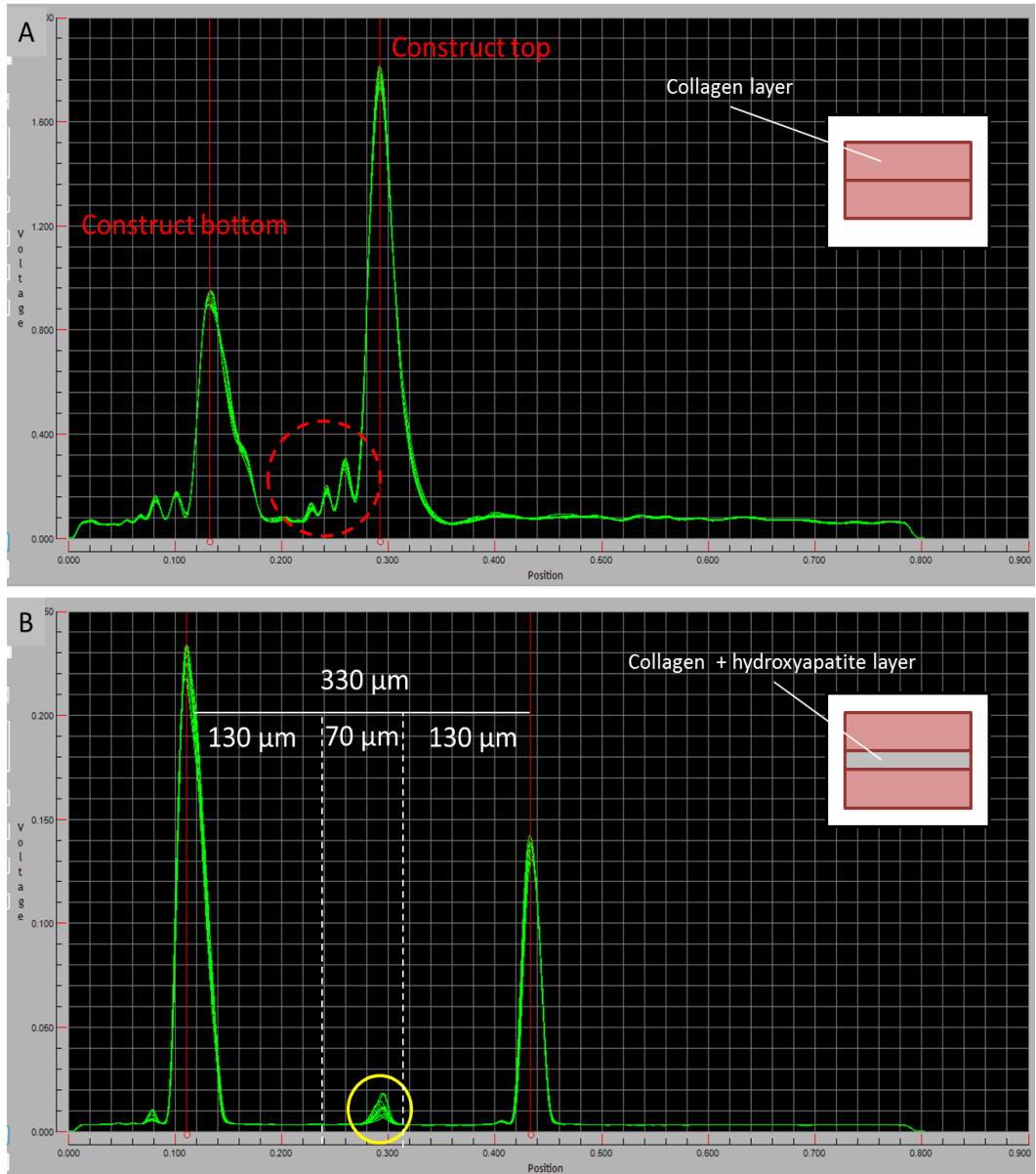


Figure 3.15: (A) A screenshot of a scan of a 1.5 ml (initial volume) compressed collagen construct. The two main peaks demarcate the top and bottom of the construct, and in this case, there are 3 small peaks within the construct (red dotted circle). These could be structures in the construct reflecting light, or may just be part of the characteristic peak shape. (B) A scan of a triple-layered compressed collagen construct. A 0.5 ml layer containing hydroxyapatite particles was sandwiched in between two 1.0 ml layers. The small peak marked by the yellow circle possibly indicates the detection of this middle layer.

3.4. Primary and secondary FLS generation

The process of compressing collagen gels causes a unidirectional flow of fluid towards and out of the top surface (FLS). This upward fluid motion combined with the downward applied force causes lamellae formation in the x-y plane with an anisotropic distribution, having the greatest accumulation of collagen fibrils at the FLS giving it the characteristic intense staining seen in histology. Using the collagen density analysis described above, this dense layer can clearly be seen as a region of markedly intense staining (Figure 3.16).

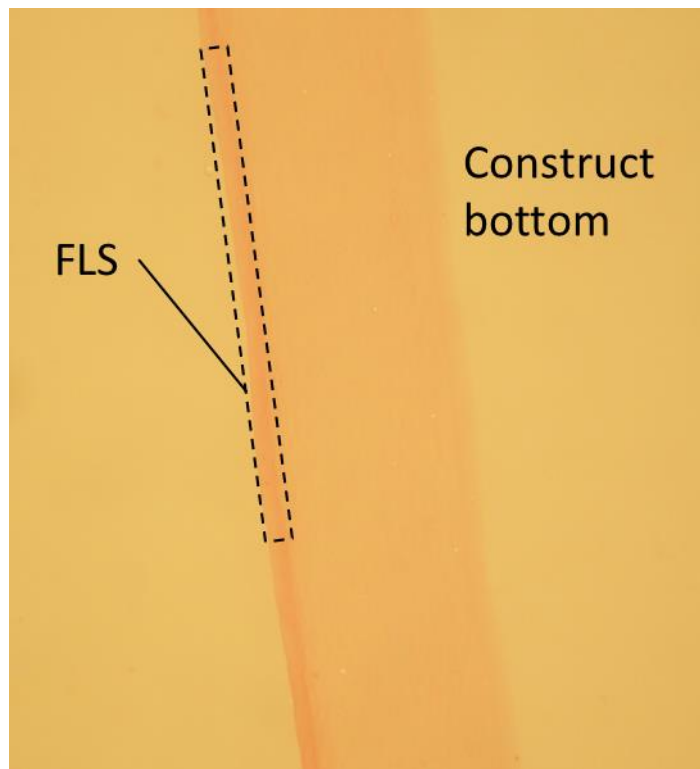


Figure 3.16: Histology image of an acellular compressed collagen construct stained with eosin only. An intense band can be seen at the top of the construct. This is the fluid leaving surface (FLS), caused by a dense accumulation of collagen fibrils during compression.

The generation of this anisotropic layout of collagen fibrils provides a mechanism for fabricating density gradients through the thickness of the construct. This serves as a means of studying cell responses (proliferation, differentiation, migration) to different levels of stiffness. Fabrication of stable micro-scale structures is possible on the FLS, but cannot be achieved on the opposite surface (non-FLS) [244]. FLS formation provides a unique mechanism for the fabrication of micro-scale architecture which renders the structures stable in culture over weeks.

Surprising observations were made when larger initial volume gels (1.5, 2.0 ml in 24-well plates) were compressed. Histology of these thicker constructs revealed the presence of a second intensely-stained band on their bottom surfaces (i.e. the non-FLS) which was not present when 0.5 and 1.0 ml gels were compressed. Since we now know that collagen accumulation occurs as a consequence of fluid movement, this second region of dense collagen indicates that at some point, fluid flow was reversed to produce another fluid leaving surface on the opposing, bottom surface. Since this is adjacent to the plastic well, we suggest that fluid escaping from the secondary FLS lifted up the construct to escape.

The generation of a secondary FLS during the compression of larger initial volume gels may be explained by Darcy's law, the Mandel-Cryer effect and viscous effects [348-351]. Darcy's law describes the ability of a fluid in flowing through a porous medium (in our case, a collagen fibril network). The equation has been adapted for the compression of collagen hydrogels [320,352]. During compression, the pressure on the gel is constant, but fibrils accumulate at the primary fluid leaving surface

(FLS), increasing the collagen density and reducing the pore sizes in the meshwork, therefore increasing the hydraulic resistivity of the FLS and the fluid outflow rate (R_{FLS} ; m^{-1}). The rate of drainage (Q ; m^3/s) of the fluid with dynamic viscosity (μ ; Pa.s) through the primary FLS (with an area A ; m^2) is correspondingly decreased. This rate, Q , is not a constant through compression as the pressure difference (ΔP ; Pa) across the FLS changes during the process.

$$Q = \frac{A \cdot \Delta P}{\mu \cdot R_{FLS}}$$

The Mandel-Cryer effect is described by the behavior of increasing pore pressures caused by a constant load before decreasing to zero. Pore pressure generation due to the application of a constant load is immediate but pressure reduction due to the discharge of the fluid is hindered by the permeability and the distance to the drainage border. The Mandel-Cryer effect does not initially apply to this system of plastic compression since a component of the load applied is absorbent, thus aiding fluid discharge from the gel. However, as compression progresses, the FLS becomes increasingly more compact which reduces the ease of fluid escape, thus increasing the hydraulic resistance of the FLS. In the case of gels with smaller initial volumes (<1.5 ml in the 24-well format), compression is completed by the time the FLS becomes dense enough to block fluid escape. But with larger gels, significant amounts of fluid remain in the gel. This causes a buildup of pressure within the gel which eventually forces fluid out of the gel through other surfaces, mainly the opposite (bottom) surface of the gel (Figure 3.17). Drainage of the fluid reduces the

pressure within the gel, allowing compression to continue. The downward escape of fluid facilitates the accumulation of collagen fibrils at the secondary fluid leaving surface resulting in the intense staining of this area which reflects the density of collagen.

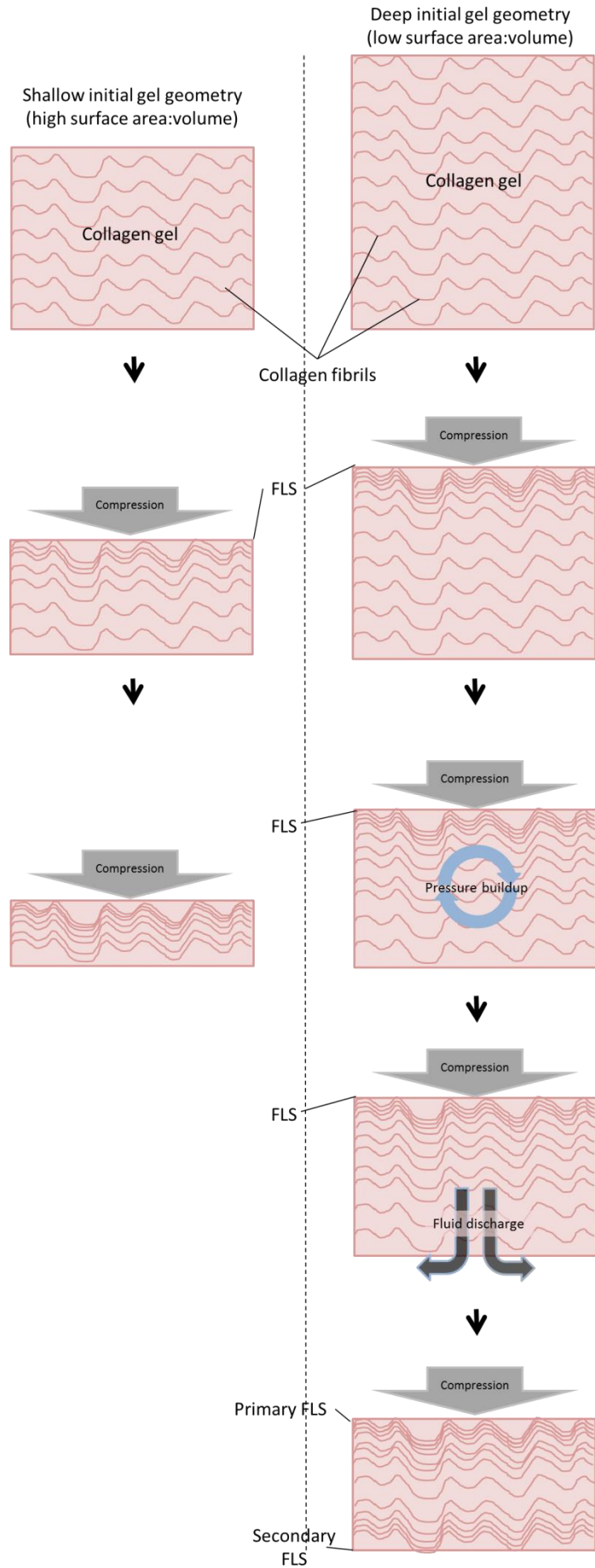


Figure 3.17: Schematic on FLS and secondary FLS formation and collagen accumulation during the compression of thinner gels (0.5, 1.0 ml; left column) and thicker gels (1.5, 2.0 ml; right column). In the initial stage of compression, fluid flows out of the gel through the top surface, or the FLS. At the same time, the gel is pushed downwards, causing the fibrils at the FLS to compact. The FLS begins to hinder fluid escape and slows down the compression. At this point, the thinner gels are close to complete compression if not already fully compressed. For the thicker gels however, significant amounts of fluid still remain in the gel. The constant pressure and the lack of drainage causes a pressure buildup in the gel which eventually forces the fluid out through the bottom surface, thus creating a secondary FLS. This suggests that there is a critical FLS surface area to volume ratio, corresponding to the tendency for any given collagen gel and composition to block.

The network of collagen fibrils at the FLS becomes very tightly packed during compression which begins to block outward movement of molecules and larger particles. This is evident when 500 nm hyaluronan nanoparticles (HA-NP) were incorporated in the collagen gels (Chapter 6). These particles were loaded with fluorescein isothiocyanate (FITC) which allowed the visualisation of particle distribution using fluorescence microscopy. The hypothesis was that due to their small size, the HA-NP would be carried by the moving fluid during compression and leave the gel until the FLS becomes dense enough to block their escape. At which point, the HA-NP would begin to accumulate at the FLS, resulting in a distribution similar to the collagen fibrils within the construct.

0.1 mg/ml HA-NP was loaded into 0.5, 1.0, 1.5 and 2.0 ml collagen gels and evenly distributed prior to gelation. The nanoparticle-loaded solutions were allowed to set at 37°C for 30 min. Plungers were then placed on top of the set gels to initiate plastic compression, after which the constructs were fixed with formalin, processed for histology and embedded in paraffin for sectioning. 8 µm sections were taken and placed onto microscope slides and left at 59°C overnight to dry. The dried samples were then imaged using an Olympus BX61 microscope.

Fluorescence microscopy revealed that the hypothesis was correct (Figure 3.18). A bright band of fluorescence can be clearly seen at the FLS of all constructs (0.5, 1.0, 1.5 and 2.0 ml). A key difference between the thinner 0.5 and 1.0 ml constructs and the thicker 1.5 and 2.0 ml constructs was the presence of a second bright fluorescent band at the bottom surface. 0.5 and 1.0 ml constructs display a decreasing fluorescence gradient towards the bottom surface. 1.5 and 2.0 ml constructs on the other hand, appear to have a more uniform distribution of fluorescence through the constructs, with the addition of a second intense fluorescent band at the bottom surfaces.

This distribution of HA-NP is remarkably similar to the distribution of collagen (Figure 3.19) and possibly provides further evidence of a secondary fluid leaving surface. It appears that the HA-NP did indeed move with the flowing fluid upwards towards the absorbent plunger resulting in a low to high density of particles from the bottom to the top of the construct. The tightly-packed collagen mesh at the FLS would have trapped the upward flowing HA-NP to create a collagen-HA-NP cake

layer, blocking further discharge of fluid and particles. With the smaller gels, this probably occurred towards the end of compression before a reversal of flow (to any FLS) could occur. But with the deeper gels, this likely occurred midway through compression. With excess fluid still remaining in the collagen along with the pressure bearing down on the gel, pressure builds up within, as discussed above. The pressure then forces the nanoparticle-carrying fluid out of the compressing gel via the bottom surface. The collagen mesh builds up at the secondary FLS and begins trapping HA-NP in the same way the primary FLS trapped particles, eventually creating a construct with two regions of dense collagen and high HA-NP concentrations.

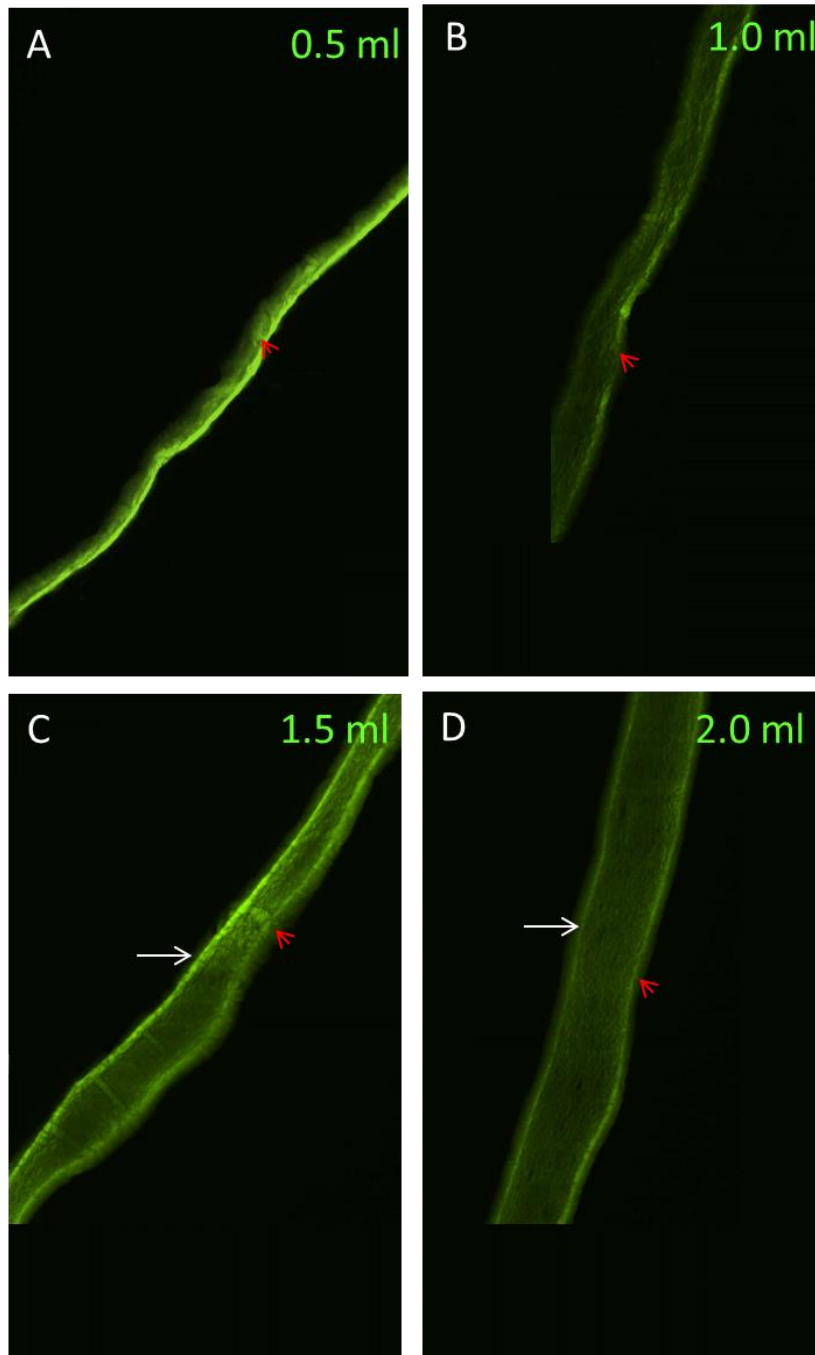


Figure 3.18: Fluorescence micrographs of cross-sections of 0.5, 1.0, 1.5 and 2.0 ml (initial volume) compressed collagen constructs (the samples had not been stained). The fluorescence came from the FITC present in the HA-NP retained in the constructs. The red arrowheads mark the primary FLS, which appears as a bright fluorescent band. White arrows mark the presence of a secondary FLS which is only seen in the 1.5 and 2.0 ml constructs (C, D), also appearing as a bright fluorescent band.

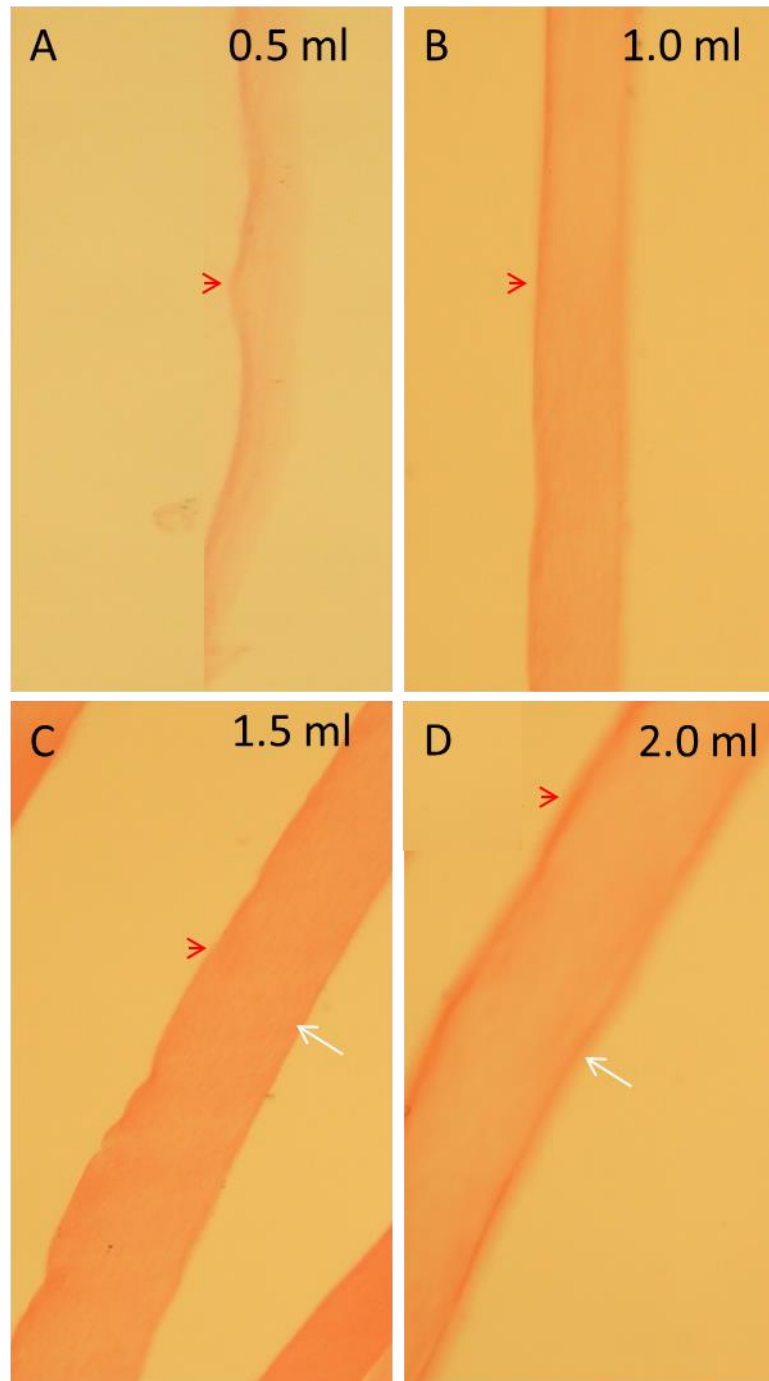


Figure 3.19: Light micrographs of cross-sections of 0.5, 1.0, 1.5 and 2.0 ml (initial volume) compressed collagen constructs stained with Sirius red, showing the distribution of collagen within the constructs. The red arrowheads mark the primary FLS, which appears as a dark shade of red. White arrows mark the presence of a secondary FLS (deep red colouration) which is only seen in the 1.5 and 2.0 ml constructs (C, D).

Using the above collagen density detection method, HA-NP distribution could be analysed. Fluorescence micrographs of nanoparticle-loaded compressed constructs were first converted to greyscale. Line selections and measurements were then made (Figure 3.20A - D), and the resulting pixel intensity profiles plotted (Figure 3.20E - H). Figure 3.20E shows the plot profile of the 0.5 ml construct. There is an increasing gradient of pixel intensities moving from the bottom of the construct to the top, where there is a sharp peak with a maximum of 133.9 a.u.. In Figure 3.20A, the FLS appears almost like another layer of collagen. The pixel scan appears to have picked this up, perhaps indicating the high degree of collagen density and compaction in this region. In Figure 3.20E, there is a step in the slope of the graph, which corresponds to the start of the FLS region in terms of position. This shows that a large proportion of retained nanoparticles was trapped within the dense collagen mesh at the FLS. Figure 3.20F shows the plotted graph for the 1.0 ml construct. Here the slope is gentler through 2/3 of the construct and then the pixel intensities spike up to 99.1 a.u., more than twice that of pixels below the FLS. Again, the start of this large peak appears to correspond to the beginning of the FLS region in Figure 3.20B. The analysis for the 1.5 ml construct shows a very different graphical shape to the previous two (Figure 3.20G). A large peak with a maximum of 75.4 a.u. exists at the bottom of the construct which then drops sharply to about half the intensity before very gradually decreasing towards the upper 1/4 of the construct, where the pixel intensities rise abruptly to 68.8. The first and second peaks here highlight the presence of the secondary and primary FLS's respectively. The 2.0 ml construct shows a similar HA-NP distribution to the 1.5 ml constructs (Figure 3.20H). Two peaks at the bottom and top of the construct are shown, with

maximum values of 54.6 a.u. and 67.7 a.u. respectively. There was a gradual decrease in pixel intensities following the peak at the bottom of the construct. Around halfway through the construct, pixel intensities began to rise gently until the FLS region where the increase was dramatic.

These scans confirm the presence of intense bands of fluorescence at the top of all the constructs, and also at the bottom of the 1.5 and 2.0 ml constructs (Figure 3.20G & H), providing a semi-quantitative analysis of the HA-NP distribution to add to the qualitative micrographs.

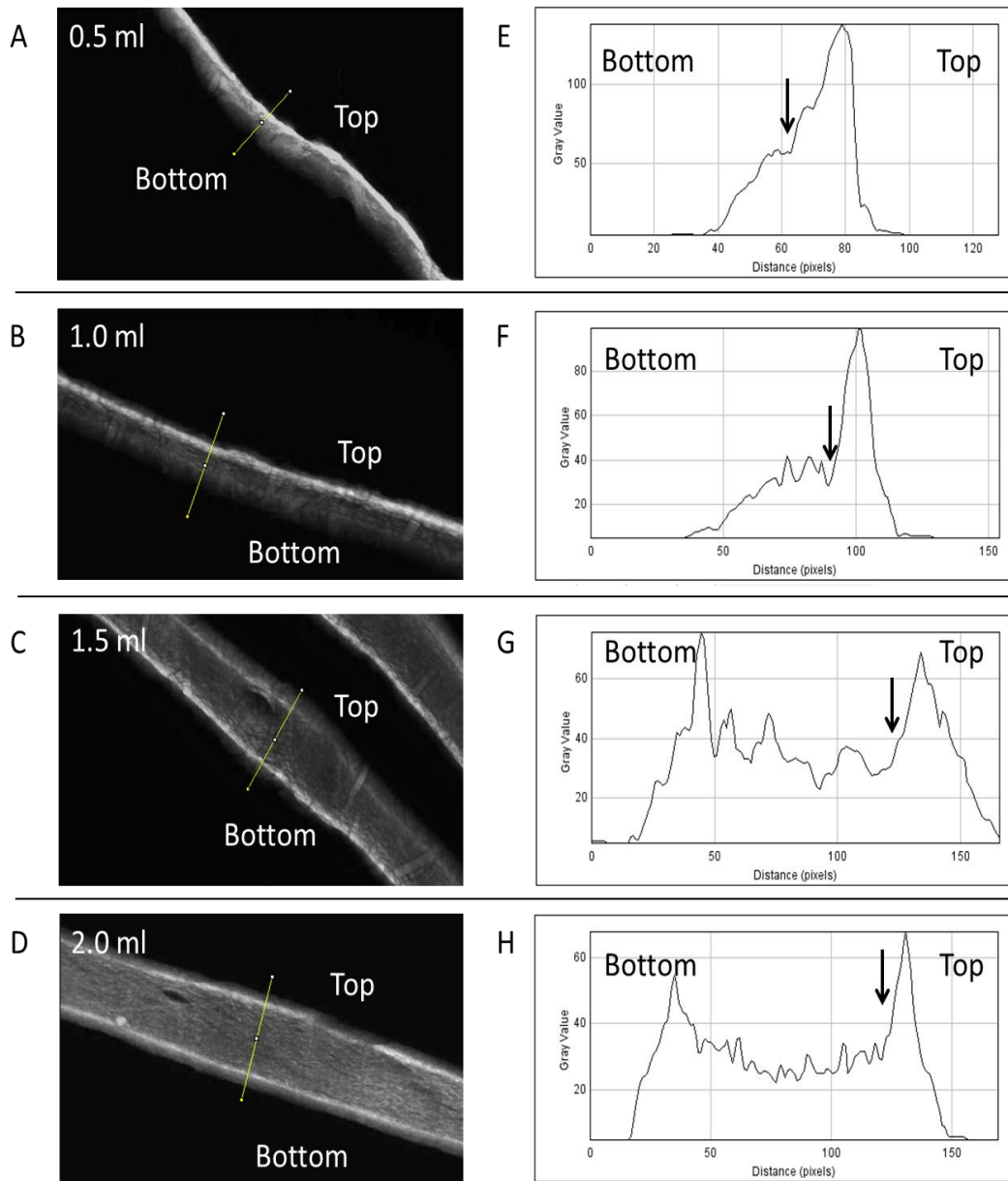


Figure 3.20: Analysis of fluorescent HA-NP distribution within compressed collagen constructs. A – D: Fluorescence micrographs of 0.5, 1.0, 1.5 and 2.0 ml constructs converted to greyscale for the analysis. The yellow line is the region within which pixel intensities were measured. E – H: Graphical representations of the intensity profiles of pixels within the yellow line. Black arrows point to the nominal start of the primary FLS region.

Analyses of light micrographs of Sirius red-stained constructs revealed similar distributions of collagen to HA-NP (Figure 3.21). The resulting scans of the Sirius red-stained 0.5, 1.0, 1.5 and 2.0 ml constructs were very similar in shape to those in Figure 3.20E – H, with a single distinct peak in the 0.5 and 1.0 ml constructs of 185.9 and 154.8 a.u. respectively (Figure 3.21E & F), and two peaks at either end of the 1.5 (top: 84.0 a.u.; bottom: 83.3 a.u.) and 2.0 ml (top: 142.5 a.u.; bottom: 142.9 a.u.) constructs (Figure 3.21G & H). Figure 3.21E and F show a general decline in pixel intensities towards baseline values following the large peak corresponding to the FLS. Like in Figure 3.20G & H, the graphical representations of pixel intensities in Figure 3.21G & H show regions of rather constant intensity values in the middle sections of the constructs in between the two peaks.

These collagen distributions show that collagen movement and nanoparticle movement during compression are correlated and are both affected by fluid flow as indicated by the presence of secondary FLS's in the thicker (1.5 and 2.0 ml) constructs.

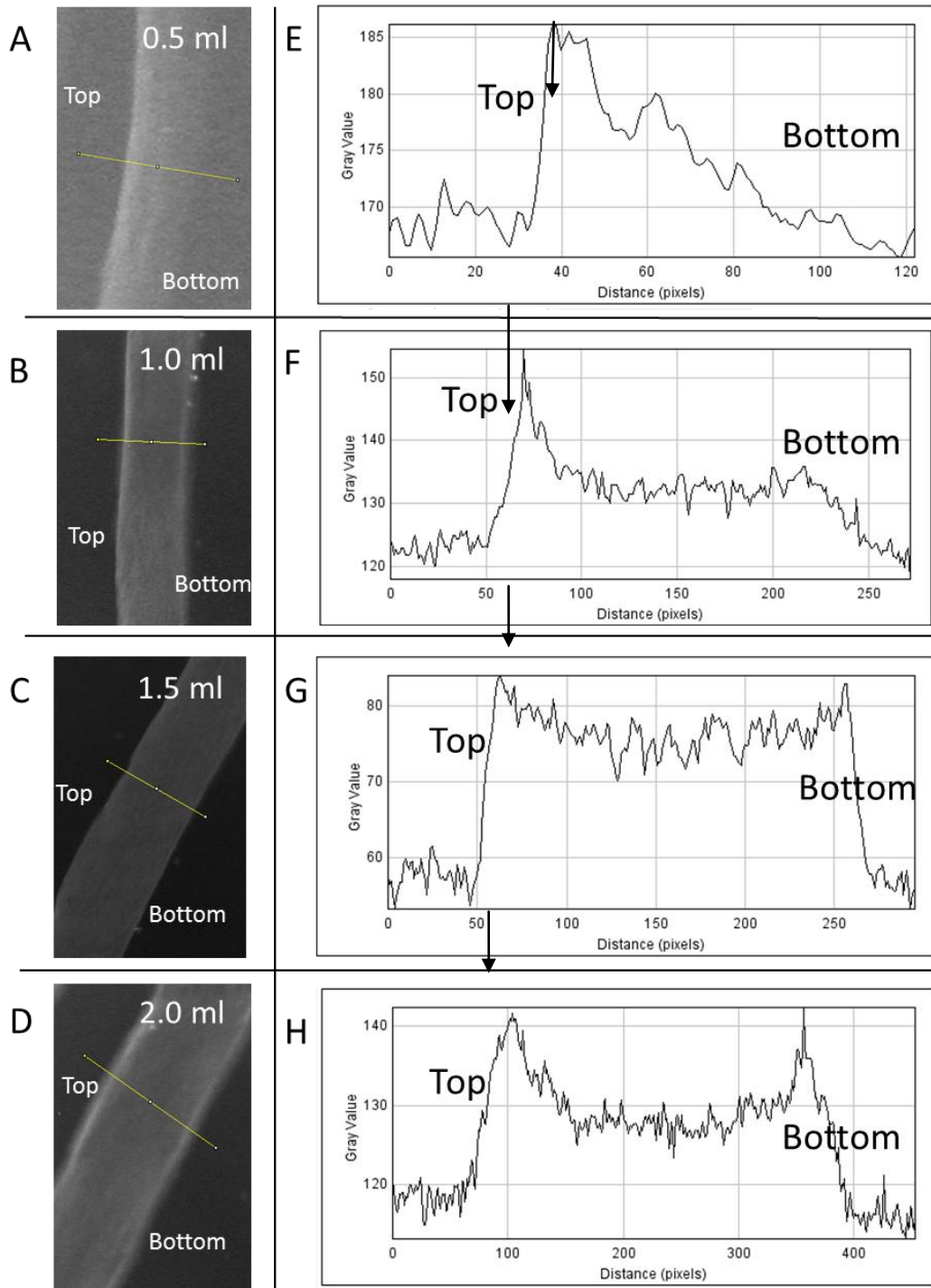


Figure 3.21: Analysis of Sirius red (collagen) distribution within compressed collagen constructs. A – D: Light micrographs of 0.5, 1.0, 1.5 and 2.0 ml constructs converted to greyscale for the analysis. The yellow line is the region within which pixel intensities were measured. E – H: Graphical representations of the intensity profiles of pixels within the yellow line. Black arrows point to the nominal start of the primary FLS region.

3.5. Discussion

Here we described the setting up of the scaled-up system with smaller plungers but keeping the compression pressure the same when using the paper plunger system. An alternative plunger system was investigated which subjects much less pressure on the gels, and thus requiring greater compression times to produce similar constructs to that prepared using the paper plunger system. With a smaller well system, the greater the possibility of interference from the meniscus of the collagen with compression. The initial contact area with the plunger would thus be different to that in 12-well plates (with less pronounced meniscus). There may be slight non-homogeneities across the FLS of the construct due to initial fluid loss through the outer edges of the gel upon contact with the plunger. Furthermore, like the wedge-shaped gel used to create a horizontal gradient described above, there would be more collagen along the edge of the gel due to the raised meniscus. However, this is likely to be minimal and insignificant as the amount of collagen within the area of raised collagen would be tiny, and the weight of the plunger would push down on it and flatten the meniscus almost instantaneously.

A novel collagen density analysis method was validated, showing that local collagen density differences can be detected by staining collagen with Sirius red and using image analysis. Using this analysis method, primary and secondary FLS's were detected in thicker constructs but not in thinner constructs, as evidenced by accumulations of collagen as well as hyaluronan nanoparticles. This, along with the calculations of the hydraulic resistance of the FLS, point towards a period during compression of thicker gels when the primary FLS becomes blocked, causing a build

up of pressure within the gel (Figure 3.17). Eventually, this internal pressure forces the remaining fluid out from the gel through the unblocked bottom surface, thus generating the secondary FLS.

In this chapter, the optical confocal device was also tested to gain a better understanding of how it works and its application to compressed constructs. Constructs measured in this way were consistently thicker than when measured by histology (which likely causes shrinkage due to heavy processing steps), showing that the optical confocal meter is a more accurate and quicker way to determining construct thicknesses.

Chapter 4: Characterisation of Compressed Collagen Constructs/Measurement of Compressed Collagen Scaffold Thickness

4.1. Introduction

It is important to characterise systems in order to determine how best to employ them, as well as to understand their limitations. In this chapter, we explore the effects of plastic compression on collagen hydrogels and the changes that it brings.

Hydrogels (hydrophilic gels) are hydrophilic networks of cross-linked polymer which are able to retain hundreds or thousands of times their dry weight in water. Water binds to the hydrophilic groups of the polymers as well as interacting with their hydrophobic groups resulting in 'primary' and 'secondary bound water'. In addition to this 'total bound water', there is also 'free water' within hydrogels which fill the spaces between polymer chains and pores [353,354]. All this gives hydrogels a very high water content and low polymer density.

Plastic compression exploits the fact that collagen hydrogels contain 99.5% water which is a result of the casting rather than an inherent property of the polymer chemistry. A collagen hydrogel, if left to stand under its own weight in air, will lose some of this internal liquid as it compresses under its own weight. Part of the advantage of the ~100-fold rapid shrinkage is that initial fabrication is at the gross (mm) scale but produces components with cell-scale (μm) structure. Importantly,

Chapter 4: Characterisation of Compressed Collagen Constructs/Measurement of Compressed Collagen Scaffold Thickness

plastic compression hinges on the fact that this discharged fluid does not re-enter the hydrogel [299]. Thus, by the expulsion of the excess fluid from the hydrogel, the density of the matrix can be increased to achieve tissue-like levels.

The simultaneous expulsion of water and compaction of the collagen fibrillar network result in a drastic decrease in the thickness of the scaffold, from several millimeters to tens of micrometers (Figure 4.1). This creates a very thin and dense construct with improved mechanical properties as compared to a collagen hydrogel, and also generates an anisotropic layered structure [278,299,355,356]. This method can be manipulated to speed up or slow down compression to control the final construct density, which makes this method particularly useful for producing different construct types to mimic different tissues.

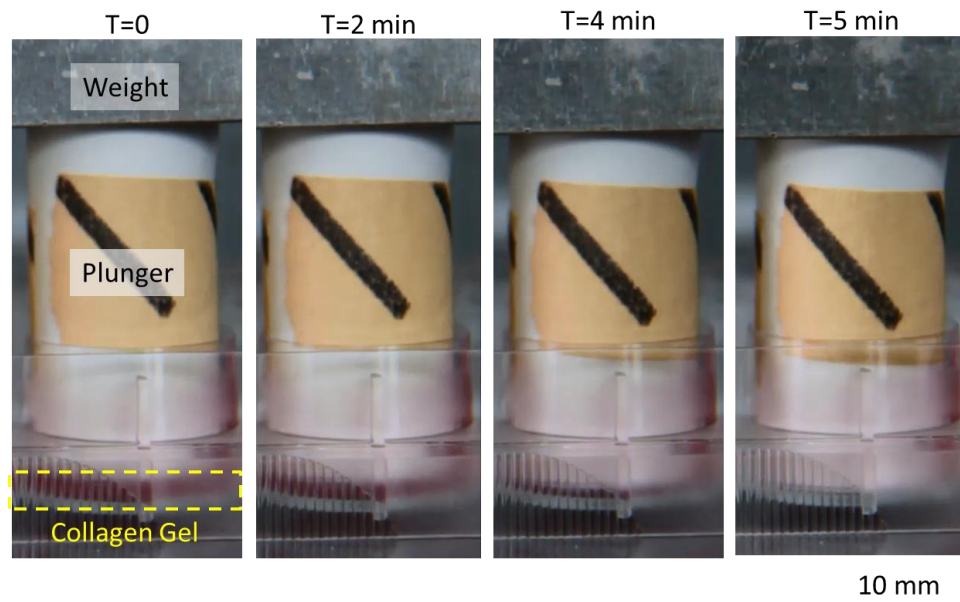


Figure 4.1: Time-lapse photographs of a collagen gel under-going plastic compression. The yellow dotted box demarcates the collagen gel. Within minutes of initiating compression, a gel several millimetres thick is reduced to just a thin sheet in the tens of micrometers.

4.2. Scaling down (in construct size)

Plastic compression is a simple and rapid process for making dense tissue constructs in any shape or size, depending on the dimensions of the collagen gel cast and the compressing plate surface. A range of rectangular moulds have been used to collagen gel formation: 33 mm x 13 mm x 4 mm [299,357], 40 mm x 30 mm x 10 mm [55,330], 40 mm x 25 mm x 11 mm [246], 22 mm x 33 mm x 10 mm [329,331] and 30 mm x 20 mm x 7 mm [244]. 20 mm and 22 mm diameter discs [304,319] have also been produced. There is more room for scaling down the compression of collagen gels with the circular type of constructs through the use of multi-well plates. Here we scale down the system to using 24-well plates which allows the fabrication of a larger number of smaller (16 mm diameter) gels simultaneously (Figure 4.2). Characterisation of the system was done by determining the rates of compression, the amount of fluid absorbed from the gels, the hydraulic resistance of the gels during compression, total volume of fluid lost due to compression, thicknesses of constructs and the re-swelling of constructs over time.

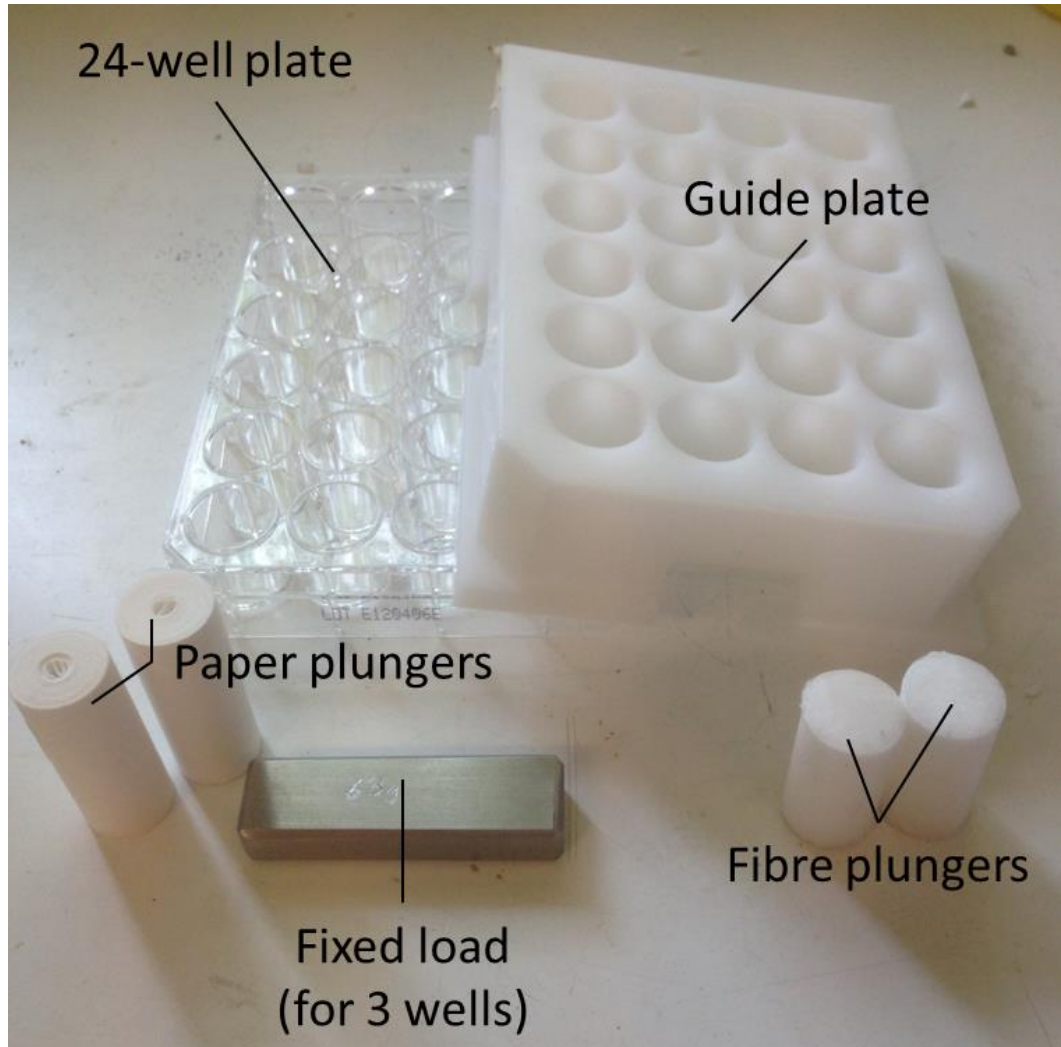


Figure 4.2: Photograph of the components used for plastic compression. Paper and fibre plunger types were used for compression in a 24-well format. A guide plate was used to keep the plungers upright.

4.3. Thickness measurements

Histology has been the primary method for determining the thicknesses of these scaffolds. However, this is only able to give end-point results. Furthermore, the heavy processing steps involved in histology to obtain a stained section ready for imaging likely alters the thicknesses of these constructs, thus giving inaccurate information. Scanning electron microscopy (SEM) can also be used to find out the thickness of a sample, but it involves radical dehydration of the sample resulting in smaller/thinner samples when imaged. A method for determining tissue thickness in real time without the need for processing and desiccation is necessary in order to make accurate measurements and to be able to study the process of plastic compression [338-340].

As described in Chapter 3, the CTS-2 (Lein Applied Diagnostics, UK) is an optical device that allows quick *in situ* measurements of construct thickness non-invasively. As individual compressed collagen scaffolds are very thin, physical handling may damage the scaffold architecture or they may be improperly placed on the instrument, giving inaccuracies in measurements. This system negates the need for sample transfer and scaffolds can be measured directly in their wells. The ability to make measurements *in situ* is a great asset as subsequent readings may be taken over long periods of time – unlike histology which is an end-point process.

4.4. Materials & Methods

Preparation and compression of collagen constructs were carried out as per Chapter 2.

4.4.1. Preparation of plastically compressed collagen

Four initial gel volumes were used – 0.5, 1.0, 1.5 and 2.0 ml, which contained 0.8, 1.6, 2.4 and 3.2 mg of collagen respectively. Two compression systems were compared here: (1) paper plungers and a fixed load and (2) fibre plungers (Figure 4.2).

4.4.2. Determination of the rate of fluid removal during plastic compression

0.5, 1.0, 1.5 and 2.0 ml collagen gels were set in 24-well plates and subjected to plastic compression using paper plungers or fibre plungers. The absorbent plungers were weighed before use, at intervals of 30 s in the first 5 min of compression, and then at 1 min intervals thereafter.

4.4.3. Measurement of total fluid lost due to plastic compression

Immediately after compression, 0.5, 1.0, 1.5 and 2.0 ml (initial volume) constructs were weighed. These compressed wet weights were then subtracted from the weight of the corresponding uncompressed hydrogels.

4.4.4. *Lein CTS-2 measurements*

Following compression, constructs were positioned over the CTS-2 window for *in situ* measurements to be taken. A minimum of 3 different regions of each construct was measured, with 30 scans per region to obtain an average readout (pControl software settings - Gain: 1.99; Filtering: 32 x3; Refractive Index: Construct (10% Collagen) - 1.335).

4.4.5. *Comparison of cell proliferation*

The proliferation of cells cultured in 2D and 3D was investigated. The 2D surfaces used were tissue culture plastic (2D TCP), on top of uncompressed collagen gels (2D UC) and on top of compressed collagen constructs (2D PC). 3D environments used were cells within uncompressed collagen gels (3D UC) and cells within compressed collagen constructs (3D PC). 5×10^4 human dermal fibroblasts per well were used. 0.5 ml collagen was used for the uncompressed gels and compressed constructs. Fibre plungers were used for the compression.

The alamar blue assay was used to compare the proliferation of cells in different culture conditions. After every 24 hours up to a period of 1 week, culture media was removed, and wells were washed with PBS. 10% Alamar Blue (Serotec, UK) solution was prepared in phenol red-free Dulbecco's modified Eagle's medium DMEM (Sigma, UK). 1 ml of this solution was added to each well. Samples were cultured at 37°C for 4 hours. 100 µl of the alamar blue solution was taken from each

Chapter 4: Characterisation of Compressed Collagen Constructs/Measurement of Compressed Collagen Scaffold Thickness

well and transferred to a white 96-well plate (NUNC, Denmark) for absorbance measurements (Excitation/Emission wavelengths: 510/590 nm) using a microplate spectrophotometer (MR 700, Dynatech Laboratories, USA). Following measurements, samples were washed with PBS and culture media added to the wells and samples returned to the incubator for continued culture.

4.5. Results

4.5.1. Determination of rate of fluid loss using paper plungers and weights

The rate of fluid removal from gels during compression was investigated to gain insight into the dynamics of the process, as well as to compare two plunger systems. The first system comprised of spooled rolls of Whatman I filter paper into plungers (referred to as paper plungers) and a fixed load of 22 g per well. The second system involved only plungers made of up of compacted fibres, generously donated by TAP Biosystems. The absorbent plungers (paper rolls or fibre) used for the compression were weighed every 30 s for the first 5 minutes, then after every 60 s thereafter to determine the amount of fluid absorbed into the plunger (= fluid loss from the gel). Figure 4.3A shows that with paper plungers and weights, the amount of fluid absorbed for 0.5, 1.0, 1.5 and 2.0 ml gels were very similar in the first 30 s of compression, albeit slightly greater with increased gel volume – 0.303 ± 0.025 , 0.333 ± 0.045 , 0.3533 ± 0.029 and 0.35 ± 0.026 ml respectively. After this point, the rate of fluid absorption of the 0.5 ml gels decreased greatly, with only a gain of 0.09 ± 0.07 ml in the next 30 s, compared to 0.187 ± 0.021 , 0.17 ± 0.01 and 0.2 ± 0.03 ml for 1.0, 1.5 and 2.0 ml gels. The 0.5 ml gels continued to lose fluid gradually up till 180 s where they reached their maximum fluid loss of 0.453 ± 0.015 ml. 1.0 ml gels took 300 s to reach completion of compression, losing 0.903 ± 0.021 ml. It took 480 s for 1.5 ml gels to be compressed fully; losing 1.34 ± 0.015 ml and 2.0 ml gels took 720 s and lost 1.79 ± 0.014 ml of fluid (Figure 4.4A). These represent 90.1, 90.3, 89.1 and 89.5 % of the total initial gel volume for 0.5, 1.0, 1.5

Chapter 4: Characterisation of Compressed Collagen Constructs/Measurement of Compressed Collagen Scaffold Thickness

and 2.0 ml gels respectively, and overall rates of fluid loss of 2.52, 3.01, 2.79 and 2.49 $\mu\text{l/s}$ respectively (Table 4.1).

Table 4.1: Total fluid loss and overall rates of fluid loss following compression using paper plungers.

Initial Gel Volume (ml)	Total Fluid Loss (ml)	Fluid Loss Percentage (%)	Overall Rate of Fluid Loss ($\mu\text{l/s}$)
0.5	0.453 ± 0.015	90.1	2.52
1.0	0.903 ± 0.021	90.3	3.01
1.5	1.34 ± 0.015	89.1	2.79
2.0	1.79 ± 0.014	89.5	2.49

4.5.2. Determination of rate of fluid loss using fibre plungers

0.5, 1.0, 1.5 and 2.0 ml gels were compressed using fibre plungers which were weighed at 30 s time intervals up to 5 minutes, and then at 60 s intervals during the compression to determine the rate of fluid loss from the collagen constructs (Figure 4.3B). With these fibre plungers, the amounts of fluid absorbed within the first 30 s were 0.237 ± 0.006 , 0.263 ± 0.012 , 0.177 ± 0.021 and 0.203 ± 0.012 ml respectively. The time it took these gels to be fully compressed were 180, 480, 780 and 900 s respectively (Figure 4.4B). The amount of total fluid lost from these gels were 0.437 ± 0.015 , 0.9 ± 0.01 , 1.197 ± 0.015 and 1.66 ± 0.029 ml respectively, representing

Chapter 4: Characterisation of Compressed Collagen Constructs/Measurement of Compressed Collagen Scaffold Thickness

87.3, 90, 79.7 and 81.3 % of the initial gel volumes respectively (Table 4.2). The overall rates of fluid loss were 2.43, 1.88, 1.54 and 1.84 $\mu\text{l/s}$ respectively.

The first notable difference in plunger performance was the compression times. Whilst the times were similar for 0.5 ml gels, they were significantly different in the thicker gels; 1.0 ml gels took 360 and 480 s using paper plungers plus weights and fibre plungers respectively, 1.5 ml gels took 480 and 780 s, and 2.0 gels took 720 and 900 s. The thicker the gels, the greater the difference in compression times between plunger set-ups (0, 180, 300 and 360 s). The second notable difference was the amounts of fluid absorbed from the larger gels (1.5 and 2.0 ml). For 1.5 ml gels, paper plungers absorbed 1.34 ± 0.015 ml whilst fibre plungers only absorbed 1.197 ± 0.015 ml. With 2.0 ml gels, these values were 1.79 ± 0.014 and 1.66 ± 0.029 ml. These were differences of 0.143 and 0.13 ml respectively

Table 4.2: Total fluid loss and overall rates of fluid loss following compression using fibre plungers.

Initial Gel Volume (ml)	Total Fluid Loss (ml)	Fluid Loss Percentage (%)	Overall Rate of Fluid Loss ($\mu\text{l/s}$)
0.5	0.437 ± 0.015	87.3	2.43
1.0	0.9 ± 0.01	90	1.88
1.5	1.197 ± 0.015	79.7	1.54
2.0	1.66 ± 0.029	81.3	1.84

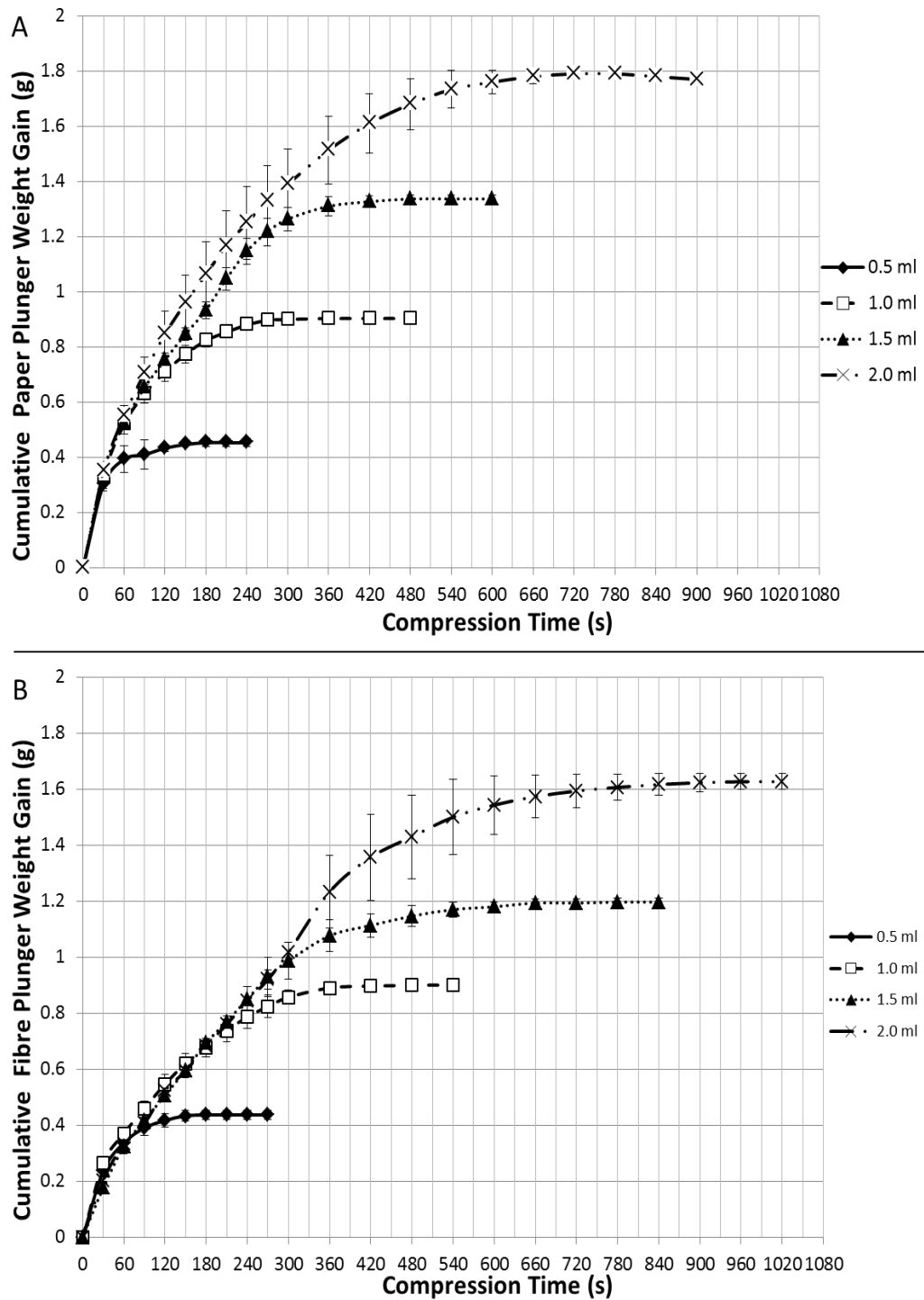


Figure 4.3: Plots showing the cumulative weight gained by paper (A) or fibre (B) plungers during compression to compare and contrast the rates of fluid absorption between plunger types. Error bars depict the standard deviations of the mean (n=9).

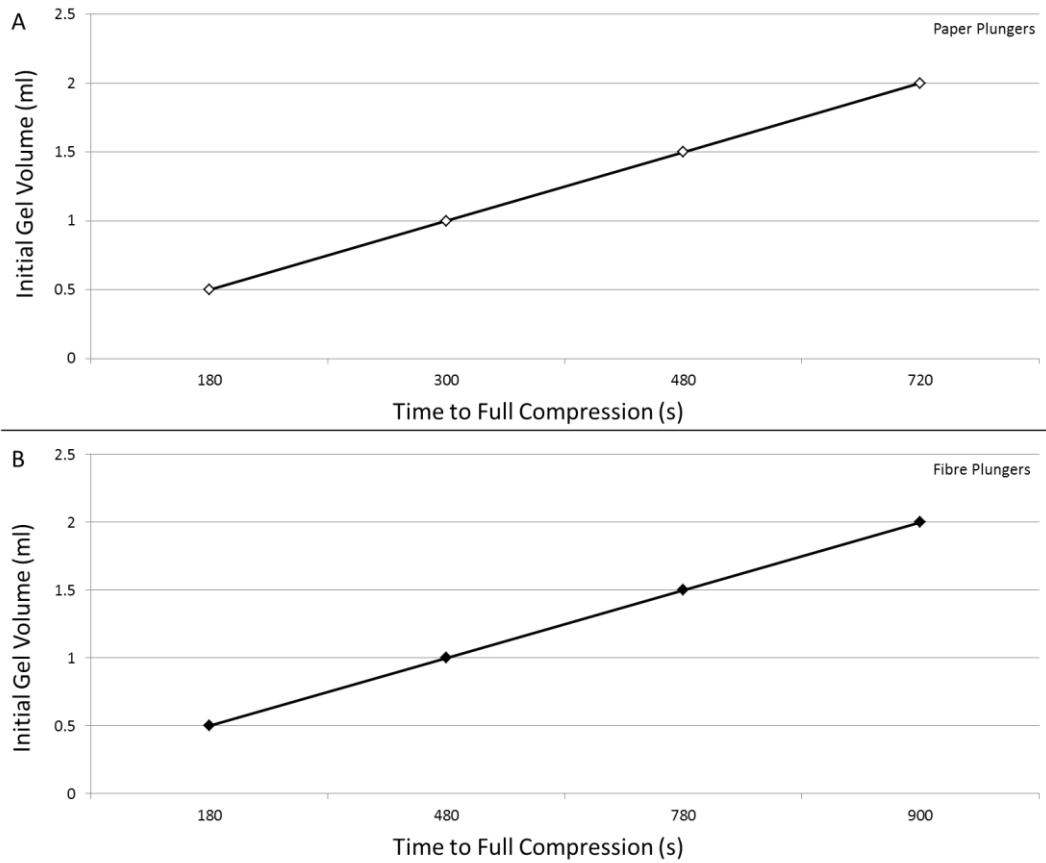


Figure 4.4: Graphs showing the time taken to reach completion of compression of 0.5, 1.0, 1.5 and 2.0 ml gels using either paper (A) or fibre plungers (B). (n=9)

Using these values, a curve of cumulative fluid loss as a percentage of the total fluid lost was plotted (Figure 4.5). When paper plungers were used, it took 180, 300, 480 and 720 s to fully compress 0.5, 1.0, 1.5 and 2.0 ml initial volume collagen gels respectively. The time it took for fibre plungers to fully compress the gels were 180, 420, 660 and 900 s respectively. Within the first minute of compression of 0.5, 1.0, 1.5 and 2.0 ml gels using paper plungers, the percentage of fluid lost was 87.1 ± 13.2 , 57.6 ± 5.2 , 39.2 ± 2.0 and 30.7 ± 1.2 % respectively. When fibre plungers were used, the fluid lost was 77.1 ± 1.5 , 41.1 ± 2.3 , 27.0 ± 2.2 and 20.5 ± 1.6 % of the initial gel volume respectively, showing a difference in the initial rates of compression, with the paper plungers absorbing more fluid within this first minute.

From this figure, the rates of fluid lost over the first 5 minutes were derived and plotted (Figure 4.6). Figure 4.6 compares the rates of fluid loss based on gel volumes and shows that the initial rates of compression of 0.5 ml gels were very similar whether paper or fibre plungers were used. The difference between plunger types was only apparent with the thicker gels (1.0, 1.5, 2.0 ml). On 0.5 ml gels, the rate during the 1st minute was 0.393 ± 0.047 ml/min, which increased to 0.52 ± 0.035 ml/min on 1.0 ml gels, and only further increased slightly to 0.523 ± 0.021 ml/min on 1.5 ml gels and 0.55 ± 0.036 ml/min on 2.0 ml gels. When fibre plungers were used, the initial rate of fluid lost did not change significantly at all volumes during the 1st minute: 0.337 ± 0.005 , 0.37 ± 0.017 , 0.323 ± 0.025 and 0.333 ± 0.029 ml/min. The initial rates of compression using paper plungers on 1.0, 1.5 and 2.0 ml gels were very similar, whilst that of the 0.5 ml gel was significantly lower. This

Chapter 4: Characterisation of Compressed Collagen Constructs/Measurement of Compressed Collagen Scaffold Thickness

points to the formation of the FLS in 0.5 ml constructs very early on during compression, probably within the first 30 seconds. The initial rates of fluid absorption using fibre plungers were the same across all gel volumes and were significantly smaller than that of the paper plunger system. This difference in rates between plunger type is due to the added pressure provided by the fixed load on the paper plungers. As shown in Chapter 3, fibre plungers have greater absorbency than the paper plungers, but here with the fixed load, paper plungers absorb fluid more readily.

To compare the differences between the rates using the two plunger types, Figure 4.7 was plotted, which displays the rates of fluid loss according to the four initial gel volumes rather than plunger type. As compression proceeded, the rates of fluid loss decreased with time (see also Figure 4.5), indicating an interference with fluid outflow from the gels. Figure 4.7A shows the rates of fluid loss in 0.5 ml gels. In the first minute, the rates were 0.393 ± 0.047 ml/min and 0.337 ± 0.005 ml/min for paper and fibre plungers respectively. In the 2nd minute, there was a dramatic decrease in both the rates of fluid loss from 0.5 ml gels. The rates dropped to 0.04 ± 0.036 and 0.08 ± 0.017 ml/min for paper plungers and fibre plungers respectively. By the 3rd minute, both rates dropped to 0.02 ± 0.026 and 0.02 ± 0.01 ml/min. Throughout the first few minutes of compression, the rates of fluid loss did not differ significantly for 0.5 ml gels.

With the thicker gels, the rates of fluid loss initially started off much higher when paper plungers were used as compared to fibre plungers. They then dropped below

Chapter 4: Characterisation of Compressed Collagen Constructs/Measurement of Compressed Collagen Scaffold Thickness

that of the fibre plungers at a point during the first 5 minutes of compression; 2 minutes for 1.0 ml gels, 3 min for 1.5 ml gels and 4.5 min for 2.0 ml gels (Figure 4.7B, C & D). On 1.0 ml constructs, the initial rate of fluid absorption using paper plungers and fibre plungers were 0.52 ± 0.035 and 0.37 ± 0.017 ml/min respectively. This then decreased to 0.19 and 0.18 ± 0.02 ml/min in the second minute, 0.11 ± 0.02 and 0.13 ± 0.01 ml/min in the third minute, 0.06 ± 0.03 and 0.11 ± 0.02 ml/min in the fourth minute and 0.02 ± 0.017 and 0.07 ± 0.017 ml/min in the fifth minute.

The rates of fluid absorption in the first 5 minutes of compression by paper and fibre plungers on 1.5 ml constructs were 0.52 ± 0.02 and 0.32 ± 0.03 ml/min, 0.23 ± 0.027 and 0.18 ± 0.025 ml/min, 0.18 ± 0.027 and 0.19 ± 0.006 ml/min, 0.21 ± 0.025 and 0.16 ± 0.04 ml/min and 0.17 ± 0.006 and 0.14 ± 0.02 ml/min. 2.0 ml constructs were dehydrated at rates of 0.55 ± 0.04 , 0.3 ± 0.06 , 0.22 ± 0.04 , 0.19 ± 0.02 and 0.14 ± 0.01 ml/min in minute 1, 2, 3, 4 and 5 using paper plungers and a fixed load. When fibre plungers were used, the rates in the first 5 minutes of compression were 0.33 ± 0.03 , 0.19 ± 0.05 , 0.16 ± 0.017 , 0.16 ± 0.03 and 0.17 ± 0.021 ml/min. With paper plungers, the rates continued decreasing in these first 5 minutes, whereas with the fibre plungers, after the third minute, the values remained more or less constant.

The drops in the rates of fluid absorption after the first minute indicate that blockages in fluid flow occurred, thus restricting fluid escape from the compressing gels.

Chapter 4: Characterisation of Compressed Collagen Constructs/Measurement of Compressed Collagen Scaffold Thickness

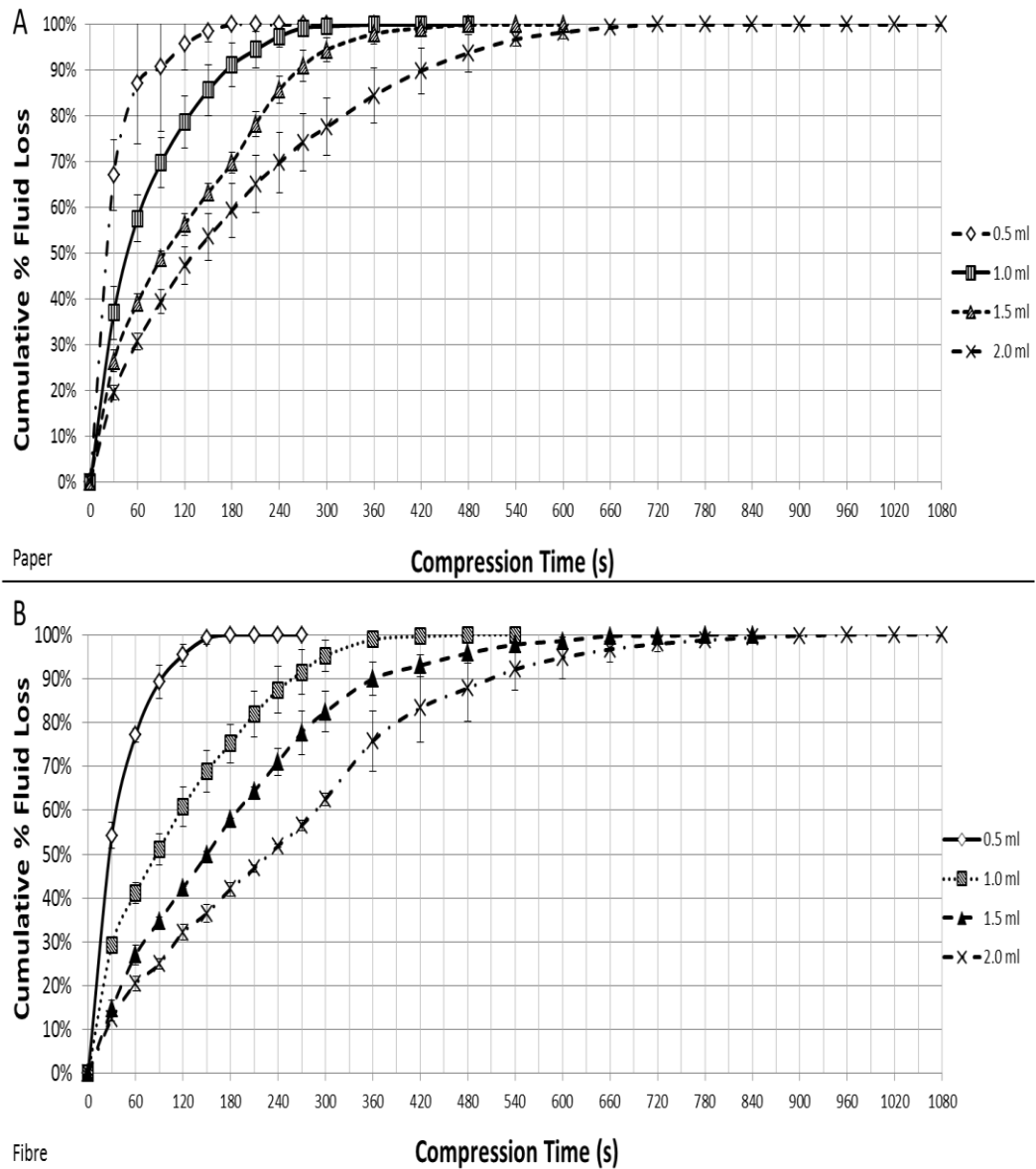


Figure 4.5: Graphs showing the rates of compression as determined by fluid loss. The cumulative fluid lost from four initial gel volumes were measured during compression using either (A) paper plungers with weights or (B) fibre plungers. 0.5 ml gels were fully compressed by 3 minutes using either plunger system. Paper plungers and a fixed load compressed the other thicker (1.0, 1.5 and 2.0 ml) gels faster than fibre plungers did. Error bars depict the standard deviations of the mean. (n=9)

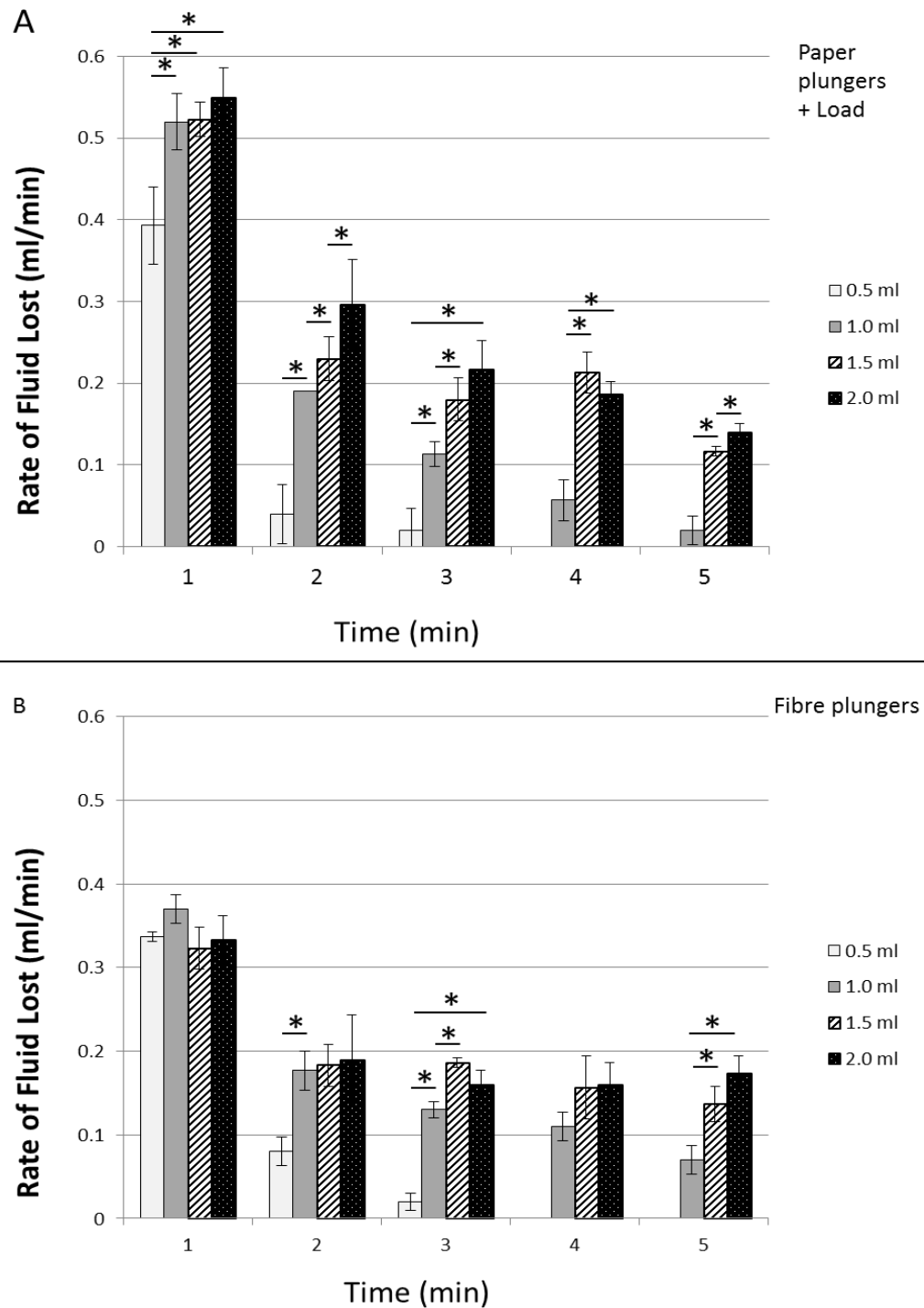


Figure 4.6: Graphs of the rates of fluid loss during the first 5 minutes of compression using either paper plungers (A) or fibre plungers (B) for different initial gel volumes. Both plunger types started off with a high rate of absorption in the first minute, followed by a drastic fall in rates by the second minute, before a more gradual decrease in rates in the third, fourth and fifth minutes. Error bars indicate the standard deviation of the mean ($p < 0.05$; $n = 9$).

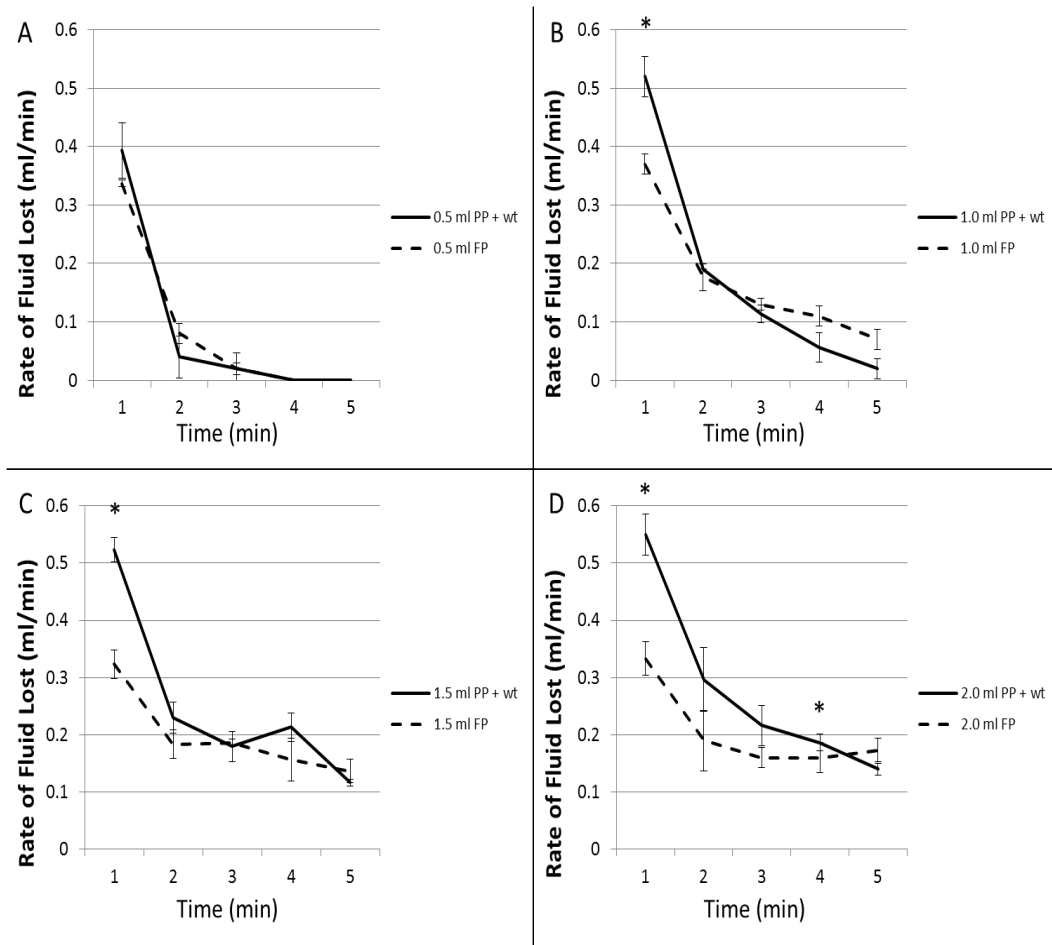


Figure 4.7: Graphs of the rates of fluid loss during the first 5 minutes of compression using either paper plungers with a weight or fibre plungers for initial gel volumes of 0.5 ml (A), 1.0 ml (B), 1.5 ml (C) and 2.0 ml (D). The initial rates of fluid loss were higher with paper plungers and an external load than with fibre plungers across all gel volumes. The fluid loss rates when using paper plungers and load decreased more rapidly than the rates when using fibre plungers which displayed more gradual declines. Error bars indicate the standard deviation of the mean ($p < 0.05$; $n = 9$).

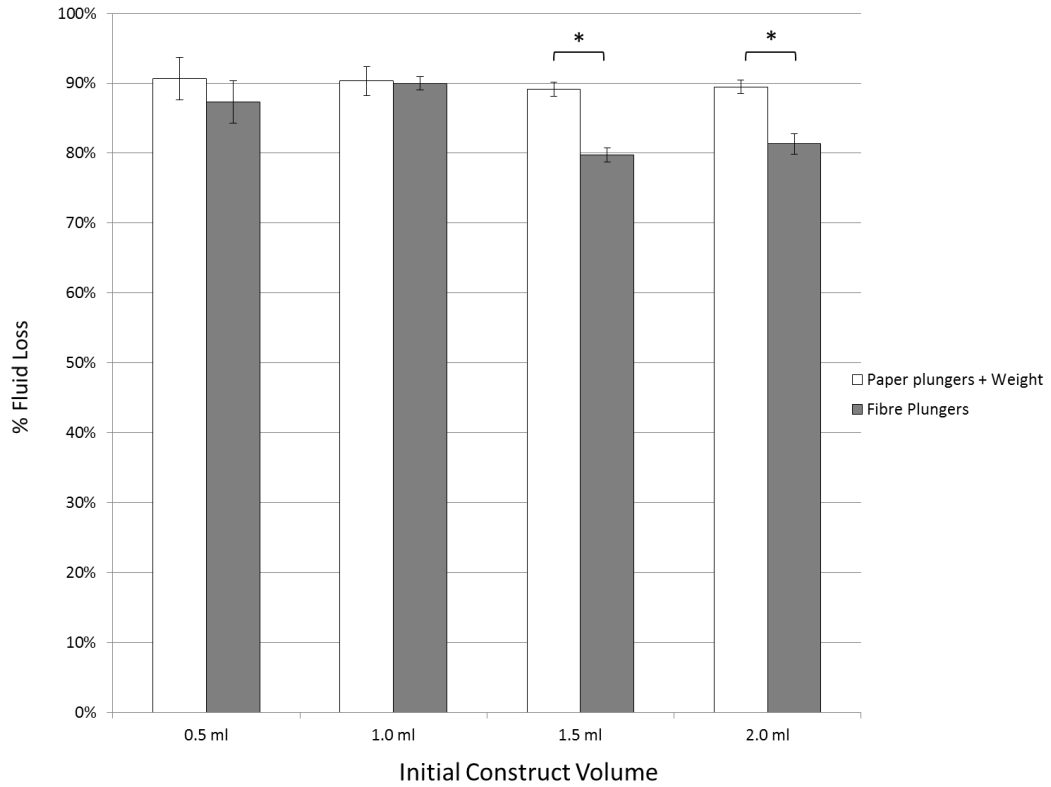


Figure 4.8: Graph showing the percentage of total fluid lost from gels of different starting volumes and compressed using the two different plunger types, as determined by plunger weight measurements. With thicker initial gel volumes, the difference in fluid absorption between plunger types was significant. Error bars indicate the standard deviation of the mean ($p < 0.05$; $n = 9$).

The full extent of compression by the plungers was compared by looking at the total amount of fluid absorbed from the four volumes of gel (Figure 4.8). The total amount of fluid absorbed as a percentage of the initial volume of the gel was similar for both plunger types (paper/fibre) with the 0.5 ml (90.1/87.3%) and 1.0 ml gels (90.3/90%). With the larger 1.5 ml and 2.0 ml gels, the paper plungers absorbed a greater percentage (89.1, 89.5%) of fluid as compared to the fibre plungers (79.7, 81.3%). However, these values are low compared to previous studies [299,355]. It was noticed that when moving the plungers from the gels to the weighing scale and back, small amounts of fluid was left on the fingertips. Evaporation of fluid from the plungers might have also altered the measurements. These losses of fluid might account for the low total percentage of fluid lost.

To determine the total fluid lost from gels after compression and to avoid technical issues, fully compressed constructs were weighed immediately after compression, instead of weighing the plungers. 0.5, 1.0, 1.5 and 2.0 ml gels were set in 24-well plates and compressed using either the paper plunger system or fibre plungers. Once compression was complete, constructs were carefully removed from their wells and placed on a weighing scale for weight measurements.

Figure 4.9 shows that 0.5, 1.0, 1.5 and 2.0 ml constructs prepared using paper plungers and a fixed load measured $2.4 \times 10^{-3} \pm 5.8 \times 10^{-5}$, $5.4 \times 10^{-3} \pm 3.2 \times 10^{-4}$, $6.3 \times 10^{-3} \pm 1.1 \times 10^{-3}$ and $1.14 \times 10^{-2} \pm 1.0 \times 10^{-3}$ g respectively. The constructs compressed with fibre plungers weighed $4.1 \times 10^{-3} \pm 4.2 \times 10^{-4}$, $6.7 \times 10^{-3} \pm 4.0 \times 10^{-4}$, $1.1 \times 10^{-2} \pm 4.7 \times 10^{-4}$

Chapter 4: Characterisation of Compressed Collagen Constructs/Measurement of Compressed Collagen Scaffold Thickness

and $1.4 \times 10^{-2} \pm 3.5 \times 10^{-4}$ respectively. These indicated a total fluid loss of $0.498 \pm 5.8 \times 10^{-5}$, $0.995 \pm 3.2 \times 10^{-4}$, $1.494 \pm 1.1 \times 10^{-3}$ and $1.99 \pm 9.0 \times 10^{-4}$ ml for constructs compressed using paper plungers, and $0.496 \pm 4.2 \times 10^{-4}$, $0.993 \pm 4.0 \times 10^{-4}$, $1.499 \pm 4.7 \times 10^{-4}$ and $1.99 \pm 3.35 \times 10^{-4}$ ml (Figure 4.10). More fluid was absorbed by paper plungers than by fibre plungers.

The differences between the total fluid absorbed by both plunger types were minimal, in the order of μl , compared to ml of the initial volume. Greater fluid absorption by the paper plunger system may be due to the added pressure from the fixed load. Fluid absorption differences between the thinner 0.5 and 1.0 ml constructs and between 1.5 and 2.0 ml constructs were similar. The difference in fluid absorption from 1.5 ml constructs was statistically significantly different to that of both the thinner constructs, whilst the difference from 2.0 ml constructs was approaching statistical significance. This could be due to the generation of a secondary fluid leaving surface (FLS). Once the primary and secondary FLS's were formed, there was insufficient pressure without additional load to force more fluid out from the constructs (see Chapter 3).

Figure 4.11 shows that the total amount of fluid lost represented 99.5 ± 0.01 , 99.5 ± 0.03 , 99.6 ± 0.07 and 99.5 ± 0.04 % (constructs made using paper plungers) and 99.2 ± 0.08 , 99.3 ± 0.04 , 99.3 ± 0.03 and 99.3 ± 0.02 % (constructs made using fibre plungers) of the initial gel volume (0.5, 1.0, 1.5 and 2.0 ml respectively). This shows the extent of dehydration plastic compression produces.

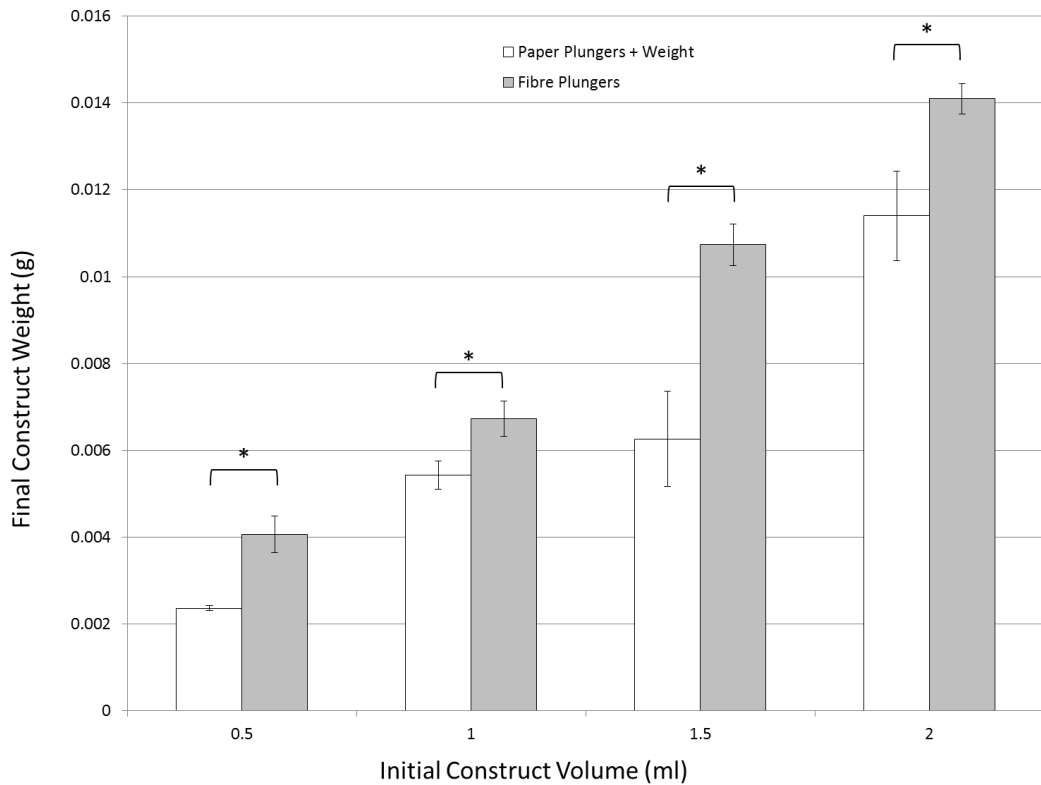


Figure 4.9: Final construct weight immediately after compression using paper plungers and a fixed load or fibre plungers. The final construct weights were roughly proportional (with respect to the initial volume) to the smallest volume (0.5 ml) gel (i.e. the 1.0, 1.5 and 2.0 ml constructs were ~2 times, 3 times and 4 times greater than the 0.5 ml constructs). There were significant differences in the final construct weights between plunger types across all initial gel volumes. Error bars indicate the standard deviation of the mean ($p < 0.05$ $n = 4$).

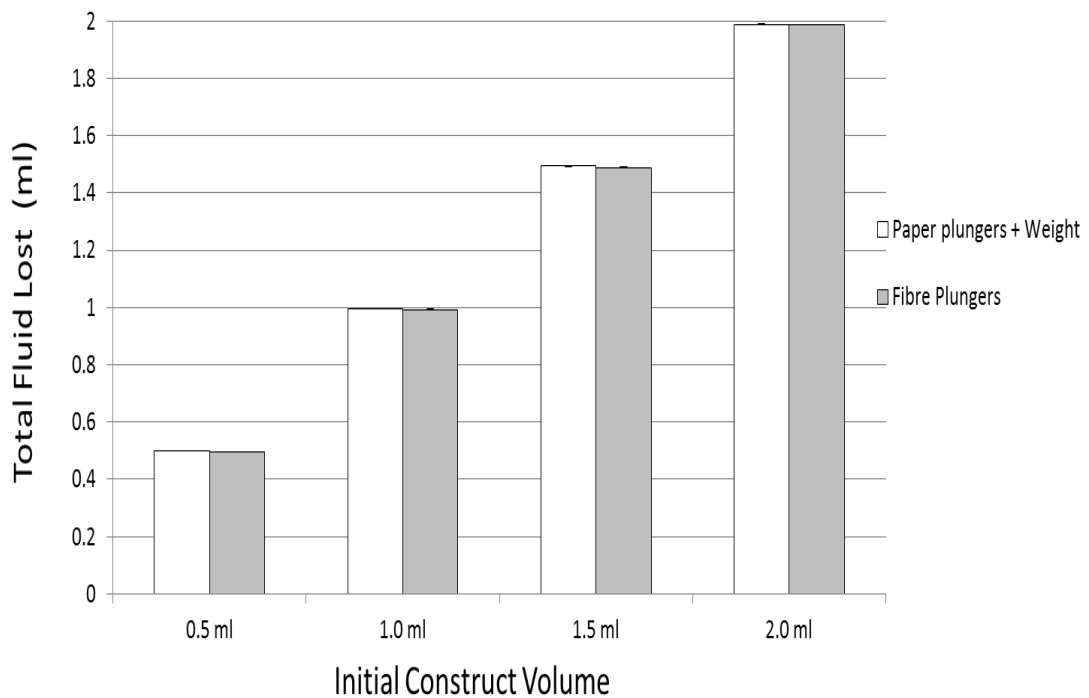


Figure 4.10: Total fluid loss from gels of different initial volumes and compressed using the two different plunger types determined by final construct weight. The differences in fluid lost from the gels between the two plunger types were minimal, indicating similar total fluid removal from the gels. Error bars indicate the standard deviation of the mean ($p < 0.05$; $n = 4$).

4.5.3. Collagen construct thickness changes after compression

Collagen constructs subjected to plastic compression undergo significant fluid loss and dramatic reductions in thickness (Figure 4.1). To determine the thicknesses of the final compressed constructs, the CTS-2 optical confocal meter was used. As this machine measures samples non-invasively, there was no handling of the constructs which may have caused micro-structural changes to the constructs or may have

Chapter 4: Characterisation of Compressed Collagen Constructs/Measurement of Compressed Collagen Scaffold Thickness

been repositioned incorrectly. A minimum of three regions around each construct was measured to obtain an average thickness across the whole construct.

0.5, 1.0, 1.5 and 2.0 ml constructs compressed with paper plungers measured 41.6 ± 1.97 , 64.3 ± 3.55 , 88.1 ± 8.47 and 121.0 ± 9.23 μm respectively (Table 4.3). Fibre plunger-compressed 0.5, 1.0, 1.5 and 2.0 ml constructs measured 47.5 ± 10.6 , 85.9 ± 13.9 , 110.9 ± 10.4 and 156.5 ± 19.3 μm respectively. These thickness differences may be due to the differences in total fluid lost (Figure 4.10). The additional pressure from the fixed load could also cause a greater degree of compaction to create thinner constructs.

The final thickness measurements of 0.5, 1.0, 1.5 and 2.0 ml constructs showed that the constructs underwent 98.5, 98.9, 99 and 98.9 % compaction, as compared to their initial starting thicknesses (Table 4.3).

Table 4.3: Changes in thickness of collagen gels in the 24-well format following plastic compression.

Initial Gel Volume (ml)	Initial Thickness (μm)	Final Thickness (μm)		% Thickness Change	
		Paper Plungers + Weight	Fibre Plungers	Paper Plungers + Weight	Fibre Plungers
0.5	2800	41.6 ± 1.97	47.5 ± 10.6	98.5%	98.5%
1.0	5700	64.3 ± 3.55	85.9 ± 13.9	98.9%	98.9%
1.5	8500	88.1 ± 8.47	110.9 ± 10.4	99.0%	99.0%
2.0	11300	121.0 ± 9.23	156.5 ± 19.3	98.9%	98.9%

4.5.4. Calculations of the hydraulic resistance of the FLS (R_{FLS})

In Chapter 3, the rates of absorption of water for both plunger types were measured. By 10 seconds, both plunger types absorbed in excess of 2 ml of water. Here it is clear that a hindrance to fluid absorption from collagen gels is present during compression. This is caused by the accumulation of collagen fibrils at the fluid leaving surface. Collagen gels are fibrillar meshworks filled with fluid and are thus porous structures. Therefore, fluid flow during plastic compression can be partially described by Darcy's law. This allows the determination of the hydraulic resistance generated during compression using the following equation:

$$R_{FLS} = \frac{A \cdot P}{\mu \cdot Q}$$

where R is the hydraulic resistance of the FLS (m^{-1}), A is the surface area (m^2), P (N) is the pressure applied to surface A, μ is the dynamic viscosity of water (1.002×10^{-3} Ns/ m^2 at 20°C) and Q is the rate of flow (m^3/s). Hydraulic resistance was calculated for every minute during compression for 0.5, 1.0, 1.5 and 2.0 ml constructs, taking into account for the increase in force with time due to the added mass from the fluid absorbed into the plungers (Figure 4.12).

4.5.4.1. Paper plungers plus fixed load

Table 4.4 shows the R_{FLS} values of 0.5, 1.0, 1.5 and 2.0 ml constructs during the first 5 minutes of compression using paper plungers and a fixed load, which are represented in a histogram in Figure 4.13A. The hydraulic resistance of 0.5 ml constructs was higher than that of all the other constructs in the first three minutes of compression, being dramatically higher by the second and third minutes. The hydraulic resistances of the 1.0, 1.5 and 2.0 ml constructs were similar in the first minute. Differences between these constructs became more apparent in the second minute of compression where after the 0.5 ml constructs, the 1.0 ml constructs generated the next largest resistance followed by the 1.5 ml constructs. The resistance produced by the 1.0 ml constructs then carried on increasing exponentially over the next 3 minutes. The hydraulic resistances of the two larger constructs grew only gradually in these first 5 minutes.

Table 4.4: R_{FLS} of constructs of different initial volumes during the first 5 minutes of compression using paper plungers with a fixed load.

Initial Gel Volume (ml)	R_{FLS} at 1 st Minute (m^{-1})	R_{FLS} at 2 nd Minute (m^{-1})	R_{FLS} at 3 rd Minute (m^{-1})	R_{FLS} at 4 th Minute (m^{-1})	R_{FLS} at 5 th Minute (m^{-1})	Max. R_{FLS} (m^{-1})
0.5	$3.87 \times 10^{10} \pm 5.7 \times 10^7$	$3.81 \times 10^{11} \pm 2.2 \times 10^8$	$7.63 \times 10^{11} \pm 9.0 \times 10^8$	-	-	$7.63 \times 10^{11} \pm 9.0 \times 10^8$
1.0	$2.94 \times 10^{10} \pm 5.6 \times 10^7$	$8.11 \times 10^{10} \pm 1.5 \times 10^8$	$1.37 \times 10^{11} \pm 2.1 \times 10^8$	$2.74 \times 10^{11} \pm 1.6 \times 10^8$	$7.76 \times 10^{11} \pm 1.7 \times 10^8$	$7.76 \times 10^{11} \pm 1.7 \times 10^8$
1.5	$2.93 \times 10^{11} \pm 8.1 \times 10^7$	$6.72 \times 10^{10} \pm 1.2 \times 10^8$	$5.16 \times 10^{10} \pm 2.7 \times 10^8$	$7.36 \times 10^{10} \pm 1.3 \times 10^8$	1.35×10^{11}	$1.58 \times 10^{12} \pm 4.0 \times 10^9$
2.0	$2.75 \times 10^{10} \pm 8.6 \times 10^7$	$5.16 \times 10^{10} \pm 2.7 \times 10^8$	$7.12 \times 10^{10} \pm 4.6 \times 10^8$	$8.32 \times 10^{10} \pm 5.8 \times 10^8$	$1.11 \times 10^{11} \pm 7.6 \times 10^8$	$1.59 \times 10^{12} \pm 4.6 \times 10^9$

4.5.4.2. Fibre plungers

The trend in the increase in hydraulic resistances in the first 5 minutes of compression was similar to when paper plungers were used (Table 4.5 & Figure 4.13B). In the first minute, all constructs showed very similar resistances. But by the second minute, the resistance generated by 0.5 ml constructs were double that of

Chapter 4: Characterisation of Compressed Collagen Constructs/Measurement of Compressed Collagen Scaffold Thickness

the other constructs, and around 8 times higher by the third minute. The resistances of the other constructs remained similar in the second minute. Only in the third minute did any differences become apparent. Like with the paper plungers, 1.0 ml constructs displayed greater increase in resistance compared to the two larger constructs. However, there was no exponential rise in resistance in these 5 minutes as there was with the paper plungers. Again, the 1.5 and 2.0 ml construct resistances increased gradually.

Looking at Figure 4.13A, the hydraulic resistance of the 1.5 constructs began increasing exponentially in minute 6 to close to double the maximum of the 0.5 and 1.0 ml constructs whilst that of the 2.0 ml constructs took a further 3 minutes before shooting to similar values. Figure 4.13B shows that with fibre plungers, the pattern of hydraulic resistance increase was similar; the difference between the 1.5 and 2.0 ml constructs became apparent in the sixth minute, with the latter showing a delayed exponential rise at 10 min. These results show that the greater the amount of fluid and collagen in the compressing gels, the greater the hydraulic resistance generated; a greater quantity of collagen present along with more fluid movement upwards leads to higher collagen deposition at the FLS.

Table 4.5: R_{FLS} of constructs of different initial volumes during the first 5 minutes of compression using fibre plungers.

Initial Gel Volume (ml)	R_{FLS} at 1 st Minute (m^{-1})	R_{FLS} at 2 nd Minute (m^{-1})	R_{FLS} at 3 rd Minute (m^{-1})	R_{FLS} at 4 th Minute (m^{-1})	R_{FLS} at 5 th Minute (m^{-1})	Max. R_{FLS} (m^{-1})
0.5	$4.39 \times 10^9 \pm 5.0 \times 10^7$	$2.09 \times 10^{10} \pm 2.5 \times 10^8$	$8.61 \times 10^{10} \pm 1.5 \times 10^9$	-	-	$8.61 \times 10^{10} \pm 1.5 \times 10^9$
1.0	$3.93 \times 10^9 \pm 5.1 \times 10^7$	$9.54 \times 10^9 \pm 1.64 \times 10^8$	$1.37 \times 10^{10} \pm 3.0 \times 10^8$	$1.68 \times 10^{10} \pm 3.2 \times 10^8$	$2.74 \times 10^{10} \pm 5.2 \times 10^8$	to $9.88 \times 10^{10} \pm 1.6 \times 10^9 m^{-1}$
1.5	$4.45 \times 10^9 \pm 5.2 \times 10^7$	$8.9 \times 10^9 \pm 1.7 \times 10^8$	$9.29 \times 10^9 \pm 1.0 \times 10^8$	$1.18 \times 10^{10} \pm 1.4 \times 10^8$	$1.42 \times 10^{10} \pm 2.1 \times 10^8$	$1.61 \times 10^{11} \pm 1.6 \times 10^9$
2.0	$4.45 \times 10^9 \pm 3.5 \times 10^7$	$8.76 \times 10^9 \pm 1.1 \times 10^8$	$1.11 \times 10^{10} \pm 9.2 \times 10^7$	$1.17 \times 10^{10} \pm 1.1 \times 10^8$	$1.13 \times 10^{10} \pm 2.0 \times 10^7$	$2.42 \times 10^{11} \pm 8.97 \times 10^8$

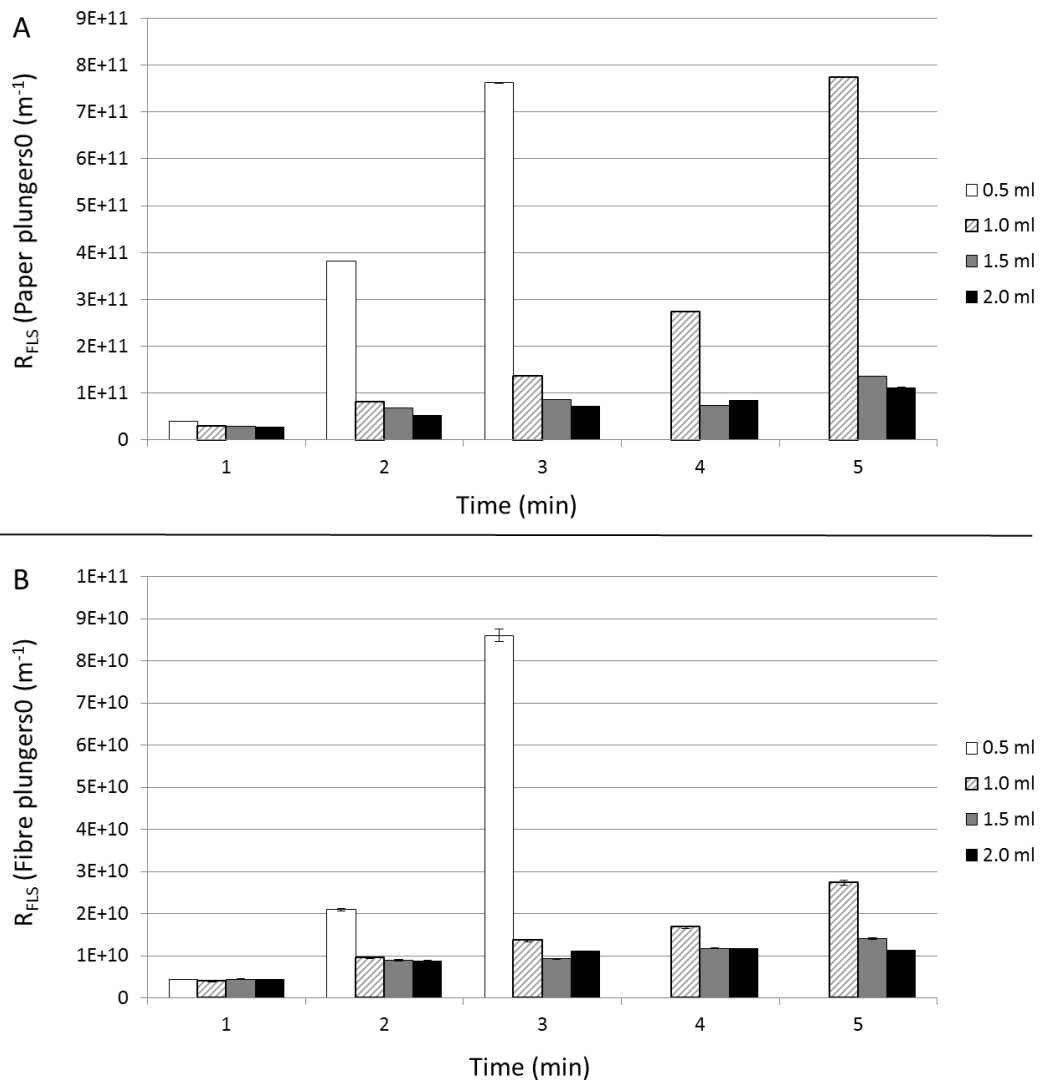


Figure 4.11: Calculated hydraulic resistances generated in 0.5, 1.0, 1.5 and 2.0 ml constructs during the first 5 min of compression, indicating greater blockage at the FLS when using paper plungers (A) than fibre plungers (B). Error bars depict the standard deviations of the mean (n=9).

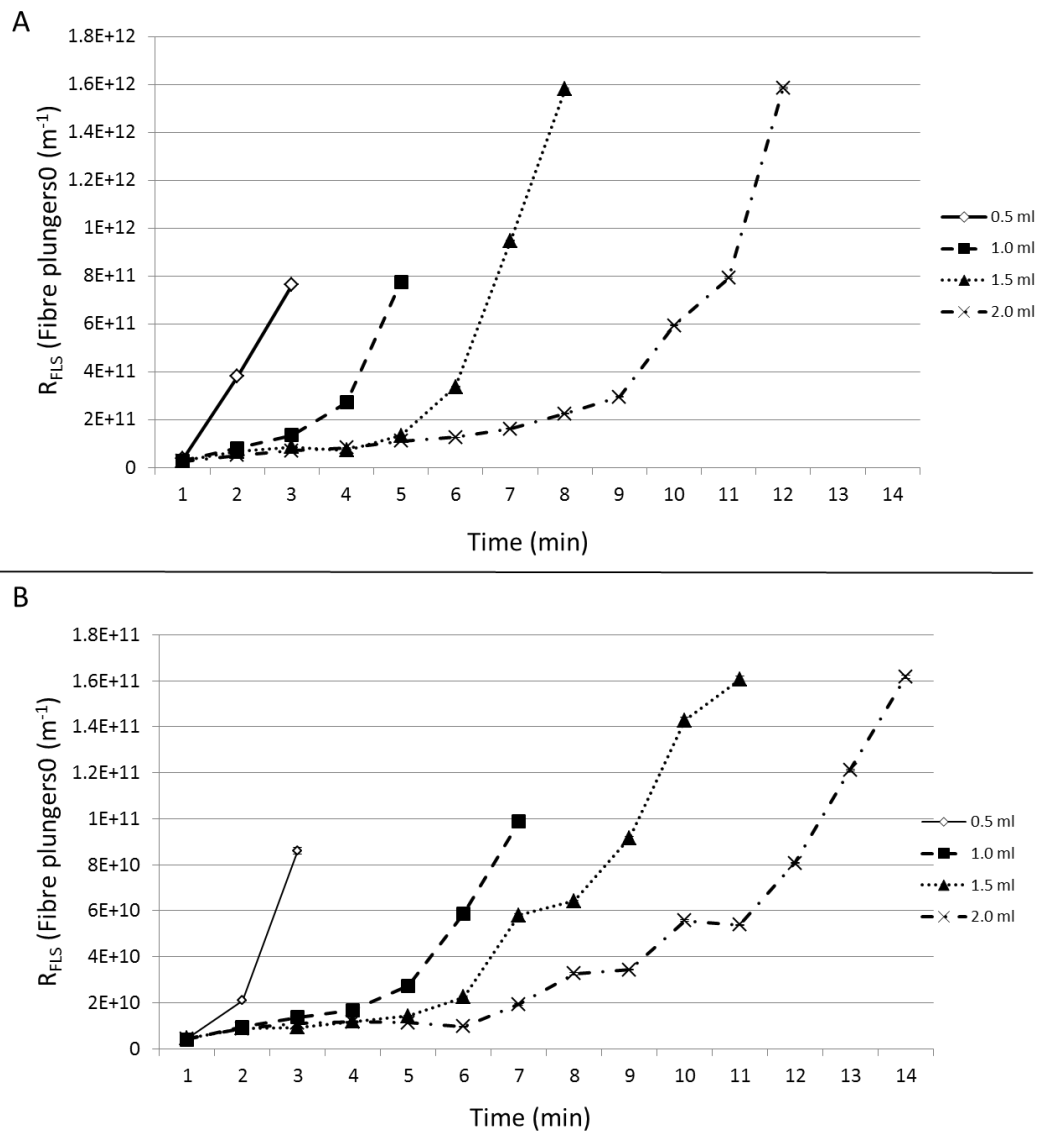


Figure 4.12: Calculated hydraulic resistances generated in 0.5, 1.0, 1.5 and 2.0 ml constructs during compression using paper plungers (A) or fibre plungers (B). The greater the initial gel volume, the higher the final R_{FLS} value. With paper plungers and a load, the R_{FLS} values across all gel volumes were greater than when fibre plungers were used, possibly indicating a thicker or denser FLS present in the constructs.(n=9)

4.5.5. Thickness measurements

$$P = \frac{(M_P + M_L)g}{A}$$

The pressure on the gels was calculated using the equation above, where P (Pa) is pressure, m_p (kg) is the mass of the plunger used, m_L (kg) is the mass of the fixed load which was 22 g in the case of the paper plunger system, g is the acceleration due to gravity (m^{-2}) and A (m^2) is the surface area of the gel. Using the paper plunger system, the pressure applied was calculated to be 1243.9 Pa, and that of the fibre plunger system was 149.8 Pa. As the pressure applied to the collagen gels during compression was higher using the paper plunger system, compared to the fibre plunger, it was hypothesised that the constructs made with the former would be compacted to a greater extent and so, thinner, than those made with fibre plungers.

Figure 4.14 shows the measurements taken of 0.5, 1.0, 1.5 and 2.0 ml initial volume gels compressed with either paper or fibre plungers. The gels compressed with paper plungers had thicknesses of 40.3 ± 2.6 , 63.0 ± 12.7 , 99.9 ± 18.7 and 107.9 ± 8.6 μm respectively, whilst the fibre plunger-compressed constructs were of 44.7 ± 9.8 , 89.5 ± 18.3 , 135.3 ± 22.5 and 179.0 ± 36.5 μm thicknesses respectively, immediately after compression. Compression using paper plungers produced thinner constructs than fibre plungers, and the difference in thicknesses was

greater with increasing initial gel volume - 4.4, 26.6, 35.5, 75.0 μm for 0.5, 1.0, 1.5 and 2.0 ml, respectively.

4.5.6. Investigation of the re-swelling of compressed constructs

The CTS-2 makes non-contact measurements of constructs *in situ*, allowing the re-measuring of constructs at different time points. As these engineered constructs underwent compaction and dehydration, there was a possibility of them re-absorbing fluid and regaining thickness. This device enabled the study of the re-swelling effects of compressed constructs. The CTS-2 greatly enhanced this study as the changes in thicknesses measured were from the same samples. Whereas with histology, measurements at different time points required different constructs.

0.5, 1.0, 1.5 and 2.0 ml collagen gels were prepared in 24-well plates and compressed using either paper plungers or fibre plungers. Immediately after compression, the constructs were measured using the CTS-2 to determine their thicknesses. The constructs were then re-measured after 24 hours to determine any changes in the thicknesses of the constructs.

As described above, 0.5, 1.0, 1.5 and 2.0 ml constructs compressed using paper plungers measured 40.3 ± 2.6 , 63.0 ± 12.7 , 99.9 ± 18.7 and 107.9 ± 8.6 μm in thickness, respectively, whilst those prepared using fibre plungers were 44.7 ± 9.8 , 89.5 ± 18.3 , 135.3 ± 22.5 and 179.0 ± 36.5 μm thick (Figure 4.14A). These constructs

Chapter 4: Characterisation of Compressed Collagen Constructs/Measurement of Compressed Collagen Scaffold Thickness

were measured again *in situ* after 24 hours to determine the degree of re-swelling (if any) of each construct. 0.5, 1.0, 1.5 and 2.0 ml constructs produced using paper plungers measured 41.39 ± 1.65 , 103.71 ± 25.4 , 145.9 ± 21.8 and 164.9 ± 11.3 μm respectively after 24 hours, showing increases of 1.1, 40.7, 46.1, 57.0 μm respectively (Figure 4.14B). Whilst those produced using fibre measured 70.7 ± 23.5 , 124.1 ± 26.2 , 189.6 ± 36.6 and 199.6 ± 11.9 μm respectively, increasing by 26.0, 34.6, 54.2, and 53.1 μm . These increases in thickness indicate that all the constructs did re-swell, and to similar degrees – apart from the 0.5 ml constructs. This re-swelling effect did not occur when the constructs were fixed in formalin following compression, and construct thickness remained constant (Figure 4.15).

Chapter 4: Characterisation of Compressed Collagen Constructs/Measurement of Compressed Collagen Scaffold Thickness

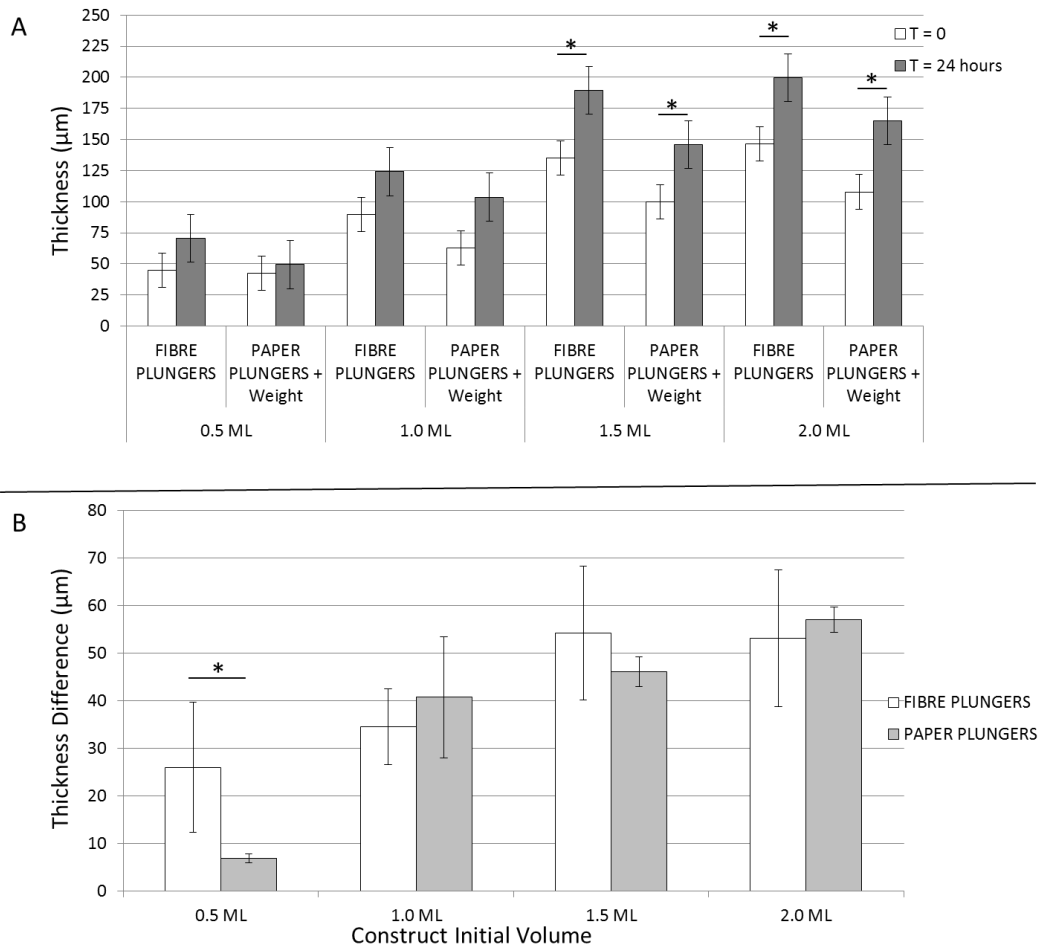


Figure 4.13: (A) Thickness measurements of 0.5, 1.0, 1.5 and 2.0 ml constructs compressed with paper plungers or fibre plungers immediately after compression and after 24 hours, showing that the constructs undergo a degree of re-swelling. (B) The difference between thicknesses at t = 0 and t = 24 h. Error bars indicate the standard deviation of the mean ($p < 0.05$; $n = 6$).

Chapter 4: Characterisation of Compressed Collagen Constructs/Measurement of Compressed Collagen Scaffold Thickness

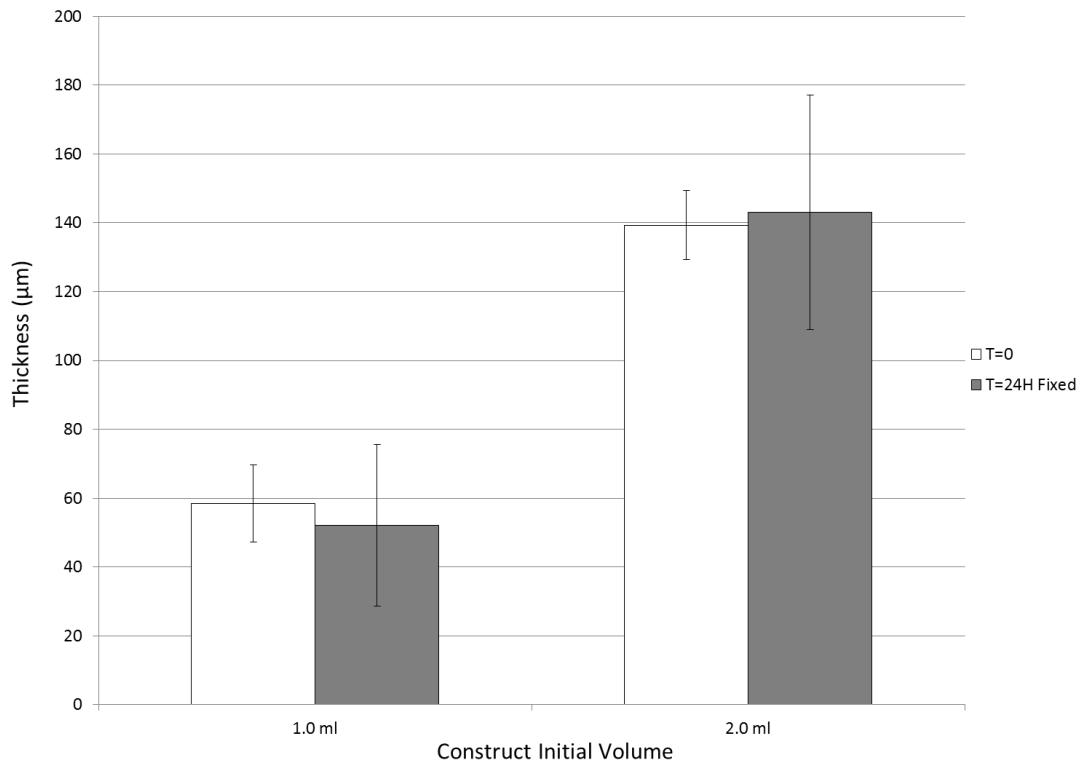


Figure 4.14: Compressed construct thickness measurements immediately after compression and 24 H later following fixation with formalin. Constructs that were fixed showed no significant changes in thickness after 24 hours. Error bars indicate the standard deviation of the mean ($p < 0.05$; $n = 4$).

4.5.7. Cell proliferation comparison

Cells were cultured in different spatial and stiffness environments to compare their behaviour in terms of proliferation. Monolayer cultures were compared with cells enmeshed within a matrix to study differences between 2D and 3D culture. The 2D set-ups used were cells cultured on standard tissue culture plastic, cells cultured on soft, compliant uncompressed collagen hydrogels and cells on top of compressed collagen constructs. These three 2D environments provided three substrates with different mechanical properties. The 3D conditions used were cells in uncompressed collagen gels and cells within compressed collagen constructs. These too, provided two environments with different mechanical properties.

Figure 4.16 shows the results of the cell proliferation (alamar blue reduction) assay. Comparing the three 2D systems, cells cultured on stiff tissue culture plastic (2D TCP) proliferated the most, followed by cells on compressed collagen (2D PC) and then cells on uncompressed collagen (2D UC). This illustrates the importance of the mechanical properties of substrates. Tissue culture plastic is unnaturally stiff; an environment that cells would not encounter in the body.

The 2D and 3D comparison shows that cells cultured as a monolayer (2D UC and 2D PC) show higher rates of proliferation in the first few days, before the cells in 3D (3D UC and 3D PC) reach similar cell numbers. This shows that cells cultured in 2D have higher proliferation rates than cells cultured in 3D. The density of collagen and

Chapter 4: Characterisation of Compressed Collagen Constructs/Measurement of Compressed Collagen Scaffold Thickness

mechanical properties of the matrix can also be seen to affect cell proliferation in 3D. Cells cultured in the stiffer compressed constructs showed greater proliferation than cells in the compliant collagen hydrogels. After the first 24 hours, cells displayed increasing levels of basal metabolism with increasing material stiffness (stiffness and detected fluorescence: 3D UC < 2D UC < 3D PC < 2D PC < 2D TCP).

This study highlights the effects substrate stiffness has on cells as well as the differences between 2D and 3D cell culture. Conventional monolayer cell culture on tissue culture plastic makes cells proliferate at an unnaturally high rate. Here we also show that fibroblasts, which normally reside within a matrix, proliferate more when cultured as a monolayer than when in a matrix. This illustrates the importance of 2D tissue-like cell culture to recapitulate normal, natural cell behaviour.

Chapter 4: Characterisation of Compressed Collagen Constructs/Measurement of Compressed Collagen Scaffold Thickness

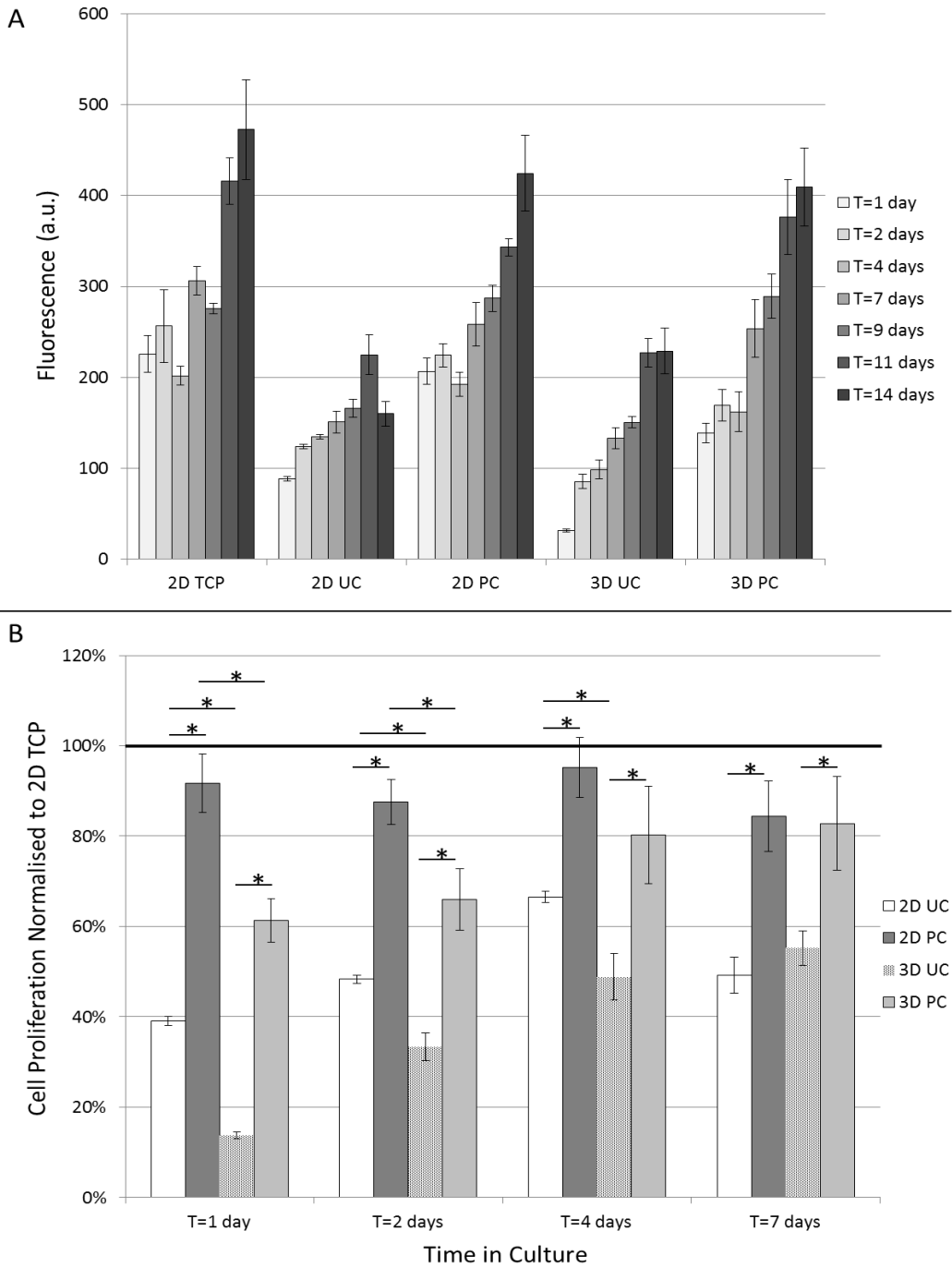


Figure 4.15: Cell proliferation rates, as determined by alamar blue reduction (A), of cells cultured in 2D on tissue culture plastic (2D TCP), compliant uncompressed collagen hydrogels (2D UC) and stiffer compressed collagen constructs (2D PC), and in 3D within uncompressed collagen hydrogels (3D UC) and within compressed collagen constructs (3D PC), showing different cell behaviour in different environments. (B): Results normalised to conventional monolayer culture on tissue culture plastic. Error bars indicate the standard deviation of the mean ($p < 0.05$; $n = 6$).

4.6. Discussion

The fibre plungers produced by TAP Biosystems were compared to the traditional paper plungers that are routinely used for plastic compression [319,320,337]. The fibre plungers were produced to absorb water at an optimal rate such that an external force (metal weight) is not needed, to simplify the compression set-up. Compression rates were different for the different plunger systems, although the total fluid lost was similar (Figure 4.10). The compression profiles were not linear (Figure 4.3), which indicates fluid outflow blockage by the compacting fibrils at the FLS. The rates of fluid absorption dropped dramatically from the first minute to the second minute (decreases of at least 0.25 ml/min with paper plungers and at least 0.14 ml/min with fibre plungers). This points towards the generation of the fluid leaving surface at this early point during compression, to restrict fluid outflow from the gel. With paper plungers and a fixed load, the rate of fluid absorption within the first minute using 0.5 ml gels was significantly lower than in the other constructs which had initial rates greater than the total initial volume of the 0.5 ml constructs. This must mean that collagen began accumulating at the FLS and limiting fluid escape in the first few seconds of compression.

Across the initial gel volumes with paper plungers and a fixed load, there was an increasing trend of the initial fluid loss rates. This could be due to the rate of FLS formation with respect to the volume of fluid remaining in the gel. This is represented by R_{FLS} , the hydraulic resistance of the fluid leaving surface during compression (Figure 4.12). Hydraulic resistance of the FLS provides an indirect

Chapter 4: Characterisation of Compressed Collagen Constructs/Measurement of Compressed Collagen Scaffold Thickness

measure of collagen density at the FLS, allowing the analyses of FLS growth with time during compression. The hydraulic resistances generated by the FLS decrease with increasing initial construct volume at a given time point – the opposite trend of fluid loss rates. This shows that the FLS developed at different rates in constructs of different initial volume, with the FLS developing faster with smaller initial gel volumes. Therefore, the greater the collagen accumulation at the FLS, the greater the hydraulic resistance to fluid flow and hence the lower the rate of fluid loss. R_{FLS} was greater using paper plungers and a fixed load than with fibre plungers. This value estimates the blockage of the FLS through accumulations of collagen, which suggests that constructs made with paper plungers have a denser FLS than those prepared using fibre plungers. A limitation to this is that fluid discharge from the gel was assumed to be unidirectional (out of the top surface only), where, especially in thicker gels, fluid is pushed out via the bottom surface (and possibly the sides) as well as the primary FLS.

In the graph showing the dynamics of the hydraulic resistances in constructs compressed using fibre plungers (Figure 4.13B), there appears to be a 'step' in the 1.5 and 2.0 ml curves at minute 7 and 10 respectively. At these times, the R_{FLS} value increased slightly for the 1.5 ml constructs and decreased minimally for the 2.0 ml constructs. This could possibly be around the time when the formation of the secondary FLS starts. As the primary FLS becomes denser and denser, hindering fluid escape possibly to the point of complete blockage. This causes a build-up of pressure in the fluid remaining in the gel as the plungers continue to press down on the constructs. Eventually, the internal pressure becomes great enough to force

Chapter 4: Characterisation of Compressed Collagen Constructs/Measurement of Compressed Collagen Scaffold Thickness

fluid out from the gel via other surfaces, generating secondary FLS's and allowing compression and fluid removal to resume (see Chapter 3). Figure 4.13B may have captured the dynamic of this process. These steps are only present in the curves of the thicker, 1.5 and 2.0 ml constructs compressed with fibre plungers. The pressure acting on the constructs compressed using paper plungers and a fixed load was much greater than that exerted by the fluid-filled fibre plungers. So the initiation of secondary FLS formation would have been much faster, and hence the dynamics of this step was not captured in this experiment when paper plungers and a fixed load were used. It may be possible to use the optical confocal meter to detect fluid outflow through the bottom surface of the constructs during compression, as this would create a new interface through which the laser would pass through. Although, the refractive indices of water and a compressing collagen hydrogel is quite similar, and the difference may not be detected.

These calculations however, were based on the assumption that the viscosity of the fluid (μ) remained constant through compression. It is possible that as fluid drained out of the compressing gel, the viscosity of the remaining fluid increased. Hubbert had previously demonstrated that the dynamic viscosity of fluid is inversely proportional to the rate of fluid discharge [358]. Thus the hydraulic resistance at the FLS would be dependent on both the blockage of fluid outflow and increases in fluid viscosity.

The CTS-2, an optical confocal device, allowed real-time determination of collagen construct thickness *in situ* rather than relying on histological methods (Chapter 3).

Chapter 4: Characterisation of Compressed Collagen Constructs/Measurement of Compressed Collagen Scaffold Thickness

This provided a more accurate method of determining final construct thickness. The paper plunger system produced thinner constructs than fibre plungers. This difference is likely due to the additional pressure from the external load used together with paper plungers (and the consequential generation of new FLS's).

Interestingly, despite being more compact and dehydrated than the construct prepared with fibre plungers, paper-plunger-compressed constructs re-swelled just as much as the former, apart from the 0.5 ml constructs which showed a significantly smaller increase in thickness than the 0.5 ml constructs prepared using fibre plungers (Figure 4.14B). It was originally thought that any re-swelling would occur at the collagen-dense FLS since it is very compact and may undergo some elastic deformation during compression. However, as mentioned earlier, the hydraulic resistance values, which provide an indication of the extent of blockage (protein accumulation), are higher for paper plunger-compressed constructs than for fibre compressed-constructs, indicating that the former had denser FLS's. This would suggest then that the paper plunger-compressed constructs should re-swell to a greater degree than the constructs produced with fibre plungers. Apart from the smallest construct size, this was not the case, meaning that re-swelling occurred either in the non-FLS regions of the constructs or throughout the whole construct, including the FLS.

One of the advantages of using compressed collagen constructs is that cells can be seeded in the gel before compression so that the collagen fibrils form around them, mimicking the *in vivo* tissue organisation. Cellular constructs would be cultured for

periods of time for various purposes. As such, it was important to determine how stable the acellular constructs were over periods of time. The non-invasiveness of the CTS-2 allowed the measuring and re-measuring of the *same* constructs immediately after compression and 1 day later, which was previously impossible.

The technology from Lein AD has greatly improved collagen construct characterisation and has helped us to understand plastic compression better with regards to compaction and re-swelling. Furthermore, this method is non-invasive, so constructs can be measured without the need for handling them which can cause damage or disruption to the structure of the collagen structure, which allows for more accurate measurements, as well as allowing for subsequent measurements to be done on the *same* construct over time (hours, days, weeks), which was impossible before.

4.7. Conclusion

Compression with the paper plunger system and the fibre plunger system resulted in different rates of compression, although the total fluid removal across all initial gel volumes was similar. The degree of compaction of the final constructs differed, with those produced using the paper plunger system being thinner than those prepared using fibre plungers. This result, along with the investigation on hydraulic resistance of the FLS, has given additional insight into the generation of the secondary FLS at the bottom surface of constructs. These 16 mm-diameter collagen constructs were shown to support cell growth. Additionally, the cells were

Chapter 4: Characterisation of Compressed Collagen Constructs/Measurement of Compressed Collagen Scaffold Thickness

demonstrated to behave differently in culture conditions of differing stiffness and dimensionality.

Chapter 5: Micro-Density Analysis of Compressed Collagen Constructs: Rapid Method Development

5.1. Introduction

Tissue development and maintenance is achieved through signalling networks of biochemical and mechanical signals from cell-cell and cell-matrix interactions [172,359,360]. These interactions govern cell function through influencing cell alignment, migration, proliferation and differentiation [361-368]. The extracellular matrix (ECM) therefore plays an important role in regulating cell behaviour. Cells respond to ECM cues such as substrate stiffness and topographical features. Where these are understood, they can be exploited for the engineering of complex, biomimetic tissue-like scaffolds.

Tissue engineering aims to reproduce functional tissues with native cell and matrix composition and organisation. It is widely known that the topography of a substrate affects cell behaviour in the way they organise themselves, in terms of morphology as well as alignment, and this affects differentiation and proliferation [369,370]. Cells on an anisotropic surface will align themselves in the direction of grooves present on the surface, and the rate at which this occurs is affected by the spacing in between grooves as well as the widths and depths of the grooves [247,248]. Fibroblasts have also been shown to sense the dimensional characteristics of features such as crypts. Berry et al. showed that there were differences in cell proliferation *on* crypts measuring 7, 15 or 25 μm in diameter, whilst cells only

entered the 25 μm crypts [245]. This seems to indicate that the cells were sensitive to the curvature of the crypts. Using 1.5-2.0 μm wide square-shaped ridges, Kim et al. showed that cells migrated towards regions of increased crypt density and anisotropy [371].

These studies have revealed the importance of topography on cell behaviour, and that to engineer a biomimetic environment for cells, topography needs to be fabricated into the microarchitecture of biomaterials. However, the materials used for engineering micro-topography have been inorganic, mostly because the techniques used to create these micro-topographies have been developed for other industries and will not work as well on softer, natural materials. Topographical patterning of more biomimetic systems like gelatin, alginate and collagen is more difficult because they are generally too compliant.

Several fabrication methods, such as micro-contact printing, microfluidic patterning, wet etching, photolithography and hot embossing have been used to create micro-scale architecture, but these have been developed for the microfabrication of non-biological materials such as glass and metals, and are unsuitable for our purpose, as discussed in Chapter 1.

Collagen, the most abundant protein in the body, is a main component in the ECM. It is therefore important not only to be able to engineer collagen into 3D tissue-like constructs, but also to be able to quantify collagen density at the cell scale. Plastic compression can be modified to produce constructs with 3-dimensional surface

Chapter 5: Micro-Density Analysis of Compressed Collagen Constructs: Rapid Method Development

topographical features by micro-moulding [244]. This is carried out in a one-step process utilising templates with grooves or other structures, at the (tens to hundreds) micron scale, pressed into the collagen gels as they are undergoing compaction and uniaxial dehydration.

During the dehydration process, fluid from within the gel flows into the absorbent material. But when an impervious object (i.e. the micro-moulding template) is placed between the collagen surface and the absorbent material during PC, fluid dynamics is disturbed as the flow is deflected around the obstacle. The rapid fluid flow through the FLS compacts the collagen fibrils and at the same time aligns them in parallel to the direction of flow around the impermeable template, resulting in a change in collagen displacement within the scaffold [240]. This added complexity can be exploited to form stable structures in the FLS which show characteristic patterns of collagen density.

Surface embossing of PC constructs has been described previously [244]. Circular cross-section (50 μm diameter) glass fibres produced grooves 55 μm wide and 25 μm deep and rectangular cross-section Kapton plastic templates (50 μm wide and 75 μm deep) generated rectangular grooves of 48.4 μm width and 34.3 μm depth. The widths of the grooves matched up to the width of the glass fibres/Kapton template, but, with both template types, the depths of the grooves produced were only about half that of the template thickness. It was also shown that patterning of the opposite surface (non-FLS) during compression was not effective. We speculate that template shape is an important influence on fluid flow and thus on collagen

compaction. Importantly, compression of deeper rectangular Kapton template ridges (100 μm) did not produce deeper grooves in the collagen (unpublished data). One objective here was to understand why the embossing of soft collagen gels produces grooves of only limited depth fidelity, with different orientations and densities of collagen.

To understand better the mechanisms involved in plastic compression and micro-moulding, we decided to investigate the relative changes in collagen density within PC collagen scaffolds generated with micro-moulding variants. We hypothesised that digital image analysis of micrographs of stained collagen sections would be a simple way to quickly detect differences in collagen distribution in PC scaffolds in a semi-quantitative way. Determining the relative collagen distribution within compressed constructs would then give insight into fluid flow and the mechanisms involved in structure generation during micro-moulding.

Constructs prepared for histology were stained with Sirius red, imaged and analysed using ImageJ (Chapter 3). This novel method of analysis of local collagen density was validated using constructs fabricated with a linear collagen density gradient as previously established [246]. Following which we used this technique to reveal collagen density distributions in three other variants of PC scaffolds (flat/non-micro-moulded, embossed with rectangular grooves or embossed with round grooves) to gain insight into the dynamics of the compression process, to enable more predictable engineering of topography with PC.

5.2. Materials & Methods

Collagen constructs were compressed, prepared for histology, stained with Sirius red, imaged and analysed as described in Chapter 2.

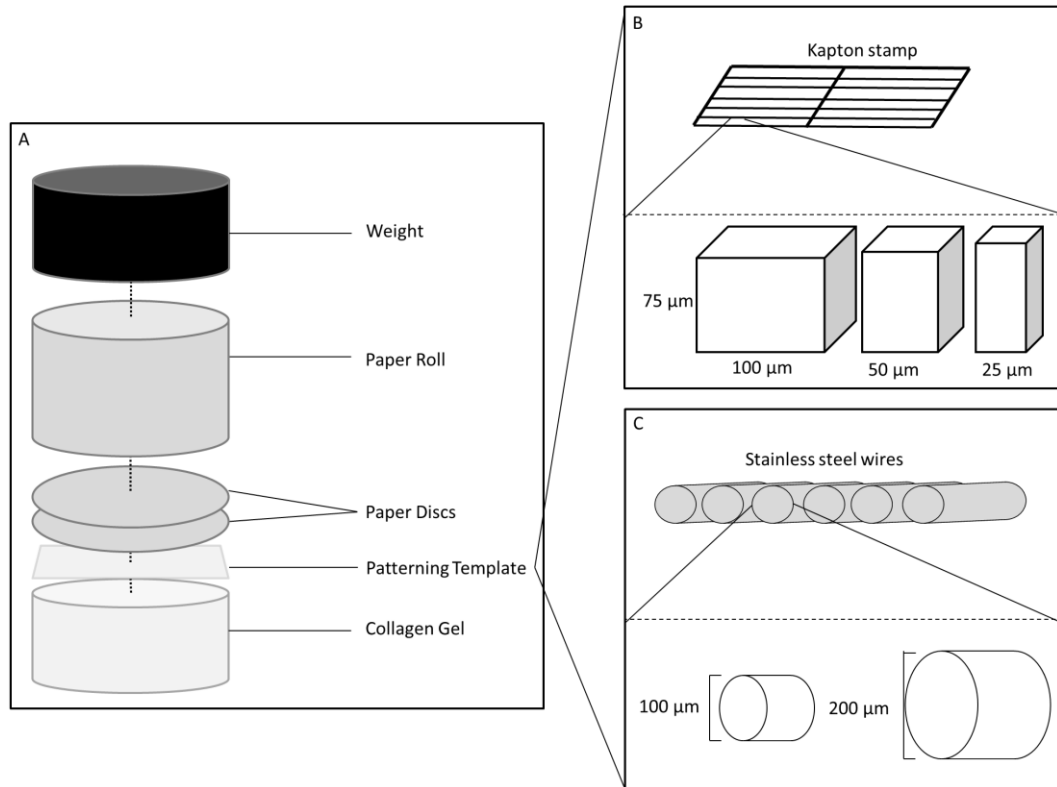


Figure 5.1: Schematic of the plastic compression set-up. Collagen gels were set in multi-well plates (12-well plates in this case). (A) Absorbent elements, consisting of two discs of Whatman I paper and a paper roll were placed on top of each gel, followed by a 43.8 g weight. Micro-moulding was carried out by placing the template on top of the collagen gels prior to compression. (B) & (C) Schematic of the templates used for micro-moulding of the collagen showing cross-sections and dimensions of the templates for generating rectangular (B) and circular (C) cross-section channels.

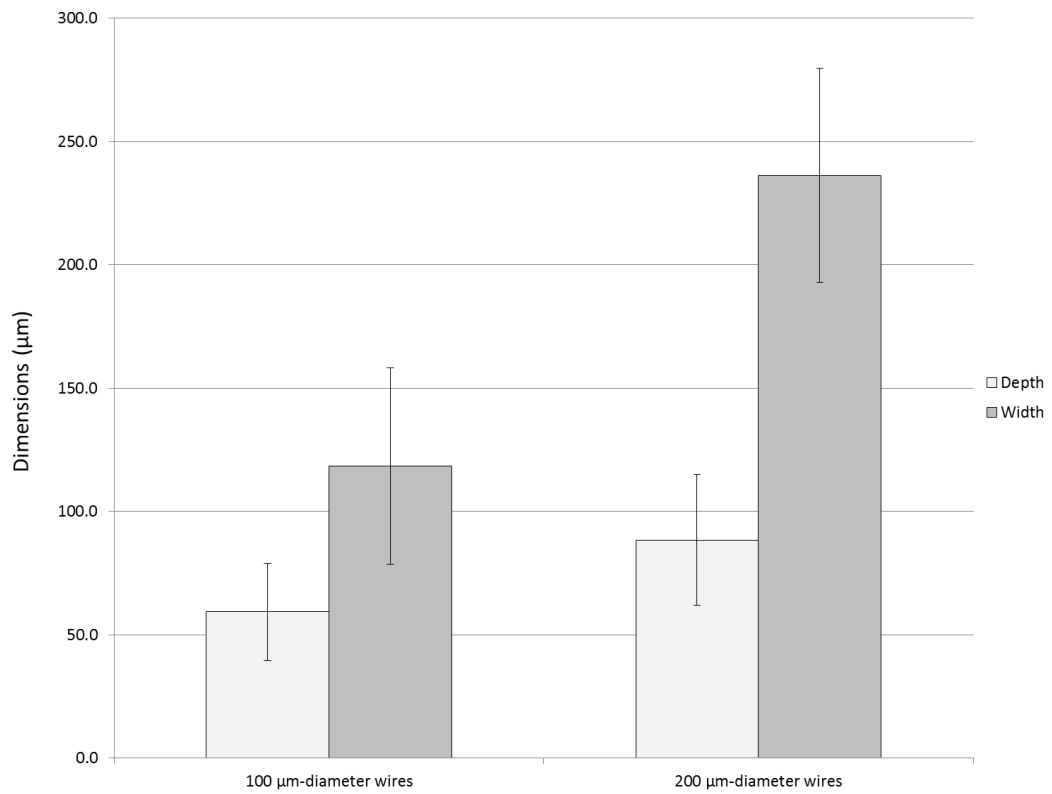


Figure 5.2: Measured dimensions of round grooves produced using 100 or 200 μm stainless steel wires. The measurements show that there was poor depth fidelity but good width fidelity in the fabricated grooves. Error bars depict the standard deviations of the mean (n=12).

5.3. Results

5.3.1. Groove depth infidelity

As outlined above, previous work on the fabrication of grooves in dense collagen constructs suggests that groove width-fidelity is good but depth-fidelity is imperfect. However the mechanism for this is unknown [244]. It is important to understand the mechanisms involved if we intend to develop a process to predictably engineer micro-topography on these dense collagen sheets for tissue engineering purposes. Firstly, the effect of using larger patterning templates (200 μm diameter wire) was investigated (previously, the largest used was 100x75 μm). Initially, 200 μm diameter wires were used on thin gels (1 ml). 6 wires of either 100 or 200 μm diameter were placed on the top surface of each collagen gel before the paper discs and plungers were added. It was expected that the wires would be pushed all the way through the construct - like cutting cheese with wire. This seemed likely since the wires were thicker than the thickness of the final compressed gel (<100 μm final construct thickness). Interestingly, the wires did not go right through the constructs, and instead created grooves on the surfaces of the constructs (Figure 5.3). To further investigate this groove formation using these bigger templates (100 & 200 μm), thicker (4 ml) constructs were used to study the full extent of groove generation more closely.

Previous findings showed that depth fidelity was poor when square-bottomed templates were used, but improved as the template width:thickness ratio increased

[320]. Micropatterning using 25 (width) x 75 (thickness) μm templates (width:thickness = 1:3) resulted in grooves with widths and depths of 22.9 and 22.1 μm respectively (92% and 29% fidelity). The depth fidelity was slightly improved to 33% (25.1 μm) when 50 x 75 μm templates (46.7 μm wide; 94% fidelity; width:thickness = 2:3) were used. And when 100 x 75 μm templates (96.6 μm wide; 97% fidelity; width:thickness = 4:3) were pushed into compressing gels, the resulting grooves were 34.3 μm deep, an increase in fidelity to 45%. Micropatterning compressed constructs in this manner creates grooves with good width fidelity but limited depth fidelity.

As the wires used here were round, thickness and width were the same (width:thickness = 1:1), so depth fidelity was expected to be close to 50%, though other factors are likely to affect groove width and depth fidelities. Figure 5.3 shows, with wires of 100 μm diameter, grooves of 118.3 ± 40 μm width and 59.3 ± 20 μm depth were generated. 200 μm -diameter wires created grooves of 236.3 ± 43 μm width and 88.4 ± 27 μm depth. This represents 118% of the expected maximum width for both wires, and 59% and 44% of total possible depth. The depth fidelity of grooves using the 100 μm -diameter wires was better than that of grooves made using the three different sizes of rectangular templates. 200 μm -diameter wires produced grooves which had better depth fidelity than rectangular-shaped grooves produced using 25 x 75 μm and 50 x 75 μm templates (29% and 33% respectively), and similar fidelity to the 100 x 75 μm template (45%).

5.3.2. Density analysis development

This discrepancy in groove depth and template thickness confirmed earlier findings suggesting that some aspect of fluid outflow was reducing the depth fidelity. The profile of the template used may contribute to the poor fidelity of groove depth since shape would alter the way the fluid flowed. To investigate the causes of this depth infidelity effect, it was necessary to develop a new, simplified system for semi-quantitative assessment of local collagen accumulation at the micro-scale (see Chapter 3). As described in the methods section, this involved the analysis of digital images obtained from sirius red stained histological sections of the embossed constructs (cross-sections of the groove profile).

Sirius red was used to stain sections as it preferentially binds to collagen fibrils in a concentration-dependent manner, making it better for this purpose than eosin. Coloured micrographs had to be split (red, green, blue) to minimise interference from other colour channels, and then converted to black and white to look purely at pixel intensities (ranging from 0 (black) – 255 (white)). The greater the amount of Sirius red bound, the brighter (whiter) the collagen appeared. So with digital image analyses, the intensity of the staining of the pixels can be correlated to collagen density. In this way, collagen densities across constructs could be assessed at a semi-quantitative level.

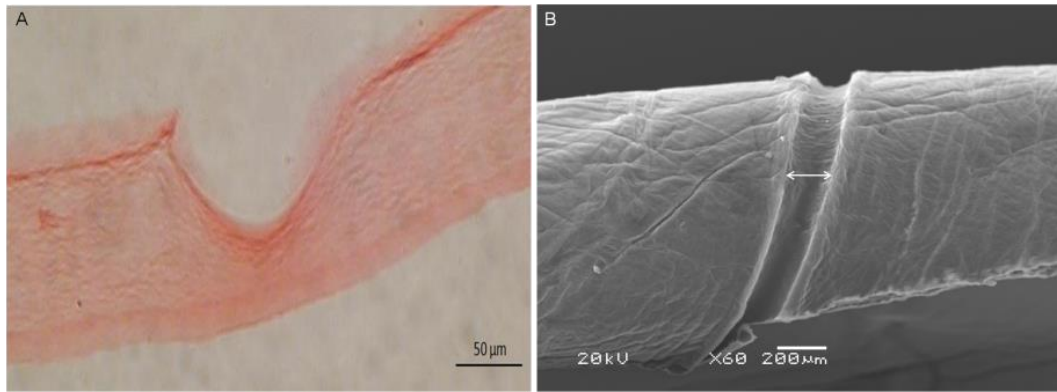


Figure 5.3: (A) Histological image of a construct micro-moulded with 100 μm stainless steel wires stained with eosin. (B): SEM micrograph of a collagen construct micro-moulded (arrowed) with stainless steel wires of 200 μm diameter.

5.3.3. *Micro-moulding - image analysis*

Micro-moulding collagen constructs generated grooves with poor depth fidelity. One possible factor affecting this is, as mentioned earlier, is the template width:thickness ratio, and another is template shape. The shape of the template is likely to play a role as it determines how fluid flows around the template (due to the template being impermeable). The templates would block the regular upward fluid flow and redirect fluid around them, which would bring about changes to collagen movement and fibril deposition during the early phases of compression when fibrils are significantly relocated and remodelled by fluid flow. With the circular wires being more hydrodynamic than the flat, square-based kapton template, it is likely that the latter would generate more resistance against the upward fluid motion and hence be pushed upwards and out of the gel to a greater extent than the wires, thus affecting depth fidelity.

Compressed constructs micro-moulded with grooves of either round or rectangular bases were fabricated and prepared for histology and stained with sirius red. Cross-sections of grooves were used for the analysis. Digital images were taken and analysed using ImageJ. Images were converted to greyscale to look purely at pixel intensities in terms of grey value (grey value; minimum: 0, maximum: 255 – since images were converted to black & white).

This was then used to measure the local differences in collagen density profiles associated with micro-moulding using different template shapes for clues to fluid movement during compression with impermeable templates. Figure 5.4 is comprised of representative images and scans of unpatterned constructs and constructs patterned with either round or rectangular grooves. Figure 5.5A shows that the unpatterned constructs showed no significant differences in collagen density from one region of interest (ROI) to another, as expected, since fluid outflow would have been uniform. Micro-moulded constructs on the other hand, had distinctive local collagen density profiles. Compressed constructs with round profiles, showed a single peak in collagen density at the base of the groove with a maximum of 108 a.u.. The densities on either side of this peak gradually decreased to around 95 a.u. toward the baseline unpatterned areas of the scaffold (Figure 5.4B). Constructs with rectangular cross-section grooves showed two peaks of high density collagen located at the two internal corners of each groove. The increase in density at the corners (148 and 150 a.u.) was greater than at the bottom of the groove (137 a.u.; Figure 5.4C) which was also higher than the baseline unpatterned

regions. This clearly shows a difference in collagen distribution within constructs at the sites of structure formation when using templates of different shapes.

To help compare these differences, the mean percentage increase in density from the baseline was calculated (Figure 5.5). The baseline was taken as the average density of the unpatterned regions on either side of a groove, from each external corner to at least 50 μm away from the groove. For rectangular grooves, there was a $16.0\pm 3.5\%$ mean increase in density at the internal corners ($15.2\pm 4\%$ at the first internal corner, and $16.9\pm 3\%$ at the second). The increase at the base of square grooves was $7.7\pm 3\%$. For round grooves, the increase in density at the base of the groove was $21.4\pm 4\%$. These were all statistically significantly different to the baseline density ($p < 0.05$).

It can be seen why then the thick wires did not cut right through the thin collagen gel during compression. As the process progressed, the area under the wire became increasingly dense and increasingly more difficult for the wire to be pushed all the way through the gel.

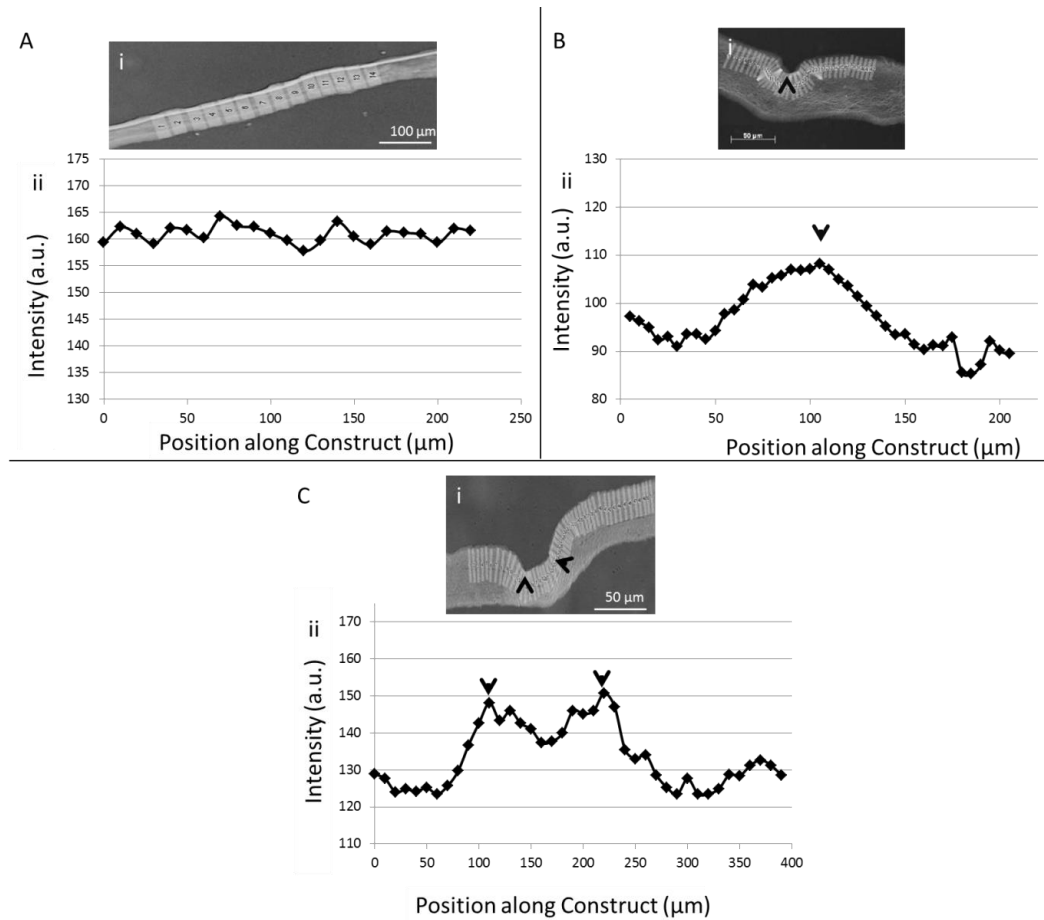


Figure 5.4: Collagen displacement analysis of an unpatterned (flat, non-micro-moulded) construct (A), a construct patterned with glass fibres (B) and a construct patterned with a Kapton template (C), showing the differences in collagen distribution in the patterned constructs. i: An image converted to greyscale with regions of interest (ROI) (grey rectangular boxes). ii: each point on the graph represents the mean pixel intensity of a ROI.

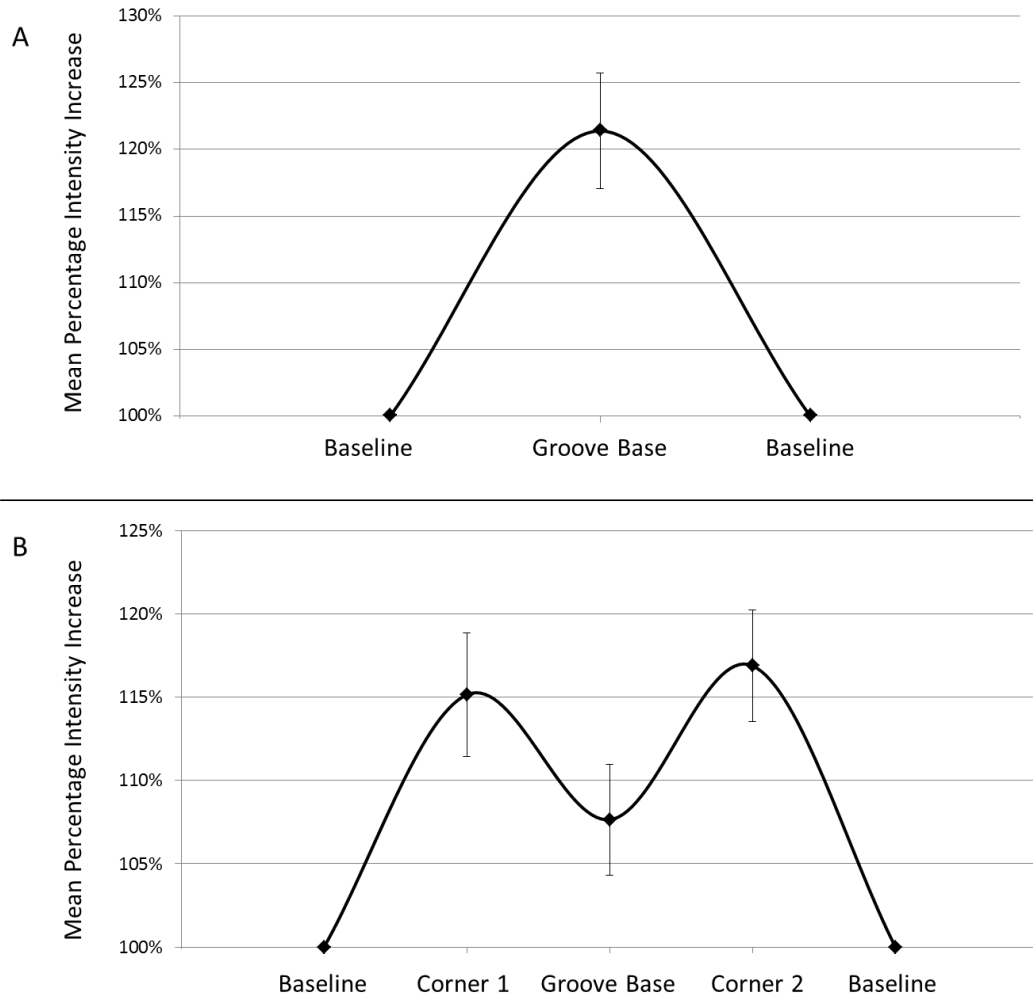


Figure 5.5: Graphs of the mean percentage increase in intensity of grooved regions, clearly showing different density distributions in differently shaped grooves. (A): The mean percentage intensity increase plot for round grooves (N=7). (B): The mean percentage intensity increase plot for rectangular grooves (N=8). Groove base compared to the baseline, corners compared to the baseline, and corners compared to the groove base. Error bars represent the standard deviation to the mean ($p < 0.05$; $n = 12$).

5.3.4. Full thickness transverse density analysis

Plastically compressed collagen constructs were produced and processed for histology and Sirius red staining. Cross-sections were imaged and analysed using ImageJ to study the distribution of collagen within constructs in the z-plane (bottom to top surfaces). The purpose of this was to look for clues on fluid movement and escape during compression. Figure 5.6 shows the analyses of light micro-graphs across the full transverse thickness of the compressed collagen layers stained with Sirius red. These graphical representations of pixel intensities assessed the relative collagen density distribution within constructs for each treatment. The presence of the FLS with its sharp peak of very high intensity can be seen in each construct. For unpatterned constructs, Figure 5.6A shows the FLS as a clear, sharp peak which was more than twice the pixel intensity than that of the rest of the construct. For round grooves, a similar collagen density distribution was seen in the unpatterned regions of the constructs, and to a lesser extent, within the grooves themselves. Figure 5.6B shows that similar to unpatterned constructs, round grooves showed a peak in pixel intensity at the top surface of the construct and then decreases towards the bottom surface. This indicates an accumulation of collagen at the base of the groove.

To quantify this, using the plot profiles, a ratio of the pixel intensity at the first peak from the top of the construct to the pixel intensity at the last peak was calculated. The top/bottom ratio for unpatterned and round grooves were 1.19 ± 0.052 and 1.35 ± 0.284 respectively (Figure 5.9), indicating that the top surfaces (with its

Chapter 5: Micro-Density Analysis of Compressed Collagen Constructs: Rapid Method Development

distinct FLS) had a greater density of collagen than the bottom surfaces. That is, the FLS was dominant on the top surface of these constructs (ratio >1 =FLS at top surface; <1 =FLS at bottom surface). Surprisingly, for rectangular grooves, the top/bottom ratio was much lower at 0.847 ± 0.084 , although the overall density was comparable with other treatments. This shows that a prominent FLS was being formed at the bottom surface of the construct with rectangular templates, which suggests that significant fluid flow within the gel had been displaced in the opposite direction, downwards by the template instead of the more normal flow upwards, and out of these respective surfaces.

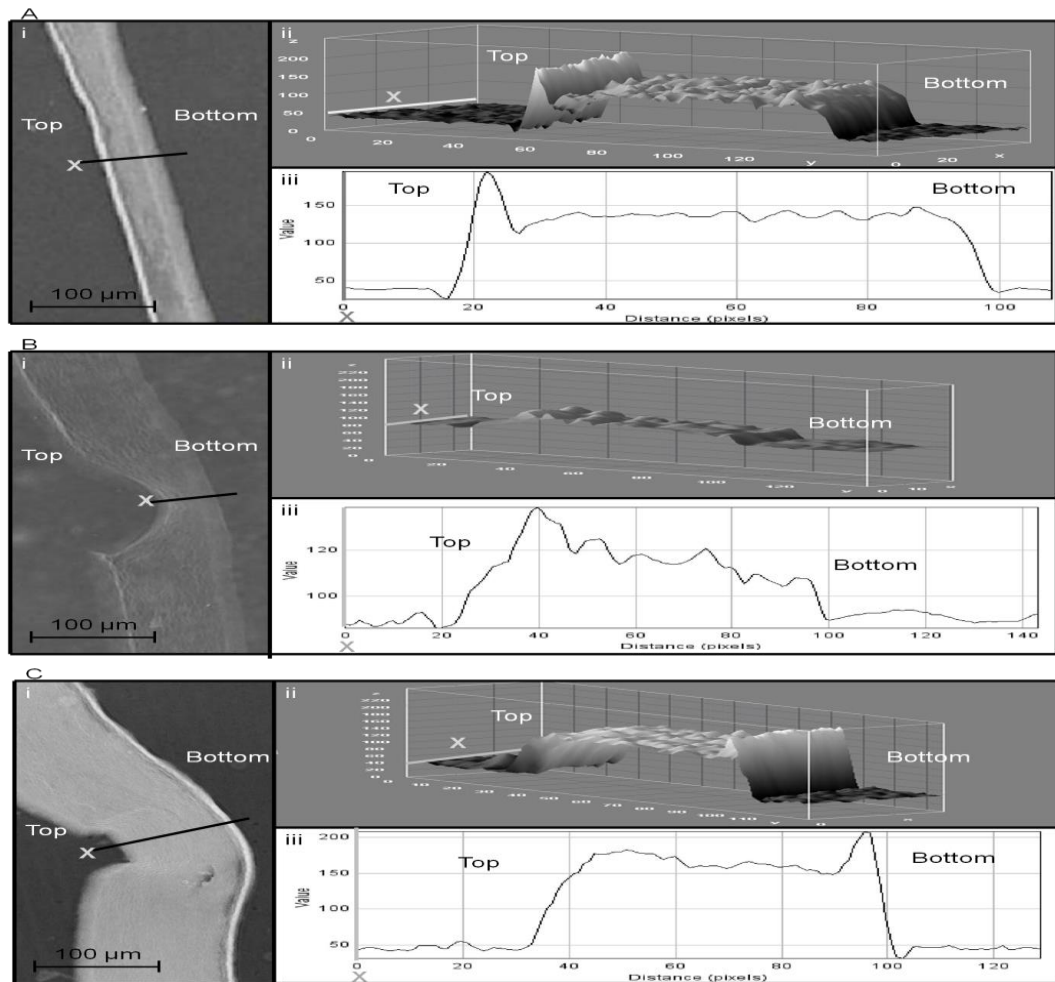


Figure 5.6: Image analysis of an unpatterned PC scaffold (A), one that is patterned with round grooves (B), and one with rectangular grooves (C). (i): Images converted to greyscale with a region of interest selected (red line). (ii): 3-dimensional plot of the region of interest. (iii): Profile plot of the region of interest. The “x” and grey lines in (ii) and (iii) correspond to the “x” and lines in (i).

The round groove constructs showed the most pronounced downward fall in density of the 3 treatments (Figures 5.5 & 5.6B iii) and this was reflected in the highest top to bottom ratio (Figure 5.7). If correct, this would suggest the least (or latest) tendency to form a second, basal FLS. This represents an interesting and potentially informative trend, though the difference between which it was different from rectangular grooves in this case did not reach conventional statistical significance (Figure 5.7).

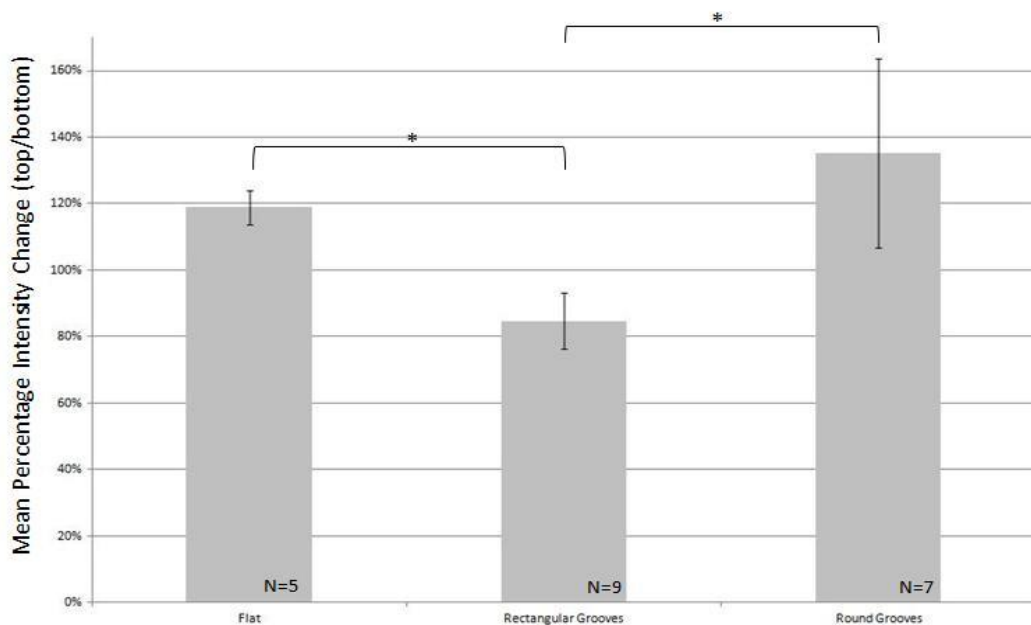


Figure 5.7: Graph showing the ratios of the pixel intensities at the top surface / bottom surface of unpatterned, rectangular-grooved and round-grooved constructs. This indicates that with flat constructs and within round grooves, there were single FLS's at the top surfaces of the constructs, whereas with rectangular grooves, there were secondary FLS's at the bottom surfaces which were denser than the primary FLS's. Error bars shown indicate standard deviations ($p < 0.05$).

5.4. Discussion

Collagen is the most abundant protein throughout the vertebrate body, and has important roles in structural stability and in influencing cell behaviour [359,361,362,365-367]. Therefore, it is critical to have effective methods for the rapid quantification of its density at the cell scale in tissues. This perhaps is even truer for engineered tissues where collagen is the 'engineered' material. It is clearly essential to be able to monitor local matrix density as these will influence tissue-cell behaviour. Here, we have described a quick and simple method using sirius red staining and image analysis to detect and quantify collagen density in PC constructs. Additionally, by using this technique, we were able to quantify the collagen distribution profiles of micro-moulded constructs to gain insight into the mechanisms and dynamics of fluid flow during the compression process.

Controlling material stiffness and engineering topography in PC collagen constructs have both been previously investigated by this group [244,246,279]. Such collagen micro-moulding is currently the only, or one of the only feasible approaches to generate predictable cell-scale topography in soft native (collagen) materials without harming resident cells. Clearly then, these mechanisms of fluid flow and collagen fibril accumulation within a collagen construct during PC need to be well understood if we are to be able to predictably mould topographical features and cell-scale density changes. However, the detailed mechanisms controlling how such topography is formed are presently unclear.

Chapter 5: Micro-Density Analysis of Compressed Collagen Constructs: Rapid Method Development

Using the novel analysis method described in this study, we have been able to measure changes in collagen micro-density which suggest mechanisms behind micro-structure formation. The collagen density profiles of micro-moulded constructs obtained may be explained, at least in part, by the obstruction to fluid flow by the template and the bifurcation of fluid flow it will produce during the compression process (Figure 5.8). During PC, fluid flows from the bottom of the gel upwards and out into the absorbent plunger. Some of this flow must divert to pass around the non-permeable template. Collagen fibrils would be deposited at these points of bifurcation, especially at the early, low density stages of compression, leading to accumulations of collagen at these points.

One hypothesis for the poor depth fidelity reported here is the generation of a secondary FLS beneath the template and the force of upward fluid flow during the compression process pushed the template up and out of the compressing gel (Figure 5.10). Initially, the pattern template was pushed fully into the collagen gel. But because the template was impermeable, fluid was unable to exit the gel at those points in contact with the template. The three different templates used (50 x 75 μm , 100 μm -diameter wires and 200 μm -diameter wires) covered 17.2, 7.0 and 14.1% of the construct surface respectively (Table 5.1). This represents a reduced area of contact between gel and absorbent, limiting fluid outflow. Collagen fibrils at the main FLS become increasingly compact as PC proceeds, until fluid escape through that surface (FLS) is restricted. With the main discharge route blocked, pressure within the compacting gel builds up due to the continual compressive force. This build-up of internal pressure then forces fluid out of the gel via other

Chapter 5: Micro-Density Analysis of Compressed Collagen Constructs: Rapid Method Development

routes, creating the secondary FLS collagen densities we located in this study. The fluid forced out of these other surfaces (i.e. under the impervious template) may cause the template to be lifted up and out of the gel by a few tens of micrometres, allowing fluid to escape and so forming another leaving surface in the process (Figure 5.9). This additional FLS would correspond to fluid flow around the stamp, and incidentally would lead to a shallower groove than expected. De facto (but paradoxically) this makes the collagen layer oddly strong in compression – i.e. it does not cut through.

Table 5.1: Area of pattern template in contact with collagen construct.

Template	Surface Area (mm ²)	Percentage of Construct Surface (%)
Kapton 50	34.5	17.2
100 µm-diameter wires	14.1	7.0
200 µm-diameter wires	28.3	14.1

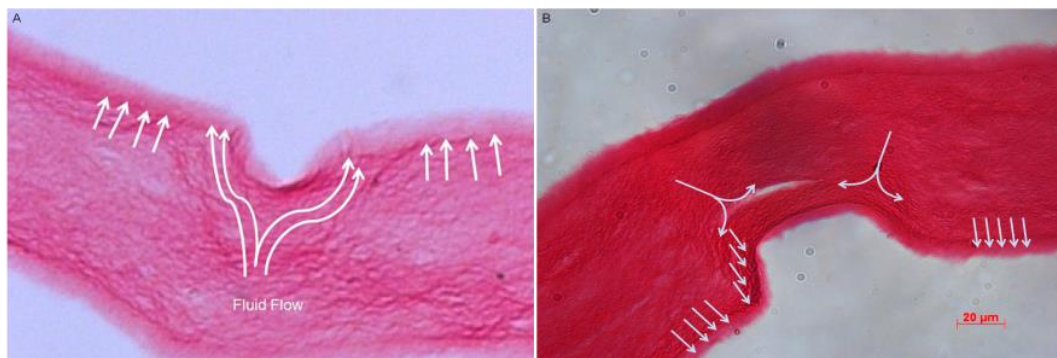


Figure 5.8: Collagen constructs stained with sirius red. (A) shows a construct patterned with round grooves, while (B) shows a construct embossed with a rectangular groove. Arrows indicate direction of hypothetical fluid flow.

Another theory for explaining limited groove depth-fidelity involves the re-swelling of compressed collagen constructs. It is already known that the plastic deformation which characterises routine collagen compression eventually becomes elastic at high collagen densities (Figure 5.10) [355,382]. Compressed constructs are very dehydrated, and may undergo partial and local reswelling-rehydration after the compressive load is removed. This reswelling is thought to be small and localised. It is likely that the regions beneath grooves ("E" in Figure 5.10) become hyper-compacted during compression and so are liable to elastic recoil and reswelling compared to the unpatterned regions of the construct surface. As such, any reswelling of these hypercompacted regions would result in a reduction in the groove depth as measured here. Clearly, any contribution from this effect would come right at the end of the compression process. These potential mechanisms for differential collagen distributions and limited depth fidelity operate individually, or may occur in sequence corresponding with the dynamic of the PC process. Bifurcation of fluid flow may explain the events that occur early, at the initial stages of the compaction process, until the main FLS becomes very dense. At this, late to middle stage of compression, formation of localised secondary FLS's would be more likely, preventing the template from sitting at the base of the groove. At the very last stages, where very dense collagen accumulations were produced at the groove base and the compression load is removed, the last effect, that of elastic recoil and local reswelling may occur.

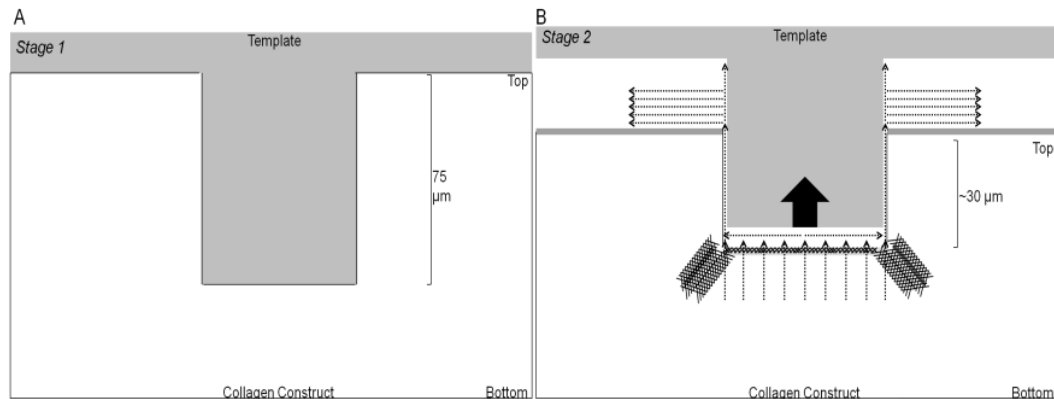



Figure 5.9: Schematic of secondary FLS formation and fluid expulsion from under the template. (A) Stage 1 – Template is pushed fully into the collagen gel. (B) Stage 2 – As the compression process proceeds, pressure lifts the template out of the groove and forms a new FLS at its rising base.  : Dense collagen.

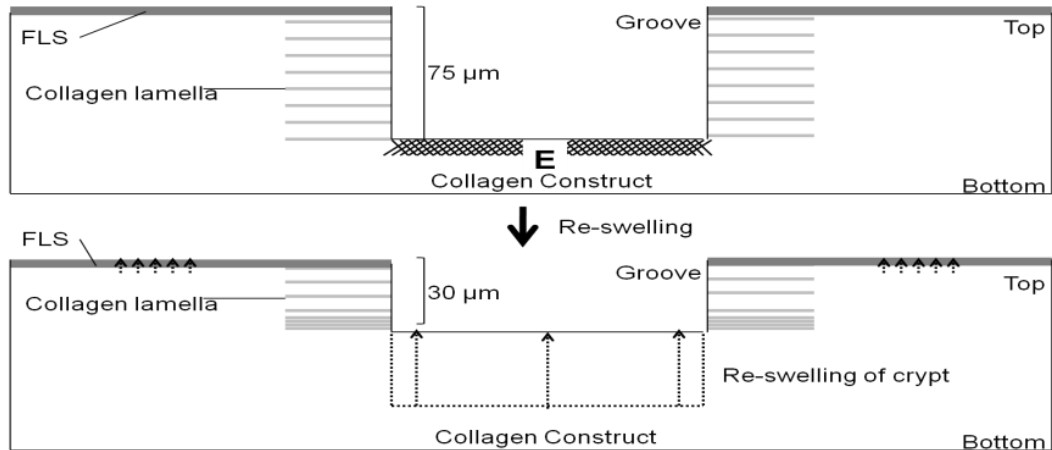


Figure 5.10: A schematic diagram of a region of a PC construct embossed with a rectangular groove. This illustrates the uneven re-swelling explanation for shallow (compared to maximum template thickness) grooves. E - zone of over-compressed collagen, i.e. compacted beyond its plastic properties, so becoming elastically compressed.

5.5. Conclusions

These studies have successfully developed a new rapid technique for measurement of changes in local (micrometer-scale) collagen fibril density. This technique has been used to plot out the spatial record of collagen accumulation, providing clues as to the mechanism by which high density (stiffer) regions of matrix are formed. In turn, it is probable, based on previous work [36,45], that these local stiff regions will significantly influence cell behaviour, providing both fine-tuning of engineered tissues and insight into natural cell mechanics. The study of local density changes also helps to explain why groove depth by micro-moulding has only limited fidelity. In turn, this is important in making predictable processes for generating soft tissue - collagen micro-topography. This is important, as plastic compression micro-moulding developed using this approach remains the only method for generating predictable soft tissue micro-topographic features, without cell-lethal conditions such as chemical cross-linking [244,267,383-388].

Chapter 6: Understanding Local Tissue Fate of Nanoparticles: The Insufficiency of *Non-2D* Cell Culture

6.1. Introduction

Almost all stromal tissue cells in the body are embedded within the local tissue and enveloped by its extracellular matrix materials, with the exceptions of surface (epithelial/endothelial) cells and cell-rich tissues like nerves and muscle. Epithelial and endothelial cells grow as a thin layer on top (epithelia) or below/inside (endothelia) tissues, forming barriers between tissues or external fluids (e.g. blood, air). These interfacial cells grow *on* extracellular matrix rather than *in* it, attaching to their substrate largely by their basal surface, with their apical surface exposed to the external environment. Cell-rich tissues contain dense cell masses (versus thin cell sheets) with predominantly cell-cell contacts and little extracellular matrix.

Most other cell types live in a relatively homogenous environment within the stroma and are surrounded by extracellular matrix proteins, unlike the polarised epithelial cells with very different apical and basal environments. This makes cell-matrix and cell-cell attachment an inevitable occurrence in the X, Y and Z planes – that is, in 3 dimensions (3D). It has been known for some time now that these 3D interactions are both unavoidable and critical cues for cell behaviour, governing how cells respond to test drug agents, particles and proteins.

Chapter 6: Understanding Local Tissue Fate of Nanoparticles: The Insufficiency of Non-2D Cell Culture

However, current standard culture systems assess cell responses based on monolayer cultures, also called "2D", though this is itself a misnomer [170]. Cells in monolayer attach on one side to ultra-stiff impermeable plastic and are covered on the other by a large excess of dilute nutrient solution [397]. Clearly the complexity of native tissue-structure is replaced by a spatially polarised, un-physiologically stiff substrate, no surrounding matrix, and with almost none of the normal nutrient and gas gradients which characterise real tissue signalling.

In effect 2D-monolayer cultures mimic few, if any, tissues we normally aim to model. Although they have provided us with valuable metabolic information, they do not predict more complex animal or human tissue responses particularly those with any spatial context. This is evident in drug discovery where therapeutic agents and nanoparticles which initially seem useful in 2D models, ultimately fail in animal and patient tests [104]. This high attrition rate is mainly due to lack of efficacy as well as toxicity in the later stages of testing [116,403,404]. These were perhaps not detected earlier because monolayer cultures provide excessively stark patterns of mechanical, spatial and gradient cues which native cells rarely or never encounter [170]. The later that a therapeutic candidate fails, the higher the costs since the costs for testing rise significantly with each stage of assessment. There is pressure, then, for 'more physiological' culture systems which are predictive, interpretable and accurate. But it is first necessary to analyse what 'more physiological' and '3D' mean, to avoid the low target of being merely '*not 2D*'.

Chapter 6: Understanding Local Tissue Fate of Nanoparticles: The Insufficiency of Non-2D Cell Culture

This is a topical issue, studied by a number of groups, and involves testing nanoparticle behaviour, in putative model systems based on hydrogels (collagen, alginate, PEG), sponges (collagen, hydroxyapatite, cellulose, silk fibroin, PLGA), cellular spheroids/aggregates (rotating wall bioreactors, hanging drop and micro-carrier systems) [69,146-150,152,153,156,159,160,162,200]. Whilst these models move from 2D towards some forms of 3D culture, they do not necessarily or automatically reproduce appropriate cell-relevant cues in their native tissue. Pseudo-3D cultures are produced by seeding (micron scale) cells onto some forms of macroporous, 3D scaffold since the scale difference only allows cell attachment to the pore-wall surfaces, like slightly curved monolayers [172]. The various forms of 3D cell-mass cultures (eg. hanging drop, spheroids, aggregates) can claim to mimic the enforced cell-cell contact and diffusion gradients of cell-rich tissues (eg. liver, muscle), but completely misrepresent matrix-rich, connective tissues. Rather we need to model those key elements of the spatial environment which characterise the tissue under test.

Specifically, to model nanoparticle delivery/fate in connective tissues, key test parameters might be movement through the model matrix, access to and uptake by cells and the influence of matrix remodelling. Cells in the body continually degrade/replace the matrix. This affects symmetry, diffusion gradients, and particle access/uptake by cells (not just from upper medium surface). Cells in tissues receive *directional* cues from diffusion gradients, including drug/protein cargos from the test nanoparticles. Key features of a model, then, are density, composition, asymmetry of the cell-support scaffold as this will affect the mobility of

Chapter 6: Understanding Local Tissue Fate of Nanoparticles: The Insufficiency of Non-2D Cell Culture

particles/molecules. The objective is then to design 3D tissue-like models providing key information for accurate translation.

The aim of this study was to develop a 3D tissue-like model specifically to predict the fate and cell-interaction of hyaluronan nanoparticles, and compare the answer to that produced using 2D monolayer cultures. Hyaluronan nanoparticles were chosen as they have the potential to be tumour cell-targetting, since it is known that cancer cells upregulate the receptor for hyaluronan, CD44 or RHAMM (receptor for hyaluronic acid-mediated mobility) [413,414]. We used cell-seeded, laminated compressed collagen as a 3D dermis model of composition, density and organisation. Since type I collagen is the predominant fibrous material in most connective tissues, the appropriate tissue cells are able to attach to and remodel its fabric. The plastic compression gives tissue-like density and anisotropy, imitating the constraints on molecular and nanoparticle mobility predicted in the target tissue. Intimate enmeshing of test cells in this tissue-density collagen around the HA-NPs exposes all 3 elements to appropriate mechanical conditions and perfusion gradients, tailored to those of the target tissue.

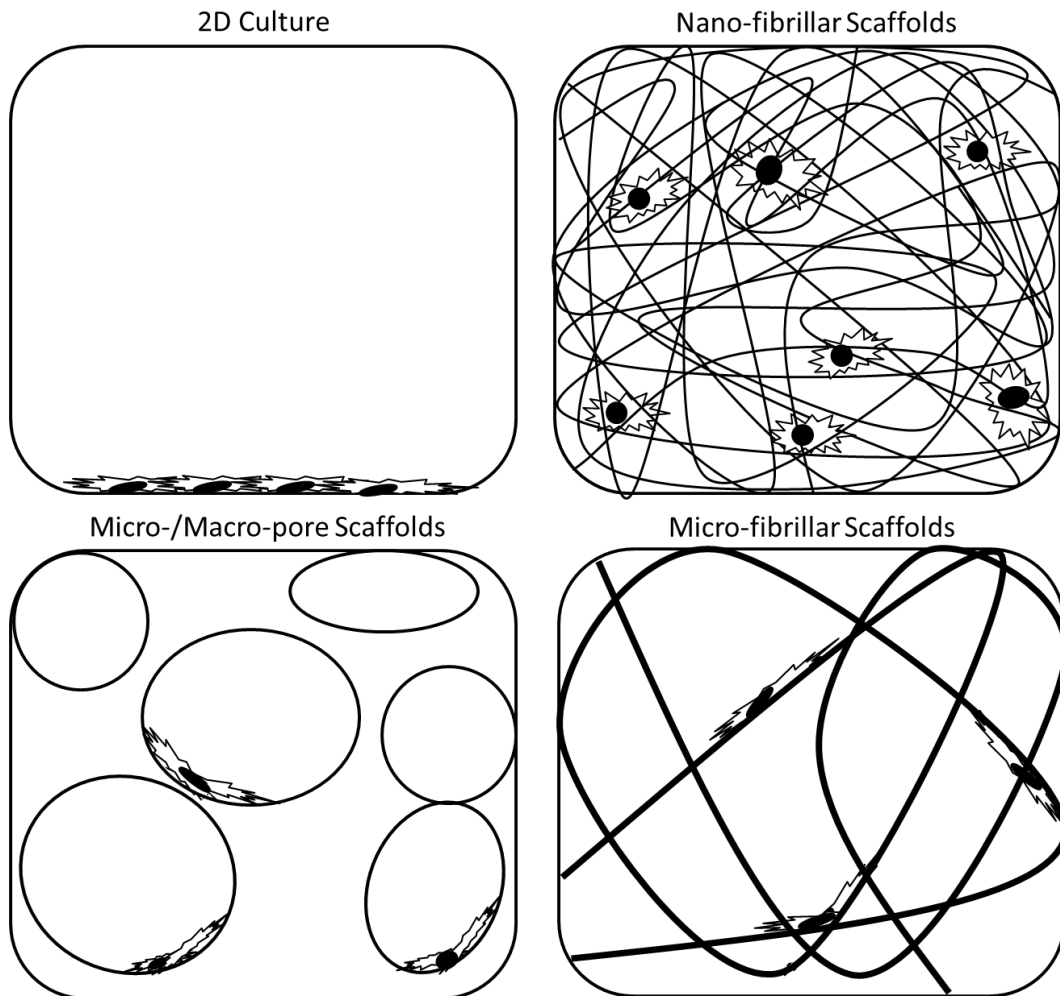


Figure 6.1: Schematic depicting the arrangements of cells in/on different substrates. Cells cultured as a monolayer on standard tissue culture plastic take up a flat polarised morphology. Micro-porous and micro-fibrillar scaffolds initially appear to give cells a 3D environment in which to grow in. However, the large scale of the pores and fibres relative to cell dimensions creates a pseudo-3D environment where cells are within a 3D structure but are still flat or curved slightly, as in monolayer cultures. On the other hand, fibrils in the nano-scale enmesh cells in the scaffold, suspending them in 3D and providing attachment sites all around.

6.2. Materials & Methods

Compressed collagen constructs were prepared as described in Chapter 2. 0.5 ml constructs set in 24-well plates were used in this chapter.

6.2.1. Multilayering

0.5, 1.0, 1.5 or 2.0 ml neutralised collagen (with/without HDFs; 10^5 cells/ml) was added on top of set collagen gels and allowed to set for 30 min at 37°C, before compression.

6.2.2. Preparation of chitosan-Nile Red nanoparticles

Chitosan nanoparticles were tested in this system as they are biomaterial-based and have the potential for delivering a variety of drugs. Also, they are of a different size range to the HA-NP so that a comparison of particle retention following PC could be made. Nile red-loaded quaternary ammonium palmitoyl glycol chitosan (GCPQ-NR) nanoparticles (62.1 nm diameter) were prepared as described by Uchegbu et al., [405]. Lyophilised GCPQ was prepared and provided by Ramesh Soundararajan (School of Pharmacy, UCL). 20 mg/ml GCPQ and 1 mg/ml Nile red (Sigma, UK) were resuspended and mixed gently in dH₂O at a 20:1 ratio to reduce foaming. Once the suspension was well-mixed, it was probe sonicated for 3x5 min on ice, with 3 min intervals in between pulses (Amplitude: 15 μ m), using a Soniprep 150 (MSE, UK). These were then sized using a Malvern Zeta Sizer 2000 (Figure 6.2).

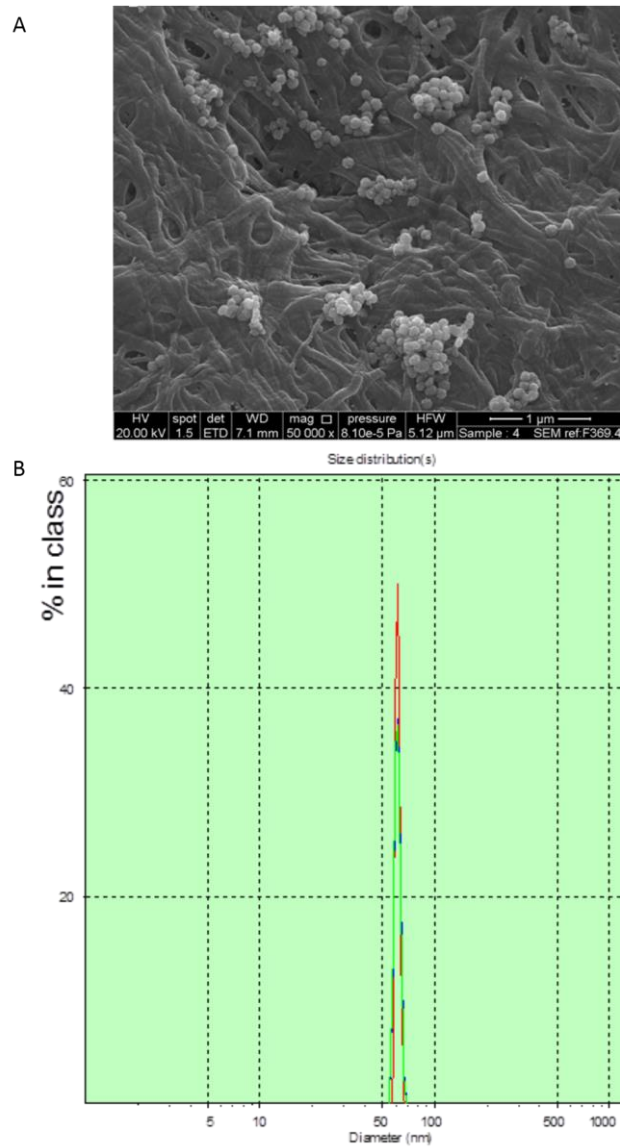


Figure 6.2: (A) SEM image of GCPQ-NR nanoparticles embedded within a compressed collagen construct. The nanoparticles were present in clusters, which may explain their higher than expected entrapment rate. (B) DLS measurement results showing the average size of the GCPQ-NR nanoparticles to be 62.4 nm.

6.2.3. Riboflavin crosslinking

Collagen hydrogels were crosslinked using topically applied riboflavin (Sigma-Aldrich, UK) with the goal of increasing fibril mesh density at the top surface to improve nanoparticle trapping. Whatman I blotting paper (Whatman) was soaked in 0.25 mM riboflavin solution. This was then placed on the top surface of collagen gels for 5 min. Photoactivation of the applied riboflavin to crosslink the collagen was done using a 455 nm light source (power: 80 mW/cm²) from a 10 cm distance for 10 min [331]. This was done on single 0.5 ml layers as well as on double layer constructs with 2.0 ml upper layer.

6.2.4. Determination of free FITC

0.5 ml HA-NP resuspended in PBS at a concentration of 20 ng/ml was placed in dialysis tubing (12-14000 Da MWCO) and dialysed into 4 ml PBS. After 2 H, the fluorescence of the dialysate was measured using a fluorometer (LS 50B, PerkinElmer, UK) and compared to the fluorescence intensity of the suspension before dialysis.

6.2.5. Measurement of cellular uptake of HA-NP

Cellular scaffolds were digested as above, centrifuged for 5 min at 700 g and supernatants removed and replaced with PBS. Pellets were shaken to wash and re-

Chapter 6: Understanding Local Tissue Fate of Nanoparticles: The Insufficiency of Non-2D Cell Culture

centrifuged for 3 times PBS washing steps, to remove free nanoparticles. After the final wash, samples were made up to 4 ml with PBS for fluorometric measurements.

6.2.6. 2D cell culture and measurement of cellular uptake of HA-NP

10^5 HDF/ml in 0.5 ml DMEM (above) and 19 $\mu\text{g}/\text{ml}$ of HA-NP were seeded into wells of a 24-well plate. This HA-NP concentration was worked out to be the same concentration as that present in the collagen scaffolds after compression. For fluorescence microscopy, cells were seeded onto 19 mm glass coverslips placed in a 12-well plate.

At set time points, DMEM from the wells were removed and the wells were washed with PBS twice, before trypsinising the cells. The detached cells were then transferred to 7 ml bijou tubes and made up to 4 ml with PBS, before fluorescence measurements, as above.

6.2.7. Histology and fluorescence microscopy

Histology samples: As per Chapter 2.

2D culture samples: Cells on coverslips were stained with Hoechst 33342 (Gibco, UK) and phalloidin (Gibco, UK) as described in Chapter 2. Coverslips were then mounted onto glass slides for imaging using an Olympus BX61 microscope.

Chapter 6: Understanding Local Tissue Fate of Nanoparticles: The Insufficiency of Non-2D Cell Culture

3D culture samples: Cells were retrieved from collagen constructs through enzymatic digestion using collagenase I. The digested mixture was centrifuged and the supernatant removed. The remaining cell pellet was then resuspended in culture media and plated out on 19 mm coverslips in 12-well plates. Cells were left to attach overnight before staining and imaging as above.

6.3. Results

6.3.1. Plastic compression, and the mobility of HA-NP

Plastic compression of collagen hydrogels resulted in the generation of dense sheets of collagen, tens of micrometers in thickness (thickness varied depending on the initial volume of collagen used). The mobility of HA-NP was investigated at this initial compression stage. In the initial stages of PC, when fluid content was high, the nanoparticles appeared highly mobile with the water flow within the compressing gel. Nanoparticle mobility reduced as the collagen fibril density increased, during the later stage of PC, and is evidenced by the retention of substantial fluorescence in the collagen at completion of compression (Figures 6.3 & 6.4). The pattern of fluorescence in histological sections of compressed collagen shows the distribution of FITC-nanoparticles. In low volume constructs (≤ 1.0 ml initial volume), a bright band of fluorescence was present at the top (fluid leaving) surface (red arrowheads), with a decreasing gradient of intensity towards the bottom of the scaffold, indicating that particles moved with the upward-flowing fluid and were trapped at the collagen-dense FLS. This simple gradient of fluorescence intensity was less clear when either more volume was used, or when cells were included in the system, due to cells obstructing the fluid flow during compression. This obstruction of HA-NP flow resulted in greater retention of particles (Figure 6.4). Figure 6.4 shows the relative fluorescence retained at various points in culture.

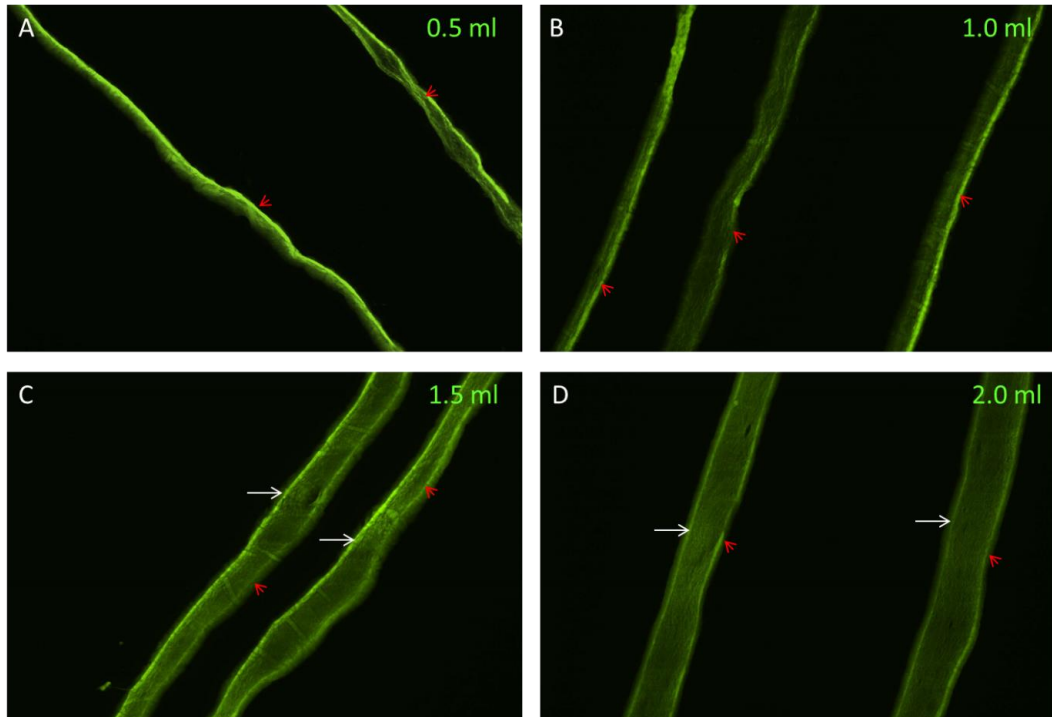


Figure 6.3: Fluorescence micrographs of cross-sections of compressed nanoparticle-loaded constructs of different initial volumes. Red arrowheads point to the main FLS. White arrows point to secondary FLS. These images show the effect of initial gel volume and the generation of a secondary FLS. Only one FLS is seen in the lower volume gels (0.5, 1.0 ml) (A & B). Secondary FLS's (white arrows) were only seen in the thicker constructs (C & D).

6.3.2. Hyaluronan nanoparticle release from compressed constructs

Diffusion of the hyaluronan (or hyaluronic acid) nanoparticles from compressed collagen constructs was investigated by culturing HA-NP-loaded constructs for up to 3 weeks. Collagen constructs were loaded with FITC-containing hyaluronan nanoparticles which were either acellular or seeded with fibroblasts, to study HA-NP release through diffusion and cell-assisted release.

Figure 6.4 shows the analysis of particle release from the constructs over incubation time with/without cells. After 24 hours incubation of the 3D model tissue without cells there was an initial release of nanoparticles of around 50%, with a decrease in fluorescence from 36.2 ± 1.6 to 14.5 ± 4.9 arbitrary units (a.u.) for acellular and 55.3 ± 3.8 to 27.9 ± 1.5 a.u. for cellular constructs. As shown in Chapter 4, there was a re-swelling of 0.5 ml constructs by $26.0 \mu\text{m}$, which is a 65% increase in construct thickness. Consequently, the compacted collagen fibrillar meshwork must have relaxed and opened up as the construct re-swelled, thus allowing some particles to escape through the enlarged gaps. After this initial release acellular construct fluorescence did not significantly change from day 1 to day 21 (gradient of 1.22). However, cellular constructs produced a comparable burst release at day 1 but then showed a gradual decrease in fluorescence intensity over the 21 days (gradient of 3.21). Histology images showed the morphology and fluorescence of constructs immediately after compression up to 21 days of culture (Figure 6.4B). From this it was clear that, over the time course, cells remodelled the collagen structure, to open up the 3D architecture of the collagen, and this was likely to explain the

Chapter 6: Understanding Local Tissue Fate of Nanoparticles: The Insufficiency of Non-2D Cell Culture

release of trapped nanoparticles (see also Figure 6.5). This supports the idea that release of HA-NP from the constructs is directly dependent on cell-based remodelling of the collagen. Hence, the NP release from this native protein model is dependent on local, resident cell activity, as would be expected to be the case *in vivo*.

Chapter 6: Understanding Local Tissue Fate of Nanoparticles: The Insufficiency of Non-2D Cell Culture

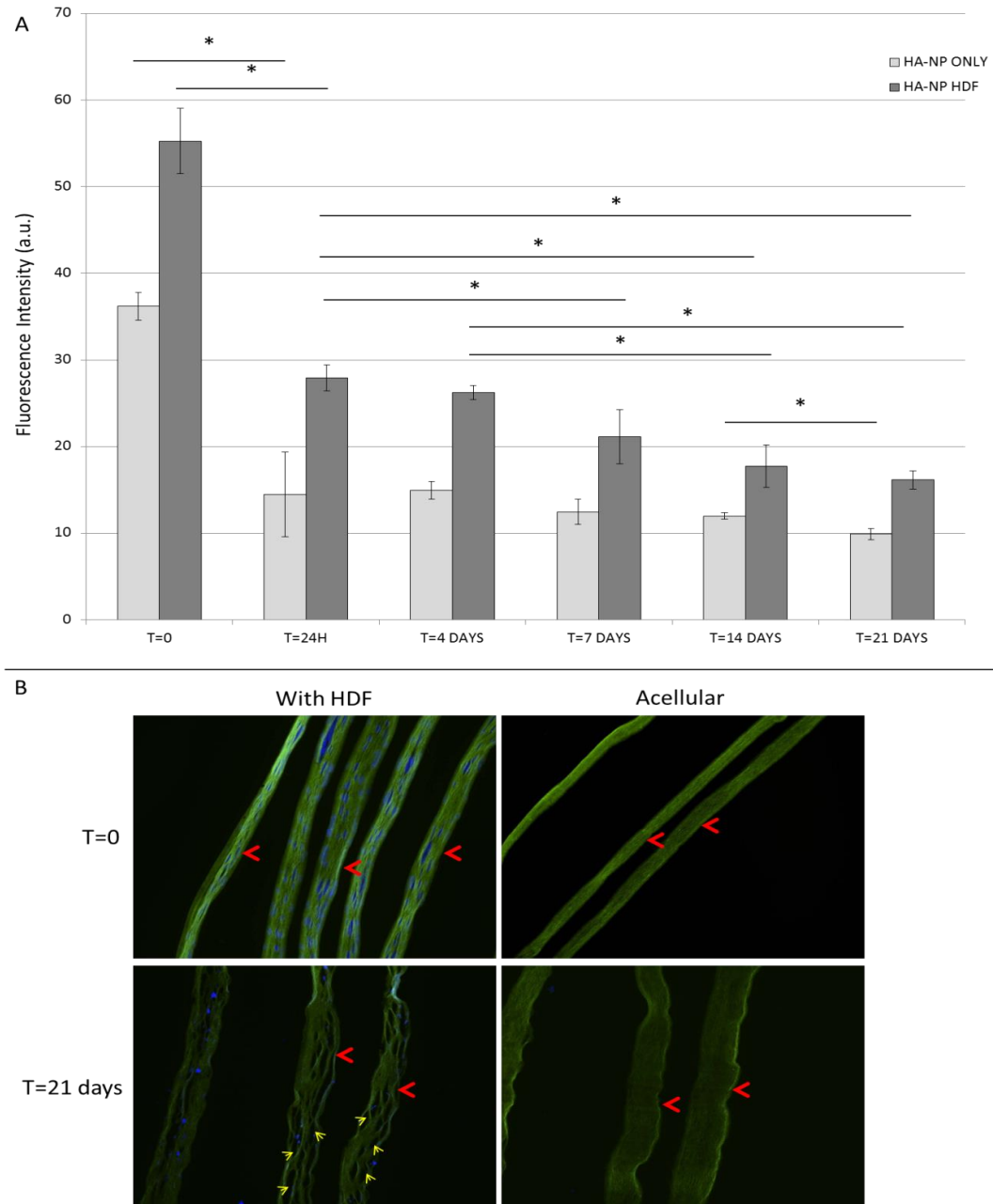


Figure 6.4: HA-NPs were retained within acellular constructs after 24 hrs post-PC, whereas when cultured with cells, HA-NPs were released gradually from the matrix due to cellular remodelling. (A): Graph comparing the retention of particles when cells were included or not. (B): Multiple replicate transverse sections of either cellular or acellular HA-NP-loaded compressed collagen constructs showing fluorescence distribution (red arrowheads mark the FLS) and appearance of lace-like remodelled collagen structure (marked by yellow arrowheads) after 3 weeks in cell culture but not in cell-free constructs. Error bars indicate standard deviation ($p < 0.05$ $n = 12$).

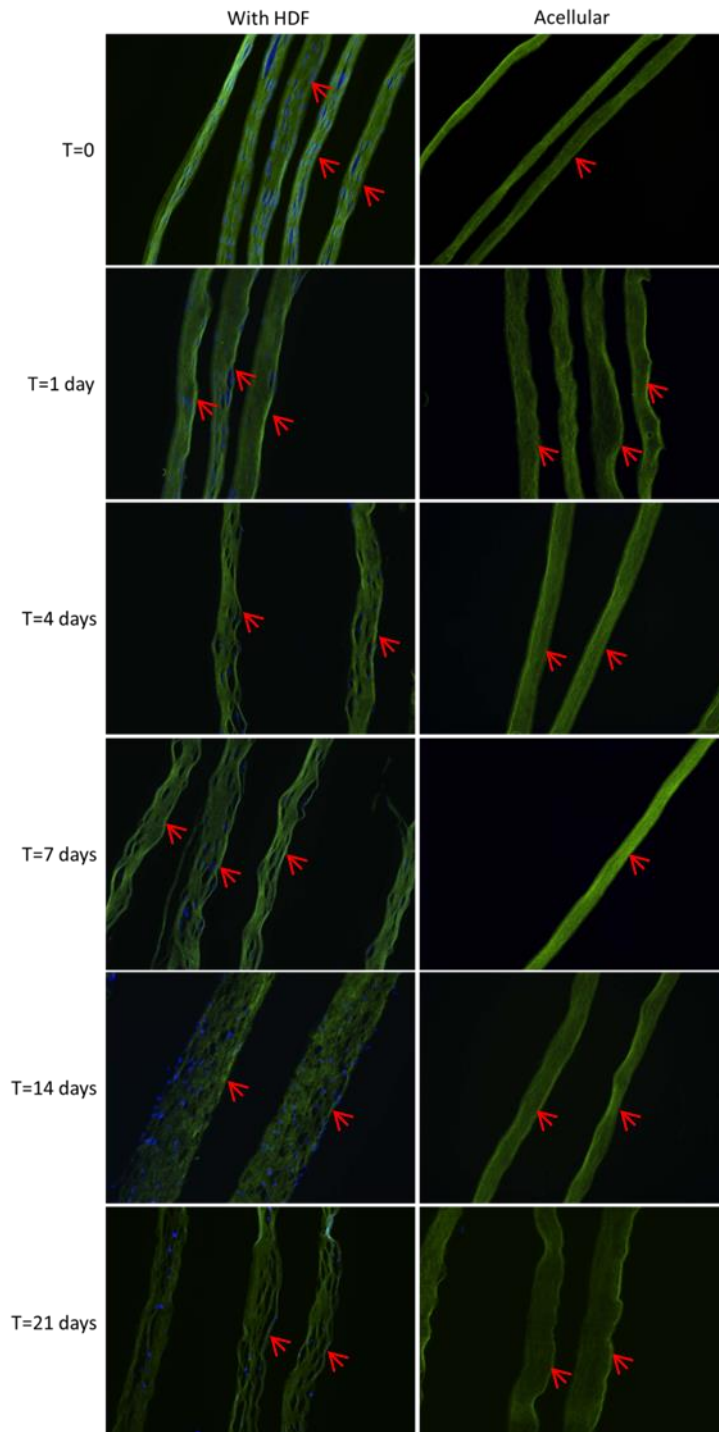


Figure 6.5: Fluorescence micrographs of sections of HA-NP-loaded compressed constructs, with or without cells, cultured over a period of 3 weeks. When constructs were cultured with cells, they appeared increasingly lacey over time due to cellular remodelling. Green: FITC, blue: Hoechst.

6.3.3. Hyaluronan nanoparticle entrapment within compressed collagen constructs

Hyaluronan nanoparticles were loaded into 0.5 ml collagen gels and allowed to set in 24-well plates. These were then compressed, or left uncompressed for fluorescence measurements of the initial load. Unloaded collagen gels were also prepared as controls. Unloaded uncompressed gels were pink due to the neutralised phenol red present in the collagen solution. Uncompressed HA-NP-loaded collagen gels were orange due to the colour of the HA-NP (Figure 6.6). After compression, unloaded constructs appeared colourless, whereas the nanoparticle-loaded constructs retained an orange hue which was less intense than the colour of uncompressed gels. This provides some evidence of HA-NP retention within the compressed constructs.

Immediately following plastic compression, constructs were solubilised and the released fluorescence was measured to determine the proportion of HA-NP remaining, compared to uncompressed hydrogels. The results indicate a mean retention of $19 \pm 1.2\%$ of the initial HA-NP load (Figure 6.7; pre-compressed gel fluorescence was nominally taken to be 100%).

As shown previously, the nanoparticles did get trapped in the collagen matrix when the collagen fibril density had become sufficiently high, we hypothesised that a greater proportion of the initial HA-NP load can be trapped if the dense FLS was formed at an earlier time during the process. We aimed to test this idea by addition

Chapter 6: Understanding Local Tissue Fate of Nanoparticles: The Insufficiency of Non-2D Cell Culture

of the second collagen (NP-free) layer, which would form its own FLS before too much of the nanoparticles has a chance to escape with the fluid, so increasing net retention.

Figures 6.6 and 6.7 indicate that this hypothesis was indeed correct. Figure 6.6 shows that the addition of a 2.0 ml unloaded collagen layer on top of the 0.5 ml HA-NP-loaded layer increased the orange colouration of the compressed constructs. This hypothesis was then tested further by using layers of different volumes (0.5, 1.0, 1.5 and 2.0 ml) and measuring the fluorescence intensities of the digested constructs.

Figure 6.7 shows that the addition of a 0.5 ml collagen gel as a second layer and subsequent co-compression of both layers together increased the proportion of trapped nanoparticles to 23.8 ± 3.1 %. This was taken further by increasing the volume of the second collagen layer to 1.0, 1.5 and 2.0 ml, further testing the hypothesis that the thicker (=larger initial volume) the second collagen layer, the earlier a retaining FLS would form relative to nanoparticle movement, and so the greater the amount of nanoparticles that will be retained. This was again the case and entrapment efficiency rose to 26.1 ± 2.4 , 28.6 ± 3.2 and 31.1 ± 3.1 % for the constructs with 1.0, 1.5 and 2.0 ml second layers respectively.

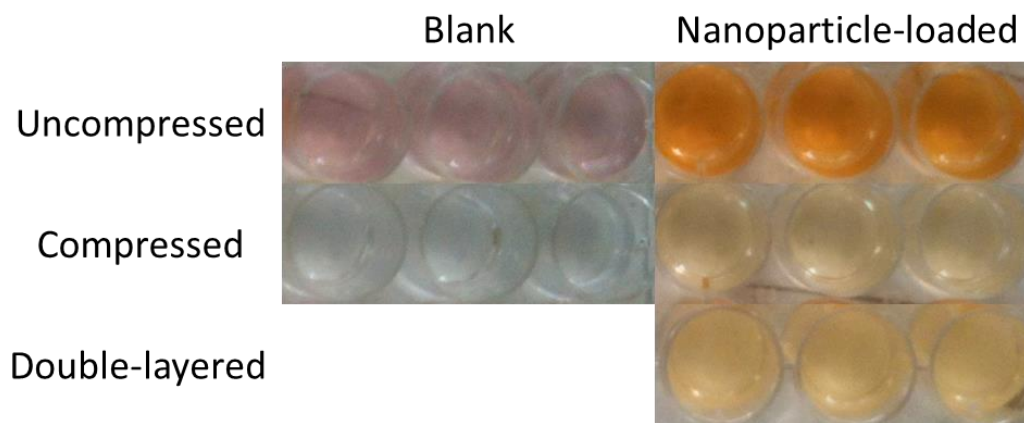


Figure 6.6: Photographs of HA-NP-loaded and unloaded collagen constructs. These photographs clearly show that there were nanoparticles in the constructs following compression. There is a significant decrease in the intensities of the orange colouration in the compressed constructs, indicating a loss of HA-NP.

Chapter 6: Understanding Local Tissue Fate of Nanoparticles: The Insufficiency of Non-2D Cell Culture

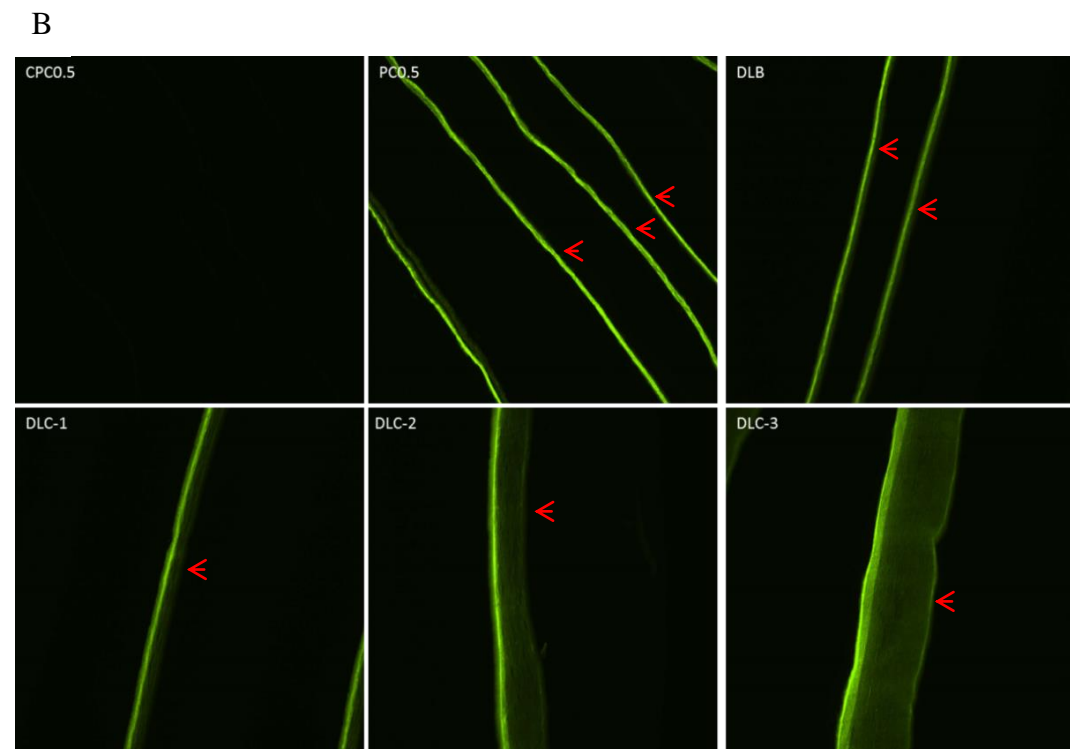
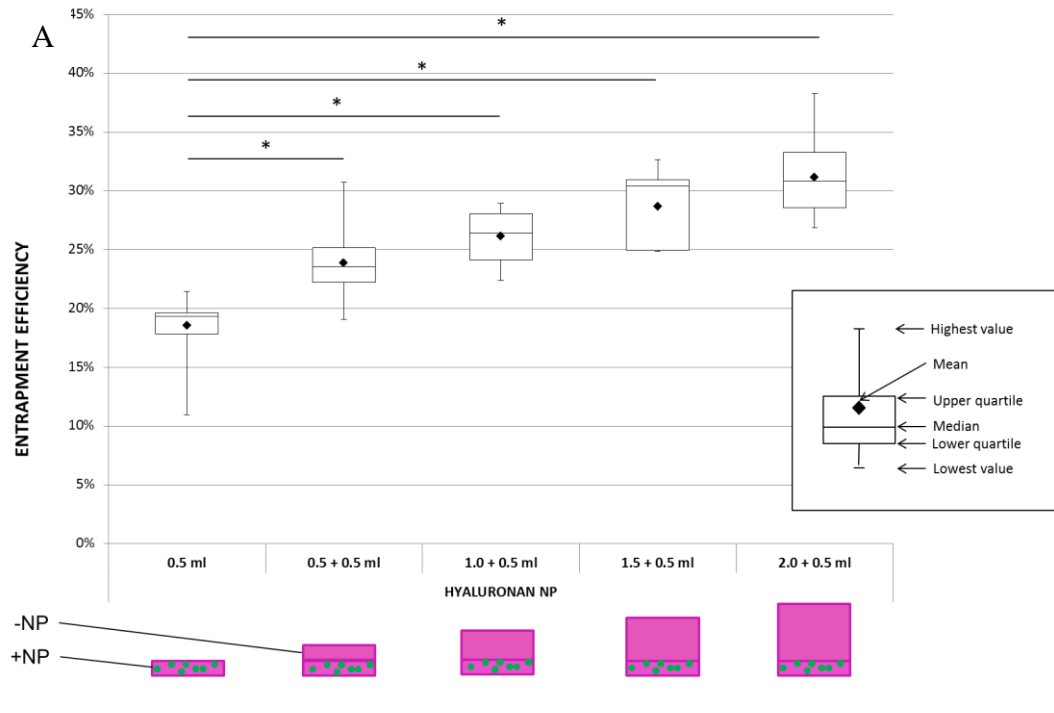


Figure 6.7: HA-NP entrapment following compression can be increased by multilayering. Results of the entrapment of HA-NP in constructs following compression (A) with micrographs of cross-sections of different construct variants (B). CPC0.5: 0.5 ml layer with no nanoparticles; PC0.5: single layer; DLB: 0.5 ml bottom layer + 0.5 ml top layer; DLC-1: 0.5 ml + 1.0 ml; DLC-2: 0.5 ml + 1.5 ml; DLC-3: 0.5 ml + 2.0 ml. Red arrowheads

6.3.4. Chitosan nanoparticle entrapment within compressed collagen

constructs

0.5 ml collagen gels were loaded with Nile red-containing chitosan nanoparticles (GCPQ-NR) and subjected to plastic compression. Figure 6.8 shows the appearance of loaded and unloaded collagen gels and compressed constructs. The Nile red in the chitosan nanoparticles gave the collagen a deep red colouration, compared to the pink of unloaded uncompressed gels or the colourless unloaded compressed constructs. Compressed GCPQ-NR-loaded constructs retained this deep red colour indicating the entrapment of the chitosan nanoparticles. The degree of particle loss through observation was less clear here than with the hyaluronan nanoparticles. These were then digested with collagenase I to retrieve nanoparticles retained in the constructs following compression for fluorescence measurements and quantitation.

Figure 6.9 shows that 18.8% of the initial chitosan nanoparticle load was trapped in the final construct. To determine if an earlier-formed FLS would improve nanoparticle trapping, a second layer of 'blank' collagen was added on top of the nanoparticle-loaded layer. The volume of this additional layer was 0.5, 1.0, 1.5 or 2.0 ml. With more collagen separating the absorbent plunger from the nanoparticles, the FLS should be denser when the nanoparticles reach it, which would result in greater nanoparticle entrapment. Figure 6.9 shows that this was indeed the case. The entrapment efficiencies for the single layer and double layers with increasing volumes were 18.8 ± 3.9 , 27.0 ± 8.2 , 27.7 ± 5.0 , 28.2 ± 7.5 and 36.2

$\pm 12.3\%$ respectively. Interestingly, the catch rates for the chitosan nanoparticles were similar to that of the hyaluronan nanoparticles (Figure 6.7).

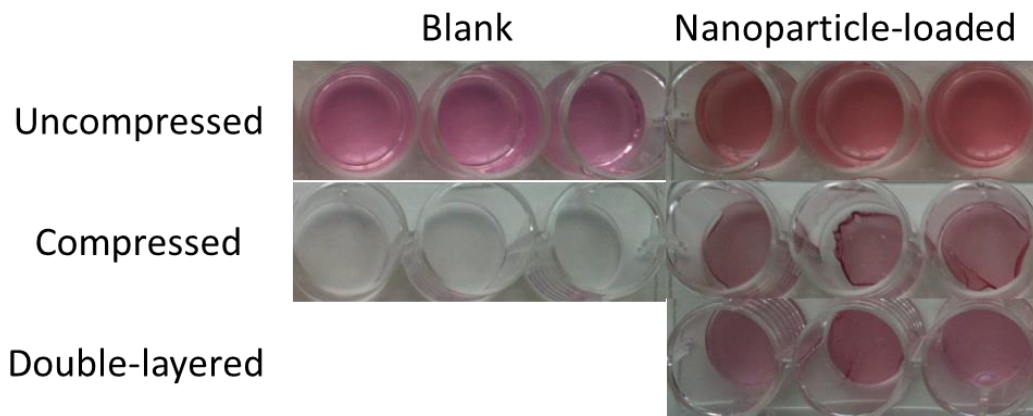


Figure 6.8: Photographs of GCPQ-NR-loaded and unloaded collagen constructs. The GCPQ-NR nanoparticles add a deep red colouration to the collagen, which is normally pink if uncompressed or colourless (or a very faint pink) if compressed. It is clear that there was nanoparticle entrapment following compression with both single and double-layered constructs.

Chapter 6: Understanding Local Tissue Fate of Nanoparticles: The Insufficiency of Non-2D Cell Culture

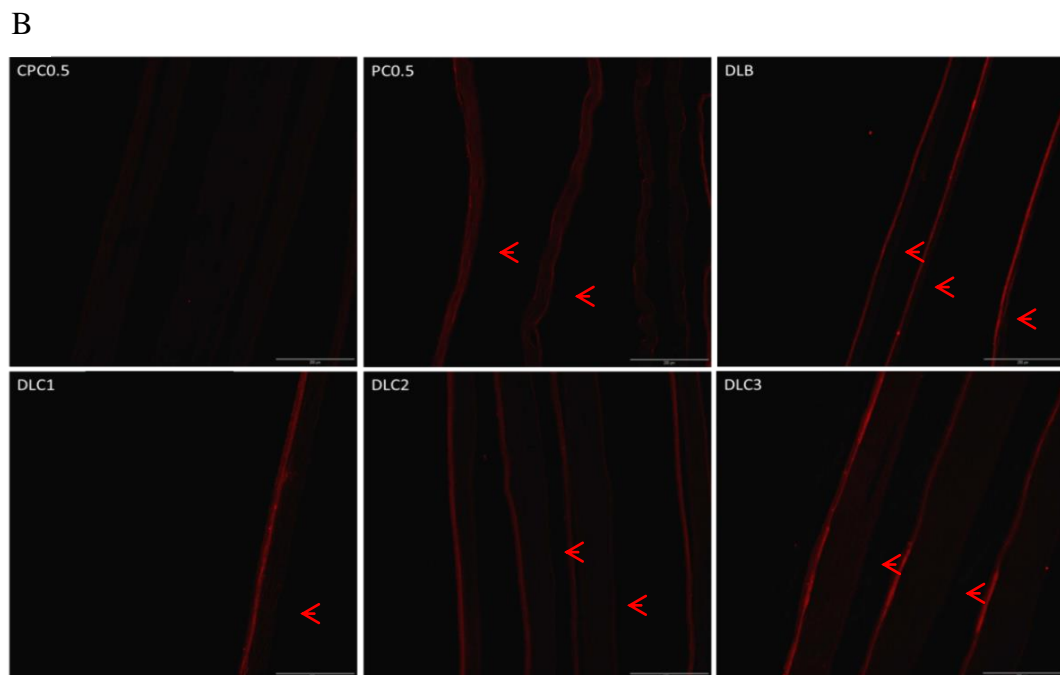
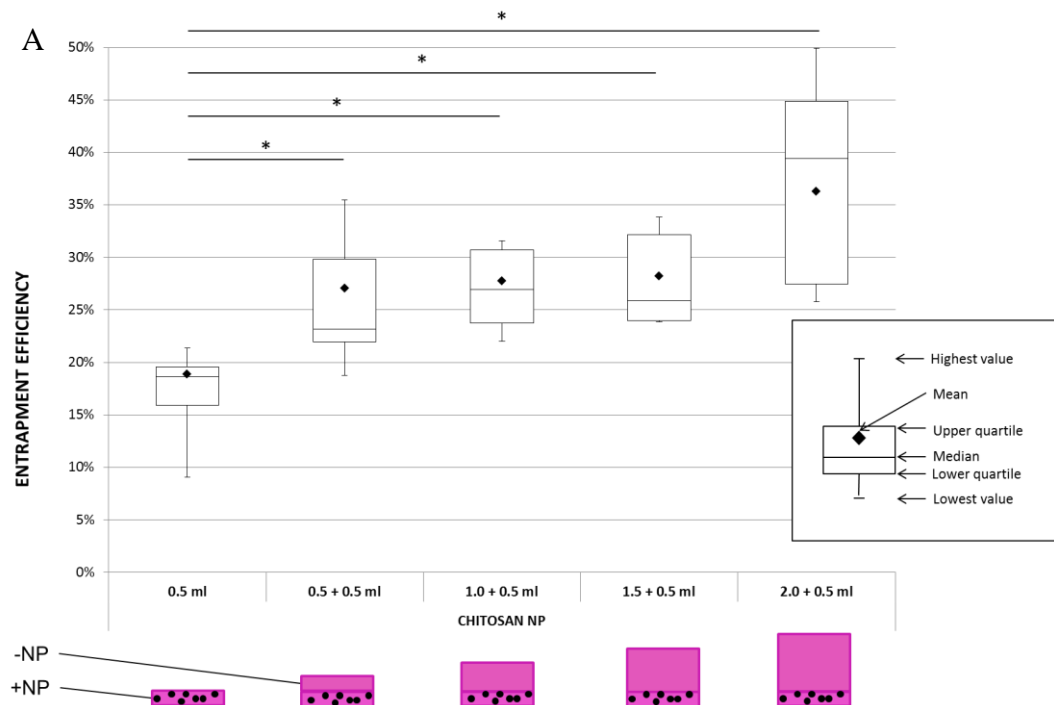


Figure 6.9: Entrapment of GCPQ-NR-NPs can be increased somewhat using multilayering. Results of the entrapment of GCPQ-NR in constructs following compression with micrographs of cross-sections of different construct variants. CPC0.5: 0.5 ml layer with no nanoparticles; PC0.5: single layer; DLB: 0.5 ml bottom layer + 0.5 ml top layer; DLC-1: 0.5 ml + 1.0 ml; DLC-2: 0.5 ml + 1.5 ml; DLC-3: 0.5 ml + 2.0 ml. Red arrowheads mark the tops of the constructs. Error bars depict the standard deviations of the mean ($p < 0.05$; $n = 6$).

6.3.5. Hyaluronan nanoparticle entrapment within compressed collagen constructs in the presence of cells

We hypothesised that the presence of cells in the collagen constructs during compression would increase nanoparticle retention. The cells would act as obstacles to fluid flow, hindering the movement of the nanoparticles, aiding the condensing collagen mesh in the FLS to hold back the nanoparticles.

Four different collagen solutions were prepared – one with hyaluronan nanoparticles, one with human dermal fibroblasts (HDF) at a seeding density of 10^5 cells/ml, one with both hyaluronan nanoparticles and HDFs and one plain solution with neither particles nor cells. These were used to produce single layers of 0.5 ml gels loaded with HA-NPs, 0.5 ml single layers with both HA-NPs and HDFs, double layered constructs with a 0.5 ml HA-NP-loaded bottom layer and a 2.0 ml ‘blank’ top layer, double layered constructs with a 0.5 ml HA-NP-loaded bottom layer and either a 0.5, 1.0, 1.5 or 2.0 ml HDF-seeded top layer (Figure 6.10).

Figure 6.11 shows the cross-sections taken of the double layered (0.5+2.0 ml) constructs with just HA-NP (A) or with both HA-NP and HDFs (B). What can be seen here is the difference in the distribution of fluorescence between the two. In Figure 6.11A, the fluorescence distribution is much more uniform through the thicker upper collagen layer, whereas in Figure 6.11B, the fluorescence distribution appears more patchy in areas where cells are present (dark gaps in the collagen layer). This, together with the HA-NP entrapment results, adds to the theory that cells

Chapter 6: Understanding Local Tissue Fate of Nanoparticles: The Insufficiency of Non-2D Cell Culture

embedded within collagen constructs help to block nanoparticle escape and increased overall particle retention.

To confirm this observation, the different construct variants were digested with collagenase I to retrieve trapped HA-NP for fluorometric measurements. Figure 6.12 shows that single 0.5 ml layers retained 17.2 ± 1.4 % of the initial HA-NP load, whilst the double layered arrangement of 0.5 + 2.0 ml layers retained 31.4 ± 5.2 %. 0.5 ml single layered HA-NP and HDF seeded constructs trapped 17.6 ± 3.1 % of the HA-NP load. The addition of a 0.5, 1.0, 1.5 or 2.0 ml cellular layer on top increased this to 22.2 ± 0.7 %, 25.6 ± 3.0 %, 30.5 ± 1.4 % and 35.5 ± 2.4 % respectively, compared to 23.8 26.1 28.6 31.1 % in the acellular versions of constructs. Cellular constructs with a 1.5 or 2.0 ml upper collagen layer, showed greater HA-NP entrapment than without a cell-seeded upper layer, although these differences are not quite statistically significant.

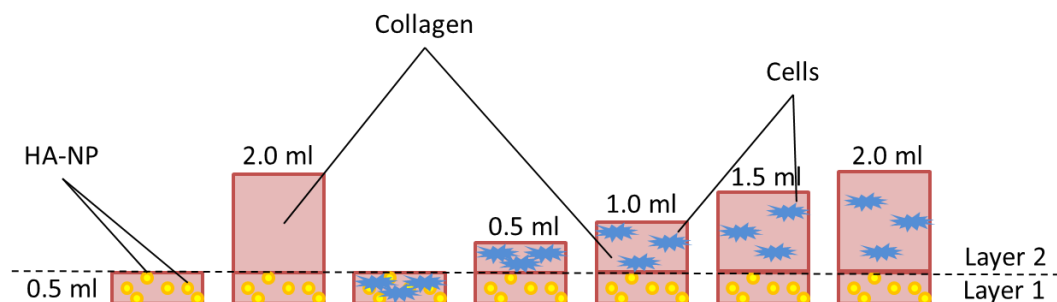


Figure 6.10: Diagram depicting the different collagen construct variants used to test the hypothesis that the inclusion of cells in collagen layers would increase nanoparticle entrapment.

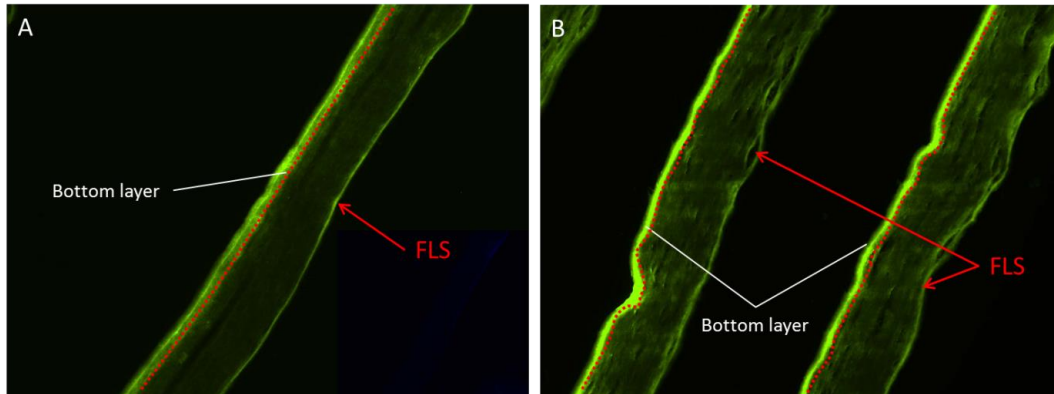


Figure 6.11: Fluorescence micrographs of double layered compressed constructs, with a 0.5 ml nanoparticle-loaded bottom layer and a 'blank' (A) or a cellular (B) 2.0 ml upper layer. The red dotted lines demarcate the boundary between the bottom nanoparticle-loaded layer and the unloaded top layer. This figure shows the effect cells have on nanoparticle retention. In both A and B, the bottom layers are brightly fluorescent and there is a bright band of fluorescence at the top (FLS) of the constructs. In A, the fluorescence in the upper layer is low with a small gradient decreasing from the FLS towards the bottom layer. In B, the fluorescence in the upper layer also shows the presence of nanoparticles, but there are also patches of bright fluorescence in the regions where cells were present (black holes).

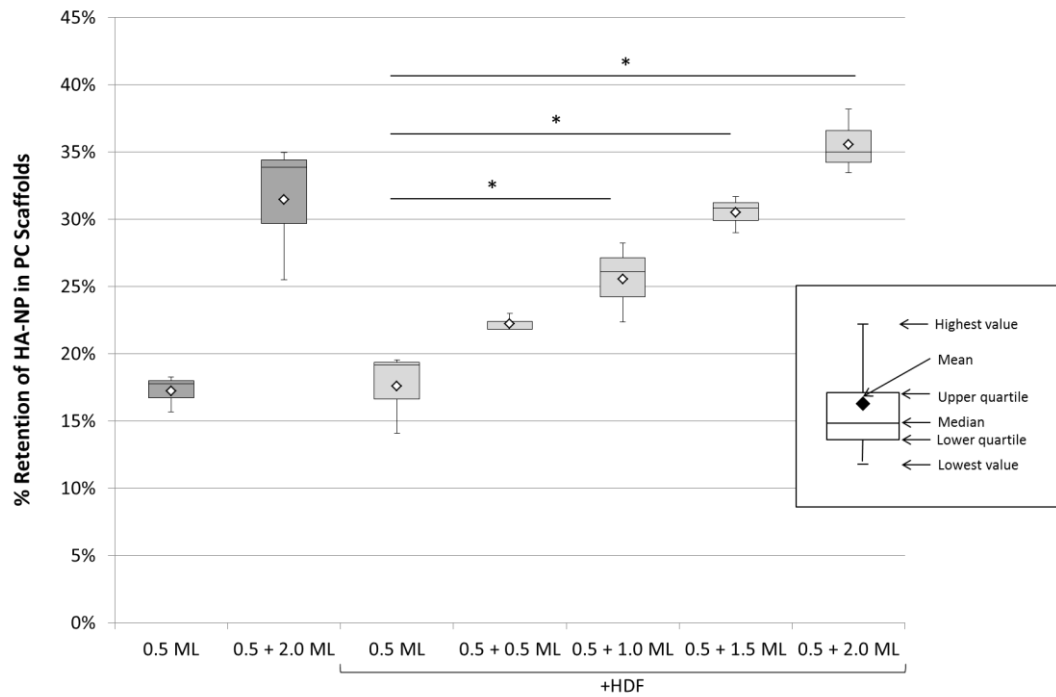


Figure 6.12: Entrapment efficiency of HA-NP in different construct variants with/without cells, showing a non-significant increase in nanoparticle entrapment. Nanoparticle entrapment in the single layer 0.5 ml and the double-layered 0.5+2.0 ml cellular constructs was slightly higher than in the acellular equivalents, although this difference did not reach statistical significance. Error bars depict the standard deviations of the mean ($p < 0.05$; $n = 5$).

6.3.6. Riboflavin crosslinking

Increasing the rate of retention of nanoparticles is important when the costs of the nanoparticles and/or cargo are high, as much of it is lost following compression. One idea to further improve nanoparticle retention was to cross-link the top surface of collagen hydrogels prior to compressing them. The hypothesis was that by crosslinking the gels, collagen fibrils would form a primitive FLS even before compression began, so that the FLS would form faster, leading to greater nanoparticle retention.

0.5 ml single layer collagen gels as well as 0.5+2.0 ml double-layered gels were prepared in 24-well plates. Riboflavin crosslinking was carried out by soaking discs of filter paper in riboflavin solution and applying the discs to the top surface of uncompressed gels for a short amount of time and photactivating the riboflavin. The short application time of riboflavin ensured that there was minimal diffusion of riboflavin from the top surface into the gel, so that photoactivated crosslinking could only occur at the top surface where the FLS would form.

16 mm discs of blotting paper were cut and soaked in a solution of riboflavin. The soaked discs were then placed on top of pre-set collagen hydrogels so that only the top surfaces of the gels come into contact with riboflavin. 455 nm light was then used to activate the riboflavin for 10 min, which has previously been shown to result in collagen crosslinking [331].

Figure 6.13 shows the effects of riboflavin crosslinking treatment of the collagen hydrogels before plastic compression, which appeared not to have an effect on the entrapment of nanoparticles. There was no significant difference in the retention of nanoparticles following compression ($17.1 \pm 2.6\%$ for single layers and $28.8 \pm 7.0\%$ for the double-layer constructs) compared to untreated constructs ($18.2 \pm 1.2\%$ and $31.2 \pm 3.6\%$ for single and double layer constructs respectively). This will be because the cross-linking occurred before compression, so it was stabilising the spaced-out fibrils rather than tightening up the collagen mesh filter. This may explain why the cross-linked samples actually showed lower nanoparticle entrapment than non-cross-linked constructs – the riboflavin treatment may have slowed down surface compaction by cross-linking the fibrils while they were widely spaced.

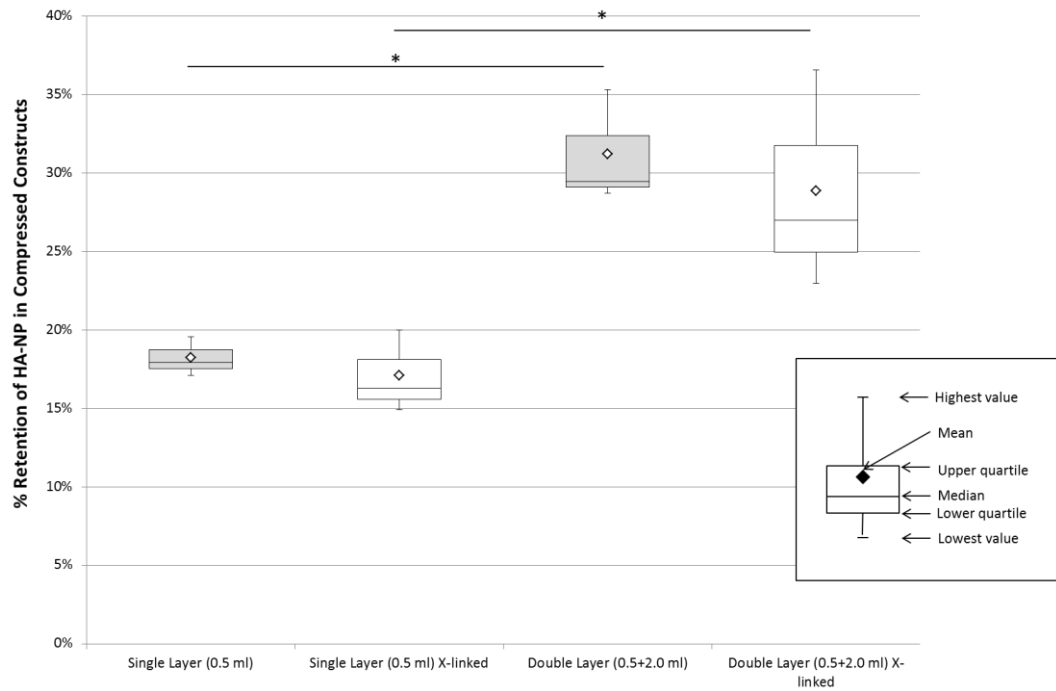


Figure 6.13: Box-and-whisker plot showing the percentage of HA-NP retained in compressed constructs following cross-linking with riboflavin. Again, the addition of a second collagen layer showed increased entrapment of nanoparticles, but riboflavin cross-linking did not affect nanoparticle entrapment ($p < 0.05$; $n = 3$).

6.3.7. Determination of release/escape of free FITC from HA-nanoparticles

The loading of FITC in the HA-NP was done through hydrophobic and hydrophilic interactions of the hyaluronan molecule used. As the HA molecules interact, FITC molecules get trapped within the particles that are formed (Figure 6.14). However, the loading process is not 100% efficient, so some FITC molecules remain un-encapsulated. Although during the processing of these loaded HA-NP, measures were taken to purify and remove any unbound FITC, some still could have remained. As such, it was important to determine the amount of free FITC present.

HA-NP suspension was dialysed to determine the proportion of any loosely-bound FITC. Figure 6.15 shows that after 2 H dialysis, the fluorescence intensity of the dialysate was 90.9 ± 9.79 a.u.. This was 12.2% of the fluorescence intensity of the HA-NP suspension before dialysis, and did not change after a further 22 H of dialysis. This shows that 12.2% of the fluorescence of the HA-NP suspension was due to free FITC (not trapped within nanoparticles). Taking the presence of free FITC into account, the real retention of HA-NP by 0.5 ml constructs was 21.3% rather than 19.0% (assuming that 12.2% of the initial nanoparticle load was free FITC).

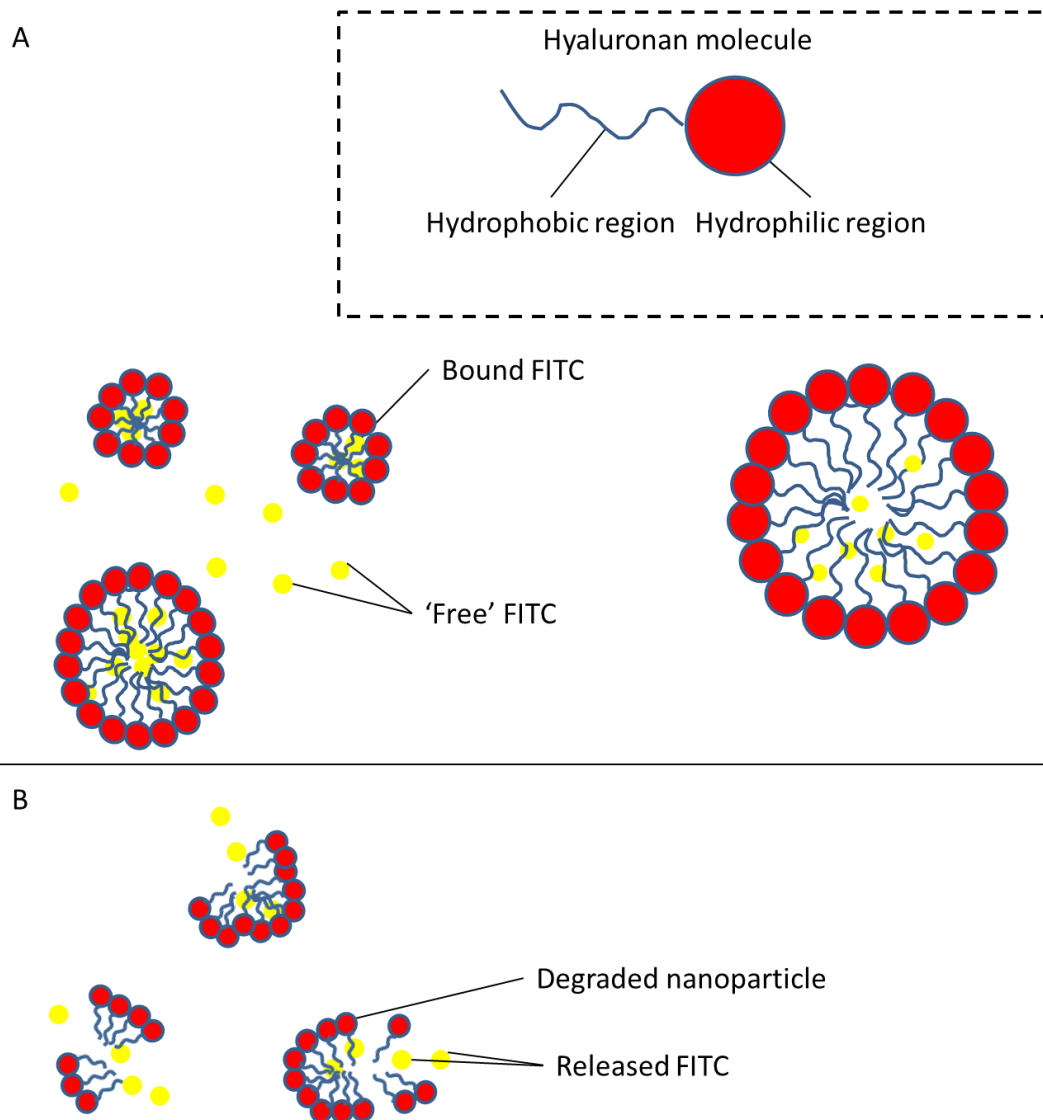


Figure 6.14: Schematic of the formation (A) of FITC-loaded hyaluronan nanoparticles, with most of the FITC encapsulated within nanoparticles, but a small proportion remains loosely associated or free. (B) Encapsulated FITC is released from the nanoparticles following nanoparticle degradation possibly either intracellularly or extracellularly.

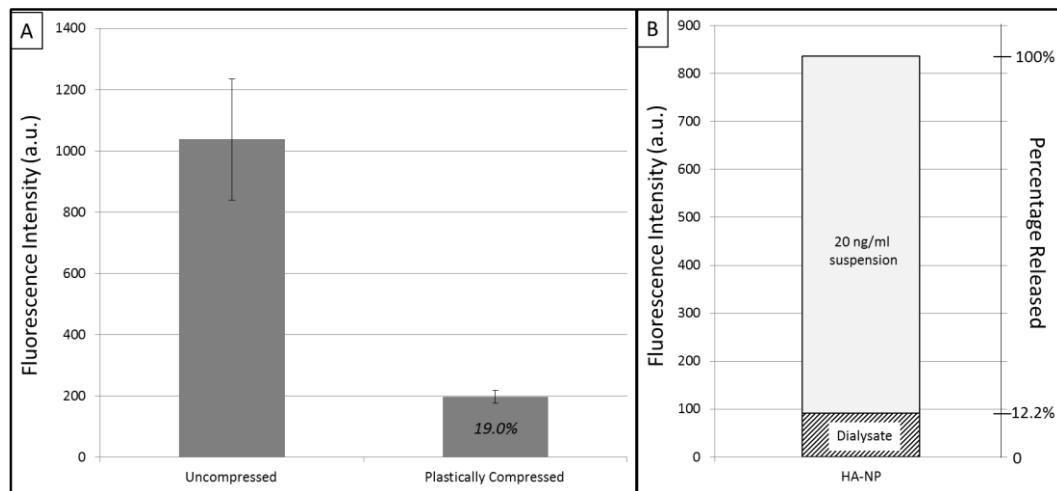


Figure 6.15: (A) Entrapment of HA nanoparticles following plastic compression. Following compression, 19% of the initial nanoparticle load was trapped in the collagen scaffolds. (B): Determination of ‘free’ FITC in HA-NP suspension. Error bars indicate the standard deviation of the mean (n=3).

6.3.8. Cell uptake of hyaluronan nanoparticles

To compare cell uptake between cells in conventional monolayer cultures and 3D cultures, the concentration of nanoparticles had to be kept constant. The amount of nanoparticles retained in constructs was measured to be 19% of the initial load – 0.95 μg . Table 6.1 shows that the volume of fluid remaining in the constructs was $1.71 \pm 0.36\%$ of the initial volume, which was 0.00855 ml. This gives a nanoparticle concentration of 111.1 $\mu\text{g}/\text{ml}$ in compressed constructs.

Table 6.1: Amount of fluid remaining in compressed constructs.

Initial Gel Mass (g)	Mass after PC (g)	Fluid Remaining in Constructs
0.5	0.00853 ± 0.00182	1.71 ± 0.36

The concentration of HA-NP in compressed scaffolds was calculated as follows:

$$\text{Concentration} = \frac{(\text{initial Concentration} \times \text{Initial Volume}) \times \% \text{ NP Retained}}{\text{Fluid remaining after PC}}$$
$$\text{Concentration} = \frac{(10 \mu\text{g} \cdot \text{ml}^{-1} \times 19\%)}{1.71\% \times 0.5 \text{ ml}}$$
$$\text{Concentration} = \underline{111.1 \mu\text{g} \cdot \text{ml}^{-1}}$$

This calculated concentration was used for the 2D cell culture as a basis for comparison of cell uptake.

6.3.9. 2D versus 3D cell culture of HA-NP uptake

For the 2D model, fibroblasts were conventionally cultured as monolayers in 24-well plates, with the culture media containing hyaluronan nanoparticles at a concentration of 111.1 µg/ml, as calculated above. Fibroblasts were seeded into HA-NP-loaded compressed collagen constructs for 3D culture. At fixed time-points, cells were retrieved from their culture systems and washed to remove any loosely-attached extracellular nanoparticles. The cells were then suspended in PBS and

Chapter 6: Understanding Local Tissue Fate of Nanoparticles: The Insufficiency of Non-2D Cell Culture

measured for fluorescence or imaged which would indicate the presence of internalised HA-NP.

Cells cultured within compressed collagen were removed from their constructs through collagenase digestion and centrifugation, and re-plated onto coverslips for fluorescence microscopy. Fibroblasts were also cultured on coverslips directly and submerged in culture medium containing suspended hyaluronan nanoparticles. Before staining, the samples were washed with PBS to remove any remaining extracellular HA-NP. Phalloidin was then used to stain the cytoskeleton of the cells to show their morphology, and Hoechst was used to stain the cell nuclei. Figure 6.16 shows the images obtained. The nanoparticles, which fluoresce green due to their fluorescein isothiocyanate (FITC) cargo, are clearly seen within the cells cultured with both 2D (Figure 6.16A-D) and 3D (Figure 6.16E-H) systems. The particles look to have been transported inwards toward the nuclei. From these images, the green fluorescence appear to be more intense and more abundant in cells cultured in 2D compared to the cells that were in compressed constructs. This could indicate that the cells cultured as a monolayer took up the particles more readily.

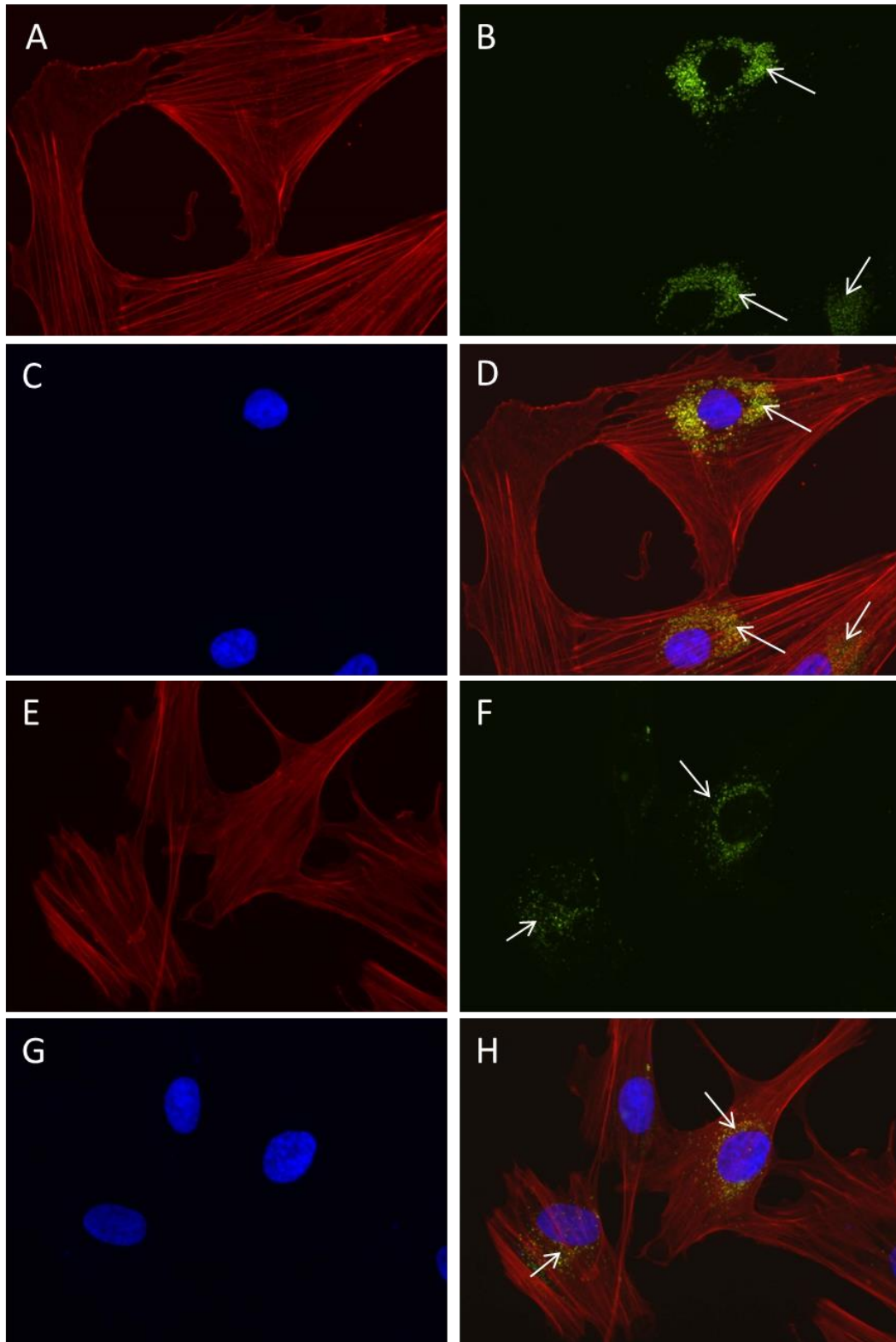


Figure 6.16: Fluorescence micrographs of cells culture as a monolayer (A - D) or cells initially cultured in 3D then re-plated onto 2D for imaging (C - H) showing the intracellular distribution of HA-NP following uptake (t= 7 days). A, E: phalloidin staining. B, F: FITC-loaded HA-NP. C, G: Hoechst. D, H: combined. Perinuclear distribution of nanoparticles was observed in cells cultured in both systems.

Chapter 6: Understanding Local Tissue Fate of Nanoparticles: The Insufficiency of Non-2D Cell Culture

Figure 6.17 shows the cell uptake dynamics of HA-NP. Cells cultured with HA-NP in 2D showed a rapid uptake from the start ($t=0$) (15.3 a.u./day); 3.4 times greater than for 3D cultures over the same period. This continued to increase to a peak of 60.1 a.u. at 3 days. This was followed by a decrease in uptake of 8.47 a.u./day. Cells cultured within collagen scaffolds showed a gradient of 4.48 a.u./day of increasing uptake with a peak of 32.8 at $t=7$ days, before tailing off with a rate of -5.42 a.u./day. This pattern was in complete contrast to cells in 3D collagen constructs where uptake was minimal over the first 3 days then rose slowly (5.7 au/day) between 3 and 7 days where it peaked at 32.8 a.u.. The nanoparticle uptake between 2D and 3D cultures were distinctive but the metabolism and loss once taken up was similar.

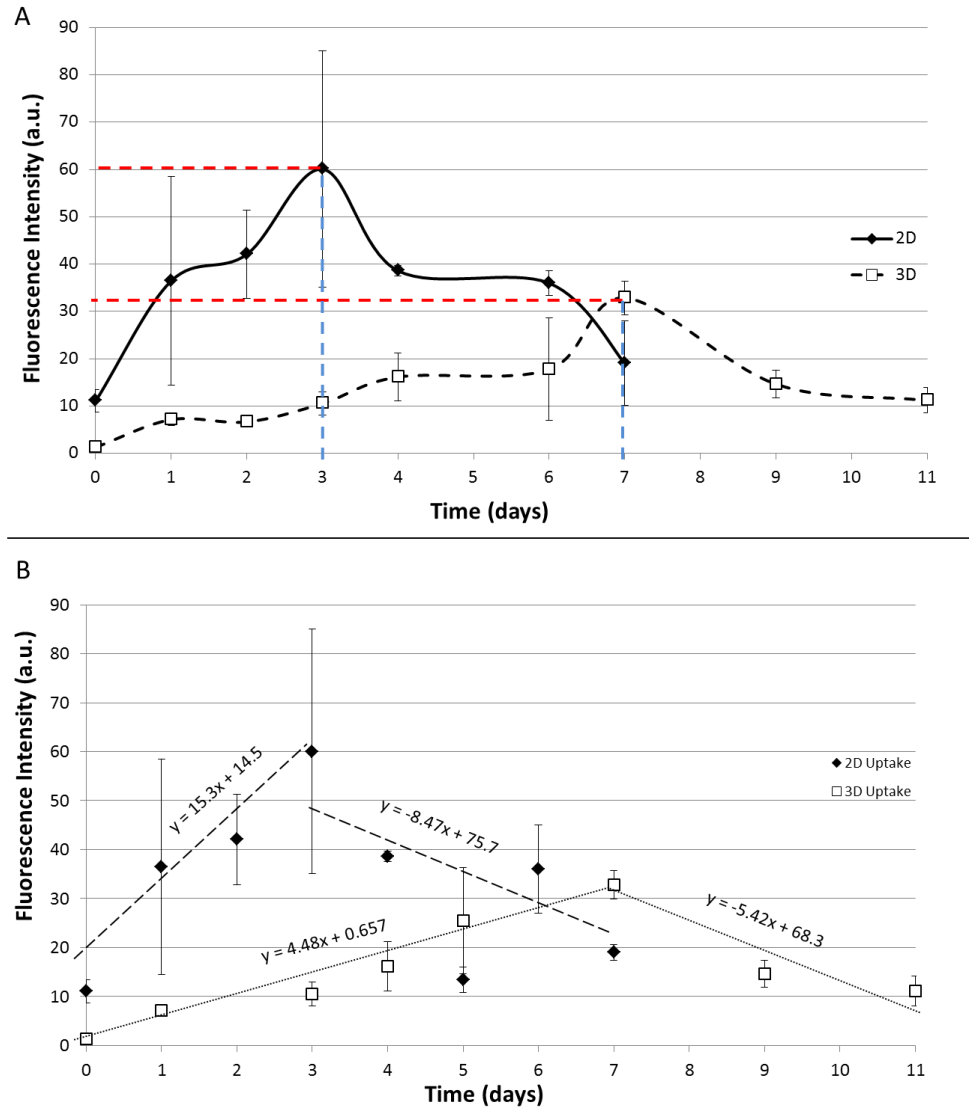


Figure 6.17: Cell uptake of HA-NP differed when cultured as a monolayer on TCP or within compressed collagen. (A) Graph comparing nanoparticle uptake by cells cultured in 2D or in 3D as determined by cell fluorescence. The blue dotted line compares the times to peak of the 2D and 3D cultures. The red dotted lines compare the peak heights. (B) The same graph as in (A) was plotted with the gradients of the increase and decrease in fluorescence calculated for both 2D and 3D cell uptake. Error bars depict the standard deviations of the mean (n=15).

6.4. Discussion

The aim of this chapter was to develop a 3D tissue-like model for testing nanoparticles *in vitro* which would more accurately predict what would happen *in vivo*. The model would thus require tissue-level densities to better mimic native tissue. Plastically compressed collagen is an excellent system for this study, not least because collagen is biological and present in abundance in many tissues, and compressed collagen is of physiological matrix density.

The importance of matrix density was evident right from the beginning of the compression process. The data from the HA-NP entrapment experiment shows that about a fifth of the initial nanoparticle load is retained in the construct following plastic compression, which indicates that 4/5 of the particles escaped with the expelled fluid. This indicates that the nanoparticles initially moved freely with the escaping fluid out of the compressing collagen hydrogel with no hindrance since matrix density was low.

Hydrogels are predominantly water (>95%), and so, at an early stage of the compression process, the collagen matrix has a density well below tissue levels. With such low density levels, molecules and larger particles (i.e. nanoparticles) are free to move about with the escaping fluid unhindered by the matrix. However, 19% of the nanoparticles were retained (Figure 6.7), indicating that at some point during the process the density of the matrix reached high enough levels to where free movement was not possible anymore, resulting in the trapping of

Chapter 6: Understanding Local Tissue Fate of Nanoparticles: The Insufficiency of Non-2D Cell Culture

nanoparticles most probably in the FLS. The collagen construct was generated through simultaneous compaction and absorption of water from the gel. The upward flow of the fluid combined with the downward pressure of the plunger led to the condensation of collagen fibrils at the FLS. The FLS became denser and denser as the compression continued, eventually blocking escape, and was where the nanoparticles accumulated (Figure 6.18). Particle aggregation could have aided the retention of the HA-NPs. It is possible that a proportion of the HA-NPs formed aggregates which were too large to pass through the collagen meshwork, whilst smaller individual particles flowed out of the gel with the fluid.

Additionally, when higher volume gels were used (>1.0 ml), the fluorescence distribution within constructs was not the simple gradient of decreasing fluorescence from the top surface to the bottom. Looking at Figure 6.3, one can see a bright green line of fluorescence on the top surface and another at the bottom surface of the construct. This indicated to us that a secondary fluid leaving surface formed at the bottom surface. This had been observed in previous studies when thicker gels were used (see Chapter 3). The accumulation of fluorescence at this second FLS points to a back-flow of nanoparticle-carrying fluid during the compression. The primary FLS must then have become so compact and dense that even fluid outflow was hindered. Thus the fluid had to escape through other surfaces, hence flowing downward and out through the bottom surface of the construct, and in doing so, created a secondary FLS where the remaining nanoparticles accumulated (Figure 6.19).

Chapter 6: Understanding Local Tissue Fate of Nanoparticles: The Insufficiency of Non-2D Cell Culture

Since a large proportion of the initial nanoparticle load was lost following compression, we wanted to see if the efficiency of capture could be improved. Initially, a pre-compressed collagen construct was placed on top of an uncompressed HA-NP-loaded collagen gel so that a FLS would thus be present right from the start, which should give the best results in terms of nanoparticle trapping. However, it proved difficult to place the compressed construct on top of an uncompressed gel without damaging both the compressed and uncompressed constructs, and ensure complete coverage of the gel. Thus, we moved on to the double uncompressed layers model (Figure 6.20). In this way we could ensure that the entire top surface of the HA-NP-loaded gel was covered with collagen.

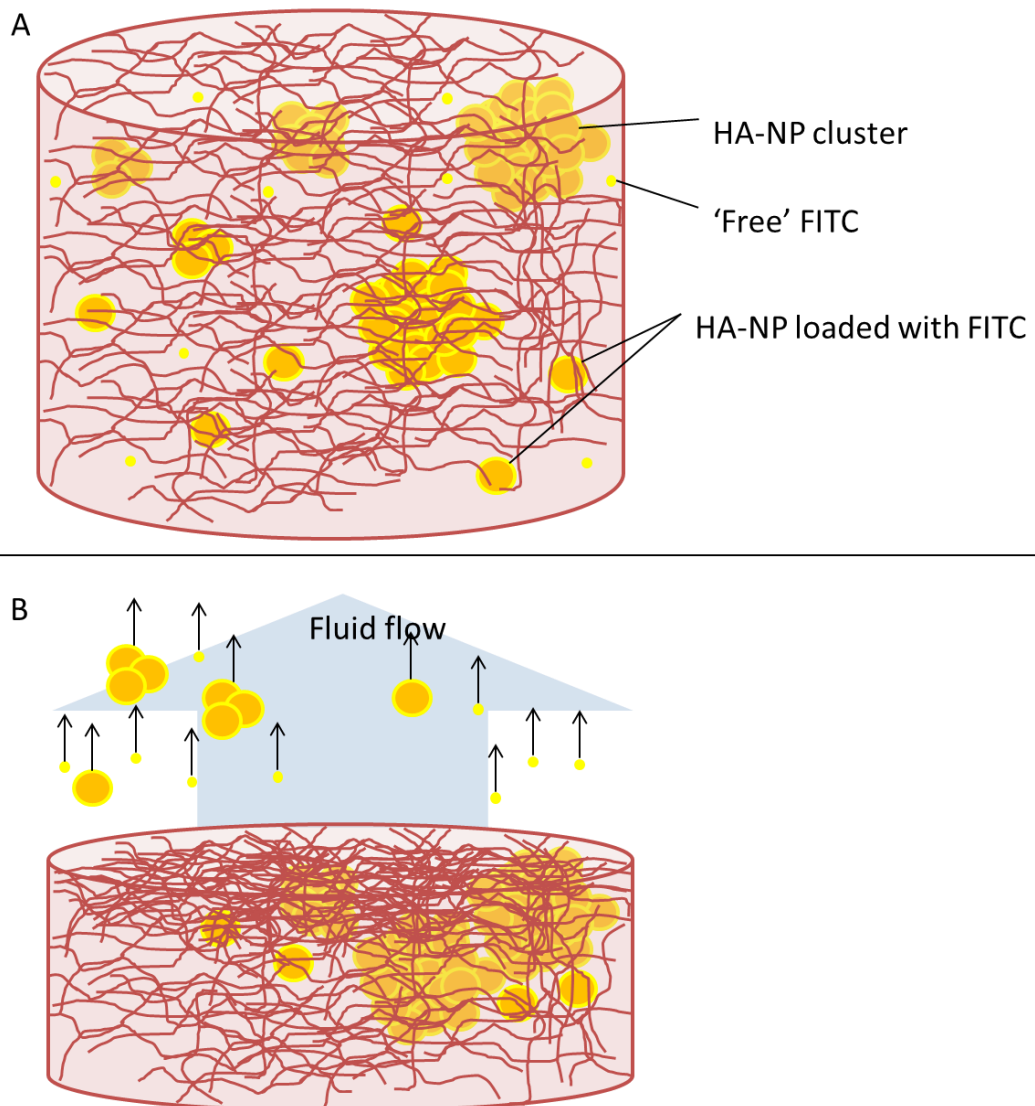


Figure 6.18: Schematic illustrating the trapping and escaping of nanoparticles/free FITC during compression. FITC-loaded HA-NP suspension is loaded into collagen solution during preparation of the gels. Within the gel there is any unbound FITC that was present in the suspension, HA-NP of different sizes, as well as clumps of HA-NP when they aggregate. During compression, free FITC, smaller HA-NP and possibly smaller aggregates of HA-NP flows with the escaping fluid out of the gel, whilst the larger molecules get trapped by the collagen fibrils and remain in the gel.

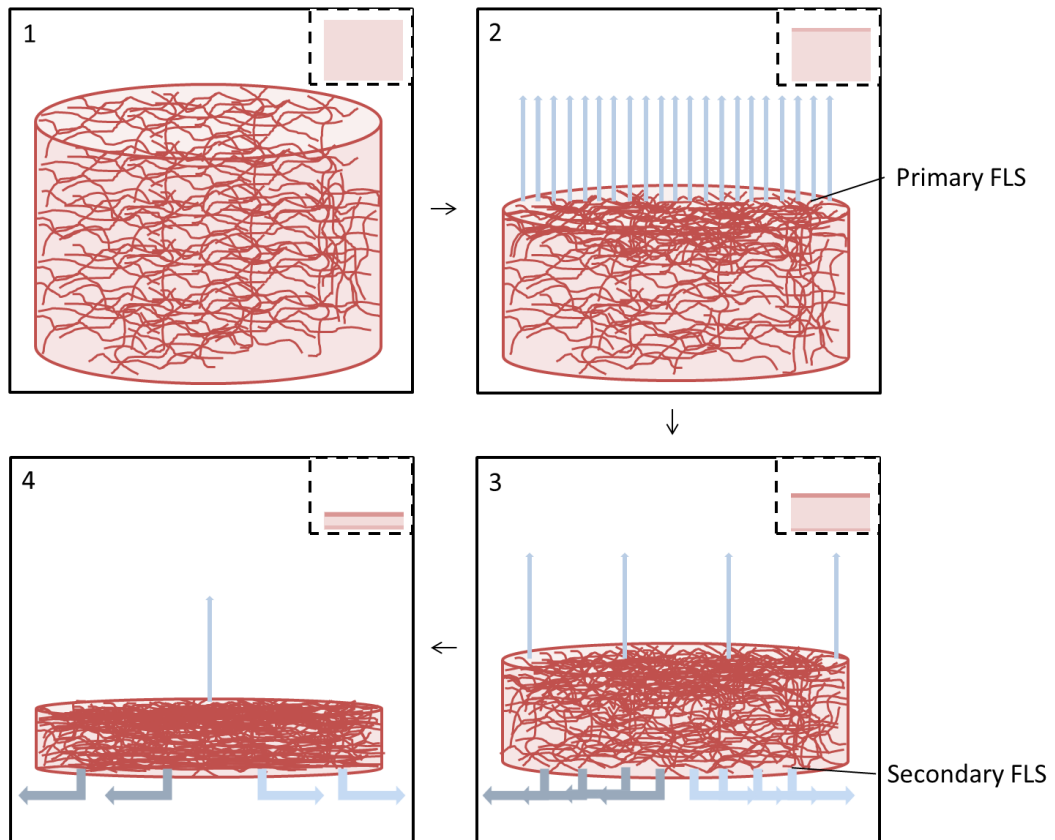


Figure 6.19: Schematic of the process of compressing a collagen hydrogel. 1: The collagen hydrogel is composed mainly of fluid and randomly-orientated fibrils. 2: As compression begins, fluid leaves through the top (fluid leaving) surface (FLS), and at the same time, pressure forces the collagen fibrils downwards. This leads to the packing of fibrils at the FLS of the construct which becomes denser and denser through the process. 3-4: The FLS eventually becomes so dense that it blocks fluid escape. The continuing pressure on the compressing gel forces the fluid out of the gel through the bottom (secondary fluid leaving) surface, resulting in a similar compaction of fibrils at this surface as at the FLS.

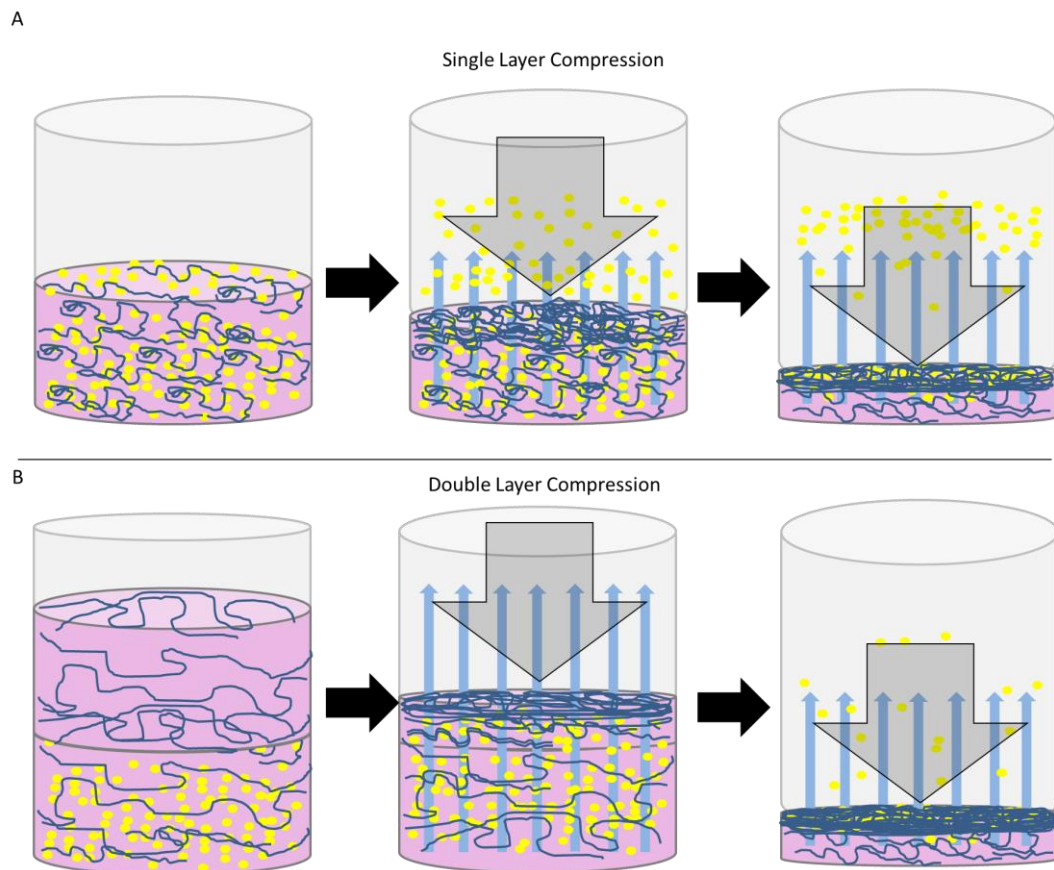


Figure 6.20: Schematic illustrating the trapping of nanoparticles during compression in single layer (A), or double layers (B). Nanoparticles escape from the compressing gel as the dense collagen lamella at the FLS forms. By adding another collagen layer on top, the collagen lamella is allowed to develop before the bulk of the nanoparticle load begins to flow out of the gel.

This proved successful with increasing nanoparticle trapping significantly, indicating that our hypothesis was correct. It appears though, that the better retention was not a direct effect of the FLS trapping nanoparticles. Figures 6.7 & 6.9 show the fluorescence images of the different double-layered variants made (with HA-NP or chitosan nanoparticles). Most of the fluorescence in each double-layered construct remained in the bottom nanoparticle-loaded layer. The top layers also showed some fluorescence, with the thicker layers fluorescing brighter. This gives us a clue as to how the nanoparticles moved with the fluid during compression. At the initiation of compression, fluid throughout the two gels moved upwards towards the absorbent plunger, until the FLS began to block fluid escape. At which point, the fluid was redirected downwards to the bottom surface. This resulted in a secondary FLS forming at the bottom surface of the constructs (as discussed above). Nanoparticles in the upper layer would then have moved back down with the backflow of fluid, hence the depletion of fluorescence. The thicker the upper layer was, the greater the remaining fluorescence in that layer (Figure 6.7). This was likely due to the greater distance the nanoparticles had to move back down, and out through the secondary FLS. Additionally, the collagen fibril mesh at the secondary FLS would have compacted and restricted nanoparticle escape as well. Some of the fluid and nanoparticles may have escaped through the sides of the construct, although this would not have been significant as there were no significant differences in fluorescence intensities in the middle of the constructs compared to the edges.

Chapter 6: Understanding Local Tissue Fate of Nanoparticles: The Insufficiency of Non-2D Cell Culture

Taking it a step further, riboflavin was used to crosslink collagen fibrils at the fluid leaving surface. The hypothesis was that nanoparticle retention could be increased if the fibrils at the FLS were crosslinked prior to compression so that the fibril mesh would start blocking fluid outflow at an earlier stage of the process. However, the retention of nanoparticles of the riboflavin-treated constructs was only slightly lower compared to untreated constructs with no significant difference (Figure 6.13). The photoactivation process might have caused some bleaching of the fluorescent nanoparticles resulting in lower nanoparticle-retention measured when the crosslinking might have actually increased it. This is unlikely since the fluorescent dye absorbs at 495 nm, although some bleaching might have occurred, but probably not to an extent as to skew the results. A more probable explanation is that the fibrils in collagen hydrogels are spaced too far apart to be affected by photoactivated riboflavin crosslinking, consistent with the very low matrix fibril density of hydrogels. Crosslinking the entire gel prior to compression could prove to be more effective, although this might affect the compression process itself.

We wanted to show that this could be done using other types of nanoparticles as well, and that this system is not limited to the hyaluronan nanoparticles. Therefore we tested the chitosan nanoparticles in this plastic compression system. The GCPQ-NR particles were not only of different material, but also of a different size. Being an order of magnitude smaller than the HA-NP, we hypothesised that much more of the initial load of GCPQ-NR would be lost following compression as the FLS would have to be a lot denser before being able to block GCPQ-NR escape.

Chapter 6: Understanding Local Tissue Fate of Nanoparticles: The Insufficiency of Non-2D Cell Culture

The results were surprising. As can be seen in Figure 6.9, the hypothesis was incorrect, and the trapping efficiency was actually quite similar to that for the HA-NP in all construct variants. It is possible that the modified chitosan binds to the collagen fibrils, making their escape from the gel more difficult. Clumping of particles could also be a contributing factor as larger clumps would trap more easily.

The effect of matrix density on nanoparticle movement was again demonstrated in these collagen constructs. In acellular nanoparticle-loaded samples, there was minimal, if any, release of nanoparticles after 3 weeks in culture (excluding the first 24 hours, which is down to re-swelling of the scaffolds, affecting both cellular and acellular samples (see also Chapter 4)). When cells were involved, remodelling of the collagen matrix resulted in the loosening of the scaffold, thus releasing trapped nanoparticles. Predictably, it is clear then, that densely packed matrix retains nanoparticles better, and that cell action allows them to move and escape. In other words, particle release from the depots is related to cell remodelling (more rapid cell-matrix remodelling, faster release).

In our comparison of HA-NP uptake by cells, differences were detected between the two systems, although further work needs to be done to verify them. Ideally, as many conditions as possible would have been kept constant bar the cells being grown in monolayer or in collagen matrices. However, this was difficult in practice, though some of these difficulties were a simple consequence of the 3D environment. In 3D cell culture, the HA-NP was contained in a 50 μ l fluid volume

Chapter 6: Understanding Local Tissue Fate of Nanoparticles: The Insufficiency of Non-2D Cell Culture

confined in space by the matrix following compression. So for a fair comparison to 2D cell culture, the same amount of HA-NP should be suspended in the same amount of liquid. This was not literally feasible because 50 μl would not cover the entire monolayer in a 16 mm diameter well. So to keep at least one component constant between 2D and 3D cell culture, the same concentration of HA-NP within compressed scaffolds (19 $\mu\text{g}/\text{ml}$) was used for the 2D cell cultures. This means that a larger total HA-NP was present in each well as 0.5 ml of culture medium to ensure the entire monolayer was submerged. But concentration, not total dose, is the governing parameter for uptake. The results of cellular uptake of nanoparticles in 2D or 3D show the differences between these two culture set-ups (Figure 6.17).

Firstly, when cells were cultured as a monolayer, uptake of nanoparticles reached a peak that was twice as high as when cells were cultured in collagen scaffolds (red dotted lines - 60 compared to 30). Secondly, the peak for monolayer cell uptake was attained twice as quickly as for 3D cultured cells (blue dotted lines - 3 days compared to 7 days). In 2D cell culture, the nanoparticles are suspended in water and have no barriers to cross to reach the cells, unlike in the *in vivo* environment. Consequently, the monolayer of cells would have come into direct contact with a large number of nanoparticles throughout the assay. This would be enhanced over time as the nanoparticles would have begun settling, thus increasing their local concentration on the surface of the monolayer (Figure 6.21) [406]. In the 2D study, cells reached their peak uptake within just 3 days compared to 7 days for cells within a dense matrix. This corresponds to around a 6-fold overestimate of uptake by cells cultured in 2D if we use the readout at 3 days. This difference may account

for the cytotoxic effects observed when certain agents are tested on monolayers, when in 3D tissues, they may not actually be all that harmful [407,408].

However, this comparison maintains HA-NP concentration as a constant in both systems, which means that cells cultured in 2D were actually exposed to a greater total amount of HA-NP than cells in collagen constructs. This may account for the faster uptake of a greater amount of HA-NP. To further examine uptake dynamics differences, the total HA-NP amount should be kept constant.

6.5. Conclusions

It was shown here that HA-NPs and GCPQ-NR-NPs can be incorporated into PC collagen constructs. This shows that other types of nanoparticles can potentially be used with PC constructs for testing. Both particle types were retained within constructs with similar efficiencies in a single layer construct but slightly different efficiencies in double-layered constructs. This perhaps indicates a complex relationship between the fluid dynamics and particle properties that requires further investigation. It appears that HA-NPs were physically trapped within the dense collagen meshwork following compression since there was little change in the entrapped amount after 3 weeks in culture without cells. With cellular remodeling of the matrix, the HA-NPs were released into the media. Cells were shown to take up HA-NP at different rates when cultured as a monolayer on TCP or within compressed constructs. This study indicates that HA-NP-loaded compressed constructs can be used as a model to study cell-nanoparticle interactions.

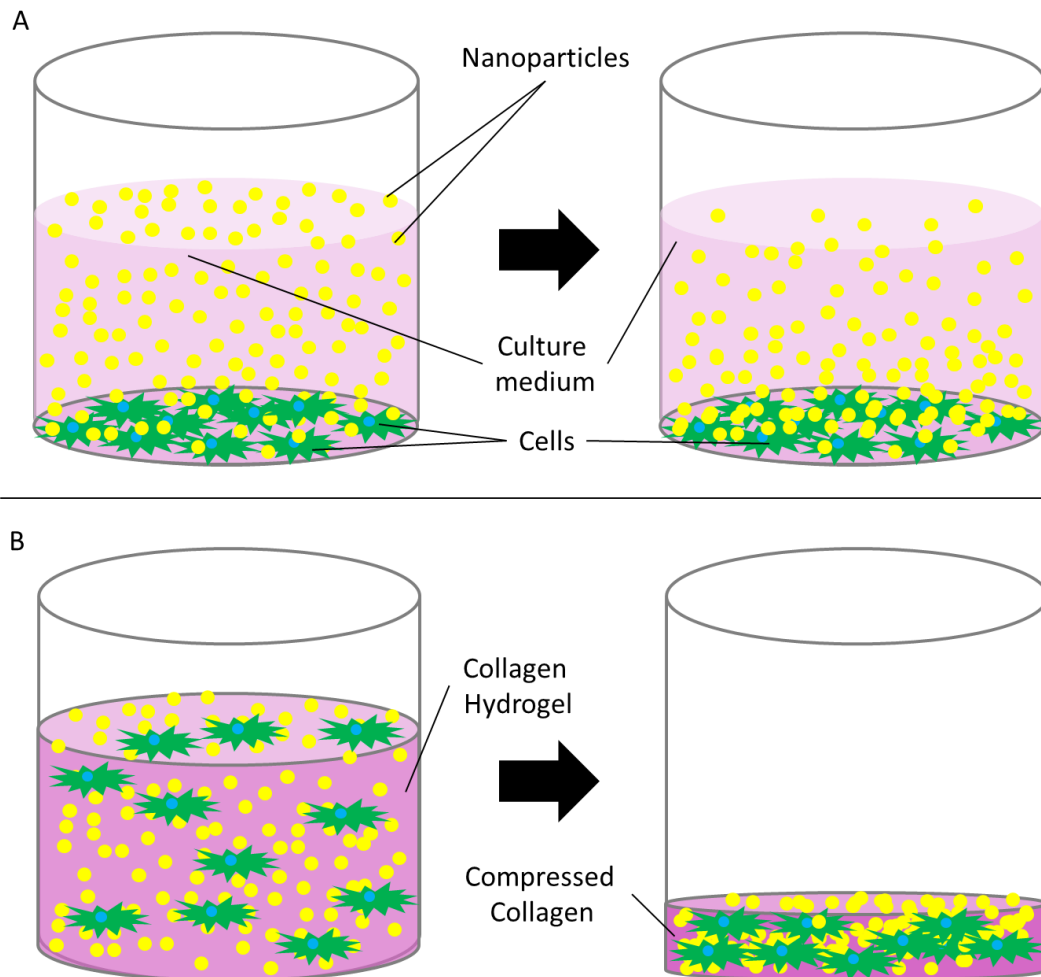


Figure 6.21: Schematic depicting cellular exposure to nanoparticles. (A): Cells cultured as a monolayer (2D) with nanoparticles dispersed in the culture medium. Only the apical surface of the cells is exposed to the nanoparticles. Over time, the nanoparticles will begin to settle, increasing the nanoparticle concentration in the locality of the monolayer. (B): Cells and nanoparticles in a collagen hydrogel before and after compression. The cells cultured in 3D are exposed to the nanoparticles from all directions. The collagen also acts as a barrier for transport, limiting nanoparticle movement and creating nutrient gradients as occurs *in vivo*.

Chapter 7: General Discussion

7.1. Summary

The aim of this project was to engineer a tissue-like *in vitro* system to assess hyaluronan nanoparticles, as an improved system to conventional monolayer cell culture. This was done by investigating the incorporation of hyaluronan nanoparticles into plastically compressed (PC) collagen constructs. Firstly, the PC system was scaled up to the 24-well format and re-characterised. The use of a new optical confocal meter for measuring construct thicknesses *in situ* was evaluated and deemed a better technique for thickness determination of compressed constructs than histology. An important finding from the use of the optical confocal meter was that the constructs re-swelled after the first 24 h post-compression. Rates of compaction can potentially be monitored in real-time using the optical confocal meter. Being non-invasive, optical confocal scans can be performed without interfering with the compression process. This real-time monitoring of construct thickness during compression will allow the user to stop compression when the desired construct thickness has been reached.

Another novel method was developed and used in this thesis. Image analysis of Sirius red-stained collagen constructs was performed to investigate the changes in collagen density distributions within constructs. This revealed the presence of secondary FLS's at the bottom of thicker constructs but not in thinner. The accumulation of HA-NP was also shown to correspond to that of collagen, which

indicated to us that the HA-NP moved with the escaping fluid and collagen during compression, until the collagen mesh became too dense for the particles to flow through. Additionally, this analysis method allowed us to better understand micro-moulding and the influence of stamp (cross-sectional) shape on groove depth – round wires generated grooves with better depth fidelities than rectangular-shaped stamps.

Finally, incorporation of hyaluronan nanoparticles into compressed constructs was shown to be feasible, albeit with a 80% reduction amount after compression. This HA-NP retention could be increased by manipulating the system for earlier FLS generation through multi-layering. The entrapment of HA-NP in constructs was possibly due to physical blockage since there was little diffusion of HA-NP from acellular constructs over three weeks in culture, whereas there was a steady release of HA-NP from cellularised constructs over the same period. This cell- and nanoparticle-loaded system was then compared to monolayer culture on tissue culture plastic. The main findings from this comparison were that cells in the monolayer system took up twice as many HA-NP as cells cultured in collagen, and in half (3 days) the time (7 days). However, this will need further investigation since the difference could simply have been due to the greater HA-NP exposure the cells in monolayer received.

During plastic compression, fluid flow is critical in determining the internal distribution of collagen within constructs (Chapters 3 and 5). However, no techniques were available to quantify this. The novel local collagen analysis has

shown that the lamellae at the FLS have much higher densities than the other lamellae within constructs as well as backing up early observations of the presence of a secondary FLS at the bottom of thicker constructs [320].

Poor groove depth fidelities have been reported when patterning compliant gels using a variety of methods [415-418]. Micro-moulding during PC too, results in grooves being shallower than expected. Density analyses have eluded clues as to why this is the case, and template shape has an important effect on groove structure. Embossing micro-topography creates unique collagen distribution profiles which help to stabilise the engineered structures ([337]; Chapter 5). Patterning on the opposite non-fluid leaving surface resulted in poor and unstable structure formation [244]. After collagen density distribution analyses, it is now clearer as to how and why patterning needs to be performed on the FLS.

The collagen density distribution analysis method has also been used to look at nanoparticle distributions within constructs following compression (Chapter 3). Hyaluronan nanoparticles were found to be distributed in the same patterns as collagen fibrils which shows that the moving fluid within compressing gels carry with it both collagen and particles. This supported the hypothesis that the FLS would be dense enough to block nanoparticle escape. The FLS was found to contain a high concentration of hyaluronan nanoparticles which could serve as a depot for studying cell-nanoparticle interactions and behaviour, drug (if loaded into nanoparticles) release kinetics and mechanisms (e.g. if particles breakdown and release drug cargo before cell interactions or if drug is released intracellularly) and

importantly, diffusion of nanoparticles through tissue *in vitro* as tissue-like matrix barriers are absent in many current *in vitro* models.

Both cells and hyaluronan nanoparticles were enmeshed within collagen fibres and cultured for periods up to 3 weeks. The key findings were that cells in compressed collagen took up hyaluronan nanoparticles at a slower rate and only took in half as many nanoparticles at peak uptake than cells cultured as monolayers on tissue culture plastic. This is similar to Biondi et al and Mansfield et al. where cells in monolayer displayed greater nanoparticle uptake, and also falls in line with other studies showing that cells cultured in a 3D environment exhibited greater drug resistance to cells on TCP [69,145,149]. Cells cultured on a flat dish are able to interact with nanoparticles suspended in the culture medium immediately. Furthermore, in time, nanoparticles will begin to settle at the bottom of the well, increasing the local concentrations at the monolayer. This allows cells cultured in 2D to interact with nanoparticles earlier in culture and with a larger number of particles than cells in a dense collagen mesh, especially so when the same concentrations of nanoparticles were used in both systems; cells on TCP would thus be exposed to HA-NP concentrations several times that within compressed constructs, and may have skewed the results. Further comparisons should be carried out by keeping the total HA-NP amount constant.

7.2. Conclusions

Here we described and developed a model of engineered tissue for assessing nanoparticle fate using a cell-independent approach to fabricating dense collagen matrices with cells and nanoparticles enmeshed within collagen fibres. This provided both cells and nanoparticles with a 3D environment as would be experienced in native tissues. Cells require 3-dimensionality to function as they would *in vivo*. The dense collagen network of compressed constructs also acts as a transport barrier for nanoparticles, which recapitulates tissue environments. This thus allows more accurate and predictive data to be generated. Drastic differences were observed when cells were cultured in 2D and in 3D in terms of nanoparticle uptake, highlighting the need for better test models, especially for the pharmaceutical industry where billions of pounds are spent on drug discovery.

Further understanding of plastic compression and the implications of fluid dynamics on collagen deposition leading to fluid leaving surface generation was obtained throughout the course of this study with the aid of the newly development collagen distribution analysis method. A more accurate and reliable method for measuring construct thickness was developed (in conjunction with Lein, A.D.).

7.3. Further work

Further investigation on the mobility of nanoparticles in compressed collagen constructs could be undertaken. Vertical movement of nanoparticles was studied in this project; determining how laterally mobile the nanoparticles are during

compression would allow the fabrication of constructs with predetermined patterns of nanoparticle distribution in the x-y plane.

Hyaluronan has great capability for swelling in aqueous conditions. It would be interesting to examine if the hyaluronan nanoparticles behave in such a way, and how HA-NP re-swelling affects the internal structure of compressed collagen constructs. Hyaluronan has also been implicated in cell migration, so determining if HA-NP have the same effect would be important to assess the possible uses of HA-NP.

The mechanism of HA-NP uptake by cells would be valuable in the advancement of these nanoparticles. Uptake mechanisms by cells cultured either in monolayers or in 3D may be compared and contrasted to identify any differences in cell behaviour in the different culture conditions. Hyaluronan binds to CD44 or RHAMM (receptor for hyaluronic acid-mediated mobility) [413,414]. Therefore, it is important to determine if expression levels of CD44 and RHAMM are similar when cells are cultured in 2D or 3D, and if these HA-NP do indeed bind to CD44, RHAMM or other receptors. Differences in expression by cells cultured in monolayer or within a matrix may account for the differences in uptake described in Chapter 6.

Investigating the intracellular distribution of the nanoparticles will be vital in determining how and when cargo is delivered to the cell. This would involve determining the HA-NP uptake mechanism and their destination, how and when the nanoparticles break down, what happens to the cargo and the nanoparticle

remnants and if and how the cell is affected by the cargo and/or the nanoparticle material.

Nanoparticle testing in this tissue model can be taken further by using drug-loaded hyaluronan nanoparticles and investigating the typical toxicological properties during testing (absorption, distribution, metabolism, excretion and toxicity). Testing the same drug-loaded nanoparticles in 2D cell cultures and animal models would make an excellent comparison and should likely strengthen the case for use of 3D *in vitro* tissue models.

Plastic compression, being a direct approach to tissue engineering, allows many levels of complexity to be built up. In this study, a basic system was used. Much more can be added to make a more sophisticated model. For example, micro-moulding can be performed to introduce micro-architecture to mimic native tissue organisation; Micro-moulding nanoparticle-loaded constructs can also be analysed to look for correlations between collagen deposition and nanoparticle distribution. Additional cell types, proteins and macromolecules can be added to the construct to incorporate additional cell interactions.

As the mechanical properties of a compressed construct is affected by the density of collagen, it will be of interest to determine how the secondary FLS affects construct stiffness. Primary and secondary FLS's may also be compared to compare and contrast the two.

Chapter 7: General Discussion

Exploration down the delivery system route would be intriguing and beneficial. Collagen constructs can potentially be used as a cell carrier and/or drug-loaded nanoparticle reservoir for controlled and sustained release.

References

- [1] A. Abbott, Cell culture: Biology's new dimension, *Nature*, 424 (2003) 870-872.
- [2] D. E. Discher, P. Janmey, and Y. L. Wang, Tissue cells feel and respond to the stiffness of their substrate, *Science*, 310 (2005) 1139-1143.
- [3] T. Elsdale and J. Bard, Collagen Substrata for Studies on Cell Behavior, *Journal of Cell Biology*, 54 (1972) 626-637.
- [4] J. A. Green and K. M. Yamada, Three-dimensional microenvironments modulate fibroblast signaling responses, *Advanced Drug Delivery Reviews*, 59 (2007) 1293-1298.
- [5] K. M. Yamada and E. Cukierman, Modeling tissue morphogenesis and cancer in 3D, *Cell*, 130 (2007) 601-610.
- [6] E. Cukierman, R. Pankov, D. R. Stevens, and K. M. Yamada, Taking cell-matrix adhesions to the third dimension, *Science*, 294 (2001) 1708-1712.
- [7] R. Damianova, N. Stefanova, E. Cukierman, A. Momchilova, and R. Pankov, Three-dimensional matrix induces sustained activation of ERK1/2 via Src/Ras/Raf signaling pathway, *Cell Biology International*, 32 (2008) 229-234.
- [8] P. Friedl and E. B. Brocker, The biology of cell locomotion within three-dimensional extracellular matrix, *Cellular and Molecular Life Sciences*, 57 (2000) 41-64.
- [9] B. Geiger, A. Bershadsky, R. Pankov, and K. M. Yamada, Transmembrane extracellular matrix-cytoskeleton crosstalk, *Nature Reviews Molecular Cell Biology*, 2 (2001) 793-805.
- [10] K. M. Hakkinen, J. S. Harunaga, A. D. Doyle, and K. M. Yamada, Direct Comparisons of the Morphology, Migration, Cell Adhesions, and Actin Cytoskeleton of Fibroblasts in Four Different Three-Dimensional Extracellular Matrices, *Tissue Engineering Part A*, 17 (2011) 713-724.
- [11] T. Tabata and Y. Takei, Morphogens, their identification and regulation, *Development*, 131 (2004) 703-712.
- [12] H. Roelink, J. A. Porter, C. Chiang, Y. Tanabe, D. T. Chang, P. A. Beachy, and T. M. Jessell, Floor Plate and Motor-Neuron Induction by Different Concentrations of the Amino-Terminal Cleavage Product of Sonic Hedgehog Autoproteolysis, *Cell*, 81 (1995) 445-455.

References

- [13] N. L. Halliday and J. J. Tomasek, Mechanical-Properties of the Extracellular-Matrix Influence Fibronectin Fibril Assembly In-Vitro, *Experimental Cell Research*, 217 (1995) 109-117.
- [14] E. Ruoslahti, Integrins as Receptors for Extracellular Matrix, in: E. D. Hay (Ed.), *Cell Biology of the Extracellular Matrix*, Plenum Press, New York, 1991, pp. 343-359.
- [15] J. L. Inman and M. J. Bissell, Apical polarity in three-dimensional culture systems: where to now, *Journal of Microscopy*, 9 (2010).
- [16] M. A. Schwartz, Integrin signaling revisited, *Trends in Cell Biology*, 11 (2001) 466-470.
- [17] R. O. Hynes, The Extracellular Matrix: Not Just Pretty Fibrils, *Science*, 326 (2009) 1216-1219.
- [18] R. L. Juliano and S. Haskill, Signal Transduction from the Extracellular-Matrix, *Journal of Cell Biology*, 120 (1993) 577-585.
- [19] S. H. Kim, J. Turnbull, and S. Guimond, Extracellular matrix and cell signalling: the dynamic cooperation of integrin, proteoglycan and growth factor receptor, *Journal of Endocrinology*, 209 (2011) 139-151.
- [20] M. E. Lukashev and Z. Werb, ECM signalling: orchestrating cell behaviour and misbehaviour, *Trends in Cell Biology*, 8 (1998) 437-441.
- [21] F. M. Watt and W. T. S. Huck, Role of the extracellular matrix in regulating stem cell fate, *Nature Reviews Molecular Cell Biology*, 14 (2013) 467-473.
- [22] H. Baharvand, S. M. Hashemi, S. K. Ashtian, and A. Farrokhi, Differentiation of human embryonic stem cells into hepatocytes in 2D and 3D culture systems in vitro, *International Journal of Developmental Biology*, 50 (2006) 645-652.
- [23] J. E. Barralet, L. Wang, M. Lawson, J. T. Triffitt, P. R. Cooper, and R. M. Shelton, Comparison of bone marrow cell growth on 2D and 3D alginate hydrogels, *Journal of Materials Science-Materials in Medicine*, 16 (2005) 515-519.
- [24] W. L. Grayson, T. Ma, and B. Bunnell, Human mesenchymal stem cells tissue development in 3D PET matrices, *Biotechnology Progress*, 20 (2004) 905-912.
- [25] G. Y. Lee, P. A. Kenny, E. H. Lee, and M. J. Bissell, Three-dimensional culture models of normal and malignant breast epithelial cells, *Nature Methods*, 4 (2007) 359-365.
- [26] T. Ma, Y. Li, S. T. Yang, and D. A. Kniss, Tissue engineering human placenta trophoblast cells in 3-D fibrous matrix: Spatial effects on cell proliferation and function, *Biotechnology Progress*, 15 (1999) 715-724.

References

- [27] S. M. Willerth, K. J. Arendas, D. I. Gottlieb, and S. E. Sakiyama-Elbert, Optimization of fibrin scaffolds for differentiation of murine embryonic stem cells into neural lineage cells, *Biomaterials*, 27 (2006) 5990-6003.
- [28] O. W. Petersen, L. Ronnovjessen, A. R. Howlett, and M. J. Bissell, Interaction with Basement-Membrane Serves to Rapidly Distinguish Growth and Differentiation Pattern of Normal and Malignant Human Breast Epithelial-Cells, *Proceedings of the National Academy of Sciences of the United States of America*, 89 (1992) 9064-9068.
- [29] H. Tanaka, C. L. Murphy, C. Murphy, M. Kimura, S. Kawai, and J. M. Polak, Chondrogenic differentiation of murine embryonic stem cells: Effects of culture conditions and dexamethasone, *Journal of Cellular Biochemistry*, 93 (2004) 454-462.
- [30] K. Bott, Z. Upton, K. Schrobback, M. Ehrbar, J. A. Hubbell, M. P. Lutolf, and S. C. Rizzi, The effect of matrix characteristics on fibroblast proliferation in 3D gels, *Biomaterials*, 31 (2010) 8454-8464.
- [31] L. Schyschka, J. J. M. Sanchez, Z. Wang, B. Burkhardt, U. Muller-Vieira, K. Zeilinger, A. Bachmann, S. Nadalin, G. Damm, and A. K. Nussler, Hepatic 3D cultures but not 2D cultures preserve specific transporter activity for acetaminophen-induced hepatotoxicity, *Archives of Toxicology*, 87 (2013) 1581-1593.
- [32] J. Solon, I. Levental, K. Sengupta, P. C. Georges, and P. A. Janmey, Fibroblast adaptation and stiffness matching to soft elastic substrates, *Biophysical Journal*, 93 (2007) 4453-4461.
- [33] V. Vogel, Mechanotransduction involving multimodular proteins: Converting force into biochemical signals, *Annual Review of Biophysics and Biomolecular Structure*, 35 (2006) 459-488.
- [34] K. Hayakawa, H. Tatsumi, and M. Sokabe, Actin stress fibers transmit and focus force to activate mechanosensitive channels, *Journal of Cell Science*, 121 (2008) 496-503.
- [35] C. Cheung, A. S. Bernardo, M. W. B. Trotter, R. A. Pedersen, and S. Sinha, Generation of human vascular smooth muscle subtypes provides insight into embryological origin-dependent disease susceptibility, *Nature Biotechnology*, 30 (2012) 165-173.
- [36] S. Sinha, M. H. Hoofnagle, P. A. Kingston, M. E. McCanna, and G. K. Owens, Transforming growth factor-beta 1 signaling contributes to development of smooth muscle cells from embryonic stem cells, *American Journal of Physiology-Cell Physiology*, 287 (2004) C1560-C1568.
- [37] P. J. Wipff, D. B. Rifkin, J. J. Meister, and B. Hinz, Myofibroblast contraction activates latent TGF-beta 1 from the extracellular matrix, *Journal of Cell Biology*, 179 (2007) 1311-1323.

References

- [38] L. Buscemi, D. Ramonet, F. Klingberg, A. Formey, J. Smith-Clerc, J. J. Meister, and B. Hinz, The Single-Molecule Mechanics of the Latent TGF-beta 1 Complex, *Current Biology*, 21 (2011) 2046-2054.
- [39] B. C. Low, C. Q. Pan, G. V. Shivashankar, A. Bershadsky, M. Sudol, and M. Sheetz, YAP/TAZ as mechanosensors and mechanotransducers in regulating organ size and tumor growth, *Febs Letters*, 588 (2014) 2663-2670.
- [40] M. Sudol and K. F. Harvey, Modularity in the Hippo signaling pathway, *Trends in Biochemical Sciences*, 35 (2010) 627-633.
- [41] S. Dupont, L. Morsut, M. Aragona, E. Enzo, S. Giulitti, M. Cordenonsi, F. Zanconato, J. Le Digabel, M. Forcato, S. Bicciato, N. Elvassore, and S. Piccolo, Role of YAP/TAZ in mechanotransduction, *Nature*, 474 (2011) 179-U212.
- [42] S. M. Thomasy, J. T. Morgan, J. A. Wood, C. J. Murphy, and P. Russell, Substratum stiffness and latrunculin B modulate the gene expression of the mechanotransducers YAP and TAZ in human trabecular meshwork cells, *Experimental Eye Research*, 113 (2013) 66-73.
- [43] M. Aragona, T. Panciera, A. Manfrin, S. Giulitti, F. Michielin, N. Elvassore, S. Dupont, and S. Piccolo, A Mechanical Checkpoint Controls Multicellular Growth through YAP/TAZ Regulation by Actin-Processing Factors, *Cell*, 154 (2013) 1047-1059.
- [44] E. Cukierman, R. Pankov, and K. M. Yamada, Cell interactions with three-dimensional matrices, *Current Opinion in Cell Biology*, 14 (2002) 633-639.
- [45] S. I. Fraley, Y. F. Feng, R. Krishnamurthy, D. H. Kim, A. Celedon, G. D. Longmore, and D. Wirtz, A distinctive role for focal adhesion proteins in three-dimensional cell motility, *Nature Cell Biology*, 12 (2010) 598-U169.
- [46] P. Friedl, F. Entschladen, C. Conrad, B. Niggemann, and K. S. Zanker, CD4(+) T lymphocytes migrating in three-dimensional collagen lattices lack focal adhesions and utilize beta 1 integrin-independent strategies for polarization, interaction with collagen fibers and locomotion, *European Journal of Immunology*, 28 (1998) 2331-2343.
- [47] B. Z. Katz, E. Zamir, A. Bershadsky, Z. Kam, K. M. Yamada, and B. Geiger, Physical state of the extracellular matrix regulates the structure and molecular composition of cell-matrix adhesions, *Molecular Biology of the Cell*, 11 (2000) 1047-1060.
- [48] W. M. Petroll, L. Ma, and J. V. Jester, Direct correlation of collagen matrix deformation with focal adhesion dynamics in living corneal fibroblasts, *Journal of Cell Science*, 116 (2003) 1481-1491.
- [49] E. Tamariz and F. Grinnell, Modulation of fibroblast morphology and adhesion during collagen matrix remodeling, *Molecular Biology of the Cell*, 13 (2002) 3915-3929.

References

- [50] X. M. Zhou, R. G. Rowe, N. Hiraoka, J. P. George, D. Wirtz, D. F. Mosher, I. Virtanen, M. A. Chernousov, and S. J. Weiss, Fibronectin fibrillogenesis regulates three-dimensional neovessel formation, *Genes & Development*, 22 (2008) 1231-1243.
- [51] N. Alam, H. L. Goel, M. J. Zarif, J. E. Butterfield, H. M. Perkins, B. G. Sansoucy, T. K. Sawyer, and L. R. Languino, The integrin - Growth factor receptor duet, *Journal of Cellular Physiology*, 213 (2007) 649-653.
- [52] M. D. Pierschbacher and E. Ruoslahti, Cell Attachment Activity of Fibronectin Can be Duplicated by Small Synthetic Fragments of the Molecule, *Nature*, 309 (1984) 30-33.
- [53] E. Ruoslahti, RGD and other recognition sequences for integrins, *Annual Review of Cell and Developmental Biology*, 12 (1996) 697-715.
- [54] S. A. Lelievre, V. M. Weaver, J. A. Nickerson, C. A. Larabell, A. Bhaumik, O. W. Petersen, and M. J. Bissell, Tissue phenotype depends on reciprocal interactions between the extracellular matrix and the structural organization of the nucleus, *Proceedings of the National Academy of Sciences of the United States of America*, 95 (1998) 14711-14716.
- [55] E. Hadjipanayi, V. Mudera, and R. A. Brown, Close dependence of fibroblast proliferation on collagen scaffold matrix stiffness, *Journal of Tissue Engineering and Regenerative Medicine*, 3 (2009) 77-84.
- [56] H. L. Ashe and J. Briscoe, The interpretation of morphogen gradients, *Development*, 133 (2006) 385-394.
- [57] A. Birgersdotter, R. Sandberg, and I. Ernberg, Gene expression perturbation in vitro - A growing case for three-dimensional (3D) culture systems, *Seminars in Cancer Biology*, 15 (2005) 405-412.
- [58] C. S. Chen, M. Mrksich, S. Huang, G. M. Whitesides, and D. E. Ingber, Geometric control of cell life and death, *Science*, 276 (1997) 1425-1428.
- [59] J. Le Beyec, R. Xu, S. Y. Lee, C. M. Nelson, A. Rizki, J. Alcaraz, and M. J. Bissell, Cell shape regulates global histone acetylation in human mammary epithelial cells, *Experimental Cell Research*, 313 (2007) 3066-3075.
- [60] G. Karp, *Cell and molecular biology: Concepts and experiments*, John Wiley and Sons, Hoboken, NJ, 2005.
- [61] T. Wakatsuki, M. S. Kolodney, G. I. Zahalak, and E. L. Elson, Cell mechanics studied by a reconstituted model tissue, *Biophysical Journal*, 79 (2000) 2353-2368.
- [62] B. Geiger and A. Bershadsky, Exploring the neighborhood: Adhesion-coupled cell mechanosensors, *Cell*, 110 (2002) 139-142.
- [63] P. C. Georges and P. A. Janmey, Cell type-specific response to growth on soft materials, *Journal of Applied Physiology*, 98 (2005) 1547-1553.

References

- [64] R. S. Gieni and M. J. Hendzel, Mechanotransduction from the ECM to the genome: Are the pieces now in place?, *Journal of Cellular Biochemistry*, 104 (2008) 1964-1987.
- [65] T. Yeung, P. C. Georges, L. A. Flanagan, B. Marg, M. Ortiz, M. Funaki, N. Zahir, W. Y. Ming, V. Weaver, and P. A. Janmey, Effects of substrate stiffness on cell morphology, cytoskeletal structure, and adhesion, *Cell Motility and the Cytoskeleton*, 60 (2005) 24-34.
- [66] A. L. Sieminski, R. P. Hebbel, and K. J. Gooch, The relative magnitudes of endothelial force generation and matrix stiffness modulate capillary morphogenesis in vitro, *Experimental Cell Research*, 297 (2004) 574-584.
- [67] B. Vailhe, X. Ronot, P. Tracqui, Y. Usson, and L. Tranqui, In vitro angiogenesis is modulated by the mechanical properties of fibrin gels and is related to $\alpha(v)\beta(3)$ integrin localization, *In Vitro Cellular & Developmental Biology-Animal*, 33 (1997) 763-773.
- [68] R. B. Vernon, J. C. Angello, M. L. Iruelaarispe, T. F. Lane, and E. H. Sage, Reorganization of Basement-Membrane Matrices by Cellular Traction Promotes the Formation of Cellular Networks In vitro, *Laboratory Investigation*, 66 (1992) 536-547.
- [69] H. K. Dhiman, A. R. Ray, and A. K. Panda, Three-dimensional chitosan scaffold-based MCF-7 cell culture for the determination of the cytotoxicity of tamoxifen, *Biomaterials*, 26 (2005) 979-986.
- [70] S. Myers and A. Baker, Drug discovery - an operating model for a new era, *Nature Biotechnology*, 19 (2001) 727-730.
- [71] A. Dove, Drug screening - Beyond the bottleneck, *Nature Biotechnology*, 17 (1999) 859-863.
- [72] K. A. Beningo, M. Dembo, and Y. I. Wang, Responses of fibroblasts to anchorage of dorsal extracellular matrix receptors, *Proceedings of the National Academy of Sciences of the United States of America*, 101 (2004) 18024-18029.
- [73] F. Grinnell, Fibroblast biology in three-dimensional collagen matrices, *Trends in Cell Biology*, 13 (2003) 264-269.
- [74] F. Berthiaume, P. V. Moghe, M. Toner, and M. L. Yarmush, Effect of extracellular matrix topology on cell structure, function, and physiological responsiveness: Hepatocytes cultured in a sandwich configuration, *Faseb Journal*, 10 (1996) 1471-1484.
- [75] C. Kiecker and C. Niehrs, A morphogen gradient of Wnt/beta-catenin signalling regulates anteroposterior neural patterning in *Xenopus*, *Development*, 128 (2001) 4189-4201.
- [76] L. Wolpert, Cell boundaries: knowing who to mix with and what to shout or whisper, *Development*, 130 (2003) 4497-4500.

References

- [77] R. Gebhardt, Metabolic Zonation of the Liver - Regulation and Implications for Liver-Function, *Pharmacology & Therapeutics*, 53 (1992) 275-354.
- [78] R. Gebhardt, J. G. Hengstler, D. Muller, R. Glockner, P. Buening, B. Laube, E. Schmelzer, M. Ullrich, D. Utesch, N. Hewitt, M. Ringel, B. R. Hilz, A. Bader, A. Langsch, T. Koose, H. J. Burger, J. Maas, and F. Oesch, New hepatocyte in vitro systems for drug metabolism: Metabolic capacity and recommendations for application in basic research and drug development, standard operation procedures, *Drug Metabolism Reviews*, 35 (2003) 145-213.
- [79] R. Gebhardt and M. Matz-Soja, Liver zonation: Novel aspects of its regulation and its impact on homeostasis, *World Journal of Gastroenterology*, 20 (2014) 8491-8504.
- [80] M. Matz-Soja, A. Hovhannisyanyan, and R. Gebhardt, Hedgehog signalling pathway in adult liver: A major new player in hepatocyte metabolism and zonation?, *Medical Hypotheses*, 80 (2013) 589-594.
- [81] R. R. Lareu, I. Arsianti, H. K. Subramhanya, Y. X. Peng, and M. Raghunath, In vitro enhancement of collagen matrix formation and crosslinking for applications in tissue engineering: A preliminary study, *Tissue Engineering*, 13 (2007) 385-391.
- [82] A. S. Zeiger, F. C. Loe, R. Li, M. Raghunath, and K. J. Van Vliet, Macromolecular Crowding Directs Extracellular Matrix Organization and Mesenchymal Stem Cell Behavior, *Plos One*, 7:5 (2012), e37094.
- [83] R. O. Hynes, Integrins: Bidirectional, allosteric signaling machines, *Cell*, 110 (2002) 673-687.
- [84] M. Larsen, V. V. Artym, J. A. Green, and K. M. Yamada, The matrix reorganized: extracellular matrix remodeling and integrin signaling, *Current Opinion in Cell Biology*, 18 (2006) 463-471.
- [85] A. Gabizon, H. Shmeeda, and Y. Barenholz, Pharmacokinetics of pegylated liposomal doxorubicin - Review of animal and human studies, *Clinical Pharmacokinetics*, 42 (2003) 419-436.
- [86] A. A. Gabizon, Selective Tumor-Localization and Improved Therapeutic Index of Anthracyclines Encapsulated in Long-Circulating Liposomes, *Cancer Research*, 52 (1992) 891-896.
- [87] M. L. Hans and A. M. Lowman, Biodegradable nanoparticles for drug delivery and targeting, *Current Opinion in Solid State & Materials Science*, 6 (2002) 319-327.
- [88] D. W. Northfelt, F. J. Martin, P. Working, P. A. Volberding, J. Russell, M. Newman, M. A. Amantea, and L. D. Kaplan, Doxorubicin encapsulated in liposomes containing surface-found polyethylene glycol: Pharmacokinetics, tumor localization, and safety in patients with AIDS-related Kaposi's sarcoma, *Journal of Clinical Pharmacology*, 36 (1996) 55-63.

References

- [89] M. Yokoyama, T. Okano, Y. Sakurai, H. Ekimoto, C. Shibazaki, and K. Kataoka, Toxicity and Antitumor Activity against Solid Tumors of Mice-forming Polymeric Anticancer Drug and Its Extremely Long Circulation in Blood, *Cancer Research*, 51 (1991) 3229-3236.
- [90] T. M. Allen and P. R. Cullis, Drug delivery systems: Entering the mainstream, *Science*, 303 (2004) 1818-1822.
- [91] H. Maeda, J. Wu, T. Sawa, Y. Matsumura, and K. Hori, Tumor vascular permeability and the EPR effect in macromolecular therapeutics: a review, *Journal of Controlled Release*, 65 (2000) 271-284.
- [92] X. F. Zhang, Y. X. Li, X. S. Chen, X. H. Wang, X. Y. Xu, Q. Z. Liang, J. L. Hu, and X. B. Jing, Synthesis and characterization of the paclitaxel/MPEG-PLA block copolymer conjugate, *Biomaterials*, 26 (2005) 2121-2128.
- [93] K. M. Dupont, K. Sharma, H. Y. Stevens, J. D. Boerckel, A. J. Garcia, and R. E. Guldberg, Human stem cell delivery for treatment of large segmental bone defects, *Proceedings of the National Academy of Sciences of the United States of America*, 107 (2010) 3305-3310.
- [94] A. Cabanes, K. E. Briggs, P. C. Gokhale, J. A. Treat, and A. Rahman, Comparative in vivo studies with paclitaxel and liposome-encapsulated paclitaxel, *International Journal of Oncology*, 12 (1998) 1035-1040.
- [95] J. M. M. Terwogt, G. Groenewegen, D. Pluim, M. Maliepaard, M. M. Tibben, A. Huisman, W. W. T. Huinink, M. Schot, H. Welbank, E. E. Voest, J. H. Beijnen, and J. H. M. Schellens, Phase I and pharmacokinetic study of SPI-77, a liposomal encapsulated dosage form of cisplatin, *Cancer Chemotherapy and Pharmacology*, 49 (2002) 201-210.
- [96] H. Hillaireau and P. Couvreur, Nanocarriers' entry into the cell: relevance to drug delivery, *Cellular and Molecular Life Sciences*, 66 (2009) 2873-2896.
- [97] L. A. Bareford and P. W. Swaan, Endocytic mechanisms for targeted drug delivery, *Advanced Drug Delivery Reviews*, 59 (2007) 748-758.
- [98] A. R. Hilgenbrink and P. S. Low, Folate receptor-mediated drug targeting: From therapeutics to diagnostics, *Journal of Pharmaceutical Sciences*, 94 (2005) 2135-2146.
- [99] S. D. Weitman, R. H. Lark, L. R. Coney, D. W. Fort, V. Frasca, V. R. Zurawski, and B. A. Kamen, Distribution of the Folate Receptor Gp38 in Normal and Malignant-Cell Lines and Tissues, *Cancer Research*, 52 (1992) 3396-3401.
- [100] W. Zauner, N. A. Farrow, and A. M. R. Haines, In vitro uptake of polystyrene microspheres: effect of particle size, cell line and cell density, *Journal of Controlled Release*, 71 (2001) 39-51.

References

- [101] M. P. Desai, V. Labhasetwar, E. Walter, R. J. Levy, and G. L. Amidon, The mechanism of uptake of biodegradable microparticles in Caco-2 cells is size dependent, *Pharmaceutical Research*, 14 (1997) 1568-1573.
- [102] O. Harush-Frenkel, N. Debotton, S. Benita, and Y. Altschuler, Targeting of nanoparticles to the clathrin-mediated endocytic pathway, *Biochemical and Biophysical Research Communications*, 353 (2007) 26-32.
- [103] K. Giese, J. Kaufmann, G. J. Pronk, and A. Klippel, Unravelling novel intracellular pathways in cell-based assays, *Drug Discovery Today*, 7 (2002) 179-186.
- [104] A. Astashkina, B. Mann, and D. W. Grainger, A critical evaluation of in vitro cell culture models for high-throughput drug screening and toxicity, *Pharmacology & Therapeutics*, 134 (2012) 82-106.
- [105] F. M. Balis, Evolution of anticancer drug discovery and the role of cell-based screening, *Journal of the National Cancer Institute*, 94 (2002) 78-79.
- [106] L. E. Dike, C. S. Chen, M. Mrksich, J. Tien, G. M. Whitesides, and D. E. Ingber, Geometric control of switching between growth, apoptosis, and differentiation during angiogenesis using micropatterned substrates, *In Vitro Cellular & Developmental Biology-Animal*, 35 (1999) 441-448.
- [107] T. R. Polte, G. S. Eichler, N. Wang, and D. E. Ingber, Extracellular matrix controls myosin light chain phosphorylation and cell contractility through modulation of cell shape and cytoskeletal prestress, *American Journal of Physiology-Cell Physiology*, 286 (2004) C518-C528.
- [108] R. Singhvi, A. Kumar, G. P. Lopez, G. N. Stephanopoulos, D. I. C. Wang, G. M. Whitesides, and D. E. Ingber, *Engineering Cell-Shape and Function*, *Science*, 264 (1994) 696-698.
- [109] J. Bertino and D. Fish, The safety profile of the fluoroquinolones, *Clinical Therapeutics*, 22 (2000) 798-817.
- [110] M. J. Liguori, E. A. G. Blomme, and J. F. Waring, Trovafloxacin-induced gene expression changes in liver-derived in vitro systems: Comparison of primary human hepatocytes to HepG2 cells, *Drug Metabolism and Disposition*, 36 (2008) 223-233.
- [111] B. L. Behan, D. G. Dewitt, D. R. Bogdanowicz, A. N. Koppes, S. S. Bale, and D. M. Thompson, Single-walled carbon nanotubes alter Schwann cell behavior differentially within 2D and 3D environments, *Journal of Biomedical Materials Research Part A*, 96A (2011) 46-57.
- [112] R. A. Ettl, J. Kuroda, S. Plassmann, and D. E. Prentice, Successful drug development despite adverse preclinical findings part 1: processes to address issues and most important findings, *J Toxicol Pathol.*, 23 (2010) 189-211.
- [113] H. Olson, G. Betton, D. Robinson, K. Thomas, A. Monro, G. Kolaja, P. Lilly, J. Sanders, G. Sipes, W. Bracken, M. Dorato, K. Van Deun, P. Smith, B.

References

- Berger, and A. Heller, Concordance of the toxicity of pharmaceuticals in humans and in animals, *Regulatory Toxicology and Pharmacology*, 32 (2000) 56-67.
- [114] N. Shanks, R. Greek, and J. Greek, Are animal models predictive for humans?, *Philosophy, Ethics, and Humanities in Medicine*, 4:2 (2009).
- [115] J. Allen, P. Jeffrey, R. Williams, and A. J. Ratcliffe, Approaches to Assessing Drug Safety in the Discovery Phase Highlights of the Society for Medicines Research Symposium Held on September 24Th, 2009, at the National Heart & Lung Institute, Kensington, London, Uk, *Drugs of the Future*, 35 (2010) 67-75.
- [116] I. Kola and J. Landis, Can the pharmaceutical industry reduce attrition rates?, *Nature Reviews Drug Discovery*, 3 (2004) 711-715.
- [117] B. Munos, Lessons from 60 years of pharmaceutical innovation, *Nature Reviews Drug Discovery*, 8 (2009) 959-968.
- [118] I. Cavero, Exploratory Safety Pharmacology: a new safety paradigm to de-risk drug candidates prior to selection for regulatory science investigations, *Expert Opinion on Drug Safety*, 8 (2009) 627-647.
- [119] S. M. Paul, D. S. Mytelka, C. T. Dunwiddie, C. C. Persinger, B. H. Munos, S. R. Lindborg, and A. L. Schacht, How to improve R&D productivity: the pharmaceutical industry's grand challenge, *Nature Reviews Drug Discovery*, 9 (2010) 203-214.
- [120] G. Oberdorster, E. Oberdorster, and J. Oberdorster, Nanotoxicology: An emerging discipline evolving from studies of ultrafine particles, *Environmental Health Perspectives*, 113 (2005) 823-839.
- [121] C. A. Poland, R. Duffin, I. Kinloch, A. Maynard, W. A. H. Wallace, A. Seaton, V. Stone, S. Brown, W. MacNee, and K. Donaldson, Carbon nanotubes introduced into the abdominal cavity of mice show asbestos-like pathogenicity in a pilot study, *Nature Nanotechnology*, 3 (2008) 423-428.
- [122] S. J. Kuhn, D. E. Hallahan, and T. D. Giorgio, Characterization of superparamagnetic nanoparticle interactions with extracellular matrix in an in vitro system, *Annals of Biomedical Engineering*, 34 (2006) 51-58.
- [123] S. Arora, J. M. Rajwade, and K. M. Paknikar, Nanotoxicology and in vitro studies: The need of the hour, *Toxicology and Applied Pharmacology*, 258 (2012) 151-165.
- [124] A. D. Lehmann, F. Blank, O. Baum, P. Gehr, and B. M. Rothen-Rutishauser, Diesel exhaust particles modulate the tight junction protein occludin in lung cells in vitro, *Particle and Fibre Toxicology*, 6:26 (2009), 1-14.
- [125] M. J. D. Clift, P. Gehr, and B. Rothen-Rutishauser, Nanotoxicology: a perspective and discussion of whether or not in vitro testing is a valid alternative, *Archives of Toxicology*, 85 (2011) 723-731.

References

- [126] D. W. Hwang, D. S. Lee, and S. Kim, Gene Expression Profiles for Genotoxic Effects of Silica-Free and Silica-Coated Cobalt Ferrite Nanoparticles, *Journal of Nuclear Medicine*, 53 (2012) 106-112.
- [127] C. Uboldi, G. Giudetti, F. Broggi, D. Gilliland, J. Ponti, and F. Rossi, Amorphous silica nanoparticles do not induce cytotoxicity, cell transformation or genotoxicity in Balb/3T3 mouse fibroblasts, *Mutation Research-Genetic Toxicology and Environmental Mutagenesis*, 745 (2012) 11-20.
- [128] J. P. Kaiser, P. Wick, P. Manser, P. Spohn, and A. Bruinink, Single walled carbon nanotubes (SWCNT) affect cell physiology and cell architecture, *Journal of Materials Science-Materials in Medicine*, 19 (2008) 1523-1527.
- [129] L. K. Limbach, Y. C. Li, R. N. Grass, T. J. Brunner, M. A. Hintermann, M. Muller, D. Gunther, and W. J. Stark, Oxide nanoparticle uptake in human lung fibroblasts: Effects of particle size, agglomeration, and diffusion at low concentrations, *Environmental Science & Technology*, 39 (2005) 9370-9376.
- [130] K. Donaldson, P. J. A. Borm, V. Castranova, and M. Gulumian, The limits of testing particle-mediated oxidative stress in vitro in predicting diverse pathologies; relevance for testing of nanoparticles, *Particle and Fibre Toxicology*, 6:13 (2009).
- [131] C. M. Sayes, K. L. Reed, and D. B. Warheit, Assessing toxicity of fine and nanoparticles: Comparing in vitro measurements to in vivo pulmonary toxicity profiles, *Toxicological Sciences*, 97 (2007) 163-180.
- [132] G. Bhabra, A. Sood, B. Fisher, L. Cartwright, M. Saunders, W. H. Evans, A. Surprenant, G. Lopez-Castejon, S. Mann, S. A. Davis, L. A. Hails, E. Ingham, P. Verkade, J. Lane, K. Heesom, R. Newson, and C. P. Case, Nanoparticles can cause DNA damage across a cellular barrier, *Nature Nanotechnology*, 4 (2009) 876-883.
- [133] B. M. Rothen-Rutishauser, S. G. Kiama, and P. Gehr, A three-dimensional cellular model of the human respiratory tract to study the interaction with particles, *American Journal of Respiratory Cell and Molecular Biology*, 32 (2005) 281-289.
- [134] L. Muller, M. Riediker, P. Wick, M. Mohr, P. Gehr, and B. Rothen-Rutishauser, Oxidative stress and inflammation response after nanoparticle exposure: differences between human lung cell monocultures and an advanced three-dimensional model of the human epithelial airways, *Journal of the Royal Society Interface*, 7 (2010) S27-S40.
- [135] A. Guillouzo, Liver cell models in in vitro toxicology, *Environmental Health Perspectives*, 106 (1998) 511-532.
- [136] E. L. LeCluyse, Human hepatocyte culture systems for the in vitro evaluation of cytochrome P450 expression and regulation, *European Journal of Pharmaceutical Sciences*, 13 (2001) 343-368.

References

- [137] A. Sivaraman, J. K. Leach, S. Townsend, T. Iida, B. J. Hogan, D. B. Stolz, R. Fry, L. D. Samson, S. R. Tannenbaum, and L. G. Griffith, A microscale in vitro physiological model of the liver: Predictive screens for drug metabolism and enzyme induction, *Current Drug Metabolism*, 6 (2005) 569-591.
- [138] E. L. LeCluyse, R. P. Witek, M. E. Andersen, and M. J. Powers, Organotypic liver culture models: Meeting current challenges in toxicity testing, *Critical Reviews in Toxicology*, 42 (2012) 501-548.
- [139] A. Moreau, P. Maurel, M. J. Vilarem, and J. M. Pascussi, Constitutive androstane receptor-vitamin D receptor crosstalk: Consequence on CYP24 gene expression, *Biochemical and Biophysical Research Communications*, 360 (2007) 76-82.
- [140] J. M. Pascussi, A. Robert, M. Nguyen, O. Wairant-Debray, M. Garabedian, P. Martin, T. Pineau, J. Saric, F. Navarro, P. Maurel, and M. J. Vilarem, Possible involvement of pregnane X receptor-enhanced CYP24 expression in drug-induced osteomalacia, *Journal of Clinical Investigation*, 115 (2005) 177-186.
- [141] A. Guillouzo and C. Guguen-Guillouzo, Evolving concepts in liver tissue modeling and implications for in vitro toxicology, *Expert Opinion on Drug Metabolism & Toxicology*, 4 (2008) 1279-1294.
- [142] S. R. Khetani and S. N. Bhatia, Microscale culture of human liver cells for drug development, *Nature Biotechnology*, 26 (2008) 120-126.
- [143] Y. A. Bi, D. Kazolias, and D. B. Duignan, Use of cryopreserved human hepatocytes in sandwich culture to measure hepatobiliary transport, *Drug Metabolism and Disposition*, 34 (2006) 1658-1665.
- [144] O. J. Trask, A. Moore, and E. L. LeCluyse, A Micropatterned Hepatocyte Coculture Model for Assessment of Liver Toxicity Using High-Content Imaging Analysis, *Assay and Drug Development Technologies*, 12 (2014) 16-27.
- [145] M. Biondi, D. Guarnieri, H. Yu, V. Belli, and P. A. Netti, Sub-100 nm biodegradable nanoparticles: in vitro release features and toxicity testing in 2D and 3D cell cultures, *Nanotechnology*, 24 (2013) 045101.
- [146] S. W. Choi, J. W. Xie, and Y. N. Xia, Chitosan-Based Inverse Opals: Three-Dimensional Scaffolds with Uniform Pore Structures for Cell Culture, *Advanced Materials*, 21 (2009) 2997-3001.
- [147] K. Domansky, W. Inman, J. Serdy, A. Dash, M. H. M. Lim, and L. G. Griffith, Perfused multiwell plate for 3D liver tissue engineering, *Lab on A Chip*, 10 (2010) 51-58.
- [148] E. Hirata, M. Uo, H. Takita, T. Akasaka, F. Watari, and A. Yokoyama, Development of a 3D Collagen Scaffold Coated With Multiwalled Carbon Nanotubes, *Journal of Biomedical Materials Research Part B-Applied Biomaterials*, 90B (2009) 629-634.

References

- [149] J. Lee, G. D. Lilly, R. C. Doty, P. Podsiadlo, and N. A. Kotov, *In vitro Toxicity Testing of Nanoparticles in 3D Cell Culture*, *Small*, 5 (2009) 1213-1221.
- [150] M. Y. Lee, R. A. Kumar, S. M. Sukumaran, M. G. Hogg, D. S. Clark, and J. S. Dordick, *Three-dimensional cellular microarray for high-throughput toxicology assays*, *Proceedings of the National Academy of Sciences of the United States of America*, 105 (2008) 59-63.
- [151] S. Levenberg, N. F. Huang, E. Lavik, A. B. Rogers, J. Itskovitz-Eldor, and R. Langer, *Differentiation of human embryonic stem cells on three-dimensional polymer scaffolds*, *Proceedings of the National Academy of Sciences of the United States of America*, 100 (2003) 12741-12746.
- [152] S. Mayer-Wagner, T. S. Schiergens, B. Sievers, J. I. Redeker, B. Schmitt, A. Buettner, V. Jansson, and P. E. Muller, *Scaffold-free 3D cellulose acetate membrane-based cultures form large cartilaginous constructs*, *Journal of Tissue Engineering and Regenerative Medicine*, 5 (2011) 151-155.
- [153] Y. S. Pek, A. C. A. Wan, A. Shekaran, L. Zhuo, and J. Y. Ying, *A thixotropic nanocomposite gel for three-dimensional cell culture*, *Nature Nanotechnology*, 3 (2008) 671-675.
- [154] N. A. Peppas, J. Z. Hilt, A. Khademhosseini, and R. Langer, *Hydrogels in biology and medicine: From molecular principles to bionanotechnology*, *Advanced Materials*, 18 (2006) 1345-1360.
- [155] C. E. Semino, J. R. Merok, G. G. Crane, G. Panagiotakos, and S. G. Zhang, *Functional differentiation of hepatocyte-like spheroid structures from putative liver progenitor cells in three-dimensional peptide scaffolds*, *Differentiation*, 71 (2003) 262-270.
- [156] T. Seyama, E. Y. Suh, and T. Kondo, *Three-dimensional culture of epidermal cells on ordered cellulose scaffolds*, *Biofabrication*, 5 (2013) 025010.
- [157] L. D. Shea, E. Smiley, J. Bonadio, and D. J. Mooney, *DNA delivery from polymer matrices for tissue engineering*, *Nature Biotechnology*, 17 (1999) 551-554.
- [158] G. A. Silva, C. Czeisler, K. L. Niece, E. Beniash, D. A. Harrington, J. A. Kessler, and S. I. Stupp, *Selective differentiation of neural progenitor cells by high-epitope density nanofibers*, *Science*, 303 (2004) 1352-1355.
- [159] S. Talukdar and S. C. Kundu, *A Non-Mulberry Silk Fibroin Protein Based 3D In Vitro Tumor Model for Evaluation of Anticancer Drug Activity*, *Advanced Functional Materials*, 22 (2012) 4778-4788.
- [160] Y. C. Tung, A. Y. Hsiao, S. G. Allen, Y. S. Torisawa, M. Ho, and S. Takayama, *High-throughput 3D spheroid culture and drug testing using a 384 hanging drop array*, *Analyst*, 136 (2011) 473-478.

References

- [161] E. K. F. Yim and K. W. Leong, Proliferation and differentiation of human embryonic germ cell derivatives in bioactive polymeric fibrous scaffold, *Journal of Biomaterials Science-Polymer Edition*, 16 (2005) 1193-1217.
- [162] M. Yu, S. H. Huang, K. J. Yu, and A. M. Clyne, Dextran and Polymer Polyethylene Glycol (PEG) Coating Reduce Both 5 and 30 nm Iron Oxide Nanoparticle Cytotoxicity in 2D and 3D Cell Culture, *International Journal of Molecular Sciences*, 13 (2012) 5554-5570.
- [163] I. Ajioka, S. Ichinose, K. Nakajima, and H. Mizusawa, Basement membrane-like matrix sponge for the three-dimensional proliferation culture of differentiated retinal horizontal interneurons, *Biomaterials*, 32 (2011) 5765-5772.
- [164] J. Blumenthal, S. I. Cohen-Matsliah, and S. Levenberg, Olfactory Bulb-Derived Cells Seeded on 3D Scaffolds Exhibit Neurotrophic Factor Expression and Pro-Angiogenic Properties, *Tissue Engineering Part A*, 19 (2013) 2284-2291.
- [165] S. E. Francioli, C. Candrian, K. Martin, M. Heberer, I. Martin, and A. Barbero, Effect of three-dimensional expansion and cell seeding density on the cartilage-forming capacity of human articular chondrocytes in type II collagen sponges, *Journal of Biomedical Materials Research Part A*, 95A (2010) 924-931.
- [166] C. Godugu, A. R. Patel, U. Desai, T. Andey, A. Sams, and M. Singh, AlgiMatrix (TM) Based 3D Cell Culture System as an In-Vitro Tumor Model for Anticancer Studies, *Plos One*, 8:1 (2013) e53708.
- [167] E. Hirata, M. Uo, Y. Nodasaka, H. Takita, N. Ushijima, T. Akasaka, F. Watari, and A. Yokoyama, 3D collagen scaffolds coated with multiwalled carbon nanotubes: Initial cell attachment to internal surface, *Journal of Biomedical Materials Research Part B-Applied Biomaterials*, 93B (2010) 544-550.
- [168] H. Hosseinkhani, M. Hosseinkhani, S. Hattori, R. Matsuoka, and N. Kawaguchi, Micro and nano-scale in vitro 3D culture system for cardiac stem cells, *Journal of Biomedical Materials Research Part A*, 94A (2010) 1-8.
- [169] S. Mohajeri, H. Hosseinkhani, N. G. Ebrahimi, L. Nikfarjam, M. Soleimani, and A. M. Kajbafzadeh, Proliferation and Differentiation of Mesenchymal Stem Cell on Collagen Sponge Reinforced with Polypropylene/Polyethylene Terephthalate Blend Fibers, *Tissue Engineering Part A*, 16 (2010) 3821-3830.
- [170] R. A. Brown, *Extreme Tissue Engineering: Concepts and Strategies for Tissue Fabrication*, Wiley-Blackwell, 2013.
- [171] N. C. Hunt and L. M. Grover, Cell encapsulation using biopolymer gels for regenerative medicine, *Biotechnology Letters*, 32 (2010) 733-742.

References

- [172] M. M. Stevens and J. H. George, Exploring and engineering the cell surface interface, *Science*, 310 (2005) 1135-1138.
- [173] J. Glowacki and S. Mizuno, Collagen scaffolds for tissue engineering, *Biopolymers*, 89 (2008) 338-344.
- [174] A. Mandal, V. Meda, W. J. Zhang, K. M. Farhan, and A. Gnanamani, Synthesis, characterization and comparison of antimicrobial activity of PEG/TritonX-100 capped silver nanoparticles on collagen scaffold, *Colloids and Surfaces B-Biointerfaces*, 90 (2012) 191-196.
- [175] J. J. Willard, J. W. Drexler, A. Das, S. Roy, S. Shilo, O. Shoseyov, and H. M. Powell, Plant-Derived Human Collagen Scaffolds for Skin Tissue Engineering, *Tissue Engineering Part A*, 19 (2013) 1507-1518.
- [176] Z. M. Xia, X. H. Yu, X. Jiang, H. D. Brody, D. W. Rowe, and M. Wei, Fabrication and characterization of biomimetic collagen-apatite scaffolds with tunable structures for bone tissue engineering, *Acta Biomaterialia*, 9 (2013) 7308-7319.
- [177] C. Lloyd, J. Besse, and S. Boyce, Controlled-rate freezing to regulate the structure of collagen-glycosaminoglycan scaffolds in engineered skin substitutes, *J Biomed Mater Res Part B*, 00 (2014).
- [178] X. Liu, L. A. Smith, J. Hu, and P. X. Ma, Biomimetic nanofibrous gelatin/apatite composite scaffolds for bone tissue engineering, *Biomaterials*, 30 (2009) 2252-2258.
- [179] X. M. Wu, L. Black, G. Santacana-Laffitte, and C. W. Patrick, Preparation and assessment of glutaraldehyde-crosslinked collagen-chitosan hydrogels for adipose tissue engineering, *Journal of Biomedical Materials Research Part A*, 81A (2007) 59-65.
- [180] J. H. Yan, X. M. Li, L. R. Liu, F. J. Wang, T. W. Zhu, and Q. Q. Zhang, Potential use of collagen-chitosan-hyaluronan tri-copolymer scaffold for cartilage tissue engineering, *Artificial Cells Blood Substitutes and Biotechnology*, 34 (2006) 27-39.
- [181] K. A. Faraj, T. H. Van Kuppevelt, and W. F. Daamen, Construction of collagen scaffolds that mimic the three-dimensional architecture of specific tissues, *Tissue Engineering*, 13 (2007) 2387-2394.
- [182] J. Barrila, A. L. Radtke, A. Crabbe, S. F. Sarker, M. M. Herbst-Kralovetz, C. M. Ott, and C. A. Nickerson, Organotypic 3D cell culture models: using the rotating wall vessel to study host-pathogen interactions, *Nature Reviews Microbiology*, 8 (2010) 791-801.
- [183] M. Eiraku, K. Watanabe, M. Matsuo-Takasaki, M. Kawada, S. Yonemura, M. Matsumura, T. Wataya, A. Nishiyama, K. Muguruma, and Y. Sasai, Self-Organized Formation of Polarized Cortical Tissues from ESCs and Its Active Manipulation by Extrinsic Signals, *Cell Stem Cell*, 3 (2008) 519-532.

References

- [184] K. V. Greco, A. J. Iqbal, L. Rattazzi, G. Nalesso, N. Moradi-Bidhendi, A. R. Moore, M. B. Goldring, F. Dell'Accio, and M. Ferretti, High density micromass cultures of a human chondrocyte cell line: A reliable assay system to reveal the modulatory functions of pharmacological agents, *Biochemical Pharmacology*, 82 (2011) 1919-1929.
- [185] R. G. Harrison, Observations on the living developing nerve fiber, *Proceedings of the Society for Experimental Biology and Medicine*, 4 (1907) 140-143.
- [186] J. M. Jukes, S. K. Both, A. Leusink, L. M. T. Sterk, C. A. van Blitterswijk, and J. De Boer, Endochondral bone tissue engineering using embryonic stem cells, *Proceedings of the National Academy of Sciences of the United States of America*, 105 (2008) 6840-6845.
- [187] I. Kehat, D. Kenyagin-Karsenti, M. Snir, H. Segev, M. Amit, A. Gepstein, E. Livne, O. Binah, J. Itskovitz-Eldor, and L. Gepstein, Human embryonic stem cells can differentiate into myocytes with structural and functional properties of cardiomyocytes, *Journal of Clinical Investigation*, 108 (2001) 407-414.
- [188] A. H. Klopp, L. Lacerda, A. Gupta, B. G. Debeb, T. Solley, L. Li, E. Spaeth, W. Xu, X. M. Zhang, M. T. Lewis, J. M. Reuben, S. Krishnamurthy, M. Ferrari, R. Gaspar, T. A. Buchholz, M. Cristofanilli, F. Marini, M. Andreeff, and W. A. Woodward, Mesenchymal Stem Cells Promote Mammosphere Formation and Decrease E-Cadherin in Normal and Malignant Breast Cells, *Plos One*, 5:8 (2010) e12180.
- [189] N. Lumelsky, O. Blondel, P. Laeng, I. Velasco, R. Ravin, and R. McKay, Differentiation of embryonic stem cells to insulin-secreting structures similar to pancreatic islets, *Science*, 292 (2001) 1389-1394.
- [190] N. C. Rivron, J. Rouwkema, R. Truckenmuller, M. Karperien, J. De Boer, and C. A. van Blitterswijk, Tissue assembly and organization: Developmental mechanisms in microfabricated tissues, *Biomaterials*, 30 (2009) 4851-4858.
- [191] N. C. Rivron, C. C. Raiss, J. Liu, A. Nandakumar, C. Sticht, N. Gretz, R. Truckenmuller, J. Rouwkema, and C. A. van Blitterswijk, Sonic Hedgehog-activated engineered blood vessels enhance bone tissue formation, *Proceedings of the National Academy of Sciences of the United States of America*, 109 (2012) 4413-4418.
- [192] H. Suga, T. Kadoshima, M. Minaguchi, M. Ohgushi, M. Soen, T. Nakano, N. Takata, T. Wataya, K. Muguruma, H. Miyoshi, S. Yonemura, Y. Oiso, and Y. Sasai, Self-formation of functional adenohypophysis in three-dimensional culture, *Nature*, 480 (2011) 57-U215.
- [193] J. Carlsson and J. M. Yuhas, Liquid-Overlay Culture of Cellular Spheroids, *Recent Results in Cancer Research*, 95 (1984) 1-23.

References

- [194] J. Friedrich, C. Seidel, R. Ebner, and L. A. Kunz-Schughart, Spheroid-based drug screen: considerations and practical approach, *Nature Protocols*, 4 (2009) 309-324.
- [195] P. Gunness, D. Mueller, V. Shevchenko, E. Heinzle, M. Ingelman-Sundberg, and F. Noor, 3D Organotypic Cultures of Human HepaRG Cells: A Tool for In Vitro Toxicity Studies, *Toxicological Sciences*, 133 (2013) 67-78.
- [196] A. Nagelkerke, J. Bussink, F. C. G. J. Sweep, and P. N. Span, Generation of multicellular tumor spheroids of breast cancer cells: How to go three-dimensional, *Analytical Biochemistry*, 437 (2013) 17-19.
- [197] V. I. Sikavitsas, G. N. Bancroft, and A. G. Mikos, Formation of three-dimensional cell/polymer constructs for bone tissue engineering in a spinner flask and a rotating wall vessel bioreactor, *Journal of Biomedical Materials Research*, 62 (2002) 136-148.
- [198] B. R. Unsworth and P. I. Lelkes, Growing tissues in microgravity, *Nature Medicine*, 4 (1998) 901-907.
- [199] M. Banerjee and R. R. Bhonde, Application of hanging drop technique for stem cell differentiation and cytotoxicity studies, *Cytotechnology*, 51 (2006) 1-5.
- [200] Y. Luo, C. M. Wang, M. Hossain, Y. Qiao, L. Y. Ma, J. C. An, and M. Su, Three-Dimensional Microtissue Assay for High-Throughput Cytotoxicity of Nanoparticles, *Analytical Chemistry*, 84 (2012) 6731-6738.
- [201] P. Bartholoma, Impidjati, A. Reininger-Mack, Z. H. Zhang, H. Thielecke, and A. Robitzki, A more aggressive breast cancer spheroid model coupled to an electronic capillary sensor system for a high-content screening of cytotoxic agents in cancer therapy: 3-dimensional in vitro tumor spheroids as a screening model, *Journal of Biomolecular Screening*, 10 (2005) 705-714.
- [202] X. L. Zhang, W. Wang, W. T. Yu, Y. B. Xie, X. H. Zhang, Y. Zhang, and X. J. Ma, Development of an in vitro multicellular tumor spheroid model using microencapsulation and its application in anticancer drug screening and testing, *Biotechnology Progress*, 21 (2005) 1289-1296.
- [203] M. Harimoto, M. Yamato, M. Hirose, C. Takahashi, Y. Isoi, A. Kikuchi, and T. Okano, Novel approach for achieving double-layered cell sheets co-culture: overlaying endothelial cell sheets onto monolayer hepatocytes utilizing temperature-responsive culture dishes, *Journal of Biomedical Materials Research*, 62 (2002) 464-470.
- [204] K. Watanabe, M. Yamato, Y. Hayashida, J. Yang, A. Kikuchi, T. Okano, Y. Tano, and K. Nishida, Development of transplantable genetically modified corneal epithelial cell sheets for gene therapy, *Biomaterials*, 28 (2007) 745-749.
- [205] T. Ide, K. Nishida, M. Yamato, T. Sumide, M. Utsumi, T. Nozaki, A. Kikuchi, T. Okano, and Y. Tano, Structural characterization of bioengineered

References

- human corneal endothelial cell sheets fabricated on temperature-responsive culture dishes, *Biomaterials*, 27 (2006) 607-614.
- [206] K. Kojima, L. J. Bonassar, A. K. Roy, H. Mizuno, J. Cortiella, and C. A. Vacanti, A composite tissue-engineered trachea using sheep nasal chondrocyte and epithelial cells, *Faseb Journal*, 17 (2003) 823-828.
- [207] T. Shimizu, M. Yamato, A. Kikuchi, and T. Okano, Cell sheet engineering for myocardial tissue reconstruction, *Biomaterials*, 24 (2003) 2309-2316.
- [208] T. Sumide, K. Nishida, M. Yamato, T. Ide, Y. Hayashida, K. Watanabe, J. Yang, C. Kohno, A. Kikuchi, N. Maeda, H. Watanabe, T. Okano, and Y. Tano, Functional human corneal endothelial cell sheets harvested from temperature-responsive culture surfaces, *Faseb Journal*, 20 (2006) 392-394.
- [209] H. Hosoya, K. Kadowaki, M. Matsusaki, H. Cabral, H. Nishihara, H. Ijichi, K. Koike, K. Kataoka, K. Miyazono, M. Akashi, and M. R. Kano, Engineering fibrotic tissue in pancreatic cancer: A novel three-dimensional model to investigate nanoparticle delivery, *Biochemical and Biophysical Research Communications*, 419 (2012) 32-37.
- [210] M. Matsusaki, K. Kadowaki, Y. Nakahara, and M. Akashi, Fabrication of cellular multilayers with nanometer-sized extracellular matrix films, *Angewandte Chemie-International Edition*, 46 (2007) 4689-4692.
- [211] J. A. Cooper, P. J. Delvecchio, F. L. Minnear, K. E. Burhop, W. M. Selig, J. G. N. Garcia, and A. B. Malik, Measurement of Albumin Permeability Across Endothelial Monolayers In vitro, *Journal of Applied Physiology*, 62 (1987) 1076-1083.
- [212] M. A. Deli, C. S. Abraham, Y. Kataoka, and M. Niwa, Permeability studies on in vitro blood-brain barrier models: Physiology, pathology, and pharmacology, *Cellular and Molecular Neurobiology*, 25 (2005) 59-127.
- [213] N. L'Heureux, S. Paquet, R. Labbe, L. Germain, and F. A. Auger, A completely biological tissue-engineered human blood vessel, *Faseb Journal*, 12 (1998) 47-56.
- [214] J. Yang, M. Yamato, T. Shimizu, H. Sekine, K. Ohashi, M. Kanzaki, T. Ohki, K. Nishida, and T. Okano, Reconstruction of functional tissues with cell sheet engineering, *Biomaterials*, 28 (2007) 5033-5043.
- [215] F. Yang, R. Murugan, S. Wang, and S. Ramakrishna, Electrospinning of nano/micro scale poly(L-lactic acid) aligned fibers and their potential in neural tissue engineering, *Biomaterials*, 26 (2005) 2603-2610.
- [216] H. Yoshimoto, Y. M. Shin, H. Terai, and J. P. Vacanti, A biodegradable nanofiber scaffold by electrospinning and its potential for bone tissue engineering, *Biomaterials*, 24 (2003) 2077-2082.
- [217] D. Kai, M. P. Prabhakaran, G. R. Jin, and S. Ramakrishna, Guided orientation of cardiomyocytes on electrospun aligned nanofibers for cardiac

References

- tissue engineering, *Journal of Biomedical Materials Research Part B-Applied Biomaterials*, 98B (2011) 379-386.
- [218] H. F. Liu, X. M. Li, G. Zhou, H. B. Fan, and Y. B. Fan, Electrospun sulfated silk fibroin nanofibrous scaffolds for vascular tissue engineering, *Biomaterials*, 32 (2011) 3784-3793.
- [219] Y. Ji, K. Ghosh, X. Z. Shu, B. Q. Li, J. C. Sokolov, G. D. Prestwich, R. A. F. Clark, and M. H. Rafailovich, Electrospun three-dimensional hyaluronic acid nanofibrous scaffolds, *Biomaterials*, 27 (2006) 3782-3792.
- [220] A. Matsuda, G. Kagata, R. Kino, and J. Tanaka, Preparation of chitosan nanofiber tube by electrospinning, *Journal of Nanoscience and Nanotechnology*, 7 (2007) 852-855.
- [221] J. H. Song, H. E. Kim, and H. W. Kim, Production of electrospun gelatin nanofiber by water-based co-solvent approach, *Journal of Materials Science-Materials in Medicine*, 19 (2008) 95-102.
- [222] J. A. Matthews, G. E. Wnek, D. G. Simpson, and G. L. Bowlin, Electrospinning of collagen nanofibers, *Biomacromolecules*, 3 (2002) 232-238.
- [223] S. P. Zhong, W. E. Teo, X. Zhu, R. W. Beuerman, S. Ramakrishna, and L. Y. L. Yung, An aligned nanofibrous collagen scaffold by electrospinning and its effects on in vitro fibroblast culture, *Journal of Biomedical Materials Research Part A*, 79A (2006) 456-463.
- [224] S. E. Badylak, The extracellular matrix as a scaffold for tissue reconstruction, *Seminars in Cell & Developmental Biology*, 13 (2002) 377-383.
- [225] T. W. Gilbert, T. L. Sellaro, and S. F. Badylak, Decellularization of tissues and organs, *Biomaterials*, 27 (2006) 3675-3683.
- [226] S. Cebotari, H. Mertsching, K. Kallenbach, S. Kostin, O. Repin, A. Batrinac, C. Kleczka, A. Ciubotaru, and A. Haverich, Construction of autologous human heart valves based on an acellular allograft matrix, *Circulation*, 106 (2002) I63-I68.
- [227] G. Steinhoff, U. Stock, N. Karim, H. Mertsching, A. Timke, R. R. Meliss, K. Pethig, A. Haverich, and A. Bader, Tissue engineering of pulmonary heart valves on allogenic acellular matrix conduits - In vivo restoration of valve tissue, *Circulation*, 102 (2000) 50-55.
- [228] R. W. Grauss, M. G. Hazekamp, F. Oppenhuizen, C. J. van Munsteren, A. C. Gittenberger-de Groot, and M. C. DeRuijter, Histological evaluation of decellularised porcine aortic valves: matrix changes due to different decellularisation methods, *European Journal of Cardio-Thoracic Surgery*, 27 (2005) 566-571.
- [229] K. Schenke-Layland, O. Vasilevski, F. Opitz, K. Konig, I. Riemann, K. J. Halbhuber, T. Wahlers, and U. A. Stock, Impact of decellularization of

References

- xenogeneic tissue on extracellular matrix integrity for tissue engineering of heart valves, *Journal of Structural Biology*, 143 (2003) 201-208.
- [230] M. P. Lutolf and J. A. Hubbell, Synthetic biomaterials as instructive extracellular microenvironments for morphogenesis in tissue engineering, *Nature Biotechnology*, 23 (2005) 47-55.
- [231] A. Evangelatov and R. Pankov, The evolution of three-dimensional cell cultures towards unimpeded regenerative medicine and tissue engineering, in: J. A. Andrades (Ed.), *Regenerative Medicine and Tissue Engineering*, InTech, 2013, pp. 221-246.
- [232] K. Chitcholtan, E. Asselin, S. Parent, P. H. Sykes, and J. J. Evans, Differences in growth properties of endometrial cancer in three dimensional (3D) culture and 2D cell monolayer, *Experimental Cell Research*, 319 (2013) 75-87.
- [233] J. F. Alvarez-Barreto, B. Landy, S. VanGordon, L. Place, P. L. DeAngelis, and V. I. Sikavitsas, Enhanced osteoblastic differentiation of mesenchymal stem cells seeded in RGD-functionalized PLLA scaffolds and cultured in a flow perfusion bioreactor, *Journal of Tissue Engineering and Regenerative Medicine*, 5 (2011) 464-475.
- [234] D. Loessner, K. S. Stok, M. P. Lutolf, D. W. Hutmacher, J. A. Clements, and S. C. Rizzi, Bioengineered 3D platform to explore cell-ECM interactions and drug resistance of epithelial ovarian cancer cells, *Biomaterials*, 31 (2010) 8494-8506.
- [235] M. C. Cushing and K. S. Anseth, Hydrogel cell cultures, *Science*, 316 (2007) 1133-1134.
- [236] D. L. Holliday, K. T. Brouillette, A. Markert, L. A. Gordon, and J. L. Jones, Novel multicellular organotypic models of normal and malignant breast: tools for dissecting the role of the microenvironment in breast cancer progression, *Breast Cancer Research*, 11 (2009).
- [237] P. Allen, J. Melero-Martin, and J. Bischoff, Type I collagen, fibrin and PuraMatrix matrices provide permissive environments for human endothelial and mesenchymal progenitor cells to form neovascular networks, *Journal of Tissue Engineering and Regenerative Medicine*, 5 (2011) E74-E86.
- [238] M. T. Valentine, Z. E. Perlman, M. L. Gardel, J. H. Shin, P. Matsudaira, T. J. Mitchison, and D. A. Weitz, Colloid surface chemistry critically affects multiple particle tracking measurements of biomaterials, *Biophysical Journal*, 86 (2004) 4004-4014.
- [239] S. Ricard-Blum, *The Collagen Family*, Cold Spring Harbor Perspectives in Biology, 3 (2011).
- [240] A. Kureshi, U. Cheema, T. Alekseeva, A. Cambrey, and R. Brown, Alignment hierarchies: engineering architecture from the nanometre to the

References

- micrometre scale, *Journal of the Royal Society Interface*, 7 (2010) S707-S716.
- [241] V. Ottani, M. Raspanti, and A. Ruggeri, Collagen structure and functional implications, *Micron*, 32 (2001) 251-260.
- [242] D. M. Maurice, The cornea and sclera, in: H. Davson (Ed.), *The Eye*, Academic Press, Inc. (London) Ltd, 1984, pp. 1-129.
- [243] D. F. Holmes, M. J. Capaldi, and J. A. Chapman, Reconstitution of collagen fibrils in vitro; the assembly process depends on the initiating procedure, *Int. J. Biol. Macromol.*, 8 (1986) 161-166.
- [244] T. Alekseeva, E. Hadjipanayi, E. A. Abou Neel, and R. A. Brown, Engineering Stable Topography in Dense Bio-Mimetic 3D Collagen Scaffolds, *European Cells & Materials*, 23 (2012) 28-40.
- [245] C. C. Berry, G. Campbell, A. Spadicino, M. Robertson, and A. S. G. Curtis, The influence of microscale topography on fibroblast attachment and motility, *Biomaterials*, 25 (2004) 5781-5788.
- [246] E. Hadjipanayi, V. Mudera, and R. A. Brown, Guiding Cell Migration in 3D: A Collagen Matrix with Graded Directional Stiffness, Cell Motility and the Cytoskeleton, 66 (2009) 121-128.
- [247] X. F. Walboomers, W. Monaghan, A. S. G. Curtis, and J. A. Jansen, Attachment of fibroblasts on smooth and microgrooved polystyrene, *Journal of Biomedical Materials Research*, 46 (1999) 212-220.
- [248] X. F. Walboomers, L. A. Ginsel, and J. A. Jansen, Early spreading events of fibroblasts on microgrooved substrates, *Journal of Biomedical Materials Research*, 51 (2000) 529-534.
- [249] P. Clark, P. Connolly, A. S. G. Curtis, J. A. T. Dow, and C. D. W. Wilkinson, Topographical Control of Cell Behavior .2. Multiple Grooved Substrata, *Development*, 108 (1990) 635-644.
- [250] P. Clark, P. Connolly, A. S. G. Curtis, J. A. T. Dow, and C. D. W. Wilkinson, Topographical Control of Cell Behavior .1. Simple Step Cues, *Development*, 99 (1987) 439-448.
- [251] G. Felsenfeld and M. Groudine, Controlling the double helix, *Nature*, 421 (2003) 448-453.
- [252] A. Malhas, C. F. Lee, R. Sanders, N. J. Saunders, and D. J. Vaux, Defects in lamin B1 expression or processing affect interphase chromosome position and gene expression, *Journal of Cell Biology*, 176 (2007) 593-603.
- [253] A. Mazumder and G. V. Shivashankar, Gold-nanoparticle-assisted laser perturbation of chromatin assembly reveals unusual aspects of nuclear architecture within living cells, *Biophysical Journal*, 93 (2007) 2209-2216.

References

- [254] I. S. Mehta, M. Amira, A. J. Harvey, and J. M. Bridger, Rapid chromosome territory relocation by nuclear motor activity in response to serum removal in primary human fibroblasts, *Genome Biology*, 11 (2010).
- [255] L. E. McNamara, R. Burchmore, M. O. Riehle, P. Herzyk, M. J. P. Biggs, C. D. W. Wilkinson, A. S. G. Curtis, and M. J. Dalby, The role of microtopography in cellular mechanotransduction, *Biomaterials*, 33 (2012) 2835-2847.
- [256] A. Li, P. J. Simmons, and P. Kaur, Identification and isolation of candidate human keratinocyte stem cells based on cell surface phenotype, *Proceedings of the National Academy of Sciences of the United States of America*, 95 (1998) 3902-3907.
- [257] H. Schluter, S. Paquet-Fifield, P. Gangatirkar, J. Li, and P. Kaur, Functional Characterization of Quiescent Keratinocyte Stem Cells and Their Progeny Reveals a Hierarchical Organization in Human Skin Epidermis, *Stem Cells*, 29 (2011) 1256-1268.
- [258] A. Webb, A. Li, and P. Kaur, Location and phenotype of human adult keratinocyte stem cells of the skin, *Differentiation*, 72 (2004) 387-395.
- [259] A. Giangreco, S. J. Goldie, V. Failla, G. Saintigny, and F. M. Watt, Human Skin Aging Is Associated with Reduced Expression of the Stem Cell Markers beta 1 Integrin and MCSP, *Journal of Investigative Dermatology*, 130 (2010) 604-608.
- [260] H. S. Dua, V. A. Shanmuganathan, A. O. Powell-Richards, P. J. Tighe, and A. Joseph, Limbal epithelial crypts: a novel anatomical structure and a putative limbal stem cell niche, *British Journal of Ophthalmology*, 89 (2005) 529-532.
- [261] M. Nikkhah, F. Edalat, S. Manoucheri, and A. Khademhosseini, Engineering microscale topographies to control the cell-substrate interface, *Biomaterials*, 33 (2012) 5230-5246.
- [262] D. Qin, Y. N. Xia, and G. M. Whitesides, Soft lithography for micro- and nanoscale patterning, *Nature Protocols*, 5 (2010) 491-502.
- [263] E. S. Gil, S. H. Park, J. Marchant, F. Omenetto, and D. L. Kaplan, Response of Human Corneal Fibroblasts on Silk Film Surface Patterns, *Macromolecular Bioscience*, 10 (2010) 664-673.
- [264] R. B. Vernon, M. D. Gooden, S. L. Lara, and T. N. Wight, Microgrooved fibrillar collagen membranes as scaffolds for cell support and alignment, *Biomaterials*, 26 (2005) 3131-3140.
- [265] R. B. Vernon, M. D. Gooden, S. L. Lara, and T. N. Wight, Native fibrillar collagen membranes of micron-scale and submicron thicknesses for cell support and perfusion, *Biomaterials*, 26 (2005) 1109-1117.

References

- [266] E. Vrana, N. Builles, M. Hindie, O. Damour, A. Aydinli, and V. Hasirci, Contact guidance enhances the quality of a tissue engineered corneal stroma, *Journal of Biomedical Materials Research Part A*, 84A (2008) 454-463.
- [267] G. D. Pins, M. Toner, and J. R. Morgan, Microfabrication of an analog of the basal lamina: biocompatible membranes with complex topographies, *Faseb Journal*, 14 (2000) 593-602.
- [268] K. M. Chrobak, D. R. Potter, and J. Tien, Formation of perfused, functional microvascular tubes in vitro, *Microvascular Research*, 71 (2006) 185-196.
- [269] A. L. Clement, T. J. Moutinho, and G. D. Pins, Micropatterned dermal-epidermal regeneration matrices create functional niches that enhance epidermal morphogenesis, *Acta Biomaterialia*, 9 (2013) 9474-9484.
- [270] M. D. Tang, A. P. Golden, and J. Tien, Molding of three-dimensional microstructures of gels, *Journal of the American Chemical Society*, 125 (2003) 12988-12989.
- [271] M. Cabodi, N. W. Choi, J. P. Gleghorn, C. S. D. Lee, L. J. Bonassar, and A. D. Stroock, A microfluidic biomaterial, *Journal of the American Chemical Society*, 127 (2005) 13788-13789.
- [272] J. Yeh, Y. B. Ling, J. M. Karp, J. Gantz, A. Chandawarkar, G. Eng, J. Blumling, R. Langer, and A. Khademhosseini, Micromolding of shape-controlled, harvestable cell-laden hydrogels, *Biomaterials*, 27 (2006) 5391-5398.
- [273] K. Sakaguchi, T. Shimizu, S. Horaguchi, H. Sekine, M. Yamato, M. Umezu, and T. Okano, In Vitro Engineering of Vascularized Tissue Surrogates, *Scientific Reports*, 3 (2013).
- [274] A. P. Golden and J. Tien, Fabrication of microfluidic hydrogels using molded gelatin as a sacrificial element, *Lab on A Chip*, 7 (2007) 720-725.
- [275] T. Alekseeva, E. A. Abou Neel, J. C. Knowles, and R. A. Brown, Development of Conical Soluble Phosphate Glass Fibers for Directional Tissue Growth, *Journal of Biomaterials Applications*, 26 (2012) 733-744.
- [276] S. N. Nazhat, E. A. Abou Neel, A. Kidane, I. Ahmed, C. Hope, M. Kershaw, P. D. Lee, E. Stride, N. Saffari, J. C. Knowles, and R. A. Brown, Controlled microchannelling in dense collagen scaffolds by soluble phosphate glass fibers, *Biomacromolecules*, 8 (2007) 543-551.
- [277] J. S. Miller, K. R. Stevens, M. T. Yang, B. M. Baker, D. H. T. Nguyen, D. M. Cohen, E. Toro, A. A. Chen, P. A. Galie, X. Yu, R. Chaturvedi, S. N. Bhatia, and C. S. Chen, Rapid casting of patterned vascular networks for perfusable engineered three-dimensional tissues, *Nature Materials*, 11 (2012) 768-774.
- [278] B. A. Roeder, K. Kokini, J. E. Sturgis, J. P. Robinson, and S. L. Voytik-Harbin, Tensile mechanical properties of three-dimensional type I collagen

References

- extracellular matrices with varied microstructure, *Journal of Biomechanical Engineering-Transactions of the Asme*, 124 (2002) 214-222.
- [279] E. Hadjipanayi, M. Ananta, M. Binkowski, I. Streeter, Z. Lu, Z. F. Cui, R. A. Brown, and V. Mudera, Mechanisms of structure generation during plastic compression of nanofibrillar collagen hydrogel scaffolds: towards engineering of collagen, *Journal of Tissue Engineering and Regenerative Medicine*, 5 (2011) 505-519.
- [280] E. Bell, B. Ivarsson, and C. Merrill, Production of A Tissue-Like Structure by Contraction of Collagen Lattices by Human-Fibroblasts of Different Proliferative Potential Invitro, *Proceedings of the National Academy of Sciences of the United States of America*, 76 (1979) 1274-1278.
- [281] W. R. Legant, J. S. Miller, B. L. Blakely, D. M. Cohen, G. M. Genin, and C. S. Chen, Measurement of mechanical tractions exerted by cells in three-dimensional matrices, *Nature Methods*, 7 (2010) 969-U113.
- [282] D. L. Butler, C. Gooch, K. R. C. Kinneberg, G. P. Boivin, M. T. Galloway, V. S. Nirmalanandhan, J. T. Shearn, N. A. Dymant, and N. Juncosa-Melvin, The use of mesenchymal stem cells in collagen-based scaffolds for tissue-engineered repair of tendons, *Nature Protocols*, 5 (2010) 849-863.
- [283] S. Thomopoulos, R. Das, V. Birman, L. Smith, K. Ku, E. L. Elson, K. M. Pryse, J. P. Marquez, and G. M. Genin, Fibrocartilage Tissue Engineering: The Role of the Stress Environment on Cell Morphology and Matrix Expression, *Tissue Engineering Part A*, 17 (2011) 1039-1053.
- [284] O. Adebayo, T. A. Hookway, J. Z. Hu, K. L. Billiar, and M. W. Rolle, Self-assembled smooth muscle cell tissue rings exhibit greater tensile strength than cell-seeded fibrin or collagen gel rings, *Journal of Biomedical Materials Research Part A*, 101 (2013) 428-437.
- [285] W. H. Eaglstein and V. Falanga, Tissue engineering and the development of Apligraf(R), a human skin equivalent, *Clinical Therapeutics*, 19 (1997) 894-905.
- [286] Z. Feng, M. Yamato, T. Akutsu, T. Nakamura, T. Okano, and M. Umezu, Investigation on the mechanical properties of contracted collagen gels as a scaffold for tissue engineering, *Artificial Organs*, 27 (2003) 84-91.
- [287] V. Charulatha and A. Rajaram, Influence of different crosslinking treatments on the physical properties of collagen membranes, *Biomaterials*, 24 (2003) 759-767.
- [288] S. Ibusuki, G. J. Halbesma, M. A. Randolph, R. W. Redmond, I. E. Kochevar, and T. J. Gill, Photochemically cross-linked collagen gels as three-dimensional scaffolds for tissue engineering, *Tissue Engineering*, 13 (2007) 1995-2001.
- [289] C. H. Lee, A. Singla, and Y. Lee, Biomedical applications of collagen, *International Journal of Pharmaceutics*, 221 (2001) 1-22.

References

- [290] D. P. Knight, L. Nash, X. W. Hu, J. Haffegge, and M. W. Ho, In vitro formation by reverse dialysis of collagen gels containing highly oriented arrays of fibrils, *Journal of Biomedical Materials Research*, 41 (1998) 185-191.
- [291] L. Besseau, B. Coulomb, C. Lebreton-Decoster, and M. M. Giraud-Guille, Production of ordered collagen matrices for three-dimensional cell culture, *Biomaterials*, 23 (2002) 27-36.
- [292] G. Mosser, A. Anglo, C. Helary, Y. Bouligand, and M. M. Giraud-Guille, Dense tissue-like collagen matrices formed in cell-free conditions, *Matrix Biology*, 25 (2006) 3-13.
- [293] Y. Wang, J. Silvent, M. Robin, F. Babonneau, A. Meddahi-Pelle, N. Nassif, and M. M. G. Guille, Controlled collagen assembly to build dense tissue-like materials for tissue engineering, *Soft Matter*, 7 (2011) 9659-9664.
- [294] C. Helary, A. Foucault-Bertaud, G. Godeau, B. Coulomb, and M. M. G. Guille, Fibroblast populated dense collagen matrices: cell migration, cell density and metalloproteinases expression, *Biomaterials*, 26 (2005) 1533-1543.
- [295] C. Helary, L. Ovtracht, B. Coulomb, G. Godeau, and M. M. Giraud-Guille, Dense fibrillar collagen matrices: A model to study myofibroblast behaviour during wound healing, *Biomaterials*, 27 (2006) 4443-4452.
- [296] J. L. Puetzer and L. J. Bonassar, High density type I collagen gels for tissue engineering of whole menisci, *Acta Biomaterialia*, 9 (2013) 7787-7795.
- [297] Z. Feng, Y. Tateishi, Y. Nomura, T. Kitajima, and T. Nakamura, Construction of fibroblast-collagen gels with orientated fibrils induced by static or dynamic stress: toward the fabrication of small tendon grafts, *J Artif Organs*, 9 (2006) 220-225.
- [298] T. S. Girton, V. H. Barocas, and R. T. Tranquillo, Confined compression of a tissue-equivalent: Collagen fibril and cell alignment in response to anisotropic strain, *Journal of Biomechanical Engineering-Transactions of the Asme*, 124 (2002) 568-575.
- [299] R. A. Brown, M. Wiseman, C. B. Chuo, U. Cheema, and S. N. Nazhat, Ultrarapid engineering of biomimetic materials and tissues: Fabrication of nano- and microstructures by plastic compression, *Advanced Functional Materials*, 15 (2005) 1762-1770.
- [300] R. A. Brown, In the beginning there were soft collagen-cell gels: towards better 3D connective tissue models?, *Experimental Cell Research*, 319 (2013) 2460-2469.
- [301] R. A. Brown, Direct Collagen-Material Engineering for Tissue Fabrication, *Tissue Engineering Part A*, 19 (2013) 1495-1498.

References

- [302] K. K. Hu, H. Shi, J. Zhu, D. Deng, G. D. Zhou, W. J. Zhang, Y. L. Cao, and W. Liu, Compressed collagen gel as the scaffold for skin engineering, *Biomedical Microdevices*, 12 (2010) 627-635.
- [303] M. Georgiou, S. C. J. Bunting, H. A. Davies, A. J. Loughlin, J. P. Golding, and J. B. Phillips, Engineered neural tissue for peripheral nerve repair, *Biomaterials*, 34 (2013) 7335-7343.
- [304] H. J. Levis, J. Menzel-Severing, R. A. L. Drake, and J. T. Daniels, Plastic Compressed Collagen Constructs for Ocular Cell Culture and Transplantation: A New and Improved Technique of Confined Fluid Loss, *Current Eye Research*, 38 (2013) 41-52.
- [305] S. L. Mi, B. Chen, B. Wright, and C. J. Connon, Plastic compression of a collagen gel forms a much improved scaffold for ocular surface tissue engineering over conventional collagen gels, *Journal of Biomedical Materials Research Part A*, 95A (2010) 447-453.
- [306] K. P. M. Ricketts, U. Cheema, A. Nyga, A. Castoldi, C. Guazzoni, T. Magdeldin, M. Emberton, A. P. Gibson, G. J. Royle, and M. Loizidou, A 3D In Vitro Cancer Model as a Platform for Nanoparticle Uptake and Imaging Investigations, *Small*, (2014) 3954-3961.
- [307] T. Alekseeva, R. E. Unger, C. Brochhausen, R. A. Brown, and J. C. Kirkpatrick, Engineering a Microvascular Capillary Bed in a Tissue-Like Collagen Construct, *Tissue Engineering*, 20 (2014) 2656-2665.
- [308] L. A. Micol, M. Ananta, E. M. Engelhardt, V. C. Mudera, R. A. Brown, J. A. Hubbell, and P. Frey, High-density collagen gel tubes as a matrix for primary human bladder smooth muscle cells, *Biomaterials*, 32 (2011) 1543-1548.
- [309] M. Ananta, R. A. Brown, and V. Mudera, A Rapid Fabricated Living Dermal Equivalent for Skin Tissue Engineering: An In Vivo Evaluation in an Acute Wound Model, *Tissue Engineering Part A*, 18 (2012) 353-361.
- [310] E. Braziulis, M. Diezi, T. Biedermann, L. Pontiggia, M. Schmucki, F. Hartmann-Fritsch, J. Luginbuhl, C. Schiestl, M. Meuli, and E. Reichmann, Modified Plastic Compression of Collagen Hydrogels Provides an Ideal Matrix for Clinically Applicable Skin Substitutes, *Tissue Engineering Part C-Methods*, 18 (2012) 464-474.
- [311] V. Serpooshan, M. M. Zhao, S. A. Metzler, K. Wei, P. B. Shah, A. Wang, M. Mahmoudi, A. V. Malkovskiy, J. Rajadas, M. J. Butte, D. Bernstein, and P. Ruiz-Lozano, The effect of bioengineered acellular collagen patch on cardiac remodeling and ventricular function post myocardial infarction, *Biomaterials*, 34 (2013) 9048-9055.
- [312] P. Sawadkar, S. Alexander, M. Tolk, J. Wong, D. McGrouther, L. Bozec, and V. Mudera, Development of a Surgically Optimized Graft Insertion Suture Technique to Accommodate a Tissue-Engineered Tendon In Vivo, *BioResearch Open Access*, 2 (2013) 327-335.

References

- [313] A. Khademhosseini and R. Langer, Microengineered hydrogels for tissue engineering, *Biomaterials*, 28 (2007) 5087-5092.
- [314] J. W. Nichol and A. Khademhosseini, Modular tissue engineering: engineering biological tissues from the bottom up, *Soft Matter*, 5 (2009) 1312-1319.
- [315] Wong, J. P. F., Baptista, D., and Brown, R. A. Pre-Crosslinked Polymeric Collagen in 3D Models of Mechanically Stiff Tissues: Blended Collagen Polymer Hydrogels for Rapid Layer Fabrication, *Acta Biomaterialia*, 10:12 (2014), 5005-5011.
- [316] R. A. Brown and J. B. Phillips, Cell responses to biomimetic protein scaffolds used in tissue repair and engineering, *International Review of Cytology - A Survey of Cell Biology*, Vol 262, 262 (2007) 75-150.
- [317] T. Yasui, Y. Tohno, and T. Araki, Determination of collagen fiber orientation in human tissue by use of polarization measurement of molecular second-harmonic-generation light, *Applied Optics*, 43 (2004) 2861-2867.
- [318] U. Cheema, S. N. Nazhat, B. Alp, F. Foroughi, N. Anandagoda, V. Mudera, and R. A. Brown, Fabricating tissues: Analysis of farming versus engineering strategies, *Biotechnology and Bioprocess Engineering*, 12 (2007) 9-14.
- [319] Alekseeva, T., Jawad, H., Purser, M, and Brown, R. A. New Improved Technique of Plastic Compression of Collagen Using Upward Fluid Flow. *International Federation for Medical & Biological Engineering* 30 (2011), 5-8.
- [320] Alekseeva, T. Introducing controllable 3D features into dense collagen constructs for tissue engineering applications, 2011, University College London.
- [321] C. B. Kim and C. B. Su, Measurement of the refractive index of liquids at 1.3 and 1.5 micron using a fibre optic Fresnel ratio meter, *Measurement Science & Technology*, 15 (2004) 1683-1686.
- [322] H. Su and X. G. Huang, Fresnel-reflection-based fiber sensor for on-line measurement of solute concentration in solutions, *Sensors and Actuators B-Chemical*, 126 (2007) 579-582.
- [323] C. Rousseau, S. Poland, J. M. Girkin, A. F. Hall, and C. J. Whitters, Development of fibre-optic confocal microscopy for detection and diagnosis of dental caries, *Caries Research*, 41 (2007) 245-251.
- [324] K. K. Buttenschoen, J. M. Girkin, and D. J. Daly, Development of a low cost confocal instrument to measure the axial dimensions of components in the anterior section of the eye, *Clinical Optometry*, 2 (2010) 67-72.

References

- [325] D. A. Ossipov, X. Yang, O. Varghese, S. Kootala, and J. Hilborn, Modular approach to functional hyaluronic acid hydrogels using orthogonal chemical reactions, *Chemical Communications*, 46 (2010) 8368-8370.
- [326] O. P. Varghese, W. L. Sun, J. Hilborn, and D. A. Ossipov, In Situ Cross-Linkable High Molecular Weight Hyaluronan-Bisphosphonate Conjugate for Localized Delivery and Cell-Specific Targeting: A Hydrogel Linked Prodrug Approach, *Journal of the American Chemical Society*, 131 (2009) 8781-8783.
- [327] X. Yang, S. Kootala, J. Hilborn, and D. A. Ossipov, Preparation of hyaluronic acid nanoparticles via hydrophobic association assisted chemical cross-linking-an orthogonal modular approach, *Soft Matter*, 7 (2011) 7517-7525.
- [328] R. J. Francis, The haematoxylin and eosins, in: J. D. Bancroft and A. Stevens (Eds.), *Theory and Practice of Histological Techniques*, Churchill Livingstone, 1990, pp. 155-175.
- [329] E. M. Engelhardt, E. Stegberg, R. A. Brown, J. A. Hubbell, F. M. Wurm, M. Adam, and P. Frey, Compressed collagen get: a novel scaffold for human bladder cells, *Journal of Tissue Engineering and Regenerative Medicine*, 4 (2010) 123-130.
- [330] E. Hadjipanayi, R. A. Brown, and V. Mudera, Interface integration of layered collagen scaffolds with defined matrix stiffness: implications for sheet-based tissue engineering, *Journal of Tissue Engineering and Regenerative Medicine*, 3 (2009) 230-241.
- [331] J. P. F. Wong, A. J. MacRobert, U. Cheema, and R. A. Brown, Mechanical anisotropy in compressed collagen produced by localised photodynamic cross-linking, *Journal of the Mechanical Behavior of Biomedical Materials*, 18 (2013) 132-139.
- [332] V. S. Constantine and R. W. Mowry, Selective Staining of Human Dermal Collagen .2. Use of Picrosirius Red F3Ba with Polarization Microscopy, *Journal of Investigative Dermatology*, 50 (1968) 419-423.
- [333] L. C. U. Junqueira, G. Bignolas, and R. R. Brentani, Picrosirius Staining Plus Polarization Microscopy, A Specific Method for Collagen Detection in Tissue-Sections, *Histochemical Journal*, 11 (1979) 447-455.
- [334] L. Rich and P. Whittaker, Collagen and Picrosirius Red Staining: A Polarized Light Assessment of Fibrillar Hue and Spatial Distribution, *Brazilian Journal of Morphological Sciences*, 22 (2005) 97-104.
- [335] F. Sweat, ROSENTHA.SI, and H. Puchtler, Sirius Red F3Ba As Stain for Connective Tissue, *Archives of Pathology*, 78 (1964) 69-72.
- [336] H. Tullberg-Reinert and G. Jundt, In situ measurement of collagen synthesis by human bone cells with a Sirius Red-based colorimetric microassay: effects

References

- of transforming growth factor beta 2 and ascorbic acid 2-phosphate, *Histochemistry and Cell Biology*, 112 (1999) 271-276.
- [337] Tan, N. S., Alekseeva, T., and Brown, R. A. Roofed grooves: rapid layer engineering of perfusion channels in collagen tissue models, *J Biomater Appl*, 2014, 0885328214538865.
- [338] C. Guidry and F. Grinnell, Studies on the Mechanism of Hydrated Collagen Gel Reorganization by Human-Skin Fibroblasts, *Journal of Cell Science*, 79 (1985) 67-81.
- [339] V. Kaya, C. A. Utine, and O. F. Yilmaz, Intraoperative Corneal Thickness Measurements During Corneal Collagen Cross-Linking With Hypoosmolar Riboflavin Solution in Thin Corneas, *Cornea*, 31 (2012) 486-490.
- [340] C. B. Raub, V. Suresh, T. Krasieva, J. Lyubovitsky, J. D. Mih, A. J. Putnam, B. J. Tromberg, and S. C. George, Noninvasive assessment of collagen gel microstructure and mechanics using multiphoton Microscopy, *Biophysical Journal*, 92 (2007) 2212-2222.
- [341] Y. Barkana, Y. Gerber, U. Elbaz, S. Schwartz, G. Ken-Dror, I. Avni, and D. Zadok, Central corneal thickness measurement with the Pentacam Scheimpflug system, optical low-coherence reflectometry pachymeter, and ultrasound pachymetry, *Journal of Cataract and Refractive Surgery*, 31 (2005) 1729-1735.
- [342] L. J. Fried and H. A. Froot, Thickness Measurements of Silicon Dioxide Films Over Small Geometries, *Journal of Applied Physics*, 39 (1968) 5732-5735.
- [343] J. S. Kim, H. Ishikawa, M. L. Gabriele, G. Wollstein, R. A. Bilonick, L. Kagemann, J. G. Fujimoto, and J. S. Schuman, Retinal Nerve Fiber Layer Thickness Measurement Comparability between Time Domain Optical Coherence Tomography (OCT) and Spectral Domain OCT, *Investigative Ophthalmology & Visual Science*, 51 (2010) 896-902.
- [344] R. E. Norman, J. G. Flanagan, S. M. K. Rausch, I. A. Sigal, I. Tertinegg, A. Eilaghi, S. Portnoy, J. G. Sled, and C. R. Ethier, Dimensions of the human sclera: Thickness measurement and regional changes with axial length, *Experimental Eye Research*, 90 (2010) 277-284.
- [345] C. O'Donnell and C. Maldonado-Codina, Agreement and repeatability of central thickness measurement in normal corneas using ultrasound pachymetry and the OCULUS pentacam, *Cornea*, 24 (2005) 920-924.
- [346] V. M. Phillips and N. A. Smuts, Facial reconstruction: Utilization of computerized tomography to measure facial tissue thickness in a mixed racial population, *Forensic Science International*, 83 (1996) 51-59.

References

- [347] R. Taylor, J. Reynolds, B. Chikkana, D. Daly, R. A. Brown, and N. S. Tan, Dimensional characterisation of collagen constructs in situ, Proc. SPIE 8946, Optical Elastography and Tissue Biomechanics, 2014, 89460W.
- [348] A. P. Bunker, The Mandel-Cryer effect in chemoporoelasticity, International Journal for Numerical and Analytical Methods in Geomechanics, 34 (2010) 1479-1511.
- [349] E. Detournay and A. H. D. Cheng, Fundamentals of poroelasticity, in: C. Fairhurst (Ed.), Comprehensive Rock Engineering: Principles, Practice and Projects, Vol. II, Analysis and Design Method, Pergamon Press, 1993, pp. 113-171.
- [350] A. P. S. Selvadurai and A. Shirazi, Mandel-Cryer effects in fluid inclusions in damage-susceptible poroelastic geologic media, Computers and Geotechnics, 31 (2004) 285-300.
- [351] J. G. Zhu and J. H. Yin, Deformation and pore-water pressure responses of elastic viscoplastic soil, Journal of Engineering Mechanics-Asce, 127 (2001) 899-908.
- [352] Hadjipanayi, E. Engineering physical structure in biomimetic collagen scaffolds: strategies for regulating cell behaviour, 2010, University College London.
- [353] A. S. Hoffman, Hydrogels for biomedical applications, Advanced Drug Delivery Reviews, 54 (2002) 3-12.
- [354] M. Shibayama and T. Tanaka, Volume Phase-Transition and Related Phenomena of Polymer Gels, Advances in Polymer Science, 109 (1993) 1-62.
- [355] E. A. Abou Neel, U. Cheema, J. C. Knowles, R. A. Brown, and S. N. Nazhat, Use of multiple unconfined compression for control of collagen gel scaffold density and mechanical properties, Soft Matter, 2 (2006) 986-992.
- [356] Z. A. Saddiq, J. C. Barbenel, and M. H. Grant, The mechanical strength of collagen gels containing glycosaminoglycans and populated with fibroblasts, Journal of Biomedical Materials Research Part A, 89A (2009) 697-706.
- [357] M. Bitar, V. Salih, R. A. Brown, and S. N. Nazhat, Effect of multiple unconfined compression on cellular dense collagen scaffolds for bone tissue engineering, Journal of Materials Science-Materials in Medicine, 18 (2007) 237-244.
- [358] M. K. Hubbert, Darcy's law and the field equations of the flow of underground fluids, Int Associ Sci Hydrology, 2 (1957) 23-59.
- [359] C. M. Nelson and M. J. Bissell, Of extracellular matrix, scaffolds, and signaling: Tissue architecture regulates development, homeostasis, and

References

- cancer, *Annual Review of Cell and Developmental Biology*, 22 (2006) 287-309.
- [360] F. Pampaloni, E. G. Reynaud, and E. H. K. Stelzer, The third dimension bridges the gap between cell culture and live tissue, *Nature Reviews Molecular Cell Biology*, 8 (2007) 839-845.
- [361] I. B. Bischofs and U. S. Schwarz, Cell organization in soft media due to active mechanosensing, *Proceedings of the National Academy of Sciences of the United States of America*, 100 (2003) 9274-9279.
- [362] A. J. Engler, M. A. Griffin, S. Sen, C. G. Bonnetmann, H. L. Sweeney, and D. E. Discher, Myotubes differentiate optimally on substrates with tissue-like stiffness: pathological implications for soft or stiff microenvironments, *Journal of Cell Biology*, 166 (2004) 877-887.
- [363] J. Folkman and A. Moscona, Role of Cell-Shape in Growth-Control, *Nature*, 273 (1978) 345-349.
- [364] S. X. Hsiong, P. Carampin, H. J. Kong, K. Y. Lee, and D. J. Mooney, Differentiation stage alters matrix control of stem cells, *Journal of Biomedical Materials Research Part A*, 85A (2008) 145-156.
- [365] C. M. Lo, H. B. Wang, M. Dembo, and Y. L. Wang, Cell movement is guided by the rigidity of the substrate, *Biophysical Journal*, 79 (2000) 144-152.
- [366] R. J. Pelham and Y. L. Wang, Cell locomotion and focal adhesions are regulated by substrate flexibility, *Proceedings of the National Academy of Sciences of the United States of America*, 94 (1997) 13661-13665.
- [367] H. B. Wang, M. Dembo, and Y. L. Wang, Substrate flexibility regulates growth and apoptosis of normal but not transformed cells, *American Journal of Physiology-Cell Physiology*, 279 (2000) C1345-C1350.
- [368] S. C. Wittelsberger, K. Kleene, and S. Penman, Progressive Loss of Shape-Responsive Metabolic Controls in Cells with Increasingly Transformed Phenotype, *Cell*, 24 (1981) 859-866.
- [369] A. L. Bauer, T. L. Jackson, and Y. Jiang, Topography of Extracellular Matrix Mediates Vascular Morphogenesis and Migration Speeds in Angiogenesis, *Plos Computational Biology*, 5:7 (2009), e1000445.
- [370] S. L. Wilson, I. Wimpenny, M. Ahearne, S. Rauz, A. J. El Haj, and Y. Yang, Chemical and Topographical Effects on Cell Differentiation and Matrix Elasticity in a Corneal Stromal Layer Model, *Advanced Functional Materials*, 22 (2012) 3641-3649.
- [371] D. H. Kim, C. H. Seo, K. Han, K. W. Kwon, A. Levchenko, and K. Y. Suh, Guided Cell Migration on Microtextured Substrates with Variable Local Density and Anisotropy, *Advanced Functional Materials*, 19 (2009) 1579-1586.

References

- [372] J. L. Charest, L. E. Bryant, A. J. Garcia, and W. P. King, Hot embossing for micropatterned cell substrates, *Biomaterials*, 25 (2004) 4767-4775.
- [373] C. Y. Hui, A. Jagota, Y. Y. Lin, and E. J. Kramer, Constraints on microcontact printing imposed by stamp deformation, *Langmuir*, 18 (2002) 1394-1407.
- [374] H. Andersson and A. van den Berg, Microfabrication and microfluidics for tissue engineering: state of the art and future opportunities, *Lab on A Chip*, 4 (2004) 98-103.
- [375] J. T. Borenstein, H. Terai, K. R. King, E. J. Weinberg, M. R. Kaazempur-Mofrad, and J. P. Vacanti, Microfabrication technology for vascularized tissue engineering, *Biomedical Microdevices*, 4 (2002) 167-175.
- [376] R. Gauvin, Y. C. Chen, J. W. Lee, P. Soman, P. Zorlutuna, J. W. Nichol, H. Bae, S. C. Chen, and A. Khademhosseini, Microfabrication of complex porous tissue engineering scaffolds using 3D projection stereolithography, *Biomaterials*, 33 (2012) 3824-3834.
- [377] S. H. Lee, J. J. Moon, and J. L. West, Three-dimensional micropatterning of bioactive hydrogels via two-photon laser scanning photolithography for guided 3D cell migration, *Biomaterials*, 29 (2008) 2962-2968.
- [378] P. Zorlutuna, N. Annabi, G. Camci-Unal, M. Nikkhah, J. M. Cha, J. W. Nichol, A. Manbachi, H. J. Bae, S. C. Chen, and A. Khademhosseini, Microfabricated Biomaterials for Engineering 3D Tissues, *Advanced Materials*, 24 (2012) 1782-1804.
- [379] M. J. O'Brien, N. M. Keating, S. Elderiny, S. Cerda, A. P. Keaveny, N. H. Afdhal, and D. P. Nunes, An assessment of digital image analysis to measure fibrosis in liver biopsy specimens of patients with chronic hepatitis C, *American Journal of Clinical Pathology*, 114 (2000) 712-718.
- [380] Y. Huang, W. B. de Boer, L. A. Adams, G. MacQuillan, E. Rossi, P. Rigby, S. C. Raftopoulos, M. Bulsara, and G. P. Jeffrey, Image analysis of liver collagen using sirius red is more accurate and correlates better with serum fibrosis markers than trichrome, *Liver International*, 33 (2013) 1249-1256.
- [381] J. B. Michel, J. L. Salzmann, M. O. Nlom, P. Bruneval, D. Barres, and J. P. Camilleri, Morphometric Analysis of Collagen Network and Plasma Perfused Capillary Bed in the Myocardium of Rats During Evolution of Cardiac-Hypertrophy, *Basic Research in Cardiology*, 81 (1986) 142-154.
- [382] Anandagoda N., Ezra D.G., U. Cheema, Bailly M., and Brown R.A., Hyaluronan hydration generates 3D meso-scale structure in engineered collagen tissues, *Journal of the Royal Society Interface*, (2012), rsif20120164.
- [383] D. Falconnet, G. Csucs, H. M. Grandin, and M. Textor, Surface engineering approaches to micropattern surfaces for cell-based assays, *Biomaterials*, 27 (2006) 3044-3063.

References

- [384] A. Folch and M. Toner, Microengineering of cellular interactions, *Annual Review of Biomedical Engineering*, 2 (2000) 227-256.
- [385] S. Kobel, M. Limacher, S. Gobaa, T. Laroche, and M. P. Lutolf, Micropatterning of Hydrogels by Soft Embossing, *Langmuir*, 25 (2009) 8774-8779.
- [386] A. Mata, L. Hsu, R. Capito, C. Aparicio, K. Henrikson, and S. I. Stupp, Micropatterning of bioactive self-assembling gels, *Soft Matter*, 5 (2009) 1228-1236.
- [387] C. M. Nelson, J. L. Inman, and M. J. Bissell, Three-dimensional lithographically defined organotypic tissue arrays for quantitative analysis of morphogenesis and neoplastic progression, *Nature Protocols*, 3 (2008) 674-678.
- [388] L. Wang, S. K. Murthy, G. A. Barabino, and R. L. Carrier, Synergic effects of crypt-like topography and ECM proteins on intestinal cell behavior in collagen based membranes, *Biomaterials*, 31 (2010) 7586-7598.
- [389] R. A. Brown, R. Prajapati, D. A. McGrouther, I. V. Yannas, and M. Eastwood, Tensional homeostasis in dermal fibroblasts: Mechanical responses to mechanical loading in three-dimensional substrates, *Journal of Cellular Physiology*, 175 (1998) 323-332.
- [390] M. Eastwood, D. A. McGrouther, and R. A. Brown, Fibroblast responses to mechanical forces, *Proceedings of the Institution of Mechanical Engineers Part H-Journal of Engineering in Medicine*, 212 (1998) 85-92.
- [391] A. Glucksmann, The role of mechanical stresses in bone formation in vitro, *Journal of Anatomy*, 76 (1942) 231-239.
- [392] F. Guilak, D. M. Cohen, B. T. Estes, J. M. Gimble, W. Liedtke, and C. S. Chen, Control of Stem Cell Fate by Physical Interactions with the Extracellular Matrix, *Cell Stem Cell*, 5 (2009) 17-26.
- [393] B. M. Spiegelman and C. A. Ginty, Fibronectin Modulation of Cell-Shape and Lipogenic Gene-Expression in 3T3-Adipocytes, *Cell*, 35 (1983) 657-666.
- [394] L. Gao, R. McBeath, and C. S. Chen, Stem Cell Shape Regulates a Chondrogenic Versus Myogenic Fate Through Rac1 and N-Cadherin, *Stem Cells*, 28 (2010) 564-572.
- [395] P. D. Benya and J. D. Shaffer, Dedifferentiated Chondrocytes Reexpress the Differentiated Collagen Phenotype When Cultured in Agarose Gels, *Cell*, 30 (1982) 215-224.
- [396] H. Holtzer, J. Abbott, J. Lash, and S. Holtzer, The Loss of Phenotypic Traits by Differentiated Cells in Vitro .1. Dedifferentiation of Cartilage Cells, *Proceedings of the National Academy of Sciences of the United States of America*, 46 (1960) 1533-1542.

References

- [397] R. R. Lareu, K. H. Subrainhanya, Y. X. Peng, P. Benny, C. Chen, Z. B. Wang, R. Rajagopalan, and M. Raghunath, Collagen matrix deposition is dramatically enhanced in vitro when crowded with charged macromolecules: The biological relevance of the excluded volume effect, *Febs Letters*, 581 (2007) 2709-2714.
- [398] D. E. Ingber, Cellular mechanotransduction: putting all the pieces together again, *Faseb Journal*, 20 (2006) 811-827.
- [399] W. H. Guo, M. T. Frey, N. A. Burnham, and Y. L. Wang, Substrate rigidity regulates the formation and maintenance of tissues, *Biophysical Journal*, 90 (2006) 2213-2220.
- [400] A. J. Engler, S. Sen, H. L. Sweeney, and D. E. Discher, Matrix elasticity directs stem cell lineage specification, *Cell*, 126 (2006) 677-689.
- [401] K. Saha, A. J. Keung, E. F. Irwin, Y. Li, L. Little, D. V. Schaffer, and K. E. Healy, Substrate Modulus Directs Neural Stem Cell Behavior, *Biophysical Journal*, 95 (2008) 4426-4438.
- [402] Y. R. V. Shih, K. F. Tseng, H. Y. Lai, C. H. Lin, and O. K. Lee, Matrix Stiffness Regulation of Integrin-Mediated Mechanotransduction During Osteogenic Differentiation of Human Mesenchymal Stem Cells, *Journal of Bone and Mineral Research*, 26 (2011) 730-738.
- [403] J. Arrowsmith and P. Miller, Phase II and Phase III attrition rates 2011-2012, *Nature Reviews Drug Discovery*, 12 (2013) 568.
- [404] A. Mullard, 2012 FDA drug approvals, *Nature Reviews Drug Discovery*, 12 (2013) 87-90.
- [405] I. F. Uchegbu, L. Sadiq, M. Arastoo, A. I. Gray, W. Wang, R. D. Waigh, and A. G. Schatzleina, Quaternary ammonium palmitoyl glycol chitosan - a new polysoap for drug delivery, *International Journal of Pharmaceutics*, 224 (2001) 185-199.
- [406] E. Mansfield, T. L. Oreskovic, N. S. Rentz, and K. M. Jeerage, Three-dimensional hydrogel constructs for exposing cells to nanoparticles, *Nanotoxicology*, 8 (2014) 394-403.
- [407] J. Chen, J. Wang, Y. Zhang, D. Chen, C. Yang, C. Kai, X. Wang, F. Shi, and J. Dou, Observation of ovarian cancer stem cell behavior and investigation of potential mechanisms of drug resistance in three-dimensional cell culture, *J Biosci Bioeng*, 118 (2014) 214-222.
- [408] M. Hashimoto, H. Toshima, T. Yonezawa, K. Kawai, M. Iijima, and K. Endo, Evaluation of Silver Nanoparticle Toxicity to RAW264.7 Cells in a Three-Dimensional Cell Culture, *Journal of Biomaterials and Tissue Engineering*, 4 (2014) 51-58.
- [409] J. H. Sung and M. L. Shuler, In vitro microscale systems for systematic drug toxicity study, *Bioprocess and Biosystems Engineering*, 33 (2010) 5-19.

References

- [410] S. Aznavoorian, M. L. Stracke, H. Krutzsch, E. Schiffmann, and L. A. Liotta, Signal Transduction for Chemotaxis and Haptotaxis by Matrix Molecules in Tumor-Cells, *Journal of Cell Biology*, 110 (1990) 1427-1438.
- [411] S. M. Moghimi, A. C. Hunter, and T. L. Andresen, Factors Controlling Nanoparticle Pharmacokinetics: An Integrated Analysis and Perspective, *Annual Review of Pharmacology and Toxicology*, Vol 52, 52 (2012) 481-503.
- [412] J. A. Setterstrom, T. R. Tice, and W. E. Meyers, Development of Encapsulated Antibiotics for Topical Administration to Wounds, *Recent advances in drug delivery systems*, Springer US, (1984) 185-198.
- [413] S. R. Hamilton, S. F. Fard, F. F. Paiwand, C. Tolg, M. Veiseh, C. Wang, J. B. McCarthy, M. J. Bissell, J. Koropatnick, and E. A. Turley, The hyaluronan receptors CD44 and Rhamm (CD168) form complexes with ERK1,2 that sustain high basal motility in breast cancer cells, *Journal of Biological Chemistry*, 282 (2007) 16667-16680.
- [414] S. Nedvetzki, E. Gonen, N. Assayag, R. Reich, R. O. Williams, R. L. Thurmond, J. F. Huang, B. A. Neudecker, F. S. Wang, E. A. Turley, and D. Naor, RHAMM, a receptor for hyaluronan-mediated motility, compensates for CD44 in inflamed CD44-knockout mice: A different interpretation of redundancy, *Proceedings of the National Academy of Sciences of the United States of America*, 101 (2004) 18081-18086.
- [415] S. S. Li, J. Shi, L. Liu, J. J. Li, L. M. Jiang, C. X. Luo, K. Kamei, and Y. Chen, Fabrication of gelatin nanopatterns for cell culture studies, *Microelectronic Engineering*, 110 (2013), 70-74.
- [416] L. J. Yang, Y. C. Ou, The micro patterning of glutaraldehyde (GA)-crosslinked gelatin and its application to cell culture, *Lab on a Chip*, 5:9 (2005), 979-984.
- [417] J. P. Soleas, T. K. Waddell, A. P. McGuigan, Topographically grooved gel inserts for aligning epithelial cells during air-liquid-interface culture, *Biomaterials Science*, 3:1 (2015), 121-133.
- [418] K. Tsang, N. Annabi, F. Ercole, K. Zhou, D. J. Karst, F. Li, J. M. Haynes, R. A., Evans, H. Thissen, A. Khademhosseini, and J. S. Forsyth, Facile one-step micropatterning using photodegradable gelatin hydrogels for improved cardiomyocyte organization and alignment, *Advanced Functional Materials*, 25:6 (2014), 977-986.

List of Conference Abstracts

1. T Alekseeva, **NS Tan**, MH Purser and RA Brown. Multi-layered collagen scaffolds with engineered microchannels for skin tissue engineering applications. *European Cells and Materials* Vol. 22. Suppl. 3, 2011 (page 27) *Abstract*
Tissue and Cell Engineering Society (TCES) meeting. Leeds, UK, 2011.
2. T Alekseeva, **NS Tan**, MH Purser and RA Brown. Engineering a vascular bed for implant perfusion: 'roofed-micro-channels' within dense collagen scaffolds. *Tissue Engineering and Regenerative Medicine International Society (TERMIS) meeting*, Granada, Spain, 2011
3. **N Tan**, R Drake and RA Brown. Rapid fabrication of density gradient 3D collagen constructs. *European Cells and Materials* Vol. 22. Suppl. 3, 2011 (page 12) *Abstract*
Tissue and Cell Engineering Society (TCES) meeting. Leeds, UK, 2011
4. M Gonzalez Andrades, **NS Tan**, T Alekseeva, CA Mosse and RA Brown. Corneal stromal substitute by aligned multilayer of compressed native collagen: measuring and improving corneal transparency. *Journal of Tissue Engineering and Regenerative Medicine* (2012) 6 140 - 140. *Abstract*
Tissue Engineering and Regenerative Medicine International Society (TERMIS) meeting, Vienna, Switzerland, 2012.
5. **NS Tan** and RA Brown. Semi-quantitative method for collagen density analysis: use in rapid tissue fabrication.
Tissue Engineering and Regenerative Medicine International Society (TERMIS) meeting, Vienna, Switzerland, 2012.
6. T Alekseeva, **NS Tan**, HJ Levis and RA Brown. Rapid layer-engineering of a stromo-epithelial tissue: epilayering.

Tissue Engineering and Regenerative Medicine International Society (TERMIS) meeting, Vienna, Switzerland, 2012.

7. **NS Tan**, T Alekseeva and RA Brown. Semi-quantitative method for collagen density analysis: use in rapid tissue fabrication. *European Cells and Materials* Vol. 23. Suppl. 4, 2012 (page 27) *Abstract*
Tissue and Cell Engineering Society (TCES) meeting. Liverpool, UK, 2012
8. F Godarzi, **NS Tan** and RA Brown. Engineering a mimetic basement membrane: integration of laminin into plastic compressed collagen gels. *European Cells and Materials* Vol. 26. Suppl. 7, 2013 (page 58) *Abstract*
Tissue and Cell Engineering Society (TCES) meeting. Cardiff, UK, 2013
9. **NS Tan**, N Bedi, D Ossipov, J Hilborn, NL Tint, IF Uchegbu and RA Brown. Tissue engineered amniotic membrane substitute for drug delivery to the ocular surface. *European Cells and Materials* Vol. 26. Suppl. 7, 2013 (page 87) *Abstract*
Tissue and Cell Engineering Society (TCES) meeting. Cardiff, UK, 2013
10. **NS Tan**, X Yang, D Ossipov, J Hilborn and RA Brown. Assessing nanoparticles in an engineered 3D in vitro model tissue system. *European Cells and Materials* Vol. 26. Suppl. 7, 2013 (page 36) *Abstract*
Tissue and Cell Engineering Society (TCES) meeting. Cardiff, UK, 2013
11. **NS Tan**, N Bedi, D Ossipov, J Hilborn, NL Tint, IF Uchegbu and RA Brown. Tissue engineered drug delivery system for ocular surface treatment.
Tissue Engineering and Regenerative Medicine International Society (TERMIS) meeting, Istanbul, Turkey, 2013.
12. **NS Tan**, X Yang, D Ossipov, J Hilborn and RA Brown. Engineered 3D in vitro model tissue system to assess nanoparticle fate.
Tissue Engineering and Regenerative Medicine International Society (TERMIS) meeting, Istanbul, Turkey, 2013.

List of Publications

1. R Taylor, J Reynolds, B Chikkana, D Daly, RA Brown, **NS Tan**, "Dimensional characterisation of collagen constructs in situ", Proc. SPIE 8946, Optical Elastography and Tissue Biomechanics, 89460W (February 26, 2014).
2. **NS Tan**, T Alekseeva and RA Brown, Roofed grooves: rapid layer engineering of perfusion channels in collagen tissue models. J Biomater Appl 2014, 29(4):605-616.